University of Southern Queensland

Faculty of Health, Engineering and Sciences

Smart Composite Wind Turbine Blades
- A Pilot Study

A Dissertation Submitted by

Eris Elianddy Supeni, B.Eng.(Hons), M.Sc.(Mech. Eng.)

For the Award of

Doctor of Philosophy

2015

Abstract

Wind energy is seen as a viable alternative energy option to meet future energy demands. The blades of wind turbines have been long recognised as the most critical component of the wind turbine system. The turbine blades interact with the wind flow to turn the wind turbine, in effect acting as a tool to extract the wind energy and turn it into electrical energy.

As the wind industry continues to explore new technologies, the turbine blade is a key aspect of better wind turbine designs. Harnessing greater wind power requires larger swept areas. Increasing the length of the turbine blades increases the swept area of a wind turbine, thereby improving the production of wind energy. However, longer turbine blades significantly add to the weight of the turbine, and they also suffer from larger bending deflections due to flapwise loads. The flapwise bending deflections not only result in a lower performance of electrical power generation but also increase in material degradation due to high fatigue loads and can significantly shorten the longevity for the turbine blade.

To overcome this excessive flapwise deflection, it is proposed that shape memory alloy (SMA) wires be used to return the turbine blade back to its optimal operational shape. The work presented here details the analytical and experimental work that was carried out to minimise blade flapping deflection using SMA.

This study proposes a way to overcome the wind blade deflection using shape memory alloy (SMA) wires. A finite element model has been developed for the

simulation of the deflection response of a horizontal axis wind turbine blade using an SMA wire arrangement. The model was developed on the commercial finite element ABAQUS®, and focused on design and analysis, to predict the structural response. Experimental work was carried out to investigate the feasibility of the model based on a plate-like structure. An Artificial Neural Network (ANN) was used to predict the performance of the smart wind turbine blades.

From this study, the model of a smart wind turbine, incorporating SMA wires, was determined to be capable of recovering from large deflections. The coefficient of performance of the smart wind turbine blade was also determined to be higher than the coefficient for a conventional turbine blade. The results showed that by increasing the number of SMA wires, the actuation provided is sufficient to recover from significant blade deflection resulting in a significant increase in the lift produced by the blade. It was determined that the coefficient of performance for turbine blades with SMA wires is 0.45 compared to 0.42 for turbine blades without SMA. These findings will be a significant achievement in the development of a smart wind turbine blade.

It is expected that the use of smart wind turbine blades, incorporating SMA in their design, will not only increase the power output of the wind turbine but also prolong the lifetime of the turbine blade itself through a reduction of the bending deflections.

List of Publications Arising from this Study

Most of the discussion and results presented in the thesis are based on the following publications. Several passages in this thesis contain materials that have been copied verbatim, or with some adaptation, from thesis publications. All such copied materials were originally written by myself.

(i) Supeni E.E., Epaarachchi J.A., Islam M.M. and Lau K.T., "Smart Structure for Small Wind Turbine Blades", *The 4th International Conference on Smart Materials and Nanotechnology in Engineering (SMN2013)*, Hotel Grand Chancellor Surfer Paradise, Gold Coast, Queensland, Australia, Volume 8793, pp1–10, 10–12 July 2013, Society of Photo-Optical Instrumentation Engineers (SPIE) http://dx.doi.org/10.1117/12.2027725

(ii) Supeni E.E., Epaarachchi J.A., Islam M.M. and Lau K.T., "Genetic Algorithm Based for Artificial Neural Network for Predicting the Deflection of Self-Straightening Wind Turbine Blade", *The 3rd Malaysian Postgraduate Conference (MPC2013)* Sydney, New South Wales, Australia, MPC2013–27, pp233–242, 3–4 July 2013

(iii) Supeni E.E., Epaarachchi J.A., Islam M.M. and Lau K.T., "Development of Smart Wind Turbine Blades", *The 8th Asian-Australasian Conference on Composite Materials (AACM8)*, Petronas Kuala Lumpur Convention Centre,

Malaysia (KLCC), Kuala Lumpur, Malaysia, pp199–205, 6–8 November 2012, http://eprints.usq.edu.au/id/eprint/22295

(iv) Supeni E.E., Epaarachchi J.A., Islam M.M. and Lau K.T., "Design of Smart Structures for Wind Turbine Blades", *The 2nd Malaysian Postgraduate Conference (MPC2012)*, Bond University, Gold Coast, Queensland, Australia, pp20–36, 7–9 July 2012 , http://eprints.usq.edu.au/21673

(v) Supeni E.E., Epaarachchi J.A., Islam M.M. and Lau K.T., "Design and Analysis of a Smart Composite Beam for Small Wind Turbine Blade Construction", *The Southern Region Engineering Conference (SREC)*, USQ, Toowoomba, Australia, 1 September 2012

(vi) Supeni E.E., Epaarachchi J.A., Islam M.M. and Lau K.T., "Smart Structure Wind Blade", *Fibre-Reinforced Composites Development and Applications in Renewable Energy Workshop* , Composites Australia, USQ Toowoomba, Queensland, Australia, 4 June 2012

(vii) Supeni E.E., Epaarachchi J.A., Islam M.M. and Lau K.T., "Development of Smart Wind Turbine Blades", *Engaged Research Evening Posters*, Toowoomba, Queensland, Australia, 26 April 2012

(viii) Supeni E.E., Epaarachchi J.A., Islam M.M. and Lau K.T., "Development of Artificial Neural Network in Predicting Performance of the Smart Wind Turbine Blade", *Journal of Mechanical Engineering and Sciences (JMES)*, ISSN (Print): 2289-4659; e-ISSN: 2231-8380; Volume 6, pp. 734-744, June 2014

Certification of Dissertation

I certify that the ideas, designs and experimental work, results, analyses and conclusions set out in this dissertation are entirely my own effort, except where otherwise indicated and acknowledged. The work is original and has not been previously submitted for assessment in any other course or institution, except where specifically stated.

ERIS ELIANDDY SUPENI, B.ENG.(HONS), M.SC.(MECH. ENG.)

W0106520

_____

Signature of Candidate

Date

ENDORSEMENT

Supervisory Team

_____   _____

Dr. Jayantha A. Epaarachchi   Dr. Md. Mainul Islam

Signature of Principal Supervisor   Signature of Associate Supervisor

Date   Date

_____

Prof. Dr. Alan Kin-tak Lau

Signature of Associate Supervisor

Date

Acknowledgments

I would like to thank Dr. Jayantha Epaarachchi, who served as a supervisor of my thesis committee and as my advisor for the last three years. He has been there for me through thick and thin; we have had long conversations about school and research. I consider him a great advisor, an excellent mentor, and a caring friend. I also want to thank Dr. Md. Mainul Islam and Prof. Alan Kin-tak Lau for serving on my committee and for offering their knowledge through meetings and words of encouragement throughout my time at USQ. I thank my fellow Dr. Gayan, Dr. Hafizi, Dr. Muhamad, Dr. Zamir, Wayne, Martin, Dr. Salahudin, Anthony and CEEFC USQ Australia members for their support, and last but not least the Malaysian Government Scholarships. Not forgotten, thank God Almighty, who has given me strength and energy for my daily life. Special thanks also go to my parents, Supeni, Norhanah, late Mohd Yusoff and Mariam, who have always praised me when I was doing well and offered support and motivation when I was down. I must also thank my wife, Yusmaria, for always standing by my side and keeping me focused during times of stress and distraction. My children Nazmeen, Nazim and Nuha, who provided me with unconditional advice and love. Finally, I wish to thank a group of people whom I never met, but I have widely used their products, the ABAQUS/CAE team, MATLAB team, LaTeX group, WinEdt, TeXstudio, among others, who provide free-open source software package to the community.

ERIS ELIANDDY SUPENI, B.ENG.(HONS), M.SC.(MECH. ENG.)

University of Southern Queensland

22 July 2015

Contents

Chapter 3 FEA Model and ANN Model Development 93

List of Figures

List of Tables

Notation

α	angle of attack, °
θ	angle of twist, °
υ	Poison ratio
σ	stress, Pa
Γ	vortex strength
W_A	resultant velocity, ms^{-1}
r	radius of the blade section considered, m
Ω	rotational speed of the turbine, $rads^{-1}$
U_0	velocity of the wind at tip, ms^{-1}
λ	tip speed ratio
ρ	density of air, kgm^{-3}
C_p	coefficient of power
$\triangle A$	small portion area of a wind turbine blade
L_A	lift force, N
V	wind velocity, ms^{-1}
$at.wt.$	atomic weight
A_s	austenite start, °C
A_f	austenite finish, °C

M_s	martensite start, °C
M_f	martensite finish, °C
$Ac_{func.}$	active functional
ε_m^y	martensite twin strain
ε_m^d	martensite detwin strain
ε_m^y	martensite twin strain
ε_m^d	martensite detwin strain
E	Young's Modulus, MPa
$E_{m,t}$	Young's Modulus twin, MPa
$E_{m,d}$	Young's Modulus detwin, MPa
Δ	percentage difference, %
W	width, mm
D	depth, mm
H	height, mm
NW	number of SMA wires
L	applied load, N
I	applied current, Amp
N	line of vortices
d	deflection, mm
V	voltage, V
w	power, W
P_{wt}	power extracted from the wind, kW

Acronyms and Abbreviations

ANN	artificial neural network
AuCd	Aurum Cadmium
AuCu	Aurum Copper
BET	Blade Element Theory
CAD	computer aided design
CAE	computer aided engineering
CEEFC	Centre of Excellence Engineered in Fibre Composite
CuZn	Copper Zinc
EPS	expanded polystyrene
EWEA	European Wind Energy Association
FEA	finite element analysis
GFRP	glass fibre-reinforced polymer
GUI	graphical user interface
HAWT	horizontal axis wind turbine
IGES	initial graphics exchange specification
LM	Lavenberg-Marquardt
LVDT	linear variable differential transformer
MATLAB	Matrix Laboratory
MBP	multi-back propagation
ML	machine learning

MLP	multi-layer perceptron
MSE	mean square error
NARX	Non-linear autoregressive with Exogenous
NiTi	Nickel Titanium
NACA	National Advisory Committee for Aeronautics
Nitinol	Nickel Titanium Ordnance Laboratory
NREL	National Renewable Energy Laboratory
N/A	not applicable
PPE	personal protective equipment
PVC	Polyvinyl Chloride
R	correlation coefficient factor
SMA	shape memory alloy
SME	shape memory effect
SE	superelasticity
TSR	tip speed ratio
USQ	University of Southern Queensland
UPM	Universiti Putra Malaysia
UD	unidirectional
VAWT	vertical axis wind turbine

Chapter 1

Introduction

Meeting the world's growing energy demands in line with preserving the environment has led to great progress in the field of renewable energy or so-called green energy. According to the Environmental Impact Assessment International Energy Outlook, the global energy demand is expected to almost double by 2030. Population and income growth are the key drivers behind the growing demand for energy (*BP Energy outlook 2030* 2013).

Renewable energy generation in Australia has been supported by a range of measures to assist in the research and development of new technologies and the deployment of newly commercialised technologies. The main support measure driving the deployment is the Renewable Energy Target (RET) Scheme.

Considering that conventional energy production is the single largest producer of greenhouse gases, the opportunities for renewable energies have potential for vast renewable energy capabilities. More than 66 countries have renewable energy policy targets to meet. The Australian Government has set a target of 20 % by 2020, which will require 10 % of Australia's electricity to be generated from renewable sources including wind power, solar power, hydropower and bio-agricultural waste power.

Figure 1.1 depicts the Australian RET scheme. The enhanced RET scheme commenced on 1 January 2010 and was projected to deliver more than 45,000 gigawatt hours of electricity in 2020. It is expected to cost more than AUD\$ 20 billion in investment over the next decade (ACEC 2012*b*).

Figure 1.1: Australian Renewable Energy Target: 20 % by 2020 (ACEC 2012*b*)
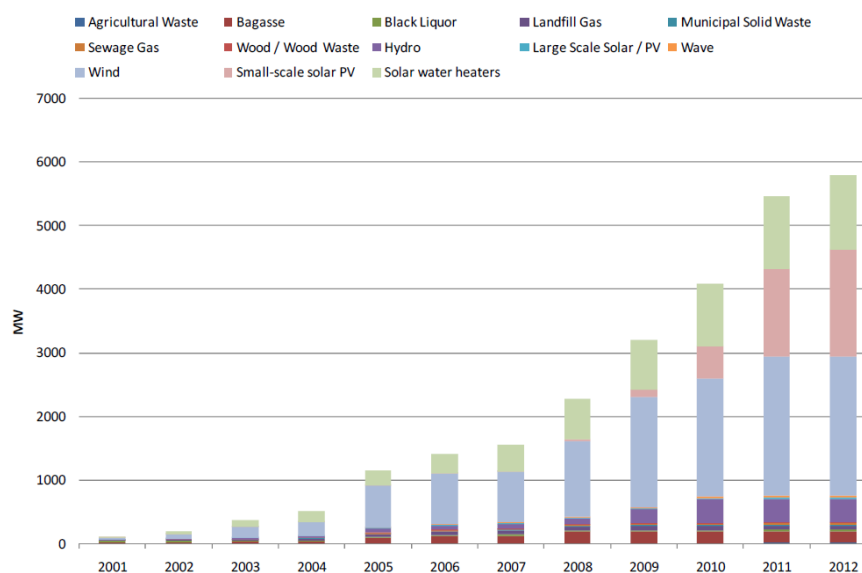
Figure 1.2: Renewable capacity installed since 2001 (ACEC 2012*a*)

As shown in Figure 1.2, renewable energy has predominantly been through wind generation, which accounted for approximately 38 % of the capacity installed since 2000, followed by small scale solar water heaters and small-scale photo-voltaic

(PV) systems which accounted for approximately 20% and 29 % , respectively. Biomass capacity comprised approximately 6 %, and new hydroelectric capacity (mainly from upgrades to existing systems) also comprised approximately 6 % of the installed capacity. Wind energy, which has been considered as lower cost, has been the dominant large scale technology under the RET with nearly 2,200 MW of wind farms developed (ACEC 2012a). This significant deployment has resulted in technological developments, including an increase in capacity and an improvement in accessibility.

1.1 Background and Significance

Nowadays, wind power technology is not new in any fundamental way, but rather the rediscovery and development of a technology with considerable heritage. It was initially ignored since the world went through the era of industrialisation. It has been proven in the past that it was used to capture the wind in order to generate power. Historically, wind energy has been utilised for at least 30 centuries, mainly for agricultural purposes. In naval transportation services, the wind has been an essential source of power. Wind energy was once an integral part of rural activities and became almost obsolete with the advent of low-cost fossil-fuelled stationary engines, and then the spread of rural electrification (Musgrove 2010).

The rotor of the wind turbine needs some sort of aerodynamic profile device, e.g., a wing or turbine blade with an aerodynamic shape, to be able to rotate. As expected, the density of the air is less than water density, and this leads to the large size of a wind turbine. Ultimately, the blade radius reflects the efficiency of the operational wind turbine in an attempt to capture as much wind as possible (Griffth & Ashwill 2011, Jensen et al. 2006).

Theoretically, the performance of the wind turbine has a maximum achievable value of 59.3 % (Betz limit). This value has been discovered by Frederic Lanchester,

a British aeronautical pioneer in 1915, and has been extensively reviewed by Albert Betz, a German aerodynamicist, in 1919 based on the well-known actuator disc theory (Eggleston & Stoddard 1987). The power coefficient of a rotor varies with the tip speed ratio and is only a maximum for a unique tip speed ratio. Incremental improvements in the power coefficient are continually being sought by detailed design changes of the rotor and by operating at variable speed it is possible to maintain the maximum power coefficient over a range of wind speeds. However, these measures will give only a modest increase in power output. Major increases in the output power can only be achieved by increasing the swept area of the rotor or by locating the wind turbines on sites with higher wind speeds.

The big argument for a size limit for wind turbines is based on the square-cube law which has been debated for a long time. The square-cube law, an idea first mentioned by Galileo (1638) in his publication entitled, *"Discourses and Mathematical Demonstrations Relating to Two New Sciences,"* practically this concept may relate to the physical and engineering basis with economies of scale. It is stated that as a wind turbine rotor increases in size, its energy output increases as the rotor-swept area (the diameter squared), while the volume of material, and therefore its mass and cost, increases as the cube of the diameter (Burton et al. 2011). In other words, at some size the cost for a larger turbine will grow faster than the resulting energy output revenue, making scaling a losing economic game. Therefore, many researchers have tried to exploit the square-cube law by changing the design rules with increasing size and removing material or by using material more efficiently either using new material or advanced material to trim weight and cost.

1.2   Problem Statement

Wind turbine blades are an important component of a wind turbine since they are responsible for converting the kinetic energy of the wind into the required

rotational motions for electrical generation. The importance of the turbine blade is such that an increase in the turbine blades efficiency would potentially result in an increase in the wind turbine efficiency as well. Efforts to increase the efficiency of the turbine blade are complicated by the combination of the varying aerodynamic effects acting on the blades and the structural stresses on the blades due to its shape. The shape of the turbine blades becomes increasingly important given the tendency of current blade design to be longer and thinner than past blade designs. Analysis of turbine blades is typically carried out using the actuator disk theory, an idealised model of the usable wind energy flowing over the turbine blades which will never be realised in the real operation of wind turbines. Based on the theory, it is impossible to extract more than 59 % of the useable amount of wind energy under ideal conditions. Previous studies of wind turbine performance utilised blade element theory in conjunction with actuator disk theory to predict the wind turbine blade performance. However, significant hurdles remain, especially when attempting to optimise the performance of wind turbine blades made from composite materials.

A composite turbine blade consists of two sides (suction side and pressure side) joined together by adhesives and stiffened by many shear webs (I section) or by a box beam (box spar). The blades are subjected to many types of loading such as: flapwise and edgewise bending, gravitational forces, tensile loading or axial loading as well as loads due to pitch acceleration. Edgewise bending is caused by gravitational forces and the torque of the blade while flapwise bending is due to differences in the air pressure. It has been determined that flapwise bending of the turbine blades plays an important part in determining the efficiency of the turbine blade, and ultimately the efficiency of the wind turbine. This is especially true for modern composite turbine blades design, which are typically longer and thinner, and made as light as possible. Together, the current trend in blade design is limited by the need for structural stiffness in the blade itself so that it is able to resist flapwise bending when in operation. Thus, current research efforts have focused on alternative methods to resist flapwise bending in turbine blades, which

would allow for thinner and longer turbine blade designs to be utilised. One promising area of research is the incorporation of Shape Memory Alloys (SMA) in the turbine blades, which are used as actuators to resist flapwise bending of the blades. The incorporation of SMAs in the turbine blade would pave the way for a new generation of thinner and more lightweight wind turbine blades that are able to better resist flapwise loads.

To determine the feasibility of incorporating SMAs as actuators to resist flapwise bending in turbine blades, a proof of concept experiment and associated Finite Element Analysis (FEA) and Artificial Neural Network (ANN) modelling were carried out in this project. Since the most important physical phenomenon under consideration is bending, the current work has assumed for simplicity, without any loss of generalisation, that the turbine blade can be modelled as a plate-like structure subjected to deflection. SMAs are then placed in different configurations on the beam to resist the bending deflection. The results are analysed, and used to verify and refine the FEA model.

1.3 Objectives of the Project

The steps taken here are to use SMA on an existing turbine blade with bending and deflection recovery action which can at least return the blade to its original form. Designing an entire smart turbine blade is not the output of the work here. The current research is primarily concerned with an innovation involving the development of a component which can be used in a thin reinforced composite wind blade turbine which is capable of maintaining performance and addressing the bending and deflection issue.

For this purpose, independent experiments were performed using SMA to demonstrate the feasibility and the effectiveness of any form of deflection to restore the original shape when a force is applied.

Associated models have been identified for the purpose of the implementation of the system as a whole. In this context, the plate-like structure model is seen to have the same features in common which are relevant to the pilot study. Towards achieving the main objective, the related aims associated are identified as follows:

(i) To determine the feasibility of using SMA wires as an actuator for a smart wind turbine blade concept to reduce flapping;

(ii) To model the smart wind turbine blade concept as a plate-like structure to allow the performance parameters to be analysed.

1.4 Research Gap and Innovation

The main objective of this project is to develop the potential of smart material application in composites for wind turbine blades, based on the plate-like structure that can alleviate or release the composite stress upon deflection by self-straightening the blade to be as close as possible to its original shape. Ultimately, the goal is to evaluate the structural analysis and incorporate it into a conceptual design which can be further enhanced for a new generation of smart blades.

Due to the limited scope of this study, it was not possible to manufacture the full scale of the actual wind turbine blade. Thus, a conceptual design prototype that imitates the principle of the beam structure has been implemented based on the cantilever plate using a plate-like structure.

Finite element analysis was used as a tool to optimise the analysis before commencing the experimental work. Simulation in FEA using ABAQUS 6.12® has been developed to imitate the model as close as possible for purpose of analysis.

After modelling, prediction using artificial neural networks (ANN) was carried out using the MATLAB® Neural Network toolbox. In this model, the correlation of

the parameters' data that was collected has been simulated to see the relationship correlation between the input and output values.

The result prediction of the work has been simulated using an ANN approach through using the NARX tool to predict the material and structural analysis response to deflection loading. Methods of obtaining data, such as the applied electrical current and the number of SMA wires, are also discussed. The information presented in this study will assist in the design of smart wind turbine blade composite structures for optimum efficiency and to combat fatigue, though it will be necessary to characterise the material combination and manufacturing process used at the detailed design stage.

Finally, structural analysis has been performed to quantify whether the expected desired outcome meets the actual operating condition. The expected outcome from this research is to manufacture new generation small smart blades which can overcome the operational distortions to the airfoil shape and the structural and property degradations of material that causes the loss of output energy of the wind turbine.

The innovations introduced are as follows:

(i) Use of SMA to minimise deflection and increase the lifetime of the blade;

(ii) Reduced deflections, which increase the power output and decrease the losses;

(iii) Reduced dependence on the electricity produced by fossil fuels by using natural resources, and decreased CO_2 emission.

1.5   Organisation of the Thesis

This thesis report is organised into six chapters which are as follows:

Chapter 1: begins with some general background, the problem statement, significance, objectives and expected outcomes;

Chapter 2: addresses the literature review regarding the analysis of wind turbine blade performance, the use of SMA, and the proposed concept of the smart wind turbine blade;

Chapter 3: discusses the FEA model and the ANN model development;

Chapter 4: describes the experimental setup;

Chapter 5: analyses the results and provides a discussion;

Chapter 6: provides some conclusions and gives recommendations for further work.

This study is concerned with the application of smart material in enhancing the structural mechanics to tackle the deformation phenomenon of wind turbine blades. The design approach concerning embedding and mounting a smart material have also been discussed. The novelty of the project is based on the modelling of the strip (plate-like structure) of material which is currently implemented in the existing blade. The combined data from experimental works, finite element modelling as well as artificial neural networks has been obtained to meet the objective of this study.

Figure 1.3 depicts the flow of the project. The flow is divided into two categories which are the current approach and the innovative approach.
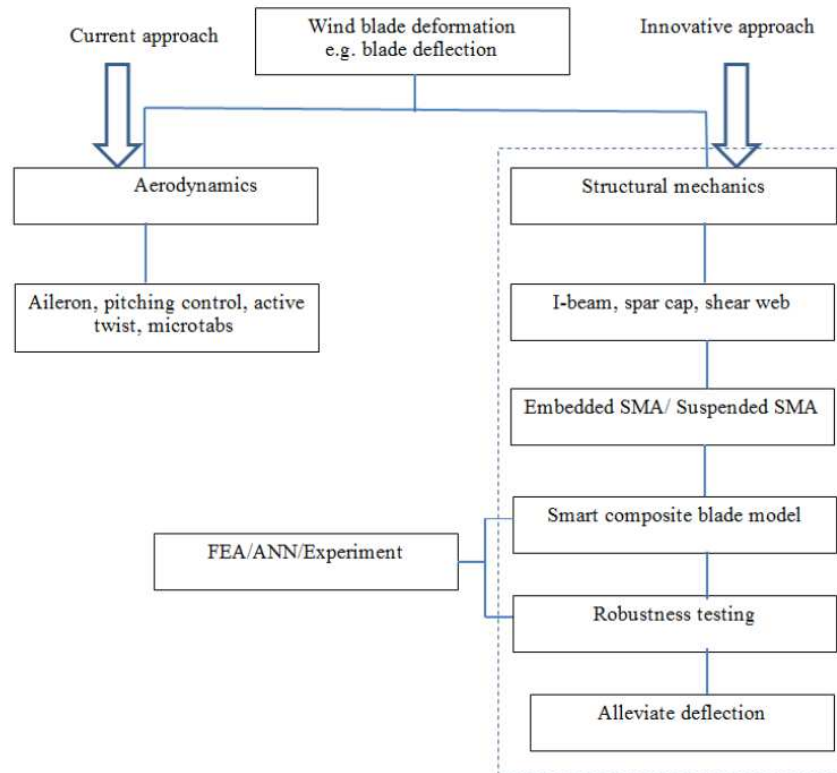
Figure 1.3: Innovative approach of the smart structure in a wind turbine blade

Chapter 2

Literature Review

2.1 Introduction

In order to understand, and place the research area into perspective, a rigorous study has been undertaken. A selection of relevant papers is reviewed. This investigation served as a basis and starting point for several decisions made during the research project. This chapter reviews the working mechanisms of the wind turbine such as aerodynamics, the development of the wind turbine, wind turbine blade construction, and the challenges and future direction of wind turbines. Next, the proposed conceptual model has also been discussed. A summary of this review chapter is presented in the final section, highlighting the research direction of the current thesis.

2.1.1 History of Wind Turbines

Wind turbines have been in use for several centuries, since early in 1600, especially for irrigation purposes, and are still operational now. Dutch windmills utilised a blade with sail canvas fabric and the low speed drag type of wind turbine.

Although today's modern technology has firmly, and maturely, established the description of a wind turbine as the prime mover of a wind machine capable of being harnessed for a number of different applications, none of which are concerned with the milling of grain or other substances (at least in industrialised countries), the term windmill was used for the whole system up to recent times, whatever its duty, be it generating electricity, pumping water, or sawing wood. Since here the historical development of the wind machine is considered, it is convenient and has a certain logic in it to retain its term, i.e. windmill in its historic sense (Nelson 2009). However, this lies in the fact that the vertical-axis Persian windmills never came into use in Europe. At the end of the twelfth century, there was an emergence of a completely different type - a horizontal-axis windmill. This development presents the future generation in the technical development of the wind turbine, which has existed several thousands years since the invention left by the Persian vertical-axis windmills (Spera 2009).

Before the invention of the European countries, horizontal-axis windmills were designed by Ebullz (1153) from Artuk Turks and were used in the region of Diyarbakir in the 1200's. However, Northwest Europe, particularly the Netherlands, France, Germany and Great Britain are considered to be the first regions that developed the most effective type of windmill, one in which the shaft carrying the sails was oriented horizontally rather than vertically as in the Persian mill. In a relatively short time, tens of thousands of the so called horizontal-axis European windmills were in use for nearly all mechanical tasks, including water pumping, grinding grain, sawing wood and powering tools. The cruciform pattern of their sails prevailed for almost 800 years, from the twelfth to the twentieth century (Spera 2009).

The horizontal-axis windmill was a considerably more complex mechanism than the Persian vertical-axis windmill since it presented several engineering problems. The three major problems are: transmission of power from a horizontal rotor shaft to a vertical shaft, on which the grindstones were set, turning the mill

into the wind, and stopping the rotor when necessary. But the adoption of the horizontal-axis windmill is readily explained by the fact that it was so much more efficient (Harrison et al. 2000).

In the historical development of windmills, a very innovative step that warrants somewhat more attention than it has received, must be considered: the use of horizontal-axis windmills instead of vertical-axis ones. Although the right angle gear mechanism allowed the rotor axis to be transposed from vertical to horizontal, the action of the sails also had to be turned through 90°.

This was revolutionary because it meant that a simple, straightforward push of the wind on the face of the sail was replaced by the action of the wind in flowing smoothly around the sail, providing a force normal to the direction of the wind. As a concept, it is a sophisticated one that was not fully developed until the advent of the airplane at the end of the 19th century, and the engineering science of aerodynamics (Manwell et al. 2009).

An innovative type of wind turbine rotor, the Savonius rotor, was named after its inventor, the Finnish engineer S.J. Savonius. This is illustrated in Figure 2.1. The inventor's interest had been aroused by the Flettner rotor ship with its large, rotating cylindrical sails. Wind passing over these cylinders created lift by the Magnus effect, which propelled the ship forward. He was intrigued by the possibility of substituting wind power for the external motor power used to rotate these cylinders on the Flettner ship. His experiments resulted in a rotor with an S-shaped cross section which, in its simplest form, could be constructed by cutting a circular cylinder in half longitudinally and rejoining the opposite edges along an axle. Different types of turbine are given in Figure 2.1.

Another innovative rotor design introduced in the early 1930s was a type of vertical-axis turbine invented by F.M. Darrieus. The Darrieus rotor, which has two or three curved blades attached to the top and bottom of a central column, accepts the wind from all directions without yawing. This column rotates on
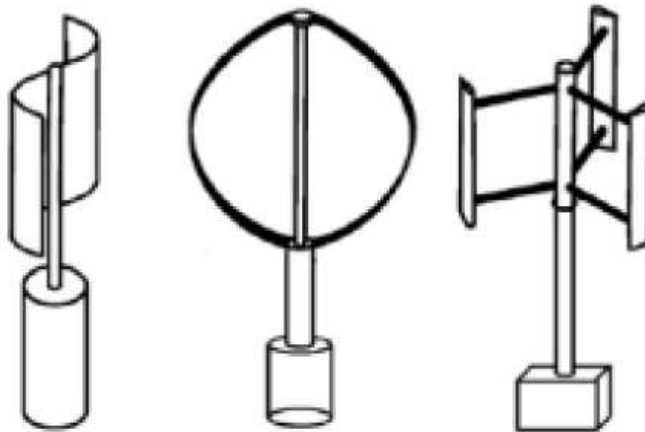
Figure 2.1: Types of wind turbine - from left, Savonius, Darrieus and
H-Rotor (Sandra et al. 2008)

upper and lower bearings, and transmits torque from the blades to the power
train, which is located below the rotor, where the maintenance is easier, and the
weight is not quite so important (Sandra et al. 2008).

The transition from windmills supplying mechanical power to wind turbines
producing electrical energy took place during the last 12 years of the 19th century.
The initial use of wind for electric generation, as opposed to mechanical power,
included the successful commercial development of small wind generator research,
and experiments using large turbines. The advent, and development of the airplane
in the first decades of the 20th century gave rise to deep analysis, and design
studies of the propeller, which could immediately be applied to the wind turbine
(Manwell et al. 2009).

The primary application of wind turbines is to generate energy from the wind.
Hence, aerodynamics is a very important aspect in the design of wind turbine
blades. The aerodynamic profiles of wind turbine blades have a vital impact on
the aerodynamic efficiency of a wind turbine.

Overall, the details of the aerodynamics depend very much on the geometrical
shape or profile of the blades. There are still some fundamental concepts that

apply to all turbines. Every blade profile has a maximum power for a given flow, and some shapes are better than others. The method used to extract power has a strong influence on this. In general all turbines can be grouped as being lift-based, or drag-based with the former being more efficient. The difference between these groups is the aerodynamic force that is used to extract the energy.

The most commonly used turbine blades are in the horizontal-axis wind turbine. The blades generate a high lift force resulting in very good performance. Accordingly, it is popular for commercial applications, and much research has been applied to this turbine. Towards the 20th century the Darrieus wind turbine was another popular lift-based alternative, but is rarely used today. In principle, the Savonius wind turbine operates based on a drag mechanism, and despite its low efficiency, it is used because it is robust and simple to build and maintain.

As discussed earlier, a wind turbine is a device that converts the power of the wind into electricity. This is in contrast to a windmill, which is a machine that converts the wind's power into mechanical power. It generally does this by using the basic aerodynamic force of drag to produce a net positive torque on a rotating shaft, resulting in the production of mechanical power. There are two great classes of wind turbines, horizontal and vertical axis wind turbines. Conventional wind turbines, horizontal-axis wind turbines (HAWT), rotate about a horizontal axis. As the name implies, a vertical-axis wind turbine (VAWT) rotates about a vertical axis.

2.2 Wind Turbine Blade Geometry

A Sandia WindPACT Blade System Design Study (BSDS) produced several innovations for large blades (Dam et al. 2005). As part of this study, the TPI-Dynamic Design-UC Davis team came up with the idea of using very thick airfoils with significantly expanded trailing edge thicknesses at the root to enhance the

structural capability. Led by Case van Dam of UC Davis, the team performed a systematic investigation into the use of a series of inboard airfoils whose thickness and trailing-edge flap could be adjusted independently to give a constant thickness for the spar cap and trailing-edge spline. This series of airfoils was developed from high-lift inboard NREL airfoils, and the LS-1 series airfoils. Representative inboard section shapes are shown in Figure 2.2a and are labeled as flatback airfoils to denote the lift-enhancing trailing edge flat.
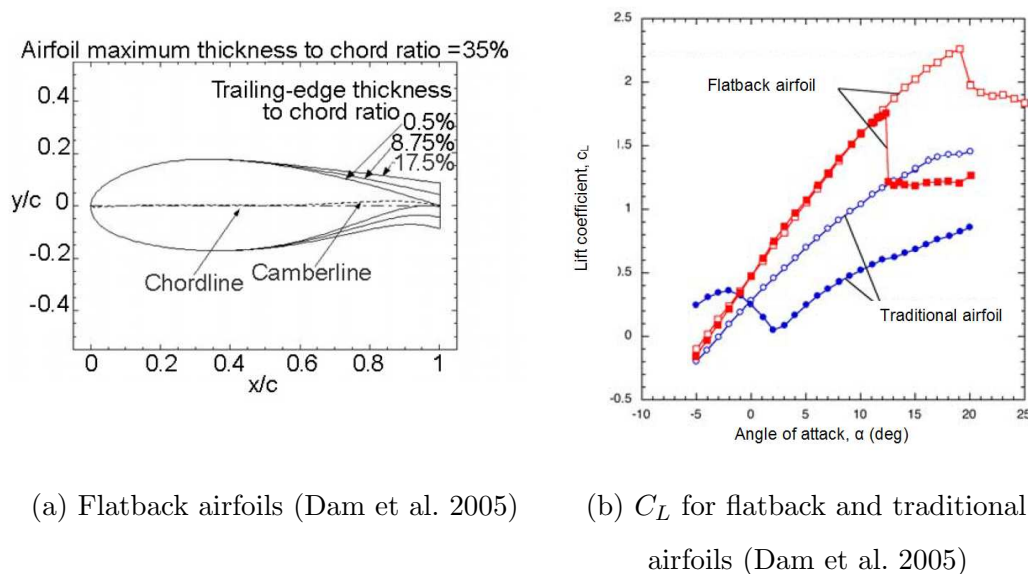
(a) Flatback airfoils (Dam et al. 2005)

(b) C_L for flatback and traditional airfoils (Dam et al. 2005)

Figure 2.2: Flatback development

Figure 2.2b illustrates the comparison of the coefficient of lift, C_L between the flatback compared to the traditional type of airfoil. These airfoils have the potential for decreasing coefficient because the thicker sections allow for a lighter blade (higher moment of inertia) and increased lift characteristics could allow for enhanced performance. However, the drag is also increased, and it is expected that trailing edge treatment, such as splitter plates, may be required to reduce the increased drag.

At present, summary reports have been published for aerodynamics control mechanisms, actuator selection, smart materials and the feasibility for wind turbine control. Among the most famous reports were those from Chopra (2002) and

Straub (1996) where all the available concepts were analysed, particularly the control concept; pitch control, twist control, camber control and a movable control device (trailing edge flaps or servo tabs actuated by smart materials) are recommended. A 1.83 m diameter scaled wind turbine smart tip wind turbine blade actuated with a piezo-induced bending-torsion couple composite beam has been developed by Chopra (2002). This showed potential control suppression vibration due to flapping deflection. Furthermore, Chopra (2002) investigated the use of SMA in a blade section model with tabs actuated by SMA wires. He demonstrated that the performance was good in terms of deflection.

The most recent in active control smart devices is that of the ADASYS project (a joint venture task between Eurocopter, EADS CRC, Daimler Chrysler Research Labs and DLR) (Enekl et al. 2002, Roth et al. 2006)

An actively actuator full-scale rotor was developed based on a BK117/EC145 utilising controlled piezoelectric actuated trailing edge flaps (Figure 2.3a, 2.3b). The system was tested during flight and showed excellent performance in reducing vibratory loads by 50–90 %.
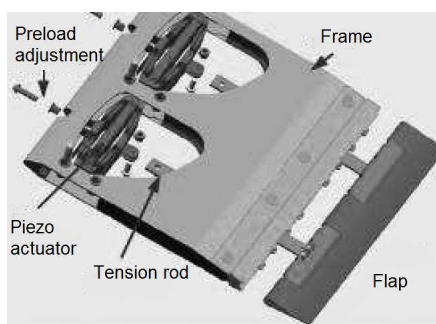
(a) Layout of the piezoelectric actuated developed in ADASYS (Enekl et al. 2002)

(b) Actively controlled piezoelectric actuated on the BK117 blade (Roth et al. 2006)

Figure 2.3: Controlling smart blades using piezoelectric

The use of aerodynamic control surfaces (trailing edges, tabs and moving tips) on the blades gives the advantage of faster control with smaller deflections (due to the

large leverage near the blade tip) for the reduction of blade root moments, without using full blade pitching, which is inefficient due to the use of the swashplate and the larger inertia.

Furthermore, a significant attempt was made to use embedded actuation on the blades which resulted in shape morphing (camber control) or twisting (active twist) as shown in Figure 2.4a. A prototype profile section of 2 m was mounted with 36 piezoelectric actuators at 10 % chord length. The idea comes from the Gurney flap in which active control microtabs were used. Microtabs are small (deployment height in the order of the boundary layer thickness) translational devices placed near the trailing edge of the airfoil as illustrated in Figure 2.4.

Microtabs are particularly attractive because of their simple shape and quick response. Simulations have shown that they exert significant control authority, but many challenges must be resolved before the economic feasibility of such devices can be demonstrated. Tabs are typically deployed approximately perpendicular to the airfoil surface, at a height that is about equal to the thickness of the boundary layer (1–2 % chord) (Nakafuji et al. 2002). The deployment effectively alters the camber as shown in Figure 2.4b, which depicts streamlines around an airfoil with microtabs from computation simulations. Deployment on the pressure side of the airfoil increases lift, and suction side deployment mitigates lift. Research efforts to study microtabs have been ongoing at UC Davis since the late 1990s (Baker et al. 2005).

(a) Thunder piezoelectric actuator
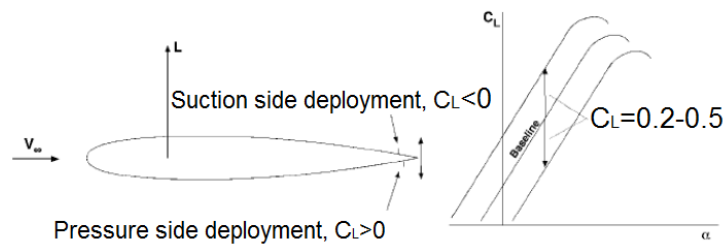
(b) Performance curve using microtab
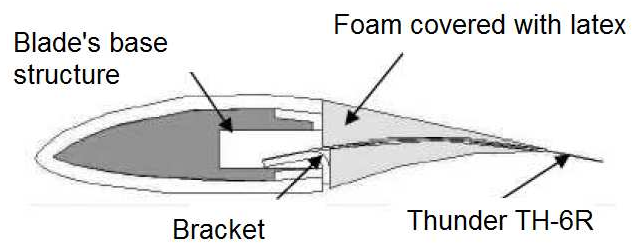
(c) Microtab concept

Figure 2.4: Smart blade concept (Bak et al. 2007)

Other developments are shown in Figure 2.5, which include bend-twist coupling, aileron, changing shape and microtab.
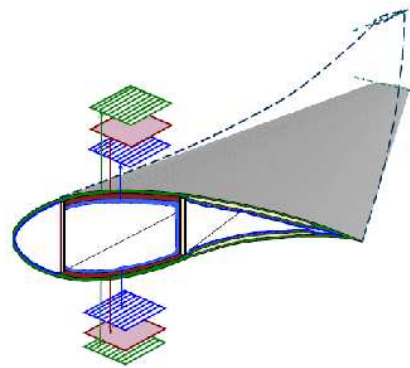
(a) Bend-twist

(b) Aileron

(c) Airfoil with changing shape
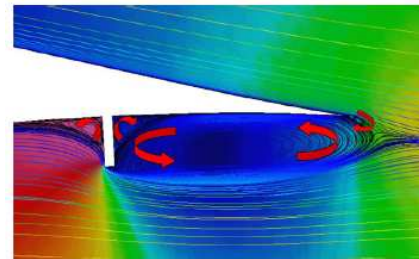
(d) Microtab

Figure 2.5: Bend-twist coupling, aileron, changing shape and microtab
(Barlas & Kuik 2007)

2.3   Modern Wind Turbines

Wind turbine technology, inactive for many years, awoke at the end of the 20th century to a world of new opportunities. Developments in many other areas of technology were adapted to wind turbines, and have helped to accelerate its re-emergence. A few of the many areas which have contributed to the new genera-tion of wind turbines include material science, computer science, aerodynamics, analytical methods, testing and power control. Material science has brought new

composites for the blades and alloys for the metal components. Developments in computer technologies facilitate design, analysis, monitoring and control. Aerodynamics design methods, originally developed for the aerospace industry, have now been adapted to wind turbines (Eggleston & Stoddard 1987). Analytical methods have now developed to the point where it is possible to have a much clearer understanding of how the new design should perform than was previously possible. Testing using a vast array of commercially available sensors and data collection and analysis equipment allows designers to understand how the new turbines actually perform. Power electronics is a relatively new area which is just beginning to be used with wind turbines. Power electronic devices can control the turbine's generator smoothly which plays a crucial role in the electrical network: allowing the turbine to run at variable speed, producing more energy, reducing fatigue damage, and benefiting the utility in the process; facilitating operation in a small, isolated network; and transferring energy to and from storage.

Materials such as fibre-reinforced composites are becoming an attractive option in the wind turbine blade industry in recent years due to their several advantages such as their high strength and light weight. Furthermore, composite structures have been used widely in industry, such as in the aerospace, marine and automotive field, and they have now transitioned to become viable materials for other applications such as mechanical structures, particularly for lightweight structural applications. One major area for the lightweight structure is wind turbine blades (Eker et al. 2006).

Fibre composites are a family of advanced materials formed by combining at least two elements together to produce properties which are different from those of the base elements. Most composites consist of a matrix material and a reinforcement material, usually in a fibre form, added primarily to increase the strength and stiffness of the matrix. Composites like Glass Fibre Reinforced Plastics (GFRP) and Carbon Fibre Reinforced Plastics (CFRP) are also non-corroding and non-magnetic, and can be directionally tailored to achieve strength, stiffness

or flexibility where it is most needed. Fibre composites are used to manufacture high-performing products and components.

Wind turbine blades are usually made in polymer matrix composites, often glued together. Such structures may lead to a number of possible failure modes. For example, cyclic loading that can ultimately results in wind turbine blades failure. Wind turbine are subjected to fluctuating wind and hence flapwise bending are acting on the blades. Components, which are subject to repeated axial bending, such as wind turbine blades, may eventually develop cracks, which ultimately may make the component, break. Therefore, failure of wind turbine blade could be a big catastrophic if there is no immediate solution for safety measures which has not been taken into consideration.

2.4   Identification of Parameters for Efficiency Improvements

In practice, wind turbine designs suffer from the accumulation of minor losses resulting from tip losses, wake effects, drive train efficiency losses and blade shape simplification losses.

The maximum theoretical efficiency will not be achieved and it is impossible. Over the centuries, many types of designs have emerged, and some are more distinguishable. The earliest designs, e.g. Persian windmills, utilised drag by means of sails made from wood and cloth. These Persian windmills were principally similar to their modern counterparts, the Savonius rotors, which can be seen in use today in ventilation cowls and rotating advertising signs. Similar in principle is the cup type differential drag rotor, utilised today by anemometers for calculating the airspeed due to their ease of calibration and multidirectional operation. The American farm windmill is an early example of a high torque lift driven rotor with a high degree of solidity, still in use today for water pumping applications. The

Dutch windmill is another example of an early lift type device utilised for grinding corn which has now disappeared from mainstream use, yet a small number still survive as tourist attractions. The Darrieus VAWT is a modern aerodynamic aerofoil blade design which despite extensive research and development has so far been unable to compete with the modern HAWT design. However, recent developments could see a resurgence of this rotor type. Due to its efficiency and ease of control, the aerofoil three bladed HAWT has become the wind turbine industry benchmark, with a fully established international supply chain securing its dominance for the foreseeable future.

In Table 2.1, brief details the revolution of wind turbines have been summarised.

Table 2.1: Summarise of modern and historical wind turbine designs (Peter & Richard 2012)

No.	Design	Orientation	Use	Propulsion	Efficiency	Diagram
1.	Savonius rotor	VAWT	historic Persian windmill to modern day ventilation	Drag	16 %	
2.	Cup	VAWT	modern day cup anemometer	Drag	8 %	
3.	American windmill	HAWT	18th century to present day, farm use for pumping water, grinding wheat, generating electricity	Lift	31 %	
4.	Dutch windmill	HAWT	16th century, used for grinding wheat	Lift	27 %	
5.	Darrieus rotor	VAWT	20th century, electricity generation	Lift	40 %	
6.	Modern wind turbine	HAWT	20th century, electricity generation	Lift	No.blade efficiency 1 43 % 2 47 % 3 50 %	

2.5   Smart Materials

As Fibre Reinforced Plastic (FRP) Composites become well-established and have been widely used in the modern wind turbine blade, more ideas arise on how best to combine different materials to enhance a variety of structural properties. The development of smart materials, such as piezoelectric materials (PZT), shape memory alloys (SMAs) and electroactive polymers, have given more spaces for the creation of smart composites (Leo 2007). Smart materials, also referred to as active/functional/intelligent materials, exhibit coupling between the mechanical field and some other physical field (thermal, electric, magnetic etc.), and thus a stimulus in one of the fields provokes a response in the coupled field. This coupling can be exploited for sensing and/or actuation as shown in Figure 2.6.
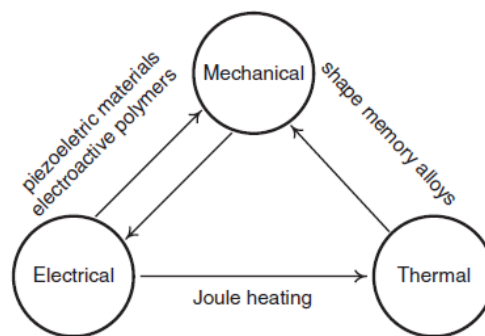
Figure 2.6: Various types of mechanism for smart materials (Leo 2007)

In sensing, a stimulus in the mechanical field provokes a response in the coupled field which can be measured, while, in actuation, the coupled field is used to provoke a mechanical response. The composite itself can exhibit smart-like properties, by embedding a smart material in the composite. Smart materials can be used for many purposes, the main idea being to control and adapt the structural properties according to a change in external conditions.

The development of smart structures faces even more challenges than conventional FRP composites. In modelling smart structures, it is necessary to take into account both the mechanical and the coupled field, thus increasing the size and

complexity of the problem and, in many cases, introducing sources of non-linearity. Moreover, in some cases the mechanisms underlying the coupled behaviour are still not fully understood, thus further investigation of the active material itself is required prior to considering the composite.

Finally, for many smart materials of recent conception, not much information is available regarding their long-term behaviour, such as their fatigue life and the stability of the response with increasing numbers of cycles. All the stated difficulties make active composites a very challenging yet promising topic for researchers, which involves many different disciplines (chemistry, material science, structural engineering etc.) working together to achieve structural performances which would have been impossible with traditional materials.

2.6 Shape Memory Alloy (SMA)

For centuries, metals have played a pivotal role as structural materials in engineering applications. Advances in material sciences over the past decade have led to the ability to develop materials, be they alloys or composites, which exhibit a multiplicity of physical properties, each tailored for a variety of applications. In a number of industries, it has become crucial to produce lighter, stronger materials that address rigorous structural requirements, and provide scientific functionality. Materials are being developed based on the core principles of physics, and one of the most prolific and most interesting classes of smart materials is the shape memory alloy (SMA). This group of materials is attracting considerable attention amongst scientists across the world and is one of the largest growing areas of research today.

The first major contribution to the field of SMAs was made in the 1890's by a German scientist named Adolf Martens. Martens, a microscopist, examined the microstructure of steel, and discovered hardened steels which were found to

have banded regions of differently orientated microcrystalline phases, compared to substandard steels which were found to have little coherent patterning. Martens discovered that steels undergo a structural phase transition. At low temperatures steels are body-centred cubic (BCC) and face-centred cubic (FCC) at high temperatures, forming martensites. This structural phase transition was named after him (Portella 2006).

This contribution to the innovation of shape memory alloys was until this point unnoticed. Wayman & Otsuka (1999) claimed that the first clear progression towards the discovery of the shape memory effect was developed in the 1930s . A Swedish Physicist named Arne Olander revealed, whilst examining the AuCd system, that a deformed AuCu alloy could return to its original shape when the material was heated above some critical temperature (Smith 2005). In 1938, Greninger & Mooradian (1938) observed the appearance and disappearance of martensitic phases in CuZn as a function of temperature, making this transition between states completely temperature dependent. However, it was not until a decade later that Kurdjumov & Khandros (1949) made the most important impact on the development of shape memory alloys. In 1949, the concept of the thermoelastic behaviour, (which is when both changes in stress and temperature alter the dimensions of an object), of the martensitic phase in AuCd, CuZn and CuAl alloys was put forward, explaining the reversible martensitic transformation based on experimental observations. Chang & Read (1951) used X-ray analysis to uncover some of the mechanisms in the AuCd system, confirming the thermoelastic behaviour of the martensite. By 1953, the presence of thermoelastic martensitic transformations was confirmed in several other systems such as NiTi and CuZn.

However, the reversible martensitic transformation, and the alloys that exhibit this effect were not utilised until 1963. The first substantial and sustained research on shape memory alloys can be attributed to William Buehler and his colleagues at the Naval Ordinance laboratories, in White Oak, Maryland. In 1961, Buehler et al. (1963) focused on NiTi based alloys including the stoichiometric NiTi alloy,

which was the invention for engineering applications of shape memory alloys. The discovery of NiTi was somewhat of an accident. Buehler et al. (1963) had investigated new materials for heat shielding when they noticed that aside from the samples good mechanical properties, comparable to most common engineering materials, the material also possessed a shape recovery capability.

The term Shape Memory Effect (SME) was given with respect to this shape recovery behaviour, which is due to the reversible martensitic transformation that the material possesses. The discovery of Nitinol contributes a large space of research into the development and refinement of Shape Memory Alloys (SMAs). For example, the effects of altering the composition, heat treatment and microstructure were thoroughly investigated, and more knowledge began to emerge from this work.

SMA is one of the exciting new technologies that offers many advantages and usages. Some of their best properties are their high force-to-weight ratio, incredibly small size and volume, as well as their low cost compared to conventional actuators. However, SMAs are not free from drawbacks such as the non-linearities and hysteresis that are present in the phase transitions, and also their limited strain and bandwidth. The potentials of SMAs and their feasibility for use in robotic or other commercial applications are still being explored.

As materials become more reliable and a deeper understanding is acquired about the mechanisms involved, technology which utilises specific properties becomes available. For decades, scientists and engineers alike have worked towards converting thermal energy into mechanical work. The first large-scale and most well-known application of SMAs according to Melton (1999) was their use as a coupling to connect hydraulic titanium tubing in the Grumman F-14 aircraft (Wayman & Harrison 1989).

However, the scope for such materials is vast in the world of engineering. Since the first development of the SMA coupling used on the Grumman F-14 aircraft,

engineers have looked to the unique properties of SMAs to solve daunting engineering problems. Space technology harnesses the most current ideas, theories and discoveries throughout all the science and engineering disciplines. Stoneham (1999) addresses some of the most promising applications for SMAs in the demanding environment of space technology and aeronautics. The implementation of SMA technology in the aerospace industry has spread across a variety of areas, such as fixed winged aircraft, rotary aircraft and spacecraft design. In 1995, the smart wing programme was developed by Kudva et al. (2002). In this development, SMA torque tubes were employed to modify the aerodynamic properties of an airfoil, which increases the lift.

Another remarkable effort to integrate SMAs into aerospace structures was a study presented by Strelec et al. (2003) which led to the development of a variable geometry airfoil. Due to the nature of SMAs, wires that have had sufficient training, begin to act as linear actuators. Generally, SMAs have unique characteristics and can remember their shape at both high and low temperatures.

With sufficient training, the system can be taught to remember the low temperature shape. This is accomplished by leaving traces of the deformed low temperature martensite in the high temperature phase. A study of the training processes was carried out by Perkins & Hodgson (1999) in detail. The most common methods of training involve: over-deformation while in the martensitic condition; shape memory cycling where the system is cooled, deformed, and then heated repeatedly; and training by pseudoelastic cycling where the system is loaded and unloaded. The study illustrated that by attaching SMA wire actuators to selected points on the inside of an aerofoil, its shape can be changed drastically thus improving the dynamics of flight.

At present, the application of SMAs is widespread due to advanced material technology, for example, spectacle frames that are amazingly bendable, medical stents for opening arteries that are implanted in a compressed form and then expand to the right size and shape when warmed by the body, tiny actuators that

eject disks from laptop computers, small microvalves and a host of other devices, all share a common material technology. The interesting behaviour of each of these devices relies upon a phenomenon called the shape memory effect that refers to the ability of a particular kind of alloy material to revert to, or remember, a previously memorised or preset shape.

In the advanced application of SMA so far, it has also been applied in aerospace technology for noise suppression. This new approach has demonstrated the feasibilty of SMAs may be used in reducing noise level. Figure 2.7a illustrates the current Boeing design for the variable geometry chevron. Note that the composite layer has been removed from the chevron for exposition of the active SMA elements. Figure 2.7b illustrates the results of current efforts to model the Boeing chevron system. Here, complex behaviours such as the elastic laminate response of the composite substrate, sliding contact, and 3D non-homogeneous SMA loading have all been considered (Hartl & Lagoudas 2007).

(a) Boeing variable geometry chevron,   (b) Stress contour results from FEA
flight testing   analysis of VGC, actuated position
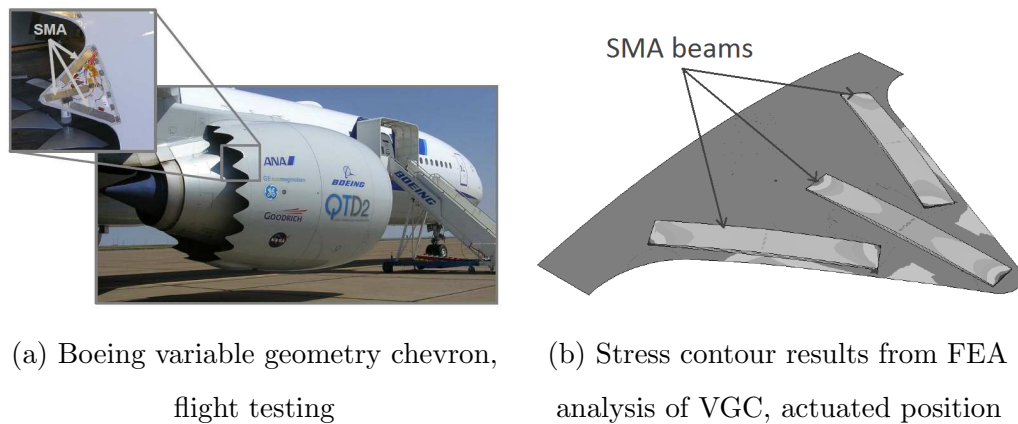
Figure 2.7: Example SMA application in Variable Geometry Chevron (VGC) for Boeing 777 (Hartl & Lagoudas 2007)

Controlling engine noise levels during takeoff and landing has become stringently regulated since there has been some evidence that peoples sensitivity to aircraft noise appears to have increased in recent (Rask et al. 2007). Designers and engineers found that installing chevrons to the rear of aircraft engines, reduced the noise dissipated by creating a slightly turbulent airflow causing the exhaust

gases to mix. One of the leading aircraft manufacturers Boeing has consequently introduced embedded SMA bar components into chevrons in aircraft engines. At low altitude flight or slow speeds, the SMA component is in its austenite phase, and the SMA chevrons can be bent into the stream of the outgases expelled by the engine. In doing so, this further increases the mixing of the outgases and further reduce noise. During high altitude flight, at higher speeds and a colder temperature, the SMA chevrons would transform into their martensite phase, straightening the chevrons forming a rigid body and boosting aircraft performance (Mabe et al. 2005).

In automotive applications, SMAs also have the ability to act as sensing devices, or as actuation and sensing devices simultaneously. An application that harnesses this ability is an SMA spring used in the variable transmission of the Mercedes Benz A-Class. The spring acting as a sensor, continuously monitors the temperature of the system, and at a specific temperature, actuates a valve, which redirects the flow of oil within the transmission (Duerig 1999). Shinkansen, which is also known as the Bullet train, is equipped with aluminium gearboxes that incorporate an automatic oil level adjusting system (valve). The valve with an SMA spring controls the oil level inside the gearbox according to the change of oil temperature which is shown in Figure 2.8. SMA springs in the automatic oil quantity adjustment unit inside the gear boxes sense the oil temperature. It will open and close automatically, and supply the optimum quantity of oil to the shaft bearings. This system helps lower electricity consumption during high-speed operation.
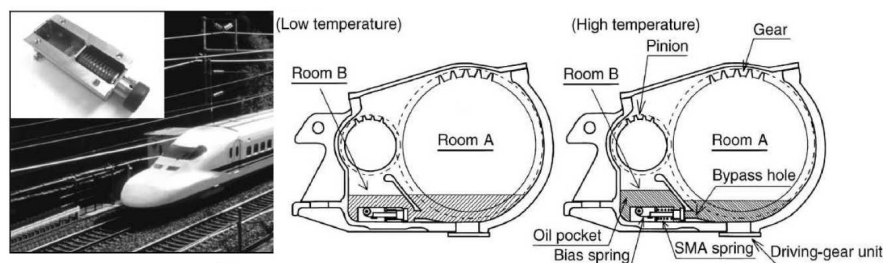
Figure 2.8: Application of SMAs to an automatic oil-level-adjustment device for the Shinkansen bullet train (Otsuka & Kakeshita 2002)

Another recent application used in the automotive industry has been implemented in Corvette cars, by the General Motors manufacturer, as shown in Figure 2.9. The SMA wire used in the new Corvette will open the hatch vent whenever the deck lid is opened, using heat from an electric current that works in a similar manner as the trunk lights. It replaces a heavier motorised part to open the vent. When activated, the wire contracts, and moves a lever arm to open the vent, allowing the trunk lid to close. Once the trunk lid is closed, the electric current switches off, allowing the wire to cool and return to its normal shape, which closes the vent to maintain cabin temperature (Auto 2013).
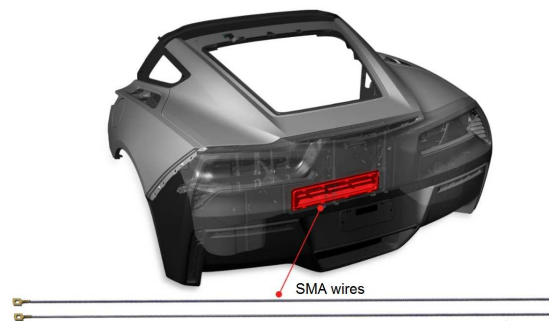
Figure 2.9: Corvette's heat-activated smart material (Auto 2013)

A solid state phase change molecular rearrangement occurs in the shape memory alloy that is temperature-dependent and reversible. For example, the material can be shaped into one configuration at a high temperature, deformed dramatically while at a low temperature, and then reverted back to its original shape upon the application of heat in any form, including by an electrical current. The phenomenon of superelasticity, which is the ability of a material to undergo enormous elastic or reversible deformations, is also related to the shape memory effect (SME). Nickel-Titanium (NiTi) alloys are commonly used in shape memory applications, although many other kinds of alloys also exhibit shape memory effects. In this project, Flexinol, which is a commercially produced NiTi, has been used in wire form for all the modelling and experiments.

2.7 Characterisation of SMA for Smart Wind Turbine Blades

SMAs are defined by their remarkable ability to sustain and then recover large super elastic strains by stress and temperature dependent crystallographic transformations. SMAs have sensing and actuating functions and have the potential to control the mechanical properties and responses of their hosts due to their inherent unique characteristics of the shape memory effect (SME) and superelasticity (SE). When integrated into structural components, SMAs perform sensing, diagnosing, actuating and repair or healing functions, thereby enhancing the performance characteristics of their hosts (Armstrong & Lilholt 2000, Zhang et al. 2007).

Figure 2.10 shows a comparison of other rival materials acting as a function of actuation stress-strain. The actuation energy density (work output per unit mass) of SMAs is among the highest at this range and is denoted in Figure 2.10 by the dotted lines at 10 MJ/m^3. The energy density is defined as the product of the actuation strain (related to the stroke of an actuator) and the actuation stress, assuming here that the active material is operating under constant stress. The specific actuation energy density for a specific active material can be calculated from Figure 2.10 by dividing the actuation energy density by the mass density. The range of the actuation lies between 4–10 % and the average maximum stress is between 100–1000 MPa with a density of 10 MJ/m^3.

Smart materials can be tailored to create a specific response to a combination of inputs (Suleman 2001). These materials include piezoelectric, electrostrictive, magnetoresistive, and SMA. Combinations of SMAs exist such as magnetic SMA and shape memory polymers.

Figure 2.11 reveals the actuation frequency of other smart materials with respect to specific actuation density. This figure shows how the specific actuator density correlates with the frequency of the actuator and is highest for the 10^3 for SMAs.
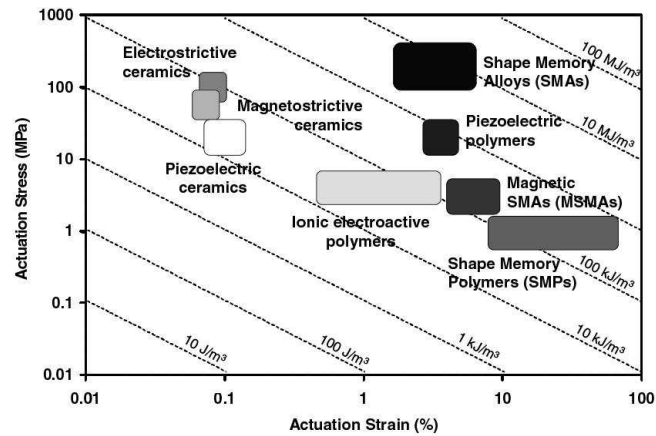
Figure 2.10: Actuation stress-strain of selected SMA (Lagoudas 2008)

They have a frequency between 0.1 to 20 Hz. However, piezoelectric was in the bottom level. The rest of the smart materials are a combination of piezoelectric polymer, SMA, magnetic and electrostrictive and are in the middle group.
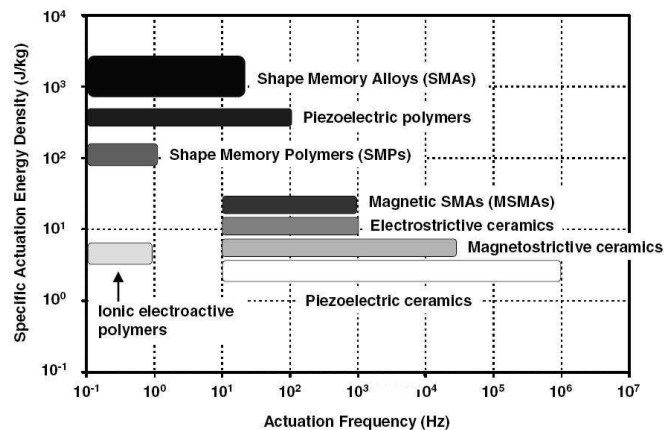
Figure 2.11: Actuation frequency diagram of different active materials

(Lagoudas 2008)

When dealing with the properties of SMA materials, they can be divided into two parts which are:

(i) the shape memory effect;

(ii) superelasticity.

2.7.1   Shape Memory Alloy Behaviour

An SMA exhibits the shape memory effect (SME) when it is deformed while in the twinned martensitic phase and then unloaded while at a temperature below the Austenite start (A_s). When it is subsequently heated above the Austenite finish (A_f), the SMA will regain its original shape by transforming back into the parent austenitic phase.

The phase of temperature of the SMA was used to set the working setting condition. It has been implemented by the heat treatment or annealing process. This phase of temperature was applied to guide the reference temperature for the development of the prototype in this study.

A heat treatment must be carried out in order to ensure that the material reaches the desired temperature which is required for a specific shape. Heat treatment methods include the use of a furnace hot chamber. The method chosen depends on the size of the SMA and the equipment available. Typically, the annealing temperature is in the range of 450°C to 550°C. However, higher temperatures will result in lower tensile strengths.

The time required for the heat treatment must be sufficiently long enough so that the material reaches the desired temperature throughout its cross-sectional area. However, the annealing period may be less for the wire than for heating small parts in the furnace hot chamber. To produce the desired shape, experimentation for the proper time and temperature is required. Based on this experience, trial and error has been performed.

2.7.2   Superelastic Behaviour of SMA

The superelastic or pseudoelastic behaviour of SMAs is associated with stress-induced transformation, which leads to strain generation during loading and

subsequent strain recovery upon unloading at temperatures above A_f . The pseudoelastic thermo-mechanical loading path generally starts at a sufficiently high temperature where the stable austenite exists, then develops under an applied load to a state at which the detwinned martensite is stable, and finally returns to the austenitic phase when returned to a zero stress state.

As shown in Figure 2.12a, at a high temperature, a large deformation can be fully recovered by simply releasing the applied load. This is the shape memory effect. While in superelasticity, as shown in Figure 2.12b, what is involved in both kinds of phenomena is either the transformation between the low temperature phase martensite or the high temperature phase austenite reorientation among different martensite variants.
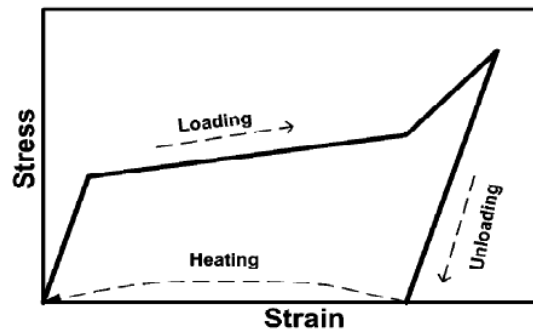
(a) Shape memory effect (SME)
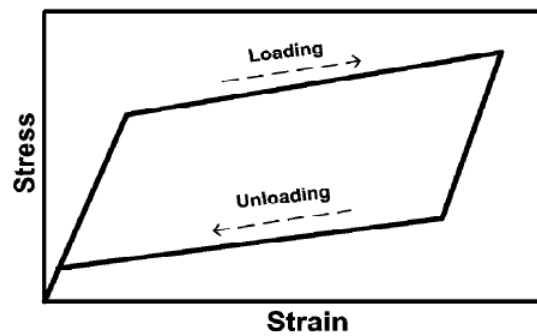
(b) superelasticity (SE)

Figure 2.12: (a) Stress-strain curve of SME and (b) SE

2.7.3   Macroscopic Behaviours of SMA

NiTi-based SMAs are reliable, can be highly biocompatible, and are largely used in engineering applications. The most effective one is NiTi commercially known as Nitinol, since significant recoverable strain was discovered at the Naval Ordnance Laboratory in 1971. The unique properties mentioned above are being applied to a wide variety of applications in a number of different fields. The shape memory effect is observed when the temperature of a piece of shape memory alloy is cooled to below the temperature of martensite formation. At this stage, the alloy is completely composed of martensite which can be easily deformed. After distortion, the SMA's original shape can be recovered simply by heating the wire above the temperature required for austenite formation. The power driving the molecular rearrangement of the alloy is derived from the heat transferred to the wire, but the alloy remains solid. The deformed martensite is now transformed to the cubic austenite phase, which is configured in the original shape of the wire.

Figure 2.13 features the microscospic and macroscospic behaviours when SMA performs SME.
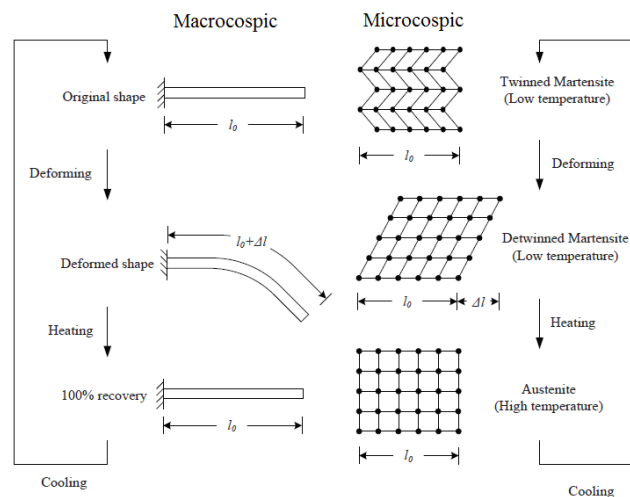
Figure 2.13: General SMA mechanism

A basic definition of an SMA is a metallic alloy that can exhibit martensitic phase transformations as a result of applied thermo-mechanical loads, and is capable of recovering permanent strains when heated above a certain temperature (Patoor et al. 2006). NiTi is the most common SMA and is the main area of interest in this work. For a NiTi alloy to exhibit shape memory and superelastic properties, it must contain 49.5–57 % nickel by atomic weight percentage as shown in Figure 2.14. Above or below these limits, the alloy no longer exhibits its unique thermo-mechanical properties. NiTi has a very ordered atomic packing structure with alternating nickel to titanium atoms.

In Figure 2.14, Nitinol SMA can also have combinations of Ti_2Ni and $TiNi_3$ based on composition and temperature. The different phase relationships of Nickel and Titanium have been known for some time, but the discovery of their unique properties occurred relatively recently.
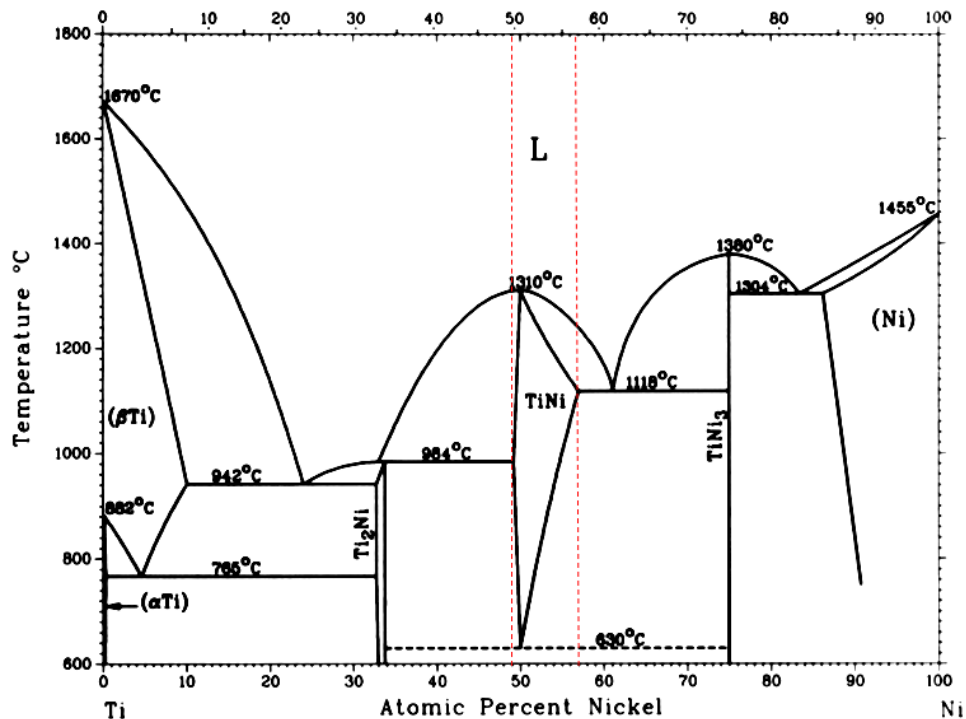
Figure 2.14: Phase diagram of a NiTi alloy in which the phase equilibrium is between 49.5–57 % nickel by atomic weight percentage (Otsuka & Ren 2005)

The stress, strain, and temperature of the SMA are interdependent. Since the SMA stress-strain relationship depends on the temperature, the Young's modulus of elasticity also depends on the temperature. The Young's Modulus is the ratio of the applied stress to the resulting strain.

Figure 2.15 shows two curves whereby the first corresponds to the material in its fully martensite state, while the second corresponds to the material in its austenite state. The high-temperature curve corresponds with the Austenite finish (A_f) while the low-temperature curve corresponds with the Martensite start (M_s). At (a), the detwinning of martensite begins. At (b), the martensite is fully detwinned. At (c), detwinned martensite deforms elastically. At (d), slip begins to occur and permanent deformation results. Martensite detwinning begins at ε_m^y while ε_m^d is the strain when the martensite becomes fully detwinned.
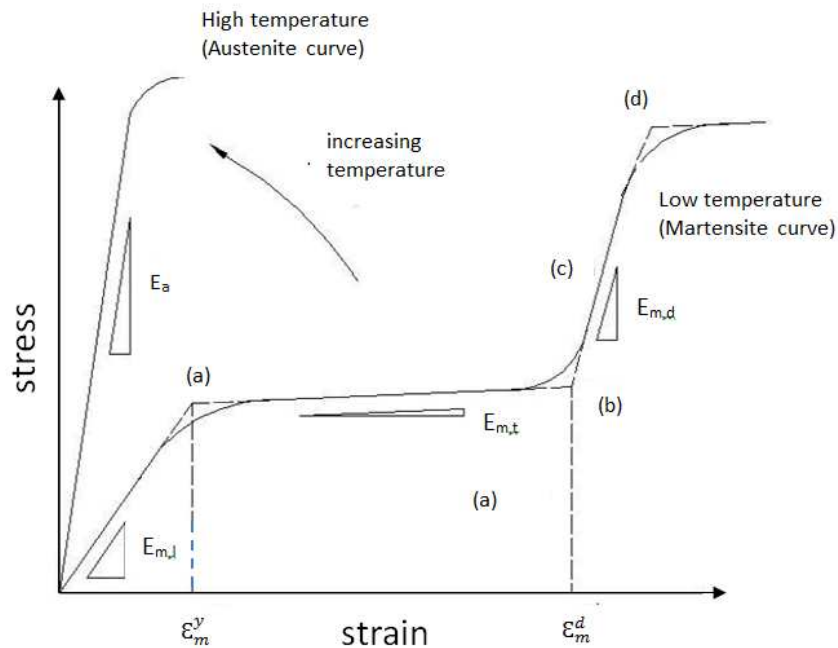
Figure 2.15: SMA stress-strain (Otsuka & Ren 2005)

There are two continuous curve segments that describe the martensite stress-strain relationship which is clearly described in Figure 2.15. Assume that initially the SMA material is fully twinned martensite with a temperature below the Martenisite finish (M_f) .

The linear portion prior to (a) corresponds to the elastic operating range of the SMA. When the SMA is under loading in this region, stress increases linearly with strain. The Young's Modulus is $E_{m,l}$ in the linear region. After the first yield point, there is an approximate plateau, from (a) to (b), where a small change in stress results in a significant change in strain. This process is called detwinning. At this stage, an externally applied stress can force all variants of the martensite into a single variant. If the external stress is removed, the martensite will recover slightly, but it will remain deformed. The Young's Modulus is $E_{m,t}$ from (a) to (b) where the material is detwinning. Point (c) indicates an elastic region where the atomic bonds within the rhombic crystalline structure can be stretched.

If the stress is removed, the martensite will return to its fully detwinned form. $E_{m,d}$ is the Young's Modulus in the elastic region corresponding to point (c). Applying severe stresses leads to slip. At point (d), atomic bonds break and permanent, irrecoverable deformation occurs. The strain where detwinning of martensite begins is ε_m^y while ε_m^d is the strain where the martensite becomes fully detwinned.

The high–temperature SMA curve has a greater slope and hence a greater Young's Modulus than the low-temperature SMA curve, which shows the Young's Modulus is E_a at high temperature (austenite curve). Therefore, an SMA device is capable of exerting a greater force in its austenitic state than in its martensitic state.

2.7.4   Microscopic Behaviours of SMA

The low temperature martensite phase has a monoclinic, twinned crystal structure with 24 variants. Twinned martensite occurs in individual grains where rows of atoms form a mirror image across a twin boundary as shown in Figure 2.16. All 24 martensite variants are possible in a NiTi material system, and with no applied stress they will align themselves in the easiest manner by twinning. But they can be aligned with the application of an applied stress by a shear-like mechanism called detwinning.

Martensite

•Low temperature phase

•Monoclinic crystal structure

Twinned Martensite

Detwinned Martensite
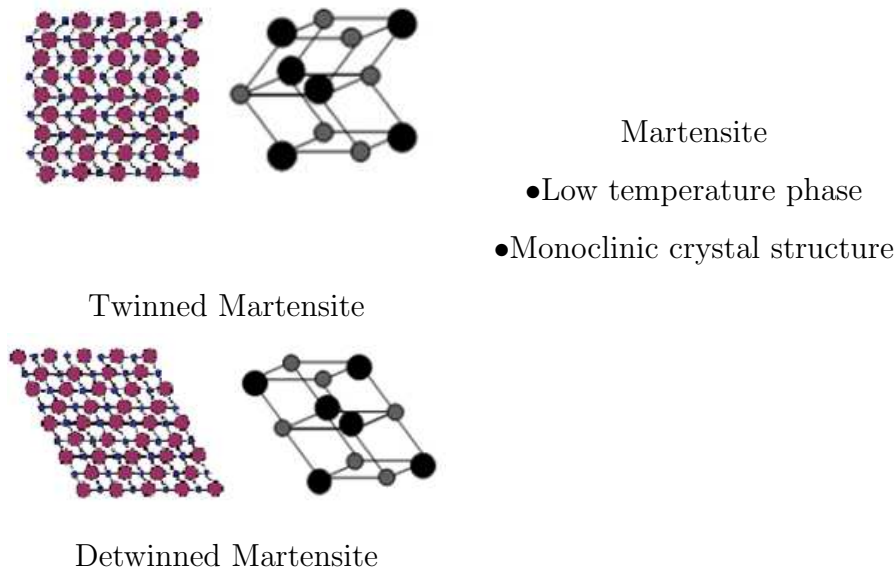
Figure 2.16: Martensite crystal structure (Volk & Lagoudas 2005)

When stress is applied, the crystalline structure detwinns, the mirror images across the twin boundary align (see Figure 2.16). The mirror images align in the grains' internal lattice. This allows the grains to change while the interface between the grains remains the same. It is important to note that no change in the crystal structure occurs, rather a reorientation of the lattice. This implies that twinning is different from slip. Both twinning and slip involve a shearing of the lattice, but slip occurs on individual lattice planes and may be many times larger than the lattice spacing. Deformation by twinning is uniformly distributed over a volume. The atoms only move a fraction of an interatomic spacing relative to each other.

Even with only moving a fraction of an interatomic space, a material that is heavily twinned, such as NiTi, will have large macroscopic deformations (Reed & Abbaschian 1992).

Austenite, in the high temperature parent phase, has an ordered body centred cubic crystal structure as shown in Figure 2.17 (titanium is represented by smaller, grey spheres). With this packing structure, the austenite phase contains 6 slip planes, each with 2 directions resulting in 12 slip systems.

The transformation from one state to another does not occur at the same temperature on heating and cooling but follows a hysteresis cycle. This hysteresis gap is described by the transformation temperatures A_f (austenite finish), A_s (austenite start), M_s (martensite start), and M_f (martensite finish)

- High temperature phase
- Body Centred Cubic crystal structure
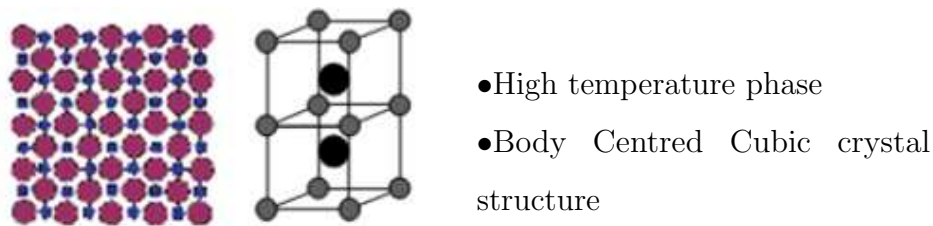
Figure 2.17: Austenite lattice crystalline structure

2.7.5   Factors Affecting the Effectiveness of SMA

The manufacturing process for SMA epoxy composites generally involves pre-straining in order to generate recoverable strain (Zheng et al. 2005). Several researchers have pre-strained SMA wires implanted into polymeric matrices with diverse levels of pre-strain ranging from 3–6 % (Umezaki 2000, Nii et al. 2007). However, Zheng et al. (2005) specifically examined the effects of the pre-strain level of the SMA wires on the recovery stress. They reported that despite the enhancement of the tensile strength of the epoxy matrix embedded with SMA with high levels of pre-strain (about 6 %), there is a demerit of excessive shear

stress at the interface between the SMA wires and the matrix, thus making the interface more susceptible to debonding and consequently the actuation ability of the composites is low. They confirmed that the maximum recovery stress decreased almost linearly with increasing pre-strain and established that a small pre-strain level is necessary to produce a reliable SMA composite. Consequently, they recommended that if the recovery stress of the SMA based composite is to be tailored, it is necessary to modify the volume fraction of the SMA components rather than alter the pre-strain level. Their further investigations on the effects of additional reinforcing fibres on SMA based composites and the maximum working temperature of SMA based composites were based on 3 % pre-strain.

Yi & Gao (2003) discovered that the transformation temperatures and other properties of SMA vary significantly as a result of relatively small changes in alloy composition or thermo-mechanical heat treatment conditions . They confirmed that identical heat treatment of the SMA wires to be embedded in the polymeric host is necessary to facilitate a uniform response. Besides, the SMA wires must be taken from the same product batch. Besseghini et al. (1999) established that aging lowers the transformation temperatures of NiTiHf SMAs. Ageing also erases the inconsistent yield point associated with the untreated SMA wire (Mukhawana 2006). The effects of volume fractions of SMA elements embedded into the polymeric matrix have been investigated by many researchers. Nii et al. (2007) reported that the natural frequency and thus the stiffness of a laminated polymeric beam increases with the increasing volume fraction of implanted SMA wires. They established that the natural frequency in the SMA laminated beam, with only about 5 % volume fraction of SMAs, is almost twice as high as that in the epoxy resin at the austenite phase transformation temperature A_f. Thus, the contribution of the SMA to the enhancement of the natural frequency of the SMA laminated beam was confirmed.

Parthenios et al. (2001) observed that an increase of 3.5 % volume fraction of the implanted SMA wires which were pre-strained by 3 % results in increasing

recovery stress. Zhang et al. (2007) confirmed that increasing the volume fraction of the SMA fibres, has increased the modulus of the SMA based composite. Thus, this decreases the deflection of the composite as well as enhances its dynamic property. Zhang et al. (2007) established that the Young's Modulus of an SMA based composite increased and the fracture deflection decreased with an increase in the volume fraction of SMA embedded into the epoxy resin. They also established that the SMA based composite is brittle in nature for high SMA fibre content. Tawfik et al. (2000) reported that an increase in the volume fraction of the NiTi SMA results in a stiffer plate. They reported that an increase in the initial strain of the NiTi SMA fibres also result in a stiffer plate and increased natural frequencies, lower thermal deflections, and higher critical temperature. Tsai & Chen (2002) reported that an increase in the number of NiTi SMA fibres increases the stiffness of an SMA based composite beam.

Embedded SMA can be activated by both direct current heating and indirectly by the isothermal surface. Shimamoto et al. (2004), however, reported that an SMA based composite, with a 3 % level of pre-strained SMA wire, that was directly activated by a current of 3 Amp for a period of 30 secs, generates more recovery stress than the composite which was activated by exposure to environmental temperature (isothermal surface). They also confirmed that the direct method of heating is more efficient than the indirect method of heating. In the latter, the host matrix prevents heat transfer to the NiTi fibre from the external energy source. Umezaki (2000) reported that heat generation by the SMA upon activation affects the interfacial bond strength between the SMA wire and the host matrix, and as such, he recommended intermittent heating of the SMA wire via a direct current supply to prevent interfacial breakdown. Tsoi et al. (2004) investigated the thermo-mechanical characteristics of shape memory alloys. They reported that at the low temperature martensitic phase, the SMA is soft and easy to deform whereas at the high temperature austenitic phase, the SMA is stiffer and more difficult to deform. The results showed that the Young's Modulus of the NiTi SMA in the austenite phase is almost twice that of the martensite phase. Rumsey

& Paquette (2008) also confirmed the temperature dependence of the mechanical properties of SMAs. They reported that the Young's Modulus of SMA in the austenite phase is higher than that of the martensite phase. Shimamoto et al. (2004) also reported that the stiffness of the SMAs is 2–3 times higher in the austenite phase than the martensite phase.

2.8   Design of General Mechanism for a Wind Turbine Blades with SMA

In order to incorporate SMAs as a smart structure component, it is very important to understand the basic working principle of the SMA. Since SMAs are sensitive to test conditions, one should be very careful when doing experiments as well as interpreting experiment data. Shaw et al. (2008) and Churchill et al. (2009) have presented numerous papers to introduce uninitiated engineers to the testing of SMAs. They introduced phenomena and subtleties that can lead to difficulties in testing SMA wire and also highlighted pitfalls in the interpretation of the results. Furthermore, they described experimental techniques that help to illuminate and quantify the macroscopic thermo-mechanical behaviour.

Despite there being many previous studies (Shaw et al. 2008, Churchill et al. 2009, Lagoudas et al. 2003), the testing of SMAs is not yet standardised and material property tables are either not available or provide incomplete, or even incorrect data. This is because SMA behaviour is non-linear, hysteretic, and extremely temperature dependent. Since each SMA is different, it is necessary to develop an experimental setup to obtain a satisfactory characterisation of the material. Besides, most previous works were based on uniaxial tensile tests. However, for this particular application, large deflection/deformation is the most important parameter to be characterised. Thus, in this study, in order to discuss the design of the smart blade, the experimental setup has been discussed. It has been used

to determine the correlation between load deflection and temperature as well as the correlation between generated force and the temperature of the SMA.

SMA wires are small diameter wires which can contract like muscles when electrically heated. Smaller than motors or solenoids, cheaper and generally easier to use, these wires perform physical movement across an extremely wide variety of applications. They can act like an actuator which is something that converts energy into motion. SMA wires' prime function is to contract in length and create force or motion when it is heated. The actuator typically is a mechanical device that takes energy which is usually energy that is created by air, electricity or liquid and converts it into some kind of motion. That motion can be in virtually any form, such as blocking, clamping or ejecting. Actuators are typically used in manufacturing or industrial applications and might be used in devices such as motors, pumps, switches and valves (Sun et al. 2012).

There are three basic types of SMA mechanism actuators, which are represented depending on the motion direction as follows:

(i) Figure 2.18a shows a one-way direction actuator. The SMA element is elongated initially at low temperature and then is heated up to pull element P to the left;

(ii) Figure 2.18b shows a biased direction actuator, which is capable of moving the element P back and forth by heating/cooling the SMA element;

(iii) Figure 2.18c shows a two-way direction actuator, which includes two one-way SMA elements. P may move back and forth by heating and cooling the two SMA elements alternatively.

SMAs may be heated up by three methods:

(i) By passing an electrical current through them. This method is only applicable to small diameter SMA wires or springs;
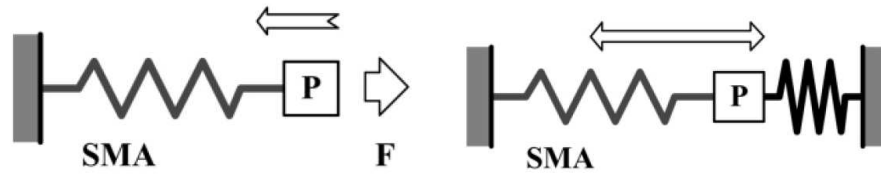
(a) One-way actuator   (b) biased actuator direction
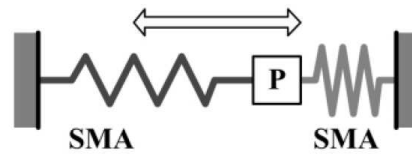
(c) two-way actuator direction

Figure 2.18: Schematic mechanism diagram of SMA actuators combined with a spring (Sun et al. 2012)

(ii) By passing an electrical current through a high resistance wire or tape wrapped around the SMA. This method is applicable for bulk SMA;

(iii) by hot air/water or exposure to thermal radiation.

It is well known that SMA is very sensitive to the exact composition, grain size, processing, heat treatment and loading conditions (Wayman & Otsuka 1999). The inclusion of additional elements in a minute quantity may change the properties of the SMA dramatically. For instance, the addition of a small amount of copper into NiTi SMA makes the transformation temperature less sensitive to composition and the hysteresis gap narrower (Lee et al. 1996). By adding a small amount of palladium into NiTi SMA, a high transformation temperature over 200°C is achievable (Huang & Toh 2000).

The sensitivity of SMA seems to be an intrinsic disadvantage. On the other hand, it provides tremendous flexibility to obtain exactly what is needed within a far broader range in comparison with traditional materials.

Unlike ordinary one-way SMA, which can only remember the high temperature austenite shape, two-way SMA, which can remember both high and low temperature shapes, is achieved by performing material training procedures. However, the phase transformation strain is significantly less and the stability and repeatability are uncertain.

2.9 Proposed Use of SMA

In this study, the NiTi, SMA alloy, (Flexinol® product) wire is proposed to be incorporated in the composite blade. It is because it has an ability to recover its original shape that it is important in this study. For further details, the specifications of this product are included in the instruction manual given in Appendix A.

It has been decided to use NiTi SMA wire as an actuator/self-straightening for a smart composite wind turbine blade structure since it has been found that the NiTi shape memory alloy can generate high recovery stresses (up to 700 MPa) for a specific actuator volume (Thompson & Loughlan 2001). Such forces could be generated and quantified by prevention of the shape memory recovery phenomenon.

2.10 Analysis of the Structural Performance of Wind Turbine Blades

2.10.1 Aerodynamics

Aerodynamics is the science and theoretical study of the physical laws of the behaviour of objects in an air flow and the forces that are produced by air flows.

From the design and manufacturing perspective, wind turbine blades have many similarities to helicopter rotor blades (Hodges & Yu 2007). The loading on the wind turbine blade and the rotor blade consists primarily of aerodynamic pressure loads. Blades are important components to preserve an optimum surface area of airfoil for aerodynamic efficiency to generate the maximum torque to drive the generators.

The modern HAWT can be summarised into a series of systems and components as illustrated in Figure 2.19.

  (i) The rotor, consists of the blades and the supporting hub;

 (ii) The powertrain, which includes the rotating parts of the wind turbine blade (exclusive of the wind turbine blade) - it usually consists of shafts, a gearbox, coupling, a mechanical brake and the generator;

(iii) The nacelle structure and the main frame - including the wind turbine housing, the bed plate and the yaw system;

(iv) The tower and the foundation;

 (v) The machine controls;

(vi) The balance of the electrical system, including the cables, the switch gear, the transformers and possibly the electronic power converters.

The design of wind turbine blades has developed from the working principle of the propeller, airplane wings and helicopter rotors. The wind turbine blade is considered to be the second most expensive component of the whole of the wind turbine assembly, representing 22 % of the total cost which is mentioned in Figure 2.19. According to one study, during the lifetime of a wind turbine, the rotor blades contribute to 34 % of the overall system downtime (Hanc et al. 2011). In the past few decades, numerous theoretical analyses and experiments have been carried out to improve the aerodynamic performance of the wind turbine blades.
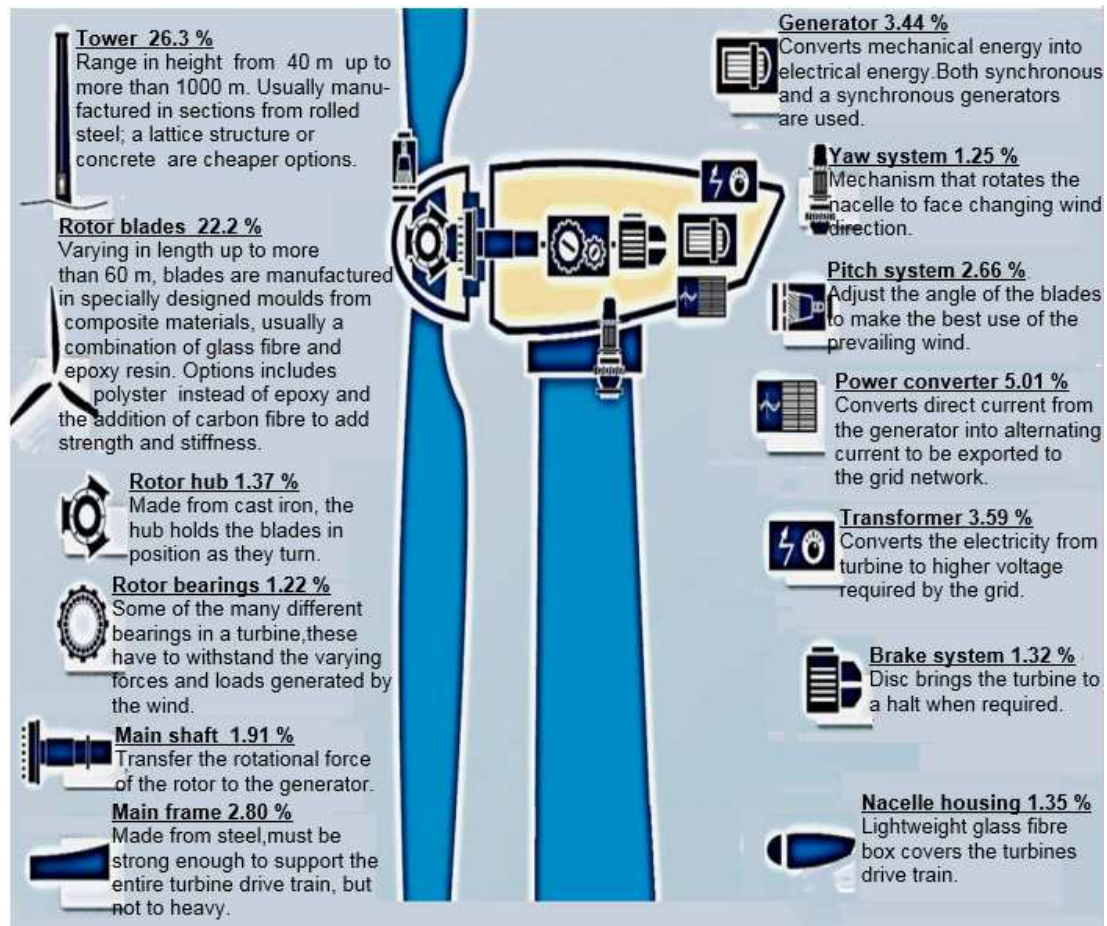
Figure 2.19: Major systems and components of a horizontal-axis wind turbine (EWEA 2006)

However, there are problems in predicting the load from unsteady aerodynamics. These loads lead to fatigue and a lower lifetime than predicted by the design (Grujicic et al. 2010, Lain et al. 2010, Epaarachchi & Clausen 2006).

Obviously, the speed of the wind turbine blade is much slower compared to the air, so it experiences much lower aerodynamic pressures. Maximum loading is experienced at the root of wind turbines, much like rotorcraft blades. The overall pressure field does not cause bending moment and torque at root only. A bending moment refers to the tendency of the wind turbine blades to bend and twist during operation, which effectively alters their angle of attack and in turn has a negative effect on loads and energy production. For these reasons, the blades are designed with a high level of bending and torsion.

The efficient use of wind turbine technology as an electrical power generator has been gradually developed since the aerodynamics aspect has been introduced. Airfoil characteristics have given wind turbines the ability to rotate at high speed and load. Generally, the early aerodynamics of wind turbines was originally based on the theory adopted from aeroplane and helicopter rotors. However, the aerodynamics of wind turbines requires a different idea from the helicopter rotor. For example, the accuracy of rotor performance analysis depends mainly on the treatment of the wake effect, because the wake of a propeller type wind turbine is induced by a large velocity in the rotor plane. Progress in the aerodynamics of wind turbines has generated the new concept design turbines, such as the stall controlled machine (Burton et al. 2011).

As the use of large scale commercial wind turbines is expanded all over the world, the wind turbine industry is facing many challenges in acquiring efficient wind turbine machines, which is caused by the inability to predict the structural loading and power output. As the wind turbines are operating in the natural environment, turbines are always subjected to unsteady conditions. However, recognising that the aerodynamics of wind turbines is associated with three-dimensional, unsteady and separated complex flows is not sufficient. The unsteady aerodynamics of wind turbines is one of the most pressing issues in wind energy research and development (Spera 2009, Manwell et al. 2009, Golding 1976). The following subjects relevant to the aerodynamics of wind turbines are now actively studied: the design of the new airfoil (Kovarik et al. 1979), the three-dimensional effect of the rotating blade (Hansen & Butterfield 1993, Gourieres 1982), the dynamic inflow effect, the dynamic stall associated with yawed inflow and so on (Glauert 1983).

The development of efficient (low-drag) airfoils was the subject of deep experimental investigations in the 1930's. These airfoils were standardised by the National Advisory Committee for Aeronautics (NACA), and extensive lists of data on lift coefficients were reported. The force that a flowing fluid exerts on a body in the flow direction is called drag. The components of the pressure and wall shear

forces in the direction normal to the flow tend to move the body in that direction and are called lift. The aspect ratio is a measure of how narrow an airfoil is in the flow direction. The lift coefficient of wings, in general, increases, while the drag coefficient decreases with increasing aspect ratio. In fact, over the past few decades, commonly used airfoil families for HAWTs such as the NACA 44-, NACA 23-, NACA 63-, and NASA LS- series airfoils, have been used in airfoil design (Tangler & Somers 1995).

For modern HAWT blades, airfoils such as the NACA series have been widely used (Hansen & Butterfield 1993). But these airfoils have been recognised to be insufficient for requirements such as the reduction of rapid stall characteristics, insensitivity to Reynolds number in the range between 500,000 and 10 million, insensitivity to leading edge roughness, and structural efficiency for the root region which is designed using a thick airfoil. For example, new airfoil families for HAWT have been developed by the Delft University of Technology (Timmer et al. 1993), the National Renewable Energy Laboratory (NREL) (Somers & Tangler 1996) and the Riso National Laboratory (Dahl et al. 1999). Figure 2.20 shows the airfoil shapes of airfoils for HAWT blades Riso A1 which were composed of seven airfoils ranging in thickness from 12 % to 30 %. The thick airfoil may not only contribute to a heavy load but lead to fatigue failure. Thus, it is possible to design slender blades while maintaining high aerodynamic efficiency because it potentially reduces both fatigue and extreme loads.
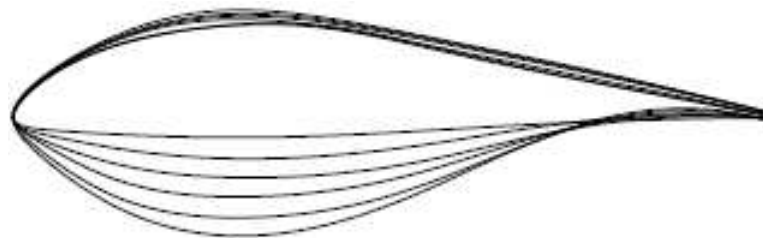
Figure 2.20: Thick airfoil shape of A1 series family (Dahl et al. 1999)

Researchers have relied on simplified models which provide a fairly accurate approximation of the real structural behaviour. Subsequently, the underlying

concepts of application of optimisation theory to the design of the conventional wind turbine will be applied. The relevant design objectives, constraints and variables, are identified and discussed. As such, Nitin et al. (2010) investigated the finite element model of the wind turbine with the NACA 634–221 airfoil using ANSYS®.

The performance analysis of the HAWT will be based on the knowledge of the air flow behaviour (aerodynamic property) over the turbine blade and how the blade reacts to the aerodynamic loads. This property is relatively easily understood through modelling, which is also one of the ways to understand the performance of the turbine blades. Diverse methods and theories are discussed in the literature, including Blade Element Theory (BET), actuator disk theory and panel code method which is shown in Table 2.2. The BET method is mainly employed as a tool of performance analysis for the HAWT. It is claimed that BET is widely used in the design and analysis of turbine blades mainly due to its simplicity and ready implementation (Hsio et al. 2013). Vortex wake methods can adequately treat the effect of wake vortices and have some advantages over BET, but have a computational burden. As computer power increases, the use of vortex wake methods has increased, and computational fluid dynamics (CFD) codes have also been applied in recent cases. This section follows the features of each method for the performance analysis of the HAWT.

Table 2.2: Analysis methods of HAWT performance

Method	Model	Researcher
Momentum	Blade Element Theory	Glauert
Momentum	Actuator Disk Theory	Bertz
Wake	Panel Code Method	Hess

2.10.2   The Blade Element Theory (BET)

In 1935, Glauert (1983) developed BET or strip theory. In BET, the system was analysed from a two-dimensional perspective. Basically, the BET theory is based on the propeller theory and modified for application to wind turbines, which is illustrated in Figure 2.21. In recent years, the BET theory has been optimised and modified to provide increasingly more accurate results. For the numerical model, the greatest difficulties are represented by determination of the axial and tangential induction factors, the lack of experimental measurements on airfoil lift and drag coefficients at high angles of attack, and their three-dimensional representation.
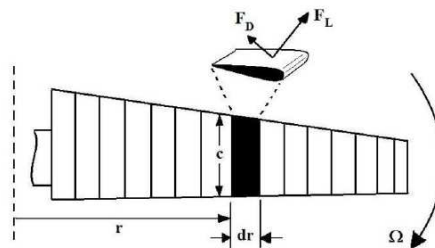
Figure 2.21: Diagram of a wind turbine blade sectioned into individual blade elements. The rotor angular velocity is Ω; r is the radius of the section, dr is the differential section thickness, and c is the section chord length. The lift, F_L and drag, F_D forces are found for every airfoil section (Eggleston & Stoddard 1987)

BET provides the possibility of performing a fluid dynamics design of wind turbine blades, and of evaluating wind turbine performance. With the implementation of this model, it is possible to design the blade, to choose the geometric characteristics of the turbine (blade diameter, aerodynamic airfoils, chord, pitch and twist), and to evaluate the forces acting on the blades, the torque and the power at the rotor shaft. With this mathematical model, it is also possible to evaluate turbine performance for a wide range of wind velocities.

Wind turbine blades, like aeroplane wings and helicopter blades, are long (high

aspect-ratio) structures with an airfoil cross-section . However, the blade of a wind turbine is rotating and statically fixed to the ground, unlike helicopter and aeroplane blades which are rotating fast with high revolutions and are not fixed to the ground. Consider the section of wind turbine blade shown in Figure 2.22. The wind turbine rotates about an axis parallel to the free stream wind velocity, U_0 with angular speed Ω. The apparent flow speed seen by the wind turbine at a radius r is 1.
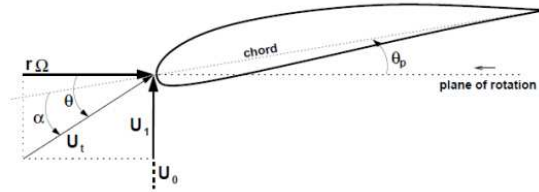
Figure 2.22: Apparent flow velocity at radius r (Eggleston & Stoddard 1987)

$$U_t = \sqrt{U_0^2 + (r\Omega)^2} \tag{2.1}$$

where U_t is the component of U_0 seen at the wind turbine. The swept blade area is denoted as A. The angle U_t makes with the plane of rotation is called the angle of incidence, and is given by :

$$\theta = \tan^{-1} \frac{U_1}{r\Omega} \tag{2.2}$$

The local speed ratio, X, is given by :

$$X = \frac{r\Omega}{U_0} \tag{2.3}$$

with special importance placed on the case of the local speed ratio occurring at radius $r=R$, where R is the length of the blade. This is called the tip speed ratio.

The angle U_t makes with the blade section's chord line is called the angle of attack

$$\alpha = \theta - \theta_p \qquad (2.4)$$

where θ_p is an arbitrary pitch angle set by the blade's designer.

2.10.3 The Actuator Disk Theory

In the 1920s, Albert Betz theoretically determined the maximum possible percentage of the power that can be extracted from the moving column of air. His calculations assumed an ideal rotor with no hub and perfectly axial flow. Additionally, the rotor analysed was considered to be massless, and the flow was considered to be incompressible. Using these assumptions, Betz determined that, ideally, 59.3 % of the energy can be extracted from the wind entering the wind turbine. By this analysis, there is no possible way to extract more power from the air by the wind turbine as shown in Figure 2.23.
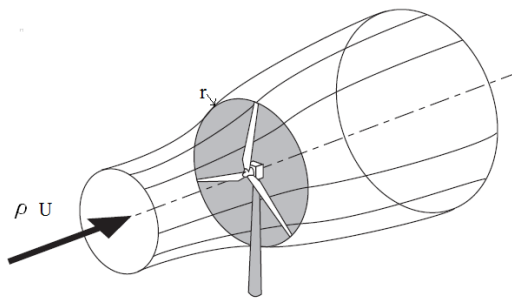
Figure 2.23: The energy extracting stream-tube of a wind turbine

(Burton et al. 2011)

Figure 2.24 represents the wind turbine between the upstream station and the downstream station. Since the same mass of air must leave the plane of the turbine as enters it, the incoming column of air must expand as it leaves the wind turbine. This causes an expansion of the flow tube. The more power that is extracted

from the column of air, the more it must expand. Therefore, if all the energy could be extracted, there would be no wind exiting the turbine violating the law of conservation of mass which states mass will never be created, or destroyed.
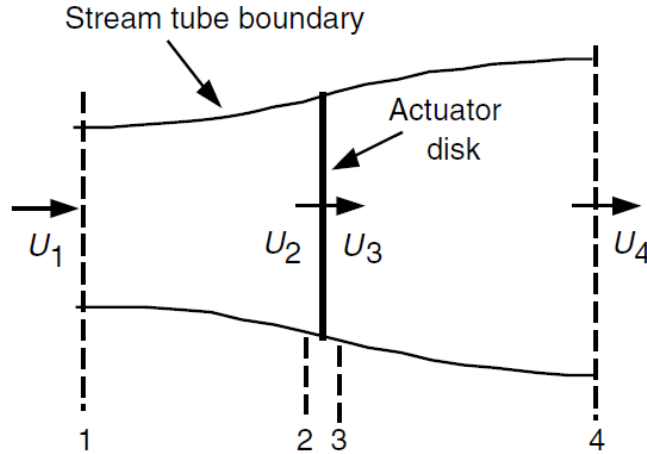
Figure 2.24: Wind turbine illustration: actuator disk model; U, mean velocity; 1, 2, 3 and 4 indicate locations (Eggleston & Stoddard 1987)

Applying the conservation of linear momentum to the control volume enclosing the whole system, one can find the net force on the contents of the control volume. That force is equal and opposite to the thrust, T, which is the force of the wind on the wind turbine. From the conservation of linear momentum for a one-directional, incompressible, time-invariant flow, the thrust is equal and opposite to the rate of change of momentum of the air stream:

$$T = U_1(\rho A U_1) - U_4(\rho A U_4) \tag{2.5}$$

where ρ is the density of air, A is the cross-sectional area, U is the wind velocity and the subscripts indicate the values at the numbered cross-section in Figure 2.24.

For steady flow, $(\rho AU)_1 = (\rho AU)_4 = \dot{m}$, where $\dot{m}$ is the flow rate. Therefore:

$$T = \dot{m}(U_1 - U_4) \tag{2.6}$$

thrust is positive, so the velocity behind the rotor, $U)_4$, is less than the free stream velocity, $U)_1$. No work done is done on the other side of the turbine rotor. Thus the Bernoulli function can be used in the two control volumes on either side of the actuator disk. In the stream tube upstream of the disk:

$$P_1 + \frac{1}{2}\rho U_1^2 = P_2 + \frac{1}{2}\rho U_2^2 \tag{2.7}$$

In the stream tube downstream of the disk:

$$P_3 + \frac{1}{2}\rho U_3^2 = P_4 + \frac{1}{2}\rho U_4^2 \tag{2.8}$$

where it is assumed that the far upstream and far downstream pressures are equal ($p_1 = p_4$) and that the velocity across the disk remains the same ($U_2 = U_3$).

The thrust can be also expressed as the net sum of the forces on each side of the actuator disk:

$$T = A_2(P_2 - P_3) \tag{2.9}$$

If one solves for $(p_2 - p_3)$ using Equation 2.7 and 2.8 and subsitutes that into Equation 2.9, this obtains:

$$T = \frac{1}{2}\rho A_2(U_1^2 - U_4^2) \tag{2.10}$$

Equating the thrust values from Equation 2.6 and 2.10 and recognising that the mass flow rate is also $\rho A_2 U_2$, obtains:

$$U_2 = \frac{U_1 + U_4}{2} \tag{2.11}$$

Thus, the wind velocity at the rotor plane, using this simple model, is the average of the upstreaam and downstream wind speeds. If one defines the axial induction factors, a, as the fractional decrease in wind velocity between the free stream and the rotor plane, then:

$$a = \frac{U_1 - U_2}{U_1} \tag{2.12}$$

$$U_2 = U_1(1 - a) \tag{2.13}$$

and

$$U_4 = U_1(1 - 2a) \tag{2.14}$$

The quantity U_1 is often referred to as the induced velocity at the rotor, in which case the velocity of the wind at the rotor is a combination of the free stream velocity and the induced wind velocity. As the axial induction factor increases from 0, the wind speed behind the rotor slows more and more. If $a=1/2$, the wind has slowed to zero velocity behind the rotor and the simple theory is no longer applicable. The power out, P, is equal to the thrust times the velocity at the disk:

$$P = \frac{1}{2}\rho A_2(U_1^2 - U_4^2)U_2 = \frac{1}{2}\rho A_2 U_2(U_1 + U_4)(U_1 - U_4) \tag{2.15}$$

Substituting for U_2 and U_4 from Equation 2.13 and 2.14 gives:

$$P = \frac{1}{2}\rho A^3 4a(1-a)^2 \tag{2.16}$$

where the control volume area at the rotor, A_2, is replaced by A, the rotor area and the free stream velocity U_1 is replaced by U.

Wind turbine rotor performance is usually characterised by its power coefficient, C_p:

$$C_p = \frac{P}{\frac{1}{2}\rho U^3 A} = \frac{rotor\, power}{power\, in\, the\, wind} \tag{2.17}$$

The non-dimensional power coefficient represents the fraction of the power in the wind that is extracted by the rotor. From Equation 2.16, the power coefficient is:

$$C_p = 4a(1-a)^2 \tag{2.18}$$

Obtaining a maximum C_p as a function of a gives $a=1/3$, so that $C_{p\,max} = \frac{16}{27} = 0.593$

$$u = \frac{2}{3}V_0 \tag{2.19}$$

$$u = \frac{1}{3}V_0 \tag{2.20}$$

The simplest model of a wind turbine attributed to Bertz is known as an actuator disk model where the turbine is imagined to be a circular disk through which the airstream flows with a velocity U_t and across which there is a pressure drop from P_1 to P_2. At the outset, it is important to stress that the actuator disk theory is

useful in discussing the overall efficiencies of turbines but it does not help at all with how to design the turbine blades to achieve the desired performance.

The analysis assumes homogeneous, incompressible, steady state fluid flow, and frictionless drag, an infinite number of blades, uniform thrust over the disk or rotor area, a non-rotating wake and the static pressure far upstream and far downstream from the rotor is equal to the undisturbed ambient static pressure. According to this theory, the theoretical maximum power efficiency C_p of any design of wind turbine is 0.593.

There is a significant amount of energy available in the wind, stored as kinetic energy, which can be extracted as usable power. The total power available in a cylindrical column of wind, $P_{available}$, is defined by the following equation.

$$P_{available} = \frac{1}{2}\rho A V^2 C_p \qquad (2.21)$$

or

$$= \frac{1}{2}C_p A V^3 \qquad (2.22)$$

Where C_p is the power coefficient , ρ is the density of air, A is the area of the rotor-plane, and V is the wind velocity.

2.10.4   The Panel Code Method

The three-dimensional panel code method using distributions of the constant source and doublet singularities over the discretised blade surface was chosen as the aerodynamic solver for the current project. A similar panel was constructed for the trailing wake, with a distribution of constant doublet singularities imposed to model the circulation shed at the trailing edge of an operating wind turbine as shown in Figure 2.25.
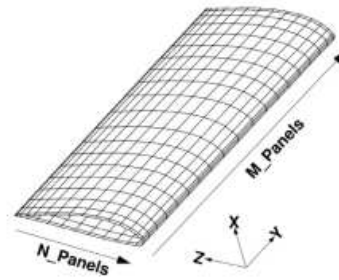
Figure 2.25: Panelling code direction (Hess & Year 1990)

This choice of this technique was made simply due to the fact that the method is capable of storing and evaluating many individual blade designs on modest commodity hardware, with acceptable accuracy and within an acceptable time (Hess & Year 1990).

This technique is very useful for a variety of simply-shaped bodies, but complicated configurations required a numerical scheme. The panel method provides a quick way of computing such flow fields. To introduce the ideas, consider the flow past a closed body in the panel method, the effect of the body is then represented by a large number, N, say, of line vortices, distributed over the surface of the body. The strengths Γ_1, Γ_2, Γ_1 and Γ_N of the vortices are essentially determined from the requirement that the normal velocity is zero at N target positions around the surface of the body. It is often convenient to take these target positions to be mid-way between the vortices as illustrated in Figure 2.26. Once the $\Gamma_n's$ are known, the velocity and pressure throughout the flow field can be readily calculated.
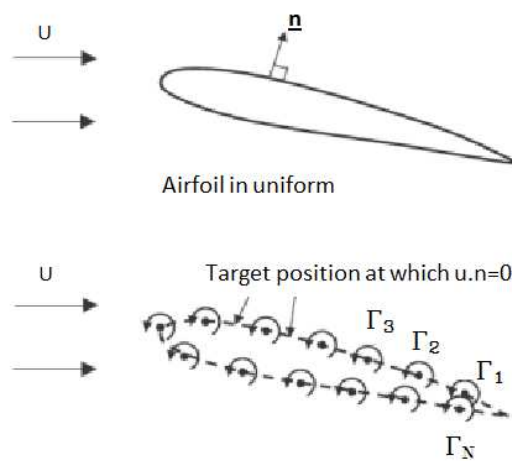
Figure 2.26: Airfoil replaced by N line vortices (Hess & Year 1990)

2.11   Design Analysis

The design analysis consists of the conceptual design, the detailed design of the components to withstand the loads they will be expected to experience, and then the testing of full wind turbines and components to ensure that they have indeed met those design goals. Wind turbine blades must be designed to convert the kinetic energy in the wind into torque, while having structural properties that ensure the required static and fatigue strength for a long operational life. Besides, they must have reduced material and manufacturing costs so that the total wind turbine system can be accepted in the market place.

Figure 2.27 shows a typical wind turbine blade section. A relatively, thin skin outside forms the outer contour of the airfoil. A longitudinal beam which is called the web or girder supports the outer shell and also carries the force acting on its shell when rotating. In order to reduce unnecessary weight in the rotor blade, the shape contour is tapered along the longitudinal direction. The airfoil was also tested to improve aerodynamic efficiency.
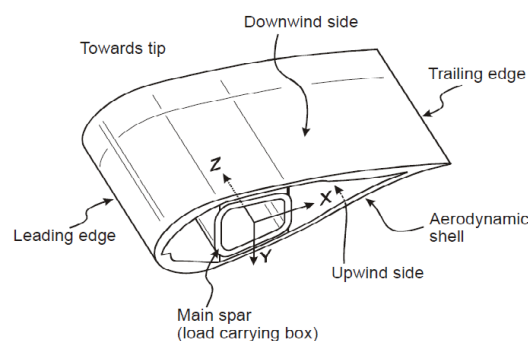
Figure 2.27: Typical cross section of wind turbine blade (Sorensen et al. 2004)

Sandwich materials are extensively used in wind turbine blades. Figure 2.28 illustrates that the sandwich panels in the webs or the girder box sides are the main materials with a biax $\pm 45°$ which is depicted in Figure 2.29, whereby skin layers with a PVC foam or balsa core take up the shear load. The sandwich panels in the shells consist of triax $\pm 45°/0°$ skin layers with a similar foam or balsa core.

The density and quality of the core materials can be varied with position on the blade.
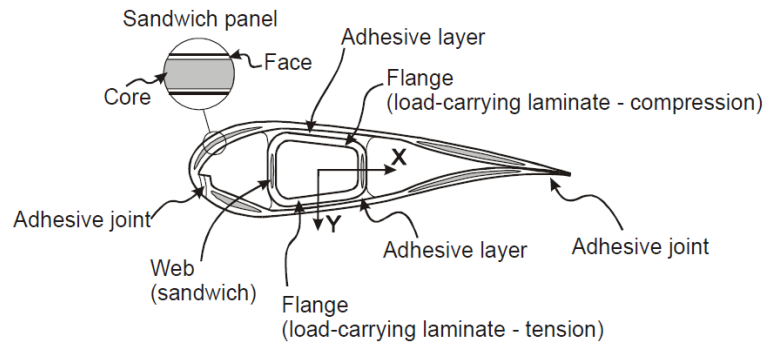
Figure 2.28: Girder box showing laminate, sandwich, adhesive bonds (Sorensen et al. 2004)
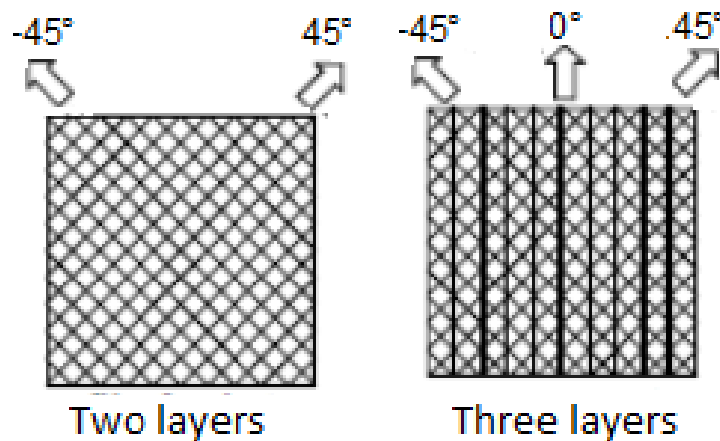
Figure 2.29: Direction of laminates (Sorensen et al. 2004)

Classification of materials for use in wind turbine blades is essential for the production quality, the performance and the lifetime of the blades. The materials, fibres, resins and core materials are required to be qualified before use in the manufacturing.

The properties of the core material influence the deflections of the shell and the tension, the compression, and the shear strength of the core are essential for the bending strength of the sandwich and the buckling load of the blade (Sorensen et al. 2004).

Figure 2.30 shows the geometrical parameters of an airfoil characteristic, which were defined by Pozrikidis (2009) are as follows:

(i) Chord line - the straight line connecting the leading edge to the trailing edge;

(ii) Chord, c - the distance from the leading edge to the trailing edge;

(iii) Camber line - the locus of points located halfway between the upper and lower surface of the airfoil;

(iv) Camber - the maximum distance of the camber line from the chord line;

(v) Thickness -the airfoil thickness along the camberline;

(vi) Angle of attack, α - the angle subtended between the incoming wind and the chord line.
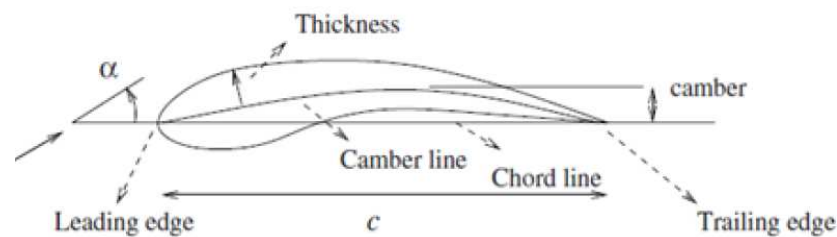
Figure 2.30: Airfoil characteristics wind turbine (Pozrikidis 2009)

As stated in the introduction, this study focuses on the design and testing of the plate-like structure for fixed pitch blades. The aerodynamic design for fixed pitch blades includes the selection of airfoils along the blade, the chord length, c, of the airfoil and the angle of twist, θ, from the direction of rotation. These parameters are shown in Figure 2.31.

The tip speed ratio as defined in Equation 2.23 must be selected for each specific system.

$$\lambda = \frac{\Omega r}{U} \tag{2.23}$$
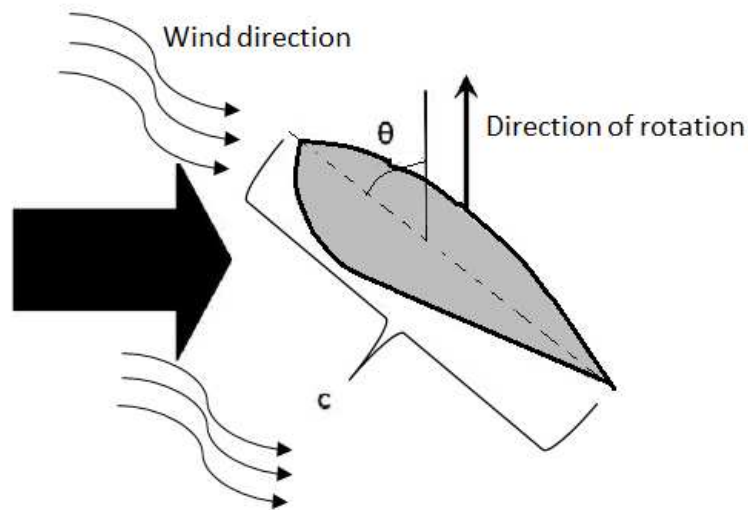
Figure 2.31: Design parameters (Eggleston & Stoddard 1987)

where Ω is the rotational velocity, r is the radius of the turbine and U is the incoming wind velocity. Depending on the type of wind turbine being designed, different tip speed ratios are recommended for maximum performance.

This can be seen in Figure 2.32. The dotted line across the top of the figure represents the Betz limit, while the others represent maximum predictions for the various types of systems.
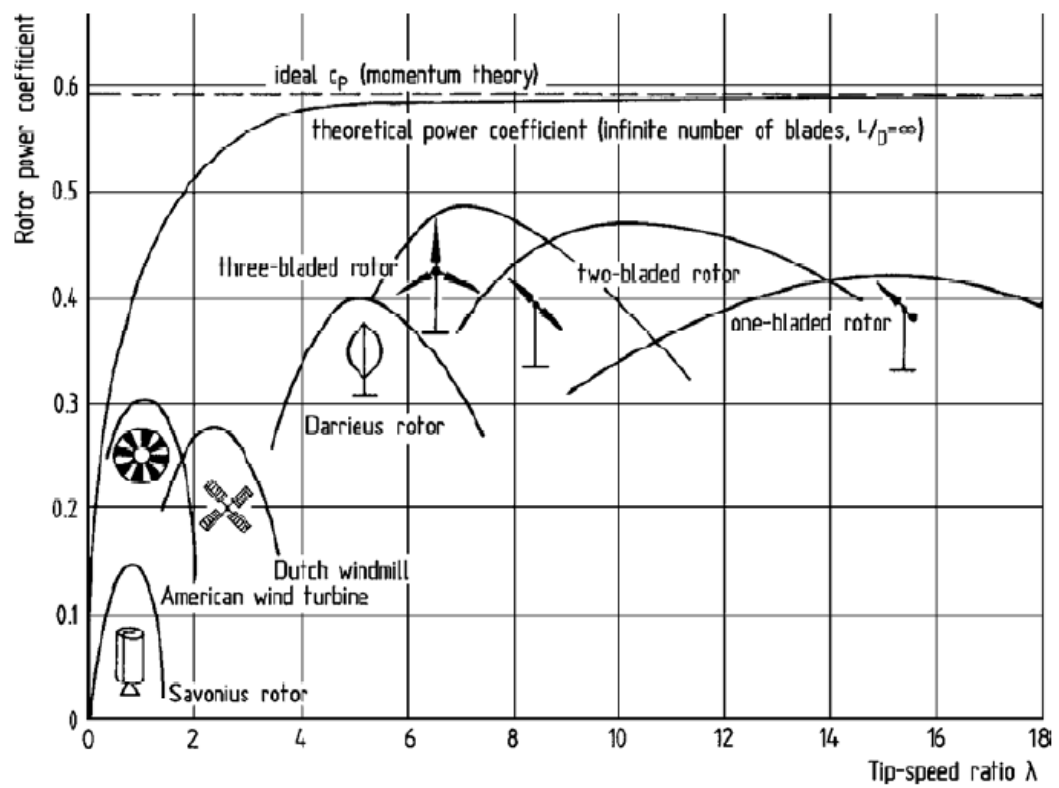
Figure 2.32: Optimum tip speed ratios for wind turbine systems (Hau 2006)

2.12   Wind Turbine Blade Fatigue Loads

The loads on wind turbine blades can be classified in two ways. The various comparisons for the study are illustrated in Figure 2.33, which shows the engineering applications of composites (from left to right: bicycle, car, aeroplane, helicopter, bridge, wind turbine). The abscissa shows the number of significant load cycles experienced during the structural lifetime, and the ordinate shows degree of variation in the load cycles.
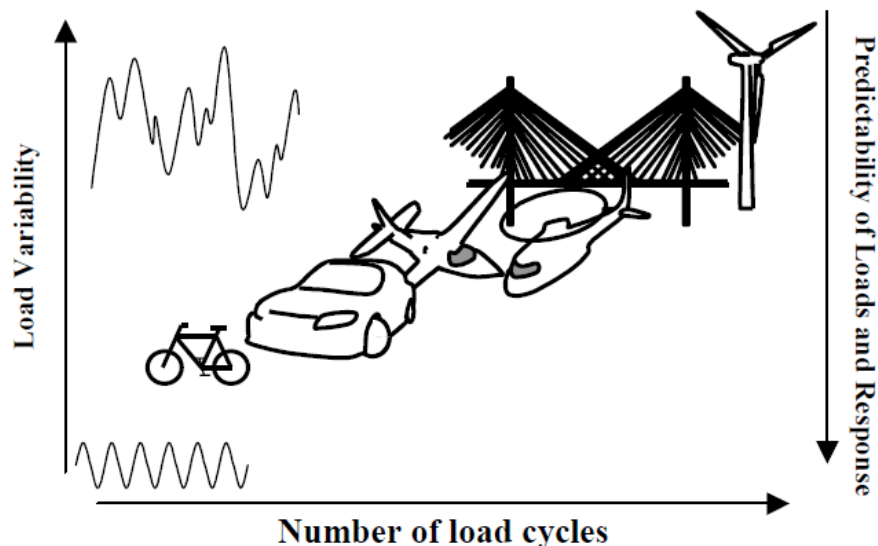
Figure 2.33: Wind turbine loading regime (Sutherland 1996)

The first y-axis represents that the variability of the loads on a rotor blade is a consequence of the stochastic nature of the wind. This is notwithstanding the fact that there are indeed some regular components of fatigue loading. These deterministic and non-deterministic components of the fatigue loads have been studied by Sutherland (1996). Wind turbine blades are subjected to a high number of loads during their targeted economical lifetime of 20 years. Estimates of the number of load cycles are up to 10^8 load cycles (Delft et al. 1997). The second y-axis shows the relationship of the predictability of loads and response.

Also indicated in Figure 2.33 is the degree of predictability of loading with respect to the number of cycles. It shows that the predictability of the loads and response

is inversely proportional to the variability of the loads. The more strongly the loads vary, the less predictable they are, and the more difficult it is to calculate the response (dynamic, fatigue) of the materials and structure. It is believed that fatigue loading would contribute to material degradation which would shorten the life span of the material.

The regions of loads on solid reinforcements are usually present in the leading and trailing edges of the blade. The remainder of the blade is generally constructed of multi-axial skin material and a sandwich structure, ensuring aerodynamic geometry, resistance to torsion, low weight and high buckling resistance. Figure 2.34 indicates what the main loads are, for different areas, in the load-bearing structure.
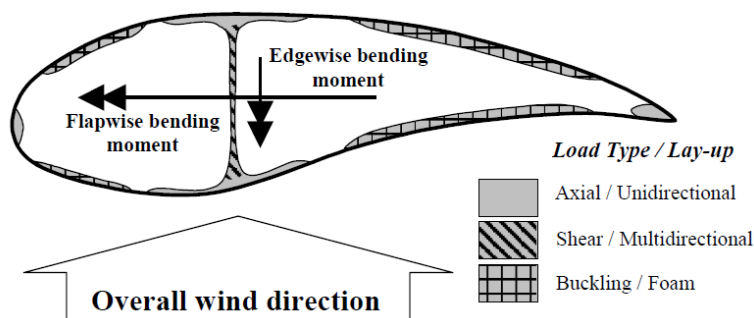
Figure 2.34: Typical wind turbine blade cross-section (Sorensen et al. 2004)

The flapwise-loads originate mainly from the wind load, acting perpendicularly on the rotor plane. These loads vary strongly in amplitude and mean. Edgewise loads originate mainly from the fact that the blade is loaded by its own weight, and by the torque loads that actually drive the turbine. The loading direction for edgewise loads changes twice during each revolution. Sutherland (1996) shows that the edgewise blade root bending moment frequency distribution from a small turbine contains two peaks: one originating from the wind loading, the other a result of the blade being loaded by its own weight. Caprile et al. (1995) presented histograms of mid-size wind turbine blade edgewise and flapwise blade root moments, showing the same peak for the edgewise loading. For larger rotor blades, the edgewise gravity fatigue loading becomes increasingly relevant for

lifetime prediction. Caprile et al. (1995) gives typical root bending moments from measurements on wind turbine blades, both in the flap and edgewise direction. Fatigue loads in wind turbine blades have a certain degree of statistical variability. Among material variability and other uncertainties, the actual varying load is an important source of scatter, as Svensson (1997), Epaarachchi (2006), and Epaarachchi & Clausen (2006) acknowledged. Lange (1996) found the fatigue reliability to be significantly affected by the type of model chosen for the loads data. He noted an increasing spread in failure probabilities for a given turbine life for flatter S-N curves. Riziotis & Voutsinas (2000) conducted numerical modelling of wind and wind turbines of the 0.5 MW class with different control strategies and identified the turbulence intensity as the most significant influence on the fatigue load contribution.

2.13   Structural Analysis of a Wind Turbine Blade

2.13.1   Considering the Blade as a Structural Beam

In the design of the model, the theory of a cantilever beam has been applied to model the actual structure of the wind turbine blade. In this theory, the wind turbine blade experiences deflection which causes shear forces and a bending moment throughout the wind turbine blade which is illustrated in Figure 2.35 (Peter & Richard 2012). The lift force on the blade, which drives the turbine round, is distributed along the blade approximately in proportion to the local radius, i.e. there is more lift force close to the tip than there is near the hub.

The lift force tends to make the blade bend. Let us consider a section of the blade at some point along its length; all the lift forces outboard of that point will have a cumulative effect on the tendency to bend, with those furthest away having the greatest effect as they have the greatest leverage. The effect is called bending moment. The bending moment is greatest at the root of the blade; at this point

there is more blade outboard (contributing to bending moment) than at any other point along the blade. At the tip the bending moment drops to zero.
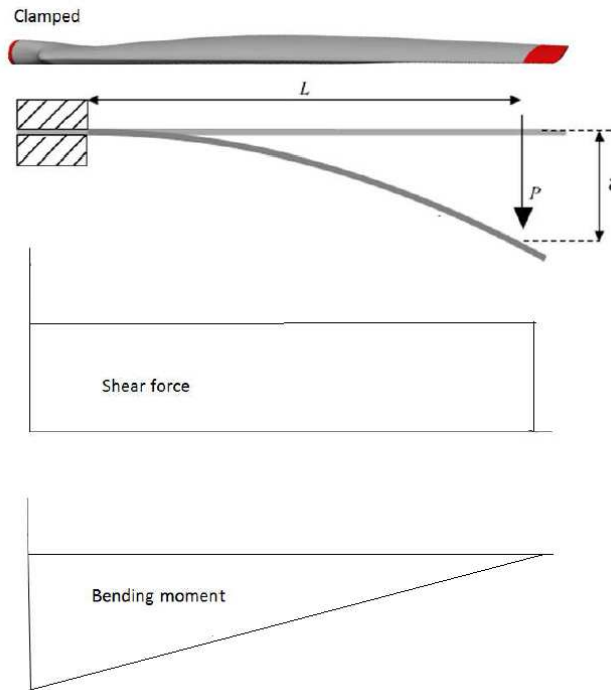
Figure 2.35: Bending moment and shear force against radius in a large turbine blade (Burton et al. 2001)

These forces arise, as a result of the blade mass, the blade rotation and gravity. A combination of aerodynamic, gravitational and inertial forces lead to two significant blade motions whilst rotating: blade flapping and blade lead-lag as illustrated in Figure 2.36a and 2.36b. Blade flapping, the motion of the blade out of its plane rotation, is fundamentally caused by variation in wind flow. Blade lead-lag is essentially caused by the operating blade rotating in a gravitational field. The centrifugal force acting on the blade creates a counter acting moment to that induced by the aerodynamic pressure. As such, centrifugal forces reduce the deflection, d, on the aerodynamically loaded blade.

Figure 2.37 shows the blade motion; let the resultant aerodynamic force be δF acting on the blade surface of δA at radius in the direction Y (Note: gravity forces and the in-plane component of the aerodynamic pressure are perpendicular

(a) Three blade motion (b) Lead-lag and flapping moment
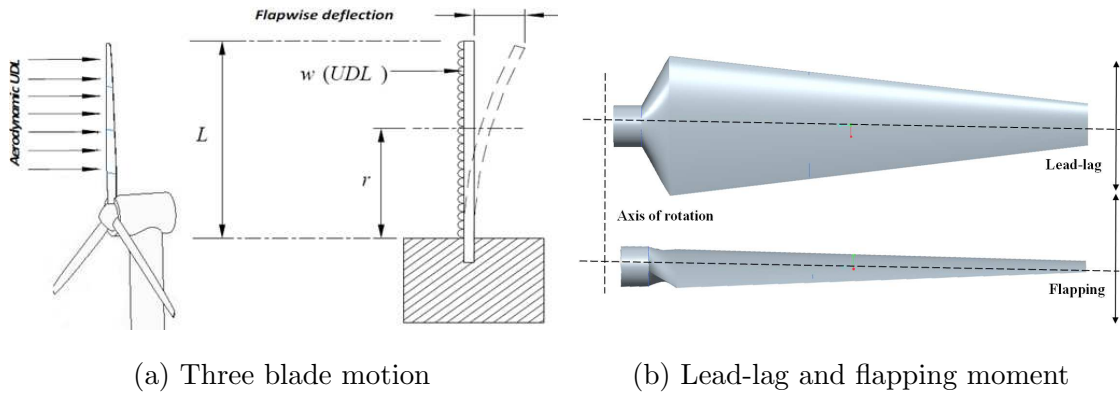
Figure 2.36: Blade load (sketch view) (Peter & Richard 2012)

to the flapping plane) on a blade in steady operation at rotational speed Ω ($<$ rated operational speed). At this particular instant, the total bending moment at the root end about the axis perpendicular the blade's rotational axis (Flapping moment) can be determined by:

$$M_{Flapping} = \Sigma_{Blade\ length}(\Sigma_{chord}\delta Fr - \Sigma_{chord}\delta M\Omega^2 rd) \tag{2.24}$$
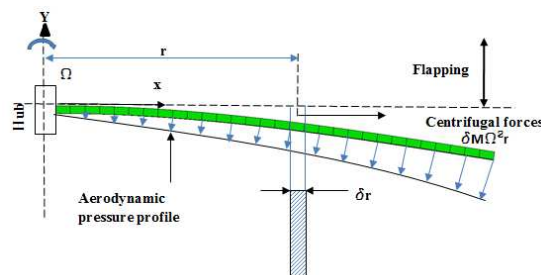
Figure 2.37: Inertial forces acting on a wind turbine blade (schematic view) (Eapaarachchi 2002)

Here, with an increase in speed up to the turbine's rated speed, d, deflection tends to increase due to the aerodynamic pressure load. However, the centrifugal force increases with the increase of the turbine speed squared, decreasing the bending moment at the root, $M_{Flapping}$ (Eggleston & Stoddard 1987).

2.13.2 Gravitational and Centrifugal Loads

The lift force on the blade, which rotates the turbine, distributed along the blade is approximately proportional to the local radius. As a result, there is more lift force closer to the tip than there is near the root. The lift force tends to make the blade bend and deflect. By considering a section of the blade at some point along its length, all the lift forces outboard of that point will have a substantial effect on the tendency to bend, with those furthest away having the greatest effect as they have the greatest leverage. The effect is called the bending moment. The bending moment is greatest at the root of the blade. At this point, there is more blade area outboard (contributing to bending moment) than at any other point along the blade (Peter & Richard 2012). At the tip, the bending moment drops to zero as shown in Figure 2.38.
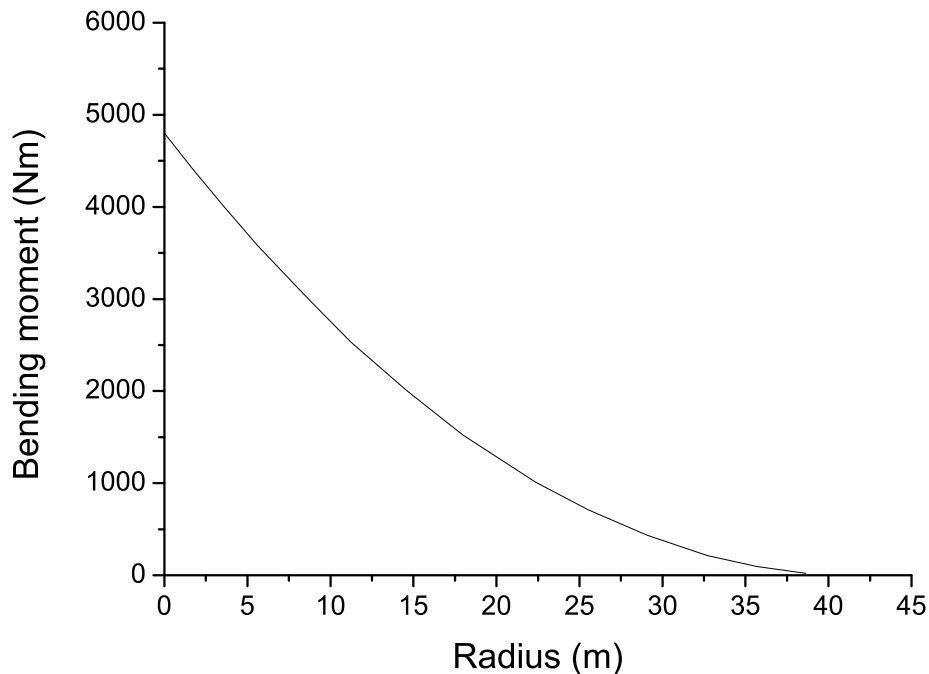
Figure 2.38: Bending moment against radius in a large turbine blade
(Nolet 2011)

The gravitational force is defined simply as mass multiplied by the gravitational constant, although its direction remains constant acting towards the centre of the earth which causes an alternating cyclic load case as the blade rotates. For smaller blades, gravity loads were not considered to be a major source of fatigue. But, as the size of the blades has become larger and leading to heavier blades, the effects of gravity cannot be ignored. Gravitational forces and generator torques result in lead-lag forces. Blade loads in this direction have a larger deterministic component. Because of the airfoil shape, wind turbine blades are typically very stiff in the lead-lag direction, and higher bending moments in the outboard sections are very large in this direction compared to flap bending moments.

The centrifugal force is a product of rotational velocity squared and mass and always acts radially outward, hence the increased load demands higher tip speeds. Centrifugal and gravitational loads are superimposed to give a positively displaced alternating condition with a wavelength equal to one blade revolution.

As the wind turbine rotates, it tries to straighten the blade by the centrifugal forces. Nevertheless, there is not enough time to take the deflection back completely to the original position. Without corrective action being taken, the blade efficiency is not compromised.

Therefore, as expected, the blade must be thickest and strongest at the root and can taper in thickness towards the tip where the bending moment is less. Theoretically, it applies to aerodynamics since the blade needs a thinner section at the tip where drag is the most critical and the local chord (width) of the blade is small. Besides, turbines rely on stall for power regulation in strong winds. A thin section stalls more easily and so is beneficial at the tip. Closer to the root the chord is wider, but to avoid making it very wide (hence expensive) the blade needs to be thicker to generate enough lift given the lower wind speed close to the hub (thicker aerofoils can generate a greater maximum lift before they stall). Unfortunately, the thickness needed to make the blade stiff and strong enough is greater than that required for aerodynamic efficiency, so a compromise must

be found between structural weight (cost) and the loss of aerodynamic efficiency (Hugh 2012).

2.13.3 Internal Beam Structure

If the blade were solid rather than hollow, the required thickness at each point along the blade would be determined by the bending moment at that point. But considering how the material in this hypothetical solid blade is working, as the blade bends downwind, the material on the upwind face of the blade stretches, carrying tension, and the material on the downwind face compresses, as illustrated in Figure 2.39. The material mid-way between the two faces, neutral axis in the middle of the blade, is neither in tension nor compression i.e. it does not do much work. So to reduce the cost of the blade it is reasonable to remove some material in the middle, and make the blade hollow.
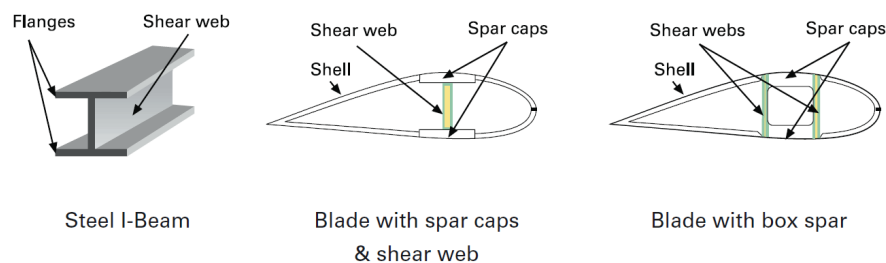
Figure 2.39: Internal structure described in I-beam (Burton et al. 2011)

In the worst case scenario, it is recommended to use two strips of material, one on the upwind face and one on the downwind face. However, this would not work for two reasons: shear strength and aerodynamics. Therefore, there must be a continuous shell to give the aerodynamic shape. Although the shear strength is less significant, it is most easily observed by considering what would happen to the two strips of material if they were not joined by anything. Definitely, they would slide relative to each other and act like two separate, very thin, blades. As a result, they would lose all the bending strength that should be maintained. In order for the blades to work properly, they must be structurally joined together.

This connection is called a shear web. The classic representation of this concept is the steel I-beam.

The major factor in understanding the concept of structural beams is that the material carrying bending loads (the spar caps) should be higher the second moment of area which is illustrated in Figure 2.39. The second moment of area is also known as the moment of inertia of a shape. The second moment of area is a measure of the efficiency of a cross-sectional shape to resist bending caused by loading. The higher the second moment of area the better structural beam resists deflection which mean the stiffer the structural in bending. Orientation can change the second moment of area. The wind turbine blade works in a similar manner to the steel I-beam except that there are shells around the outside that form the aerodynamic shape. The shells contribute some bending strength, but the majority comes from the spar caps, equivalent to the flanges of the I-beam. There are two typical ways to achieve the shear web connection: either the spar caps are built as part of the shell, and a separate shear web is bonded between them, or the shear webs and spar caps are built together as a box spar and glued into the shell.

2.13.4   Laminate Configuration

Modern wind turbine blades are constructed from glass fibre-reinforced plastics (GFRPs) which better strength-to-weight ratio in comparison to wood and metals. GFRP is particularly fabricated into long, slender structures like wind turbine blades because most of the stresses are in one direction and the fibres can be aligned to suit. It is fairly evident that most of the glass fibres in the spar caps should be oriented along the blade, since that is the direction of the bending loads (tension on the upwind side and compression on the downwind side). It can be observed that the fibres in the shear webs should be laid diagonally, so that they can carry shear loads meet the spar caps at 45° in either direction.

Let's simply consider a framework made of three bars, pin-jointed at their ends as shown in Figure 2.40.
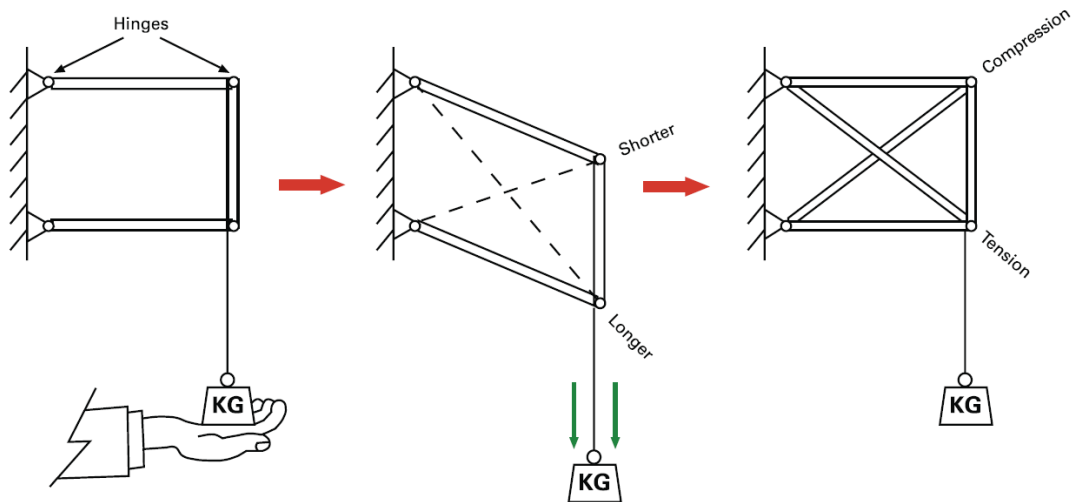
Figure 2.40: Shearing and reinforcement of a simple frame concept
(Burton et al. 2011)

If a concentrated load is applied to the structural framework, it will deform to a rhombus shape. The main thing to consider here is that the bars are still the same length, but the (imaginary) diagonal lines are not. One is now shorter and the other longer. The best way to stiffen the framework would be to add diagonal bars which act like an internal truss support structure. However, applying additional diagonal bars to the framework can be detrimental because it can cause a weight factor as well as increasing the cost of the materials.

The framework could be extended by adding more bars to form a longer beam. Each section would need a pair of diagonals to give it shear stiffness. Both diagonals are needed, where one works in tension and the other in compression. These forces balance out transversely to keep the spar caps at a constant distance apart. Longitudinally, their cumulative effect is to prevent the spar caps from sliding (shearing) relative to one another.

Two different fabric styles are typically used, to make the spar caps and the shear webs. Unidirectional fabrics are the best way to achieve the high axial fibre

content of the spar caps, while $\pm45°$ stitched biaxial fabric is used for the shear webs. The spar caps usually incorporate some biaxial to transfer load between the unidirectional fibres, either by interleaving the shear web plies (in the case of a blade with a box spar) or by including extra plies (in the case of a blade with a separate shear web). In the latter case, care needs to be taken to ensure sufficient overlap of the shear web with the spar cap to transfer all the load through the relatively weak adhesive that bonds them together.

If the load is applied to the framework, it will deform to a rhombus shape (shearing). The key thing to note here is that the bars are still the same length. However, the (imaginary) diagonal lines are not; one is now shorter and the other longer. So the best way to stiffen the framework would be to add diagonal bars as depicted in Figure 2.41.
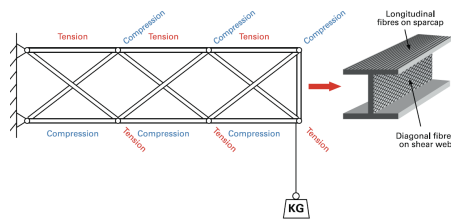
Figure 2.41: Extended framework with shear reinforcement
(Burton et al. 2011)

The ability to alter the strength of the blade without changing the outside shape (by making the spar caps thicker or thinner) gives researchers some ideas to optimise the design for minimum cost. If the blade is made thinner, it may perform better aerodynamically but thicker spar caps will be needed, making the blade more expensive. The shear web must also be stronger, but it will be narrower too, so the total amount of shear material is similar. Optimum geometry is arrived at iteratively by considering the turbine design, loads, structural design, and manufacturing costs.

2.13.5   Wind Turbine Blade's Shell

The main purpose of the shells is to provide an aerodynamic shape. This plays a structural role in stiffening and strengthening the spar, particularly to resist torsion (twisting) loads (Sorensen et al. 2004). Just as for bending, a larger section resists torsion better than a smaller one, and the blade shells are of course significantly larger in cross-sectional area than the box spar, so this is very useful in this respect. Structures loaded in torsion experience pure shear loading, so just like the spar shear webs, the shells have a proportion of fibres running diagonally.

The shells also have fibres running along the length of the blade. To some extent this assists the spar caps in flapwise bending but the main reason is to give the blade more strength in edgewise bending as structural beams work best with the load-carrying material being separated as far apart as possible. By looking at the cross-section, the shells are significantly wider than the spar so they are the most efficient way to provide edgewise bending stiffness.

Edgewise bending is primarily due to the blade's own weight. Since the centre of gravity of the blade is not very far outboard, by far the biggest edgewise bending moment is at the root. What this means is that whilst the shells can support the edgewise bending stresses for most of the length of the blade, often some extra reinforcement of the trailing edge is needed near the root.

If the blade shells were made just of GFRP, the thickness required to make them strong enough would be very small, only a few millimetres. However, since there can be a metre or more of the shell between the spar cap and the trailing edge, the shell would be too flexible if it were that thin. The flexibility is not only a problem for keeping the aerodynamic shape but also to resist buckling. Furthermore, there is a tendency for flexible structures to deflect sideways under compressive loading.

To make it thicker with more GFRP would add considerable weight and cost, so instead the shells are made as a sandwich construction of GFRP skins either side

of a low density core, usually rigid foam or balsa wood. This works along the same lines as the I-beam or box spar, with the core carrying shear loads and the skins providing bending stiffness. The foam core can be omitted where the spar caps support the shell, indeed it is advantageous to do this as it allows the spar caps to be better separated to carry the bending loads.

2.13.6   Wind Turbine Blade Root Design

The blade root generally needs to be circular in section to connect to the circular pitch bearing in the hub in order to get a uniform stress contribution. Since the blade needs to be removable for maintenance, this is invariably a bolted connection. If the spar was metal, it could have a flange welded to it but the same approach would be inefficient in glass fibre as the resin would have to support high stresses around the flange corner. Instead, most blade roots consist of thick tubes of solid laminate with studs or T-bolts screwed in or set into them with adhesive. The load can be transferred into the studs over their whole length, which suits the limited load capacity of the adhesive or threaded hole.

In manufacturing a blade, the I-section or box section spar must be joined to the cylindrical laminate at the root. For a box spar, it is possible to laminate the spar on a mandrel that is blended smoothly from circular at the root to rectangular further out, so that the thick root laminate can be interleaved seamlessly with the box spar. In practice, this can lengthen the time taken to make the spar, owing to the large number of plies that must be laid down to make the root. As a consequence, many manufacturers make the root as a separate component and bond it into the structure. Naturally if the adhesive failed, the consequences would be terminal: in short, the joint requires careful design and a strong, fatigue-resistant adhesive. In particular, great care must be taken to avoid the concentration of stress in the adhesive at either end of the joint.

2.13.7   Stiffness of Wind Turbine Blade

The blade not only needs to have strength, but also stiffness too. If the blade is not stiff enough it might suffer one of two problems, both due to the tower. If the tower is round, as most are, the wind forms a turbulent wake downwind of it. The turbine placed downwind of the tower would suffer large variations in lift force as the blades passed through the wake, leading to reduced power and high fatigue loading. So most designs put the turbine upwind of the tower. However, as the blades bend, they get closer to the tower, so must be made sufficiently stiff not to hit it. Designers typically aim for a minimum clearance between the blade tips and the tower of 30 % of the unloaded clearance under the worst-case loading.

It might seem that a simple solution would be to increase the initial tip clearance, either by putting the rotor further upwind of the tower, tilting it out at the bottom, pre-bending the blades, or coning such as angling all the blades upwind relative to the flat rotor plane. All of these approaches are impractically adopted to an extent, however, each has a cost associated with it, either in aerodynamic losses or greater manufacturing cost. For example, having a greater overhang of the rotor from the tower means that the nacelle yaw bearing must be stronger.

Another problem is that the blades still experience a pressure pulse from the air flowing around the tower even if they are upwind of it. This not only contributes to the fatigue loading, but more significantly can cause the blades to resonate. As a result, it will increases the vibration of the blade, and hence the fatigue stresses on the blade, hub and bearings. So the blade must be stiff and light enough to keep the natural frequency of vibration well above the tower passing frequency. Unfortunately, adding material to stiffen the blade increases the blade weight, and consequently it may be necessary to thicken the shape of the blade to address the natural frequency issues.
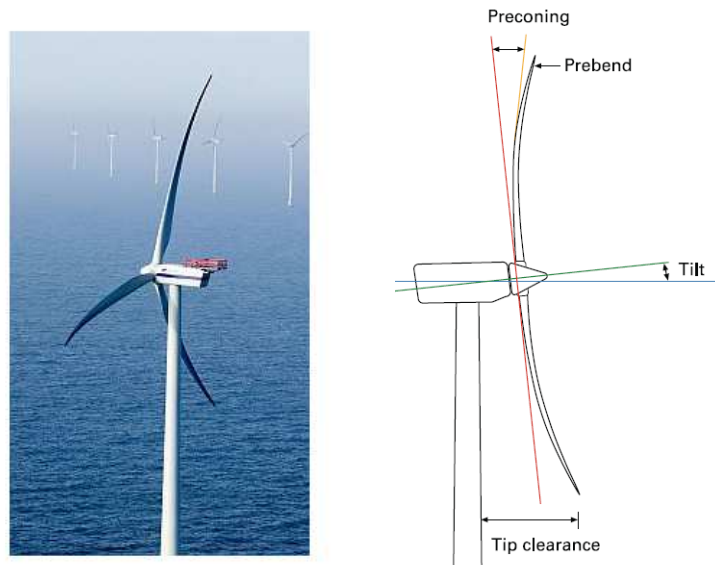
(a) Blade bending close to tower of upwind turbine

(b) Methods to increase static tip clearance of upwind turbine

Figure 2.42: Blade bending phenomenon (Burton et al. 2011)

2.14   Performance Analysis

The power coefficient, C_p, is shown as a function of the tip speed ratio, λ. The curves are based on data from different sources including a H-rotor for a British VAWT 260, which is a 100 kW, two-bladed turbine (Morgan et al. 1989), a Darrieus turbine from the turbine Sandia-34, a 500 kW turbine, developed and tested by Sandia National Laboratories (Ashwill 1992), and a HAWT from the National Renewable Energy Laboratory in the USA and is claimed to represent data for a typical HAWT (Muljadi et al. 1989).

Figure 2.43 indicates the performance for the three types of wind turbine operating at different tip speed ratios. It has been observed in Figure 2.43 that efficiency is still a major drawback to the use of VAWT's principle such as Darrieus and H-rotors in commercial power production. State of the art HAWTs have been

proven to have coefficient of performance (C_p) values approaching 0.50 while Darrieus designs have a coefficient of performance approaching 0.40, followed by H-rotor values at around 0.39 (Sandra et al. 2008). Unlike HAWTs, Darrieus and H-rotors have traditionally not been located on towers. This often limits the turbines access to higher winds and thus higher electrical production.
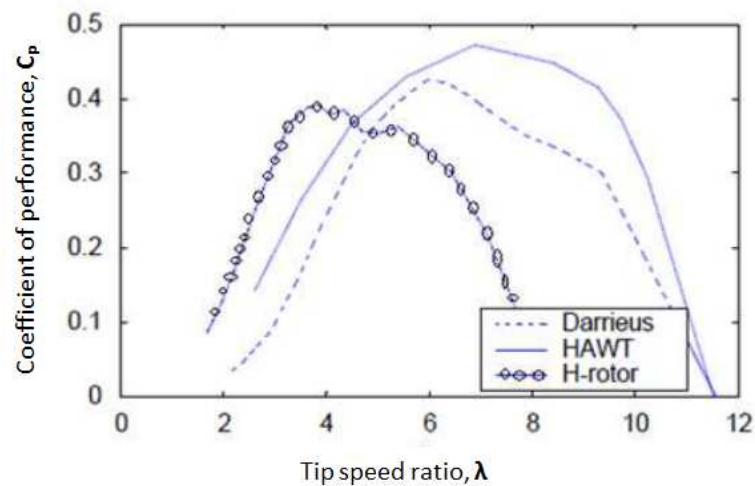
Figure 2.43: Power coefficient curves for the three different wind turbine types (Sandra et al. 2008)

One limitation of VAWTs in comparison to conventional wind turbines is that typically they produce less electricity relative to their size. The annual specific yield of VAWTs is less than that of HAWTs. As shown in Table 2.3, VAWTs generate significantly less electricity relative to their swept area than HAWTs. This is the reason why HAWTs have good economies of scale in terms of wind energy application. In fact, VAWTs cost more to operate and maintain than HAWTs.

Table 2.3: Theoretical Annual Specific Yield of HAWTs and VAWTs (Malcolm 2003)

Mean wind speed m/s	WinPACT 1.5 HAWT kWh/m^2	Indal 6400 VAWT kWh/m^2	SNL 34 VAWT kWh/m^2
6	950	500	679
6.5	1125	664	806
7	1296	846	1059
7.5	1461	1038	1255
8	1616	1235	1447
8.5	1761	1431	1631

Currently, due to the high demand for electricity and the desire for renewable energy, harnessing the wind is becoming more significant. In fact, larger diameters are needed to capture as much wind as possible. As a result, the growth of the wind turbine blade size has been tremendous as shown in Figure 2.44.
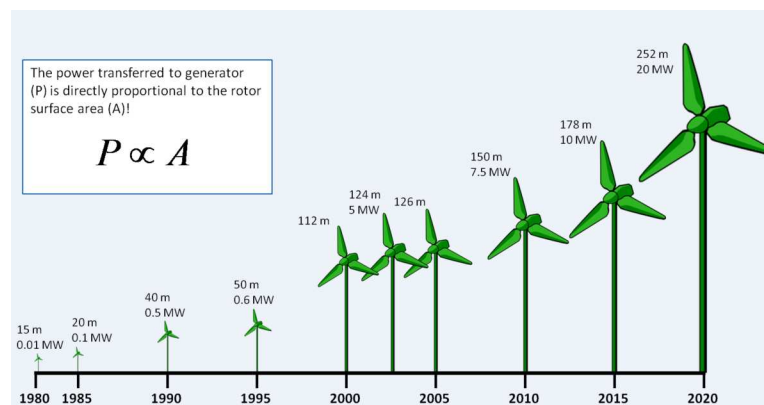
Figure 2.44: Growth of commercial wind technology (EWEA 2009)

2.15 Wind Turbine Blade Structure

At present, most wind turbines blade are built in fibre-reinforced polymer materials. Ultimately, wind turbine blades are complex composite structures containing a variety of structural details which can compromise blade performance. A ply drop off is a structural detail integrated into the thick laminates of wind turbine blades to provide thickness tapering. Stress concentration arising at this structural detail can lead to ply delamination and loss of structural integrity. Ply drop offs have been the subject of many studies in aerospace composite applications (Trethewey et al. 1990) as illustrated in Figure 2.45. They have also been adopted in wind turbine composite blades (Cairns et al. 1997).
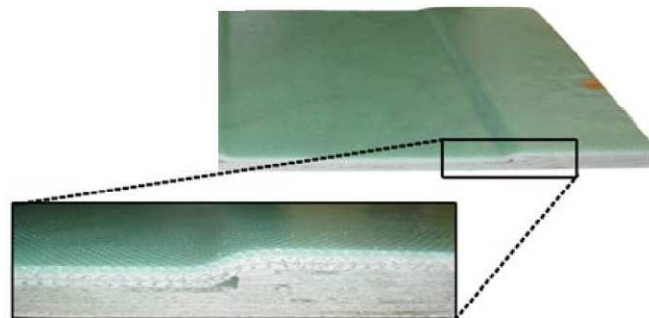
Figure 2.45: Example of ply drop off in composite materials (Trethewey et al. 1990)

The geometry of a general wind turbine blade follows a varying cross-section along its blade axis. Further, small wind turbine blades have a twisted root end for improved starting torque. Due to this reason, an asymmetric bending occurs in a wind turbine blade during the operation. This phenomenon will cause a complex stress field on the blade structure. A graded plate which is illustrated in Figure 2.46 would show a similar complex stress field due to bending and a reasonable alternative to simulate a wind turbine blade.
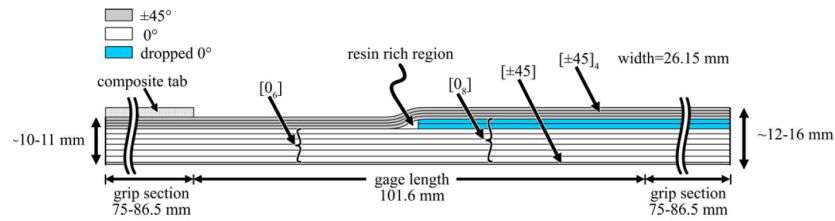
Figure 2.46: Material specimen preparation (Cairns et al. 1997)

2.16   Recovery of Wind Blade Deflection

There are small deflections in the wind turbine blade since the aerodynamic loads can be applied to the undeformed structure. Nevertheless, these assumptions are becoming less relevant with the present development of thin and flexible turbines. According to Rasmussen & Hansen (2003), the current key issues in flexible modelling are the large blade deflections which affect the loss of lift forces. The main motivation of the present study is to include the SMA wires which act as a self-straightening response with the glass fibre-reinforced plastic due to large blade deflections.

Larsen et al. (2004) has modelled the three bladed HAWT with the pitch control which correlates to the blade deflection. The turbine is divided into three substructures which are shown in Figure 2.47: the tower, the nacelle and the rotor. Each substructure has its own coordinate system which, due to a kinematic analysis of the movement and rotation of the substructure, allows for large rotations of the individual substructures with the representation of inertia loads inside the substructure. Within a substructure, which consists of several beam elements, the calculation of the deflections is linear and all the forces are placed on the structure in the undeformed state, hence large deformations within a substructure are not correctly represented.

The reason for this is that all the loads on the blades in a deflected situation will have a moment arm to the pitch axis creating a significant pitch moment contribution which is shown in Figure 2.48 in Equation 2.25.
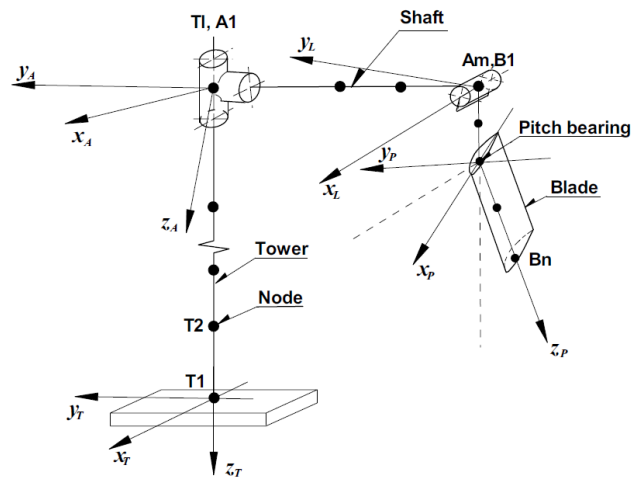
Figure 2.47: Illustration of the structural model of a three-bladed free body diagram (Larsen et al. 2004)
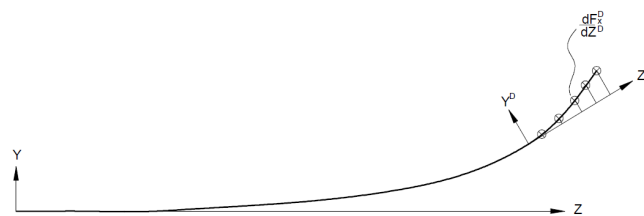
Figure 2.48: Illustration of pitch moment contributions from blade loads in the deflected location (Larsen et al. 2004)

$$M^D(z) = \int_z^{z_{max}} s^D(z) \times \frac{dF^D(z)}{dz} dz \tag{2.25}$$

$$M_n = (s_{n+1} - s_n) \times F_{akk,n+1} \tag{2.26}$$

$$F_{akk,n} = \sum_{i=n}^{n_{max}} F_i \tag{2.27}$$

A relationship states that the deflection is linear with the pitch which has been supported by the diagram shown in Figure 2.48.

2.17   Proposed Conceptual Model

In this study, the idea of the real wind turbine blade design is quite complicated such as the topology of the airfoil with the existing constraints and limitations. The proposed smart blades are made with an additional reinforcement using materials which in turn will save cost. By incorporating SMA, the blades are not only thin due to having less weight, but they have also increased in efficiency. As mentioned by Larsen et al. (2004), the reduction of power production was due to the reduced effective radius since there was a large blade deflection during the flapwise condition. He has developed an aeroelastic code, i.e. the Horizontal Wind Turbine Code (HAWTC), purposely to predict the load response for a two or three bladed HAWT.

In general, current wind turbine blade anatomy (as discussed in Section 2.11) is covered by the upper skin and lower skin as illustrated in Figure 2.49. It has a hollow space to reduce the heavy burden of the blade. As can be seen in Figure 2.49, root joints and spar caps are the most critical load bearing locations in the wind turbine blades. In order to join the two skins, the root and the spar cap were

constructed. Both of them were adhesively glued in the middle of the cross section between both skins. The root and the spar cap are considered as the backbone of the framework for the turbine blades.
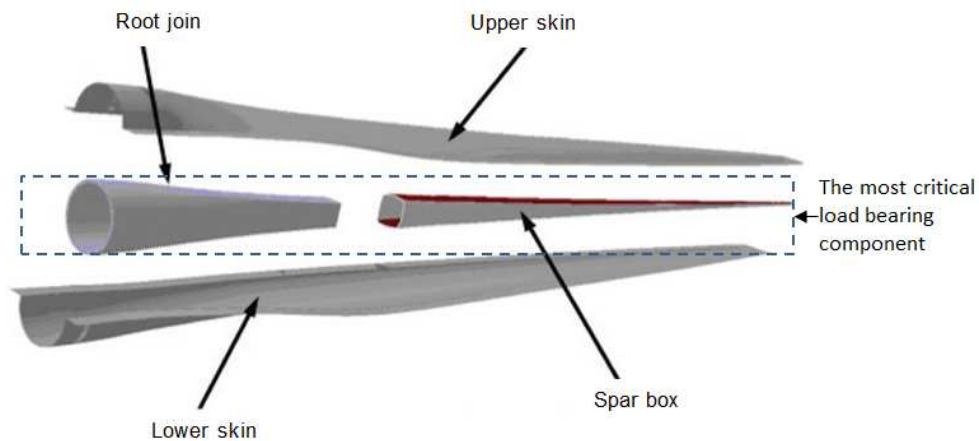
Figure 2.49: Modern wind turbine blade assembly (Petersen & Davis 2011)

In general, a wind turbine blade can be described similarly to a plate-like structure, which consists of the plate as the skin that surrounds the airfoil. The spar cap has a hollow space which has potential to be placed as the strengthening component.

To study the structural mechanisms, a plate-like structure has been modelled and an SMA component of plate-strengthening has been developed. It is desirable that this study should provide some benefit in addressing large deflections and also ease the burden of composites during bending deflection due to motion, especially at the spar box which is shown in Figure 2.50.

By using SMA wire, some relief in the composite stress recovery could be provided. In addition, the life span of the blade is improved with the efficiency of the turbine blade increasing too.

At the beginning, a simple and practical design was proposed, and has been tested in static conditions. This is the major structural component which could take-up the deflection. Thus, this study will provide a more robust analysis and some algorithms to develop existing bulky configurations of wind turbine blades.
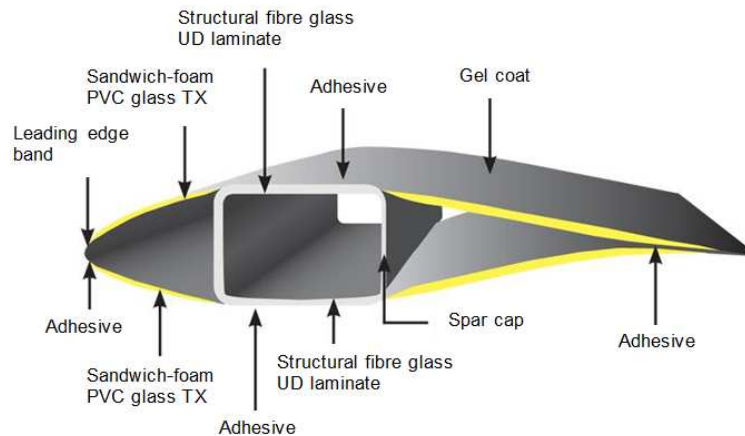
Figure 2.50: Conceptual design of plate-like structure (Petersen & Davis 2011)

Most of the modern wind turbine blades consist of a sandwich structure which is thin and light, and is made of GFRP for its high strength to weight ratio. However, it can be flexible when it is very long since it has a larger bending moment (Peter & Richard 2012).

To illustrate this point, i.e. the wind turbine blade being thin and light, a prototype of the plate-like structure is considered as a candidate for the wind turbine blade structures as shown in Figure 2.51. It is then proposed that the plate-like structure will be incorporated with SMA wires.
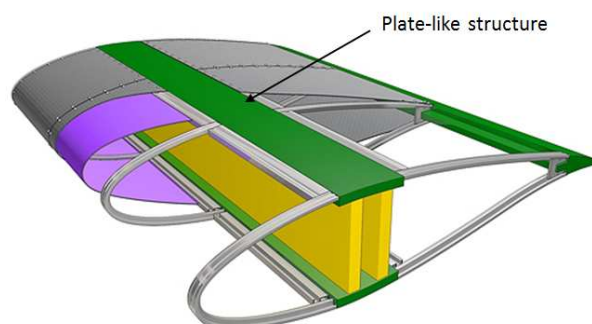
Figure 2.51: A cross section of a GFRP blade. The blade stretched over a composite frame (light grey) and central spar (yellow and green) (Petersen & Davis 2011)

2.18   Summary of Literature Review

The structural performance of a wind turbine is predominantly based on the knowledge of the air flow behaviour (aerodynamic property) over the turbine blade and how the blade reacts to the aerodynamic loads. Aerodynamic analysis and its associated theories were discussed in the literature including blade element theory, actuator disk theory and panel codes. A general Horizontal Axis Wind Turbine (HAWT) consists of three basic parts: the tower, the nacelle, and the blades. It is shown that the blades are fixed to the hub, and can be considered as a cantilever beam. The centrifugal force on the blade acts as a restoring force to the blade deflections. This phenomenon was interpreted as a stiffening of the blades, and is commonly called centrifugal stiffening. The stiffening effect is caused by rotating centrifugals, so for the rapid rotational blades with a small deformation, their stiffness will increase noticeably. On the other hand, the spin softening effect is caused by the deformation of the rotating blades; hence for the large scale blades the spin softening effect will be more significant than for the small ones. In either case, the axial force bending moment and the gravitational force become dominant as the blade gets larger, while with small wind turbines centrifugal forces usually dominate. A direct effect of the dominant role of centrifugal forces at small blades is that blades have greater stiffness (due to centrifugal stiffening) and are only lightly bent by the axial force. Slender blades have been proposed as they have been modelled in a plate-like structure. The proporsal is to analyse the load caused by the wind blade structures using finite element analysis as a tool for predicting the deflection before running the actual experiment. This study will serve as a guide in the development of smart materials for application in the wind blade design concept that will be discussed in the next chapter.

Chapter 3

FEA Model and ANN Model Development

3.1 Introduction

Chapter 3 discusses the methodology that is used in this study. This chapter is divided into two main sections which are the development of FEA for the proposed model and the ANN model related to smart wind turbine blade development. A detailed design specification of the proposed model, such as model characterisation, physical properties and simulation, are provided in the relevant section in this chapter. The first section deals with the proposed model used that is involved in the the FEA development, e.g. the type of element, the type of interaction and boundary condition. The second section describes the ANN used in the development and the performance criteria. Finally, a summary is discussed in Section 3.7.

3.2   Finite Element Model Development

Finite element analysis (FEA) is a very useful tool and has been widely used in the development of wind turbine blades for investigating the global behaviour in terms of eigen-frequencies, tip deflections, and global stress/strain. The FEA simulation usually predicts the global stiffness and stresses with a high level of accuracy. Local deformations of smart composite blades which have two different properties are often more difficult to predict and several works have been published in this area. The reason for this is that the highly localised deformations and stresses can be non-linear, while the global response appears to be linear for relatively small deflections.

Another reason is that a relatively simple shell model can be used for representing the global behaviour, while a computationally more expensive 3D solid model may be necessary to predict this localised behaviour. Even with a highly detailed 3D solid model, it would rarely be possible to predict deformations or stresses accurately without the calibration of the FE model.

This calibration is required due to large manufacturing tolerances. Features such as box girder corners and adhesive joints often vary from the specifications. Geometric imperfections are often seen and can cause unexpected behaviour, especially relating to the strength predictions but also the local deformations can be affected. The big advantage of using FEA is that, once the model is set up and calibrated, complex load cases representing actual wind conditions can be analysed.

FEA is a tool that executes a structural analysis and predicts its responses and behaviours by using physical laws and mathematical equations. By changing the variables in the simulation, predictions may be made about the behaviour of the system such as the internal forces, stresses and the deformations of structures under various load effects. Structural modelling is a tool to establish three mathematical

models, including:

(i) a structural model consisting of three basic structural members or components, joints (nodes, connecting edges or surfaces), and boundary conditions (supports and foundations);

(ii) a material model;

(iii) a load model.

Modern load analysis of a wind turbine blade would typically consist of a 3D CAD model analysed using the FEA. Certification bodies support this method and conclude that there is a range of commercial software available with accurate results. These standards allow the blade stress condition to be modelled conservatively using classical stress analysis methods.

Traditionally, the blade would be modelled as a simple cantilever beam with an equivalent point or uniformly distributed loads used to calculate the flapwise and edgewise bending moment. The direct stresses for the root sections and bolt inserts would also be calculated. The following simple analysis offers a basic insight into the global structural loading of a wind turbine blade. In practice, a more detailed computational analysis would be completed including local analysis of individual features, bonds and material laminates.

There have been many studies using FEA structural analysis in the study of wind turbine blades. Among them are Jensen et al. (2006) who worked on the structural analysis and numerical simulation of a 34 m composite wind turbine blade; the material taken in this work is GFRP. They observed the ovalisation of the load carrying box girder in the full scale test. A global non-linear FEA model of the entire blade was prepared and the boundaries of a more detailed sub-model were extracted. The FEA model was calibrated based on full-scale test measurements.

A probabilistic model for the analysis of the safety of a wind turbine rotor blade

against failure in ultimate loading is presented by Kunt & Larsen (2000). In their work, they considered the failure in flapwise bending during the normal operating condition of the wind turbine. The model is based on an extreme value analysis of the load response process in conjunction with a stochastic representation of the governing tensile strength of the rotor blade material. The probability of failure in flapwise bending of the rotor blade is calculated by means of a first order reliability method, and contributions to this probability from all local maxima of the load response process over the operational life are integrated.

Jureczko et al. (2005) investigated the problem of the multi-criteria optimum design of wind turbine blades. They developed a computer program package that would enable the optimisation of wind turbine blades with regard to a number of criteria.

In this work, a blade of length 38.95 m was designed for the 1.65 MW horizontal axis wind turbine with the help of Glauert's optimal rotor theory. Finite element analysis of the blade structure was performed using ANSYS® software and the results were compared with the work done by Jensen et al. (2006). In this work, the material were taken is E-Glass/ Epoxy prepreg material and the properties taken from the work of Brondsted et al. (2005).

3.2.1   FEA Modelling

In this analysis, three-dimensional structures under arbitrary load conditions were analysed using plate elements in order to simulate the deflection. The procedure to be adopted for the blade is illustrated using a strip blade element, a typical finite element idealisation considered in the analysis of a wind turbine blade. The blade root is fixed to the rotor hub and is treated as a cantilevered box beam.

The geometry of the test specimen was a rectangular plate of unidirectional glass fibre reinforced epoxy matrix system whose dimensions were 300(W) × 60(H) ×

4(D)mm. The ply configuration was 0º/90º/-45º/45º /45º/-45º/90º/0º/90º/0º/45º/-45º which has been modelled in ABAQUS®. The test specimen is made to enable a visualisation which is as close as possible to the real geometry. The model was classified into the S4R element type. It was assumed that the interaction of the epoxy and the glass fibre is perfectly bonded.

After the part and the material have been created, a composite layup section can be created. The composite layup editor is used to create plies and to assign materials and orientations to these plies. In this step, a composite layup that represents the specimen layup is created and defined. The thickness, the number of section points required for numerical integration through each layer, and the material name and orientation associated with each layer are specified. The Gauss integration rule and 3 integration points were used in this study.

The SMA, which has Flexinol 90 material properties, was also incorporated into the finite element model. In this model, the element type used is T2D2. The wire diameter was 0.51 mm. In order to simulate in FEA, a series of stress-strain data from uniaxial tests was used to analyse the mechanical properties of the SMA, particularly the Young's Modulus, E.

To facilitate the whole assembly of the system, the interaction of the two different materials was implemented considering there to be no errors and less warning, but if possible no warning should be displayed in the monitoring message. Figure 3.1 shows the GFRP and the SMA wires that were assembled into the whole system. Adjustable vertical heights of 60 mm, 50 mm, 40 mm and 30 mm and wire lengths of 305.9 mm, 304.2 mm, 302.7 mm and 301.5 mm were tested respectively. As the structure of the real blade is in a core sandwich panel, it is ideal to use a 30 mm height. Translation and rotation constraints were used to connect the wire into the plate during assembly. When creating each instance, the part instance was switched to auto offset. In order to locate the wire precisely, a datum reference point was used as a datum point. This datum can also be easily used as the reference point for the partition face.
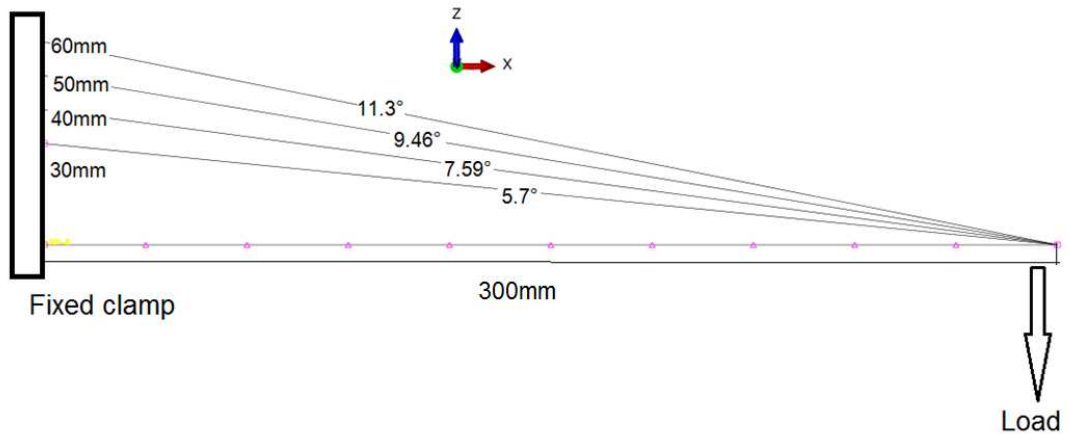
Figure 3.1: Schematic diagram of the model (side view)

Figure 3.2 depicts an example of the model of 1 SMA wire under meshing. As can be seen, the wire has been treated as the wire part element and the plate GFRP plate as the solid part element. Other assemblies of 2, 4 and 6 SMA wires have been geometrically drawn for this test.
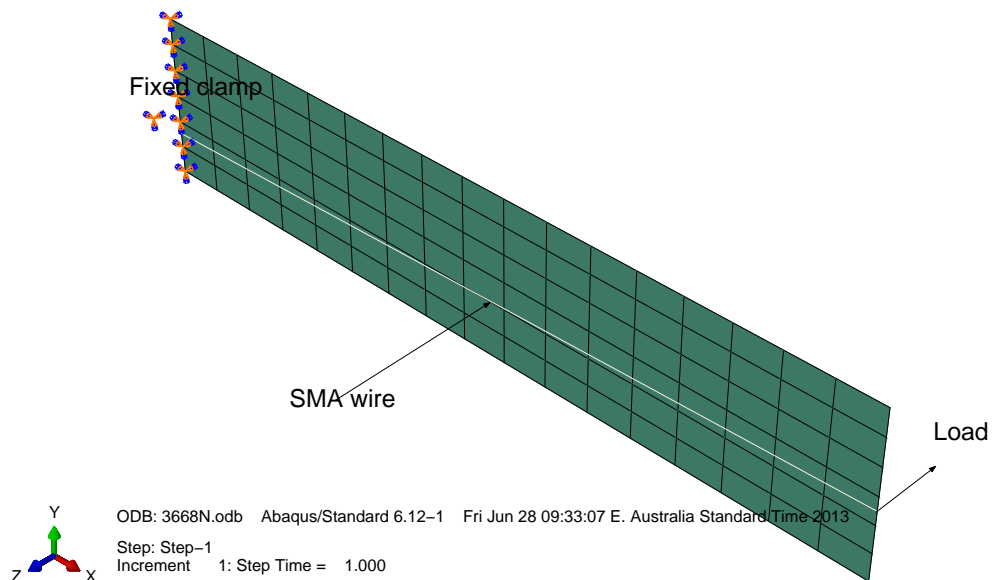
Figure 3.2: Suspended SMA of 1 wire and the GFRP which have undergone a meshing process

The whole assembly of the plate has been generated into meshes by inserting local seeds, which represent the sizing control of the mesh. For example, in this

analysis a single element for the SMA wire and ten elements for plate have been applied as depicted in Figure 3.2. In this analysis, the SMA wire is uniform in shape, and the temperature variation was assumed constant through its thickness. A single element was used during meshing. The SMA wires were suspended at the vertical height of 30 mm in which the boundary condition was fixed.

3.2.2 Preliminary Study of a Graded Plate

A numerical model has been developed to analyse the deflection behaviour of the graded GFRP beam using ABAQUS 6.12® (Simulia 2012). The ply configuration as shown in Table 3.1 and the mechanical properties as shown in Table 3.2, were used to simulate the model of a graded beam with the element type SC8R. The 3D model of the graded beam is shown in Figure 3.3. It was assumed that the interaction of the epoxy and the glass fibre is perfectly bonded.

Table 3.1: Laminate configurations

Configuration	Ply Orientation (°)	Length (mm)
1	0	600
2	90	550
3	-45	520
4	45	480
5	-45	430
6	45	410
7	90	360
8	0	320
9	90	270
10	0	220
11	45	160
12	-45	110

The material properties that are usually used for an elastic analysis are: modulus of elasticity, shear modulus, Poisson's ratio, the coefficient of thermal expansion, the mass density and the weight density. Although ABAQUS/CAE® is a unitless software which is independent of unit dimension, it also ensures all the units involved are consistently used throughout the analysis.

Table 3.2: Mechanical properties of SMA, GFRP, Epoxy and Core

Material	SMA Nitinol	Fibre E- Glass UD	Epoxy Kinetix R246TX	Core Foam
E_1 (MPa)	32000 (martensite) 83000 (austenite)	34412	10500	20
E_2 (MPa)	-	6531	-	-
ν_{12}	0.3	0.217	0.28	0.3
G_{12} (MPa)	-	2433	-	-
G_{13} (MPa)	-	1698	-	-
G_{23} (MPa)	-	2433	-	-
ρ (kg/m^3)	6450	2000	-	-
Elastic	Isotropic	Lamina	Isotropic	Isotropic

3.3   Types of Elements

To simulate the structural analysis covered in this research, the following elements from ABAQUS® were used: continuum shell elements (SC8R), conventional shell elements (S4R), and truss elements (T3D2). Solid shell continuum elements and shell elements were used to model the composite plate since it is a plate-like structure, while truss elements were used to model the SMA wire anchoring.

3.3.1   Continuum Shell Elements (SC8R)

ABAQUS® has a large library of solid elements each with a different capability, accuracy and efficiency, and a few of the typical elements are shown in Figure 3.4. SC8R is a brick element which has an integration of 8 nodes at its corners, and linear interpolation would be applied in each direction. SC8R is the most general element adopted in most of the 3D finite element models according to its quick solution and good accuracy. SC8R is generally used for a very detailed model because it has more integration points in each element compared with the S4R. This could bring some benefit when the transfers in each element are very large, but this will increase the computing time greatly. Considering both the running time and the accuracy for the numerical analysis, ABAQUS® conventional shell element type (S4R) was chosen in this numerical study.
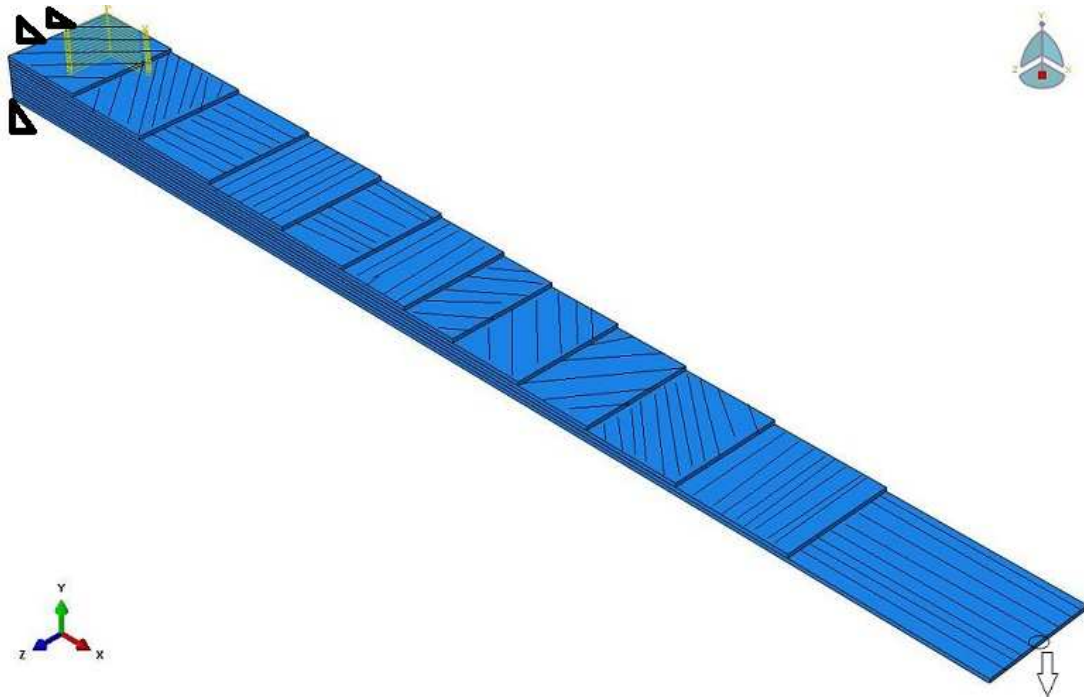
Figure 3.3: Graphical model representation with plies configuration orientation

3.3.2 Conventional Shell Elements (S4R)

Conventional shell elements are usually applied to the structure which has a significantly smaller thickness compared to the other two dimensions. Conventional shell elements may be used. Both types of shell element have similar kinematic and constitutive behaviours but the continuum shell element looks like a three-dimensional solid. Figure 3.4 compares these two types of shell element. For conventional shell element, its thickness is defined through the section property definition. In contrast, the thickness of the continuum shell element is determined by the element's nodal geometry.

3.3.3 Truss Element (T3D2)

A truss element is a two-force member that is subjected to axial loads in either tension or compression. The only degree of freedom for a truss element is axial
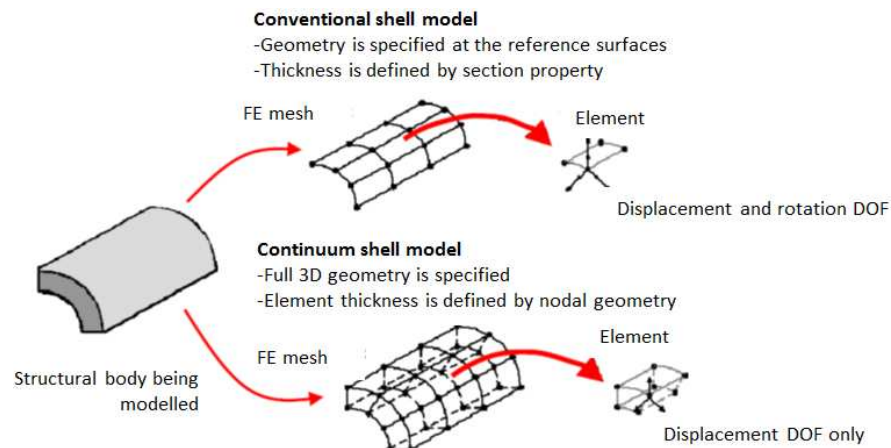
Figure 3.4: Differences between conventional and continuum shell elements (Simulia 2012)

displacement at each node. The cross sectional dimensions and material properties of each element are usually assumed constant along their length. The element may interconnect in a two-dimensional (2D) or three-dimensional (3D) configuration. Truss elements are typically used in the analysis of truss structures.

3.4 Types of Interactions and Boundary Conditions

There are a large number of interactions in the structure between different materials. It is important that these interactions are correctly treated to ensure the efficient and accurate modelling of the structural behaviour.

3.4.1 Constraint 1

For a graded plate-like structure model, Constraint 1 has been constructed. The `*TIE` was applied if there are plies to plies interfaces. In this case, it has been

assumed that most of the plies are tightly bonded to each other. Consider the first ply as the `*MASTER SURFACE`. The surface to the other adjacent ply has been considered as the `*SLAVE SURFACE`. This is treated consistently with other plies until the last ply. In this method, the discretisation of surface to surface has been implemented.

3.4.2   Constraint 2

For the SMA wire and the GFRP plate model, Constraint 2 has been applied. In this model, the composite plate and the SMA wire components of the structure are modelled using different elements. Since they can be divided into two different components, it is not appropriate to use one set of nodes to represent the two different materials initially in contact with each other. Instead of using `*TIE Constraints`, `*MPC Constraints` were applied. Denoting one master face as a control point and the slave face as a slave node, this constraint ties the slave and master faces using MPC Type with `*PIN` for the duration of the simulation. This tie means that each node on the slave surface has the same translational and rotational motion as the closest point on the master surface. The slave surface can be either an element-based or a node-based surface. The master surface can be any type of surface. Two types of formulations are available: surface-to-surface formulation or node-to-surface formulation. Figure 3.5 illustrates the side of the section on which `MPC` was applied.

3.4.3   Modelling Discretisation

The fabrication of the physical model was performed to facilitate the use of the model within the experimental work. The plate-like structure was made from fibreglass and the SMA wires were incorporated in the plate.

The formulation of a mathematical model using discrete mathematical elements
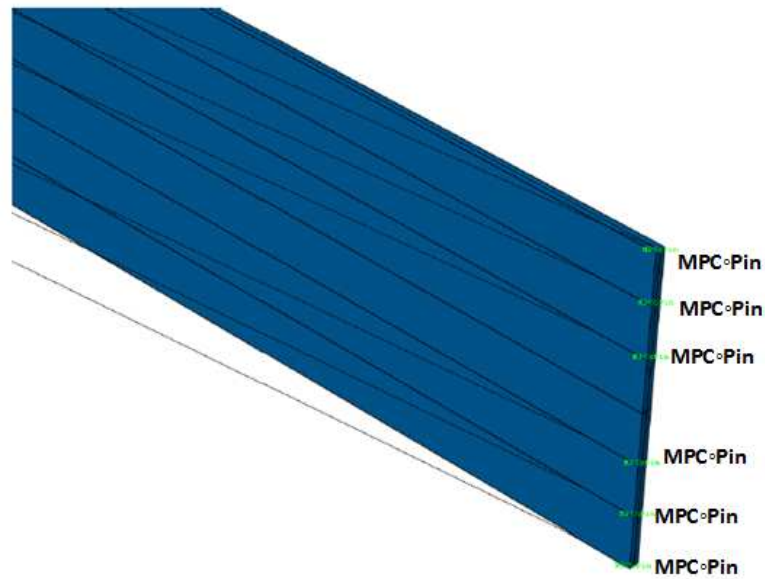
Figure 3.5: MPC implemented between the SMA wires and the GFRP plate
(end section view)

and their connections and interactions to capture the prototype behaviour is called
discretisation.

For this purpose:

(i) Joints/Nodes were used to discretise elements and primary locations in the
structure at the displacements which are of interest;

(ii) Elements were connected to each other at joints;

(iii) Masses, inertia, and loads were applied to elements and then transferred to
joints.

3.4.4 Creating Composite Layup and Defining Material Properties

After the part and the material have been created, a composite layup section
can be created. The composite layup editor is used to create plies and to assign

materials and orientations to these plies. In this step, a composite layup that represents the specimen layup is created and defined. The thickness, the number of section points required for numerical integration through each layer, and the material name and orientation associated with each layer are specified as part of the composite layup section definition. The Gauss integration rule and 3 integration points are used in this study. A part of the plate has been plotted in the S4R element type which is illustrated in Figure 3.6.
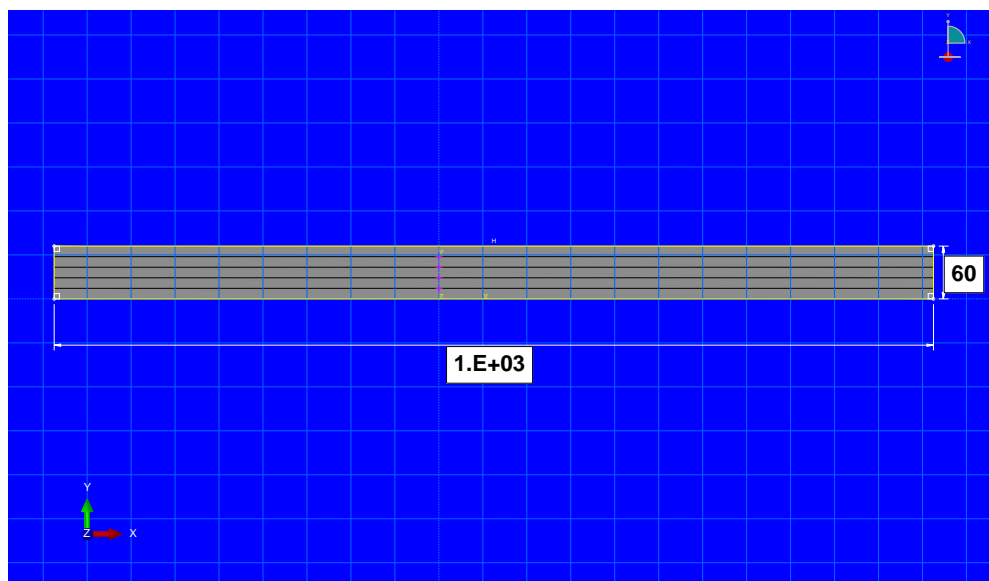
Figure 3.6: Sketching part of the plate

3.4.5   Creating SMA and Defining Properties

The SMA, which has Flexinol 90 material properties, was also incorporated into the finite element model (Flexinol 2010) as shown in Figure 3.7. In this model, the element type used was T3D2 (A 2 node linear 3D truss). The wire diameter was 0.51 mm. In order to simulate in FEA, a series of calibration data of the stress-strain data from uniaxial testing was used to analyse the mechanical properties of the SMA, particularly Young's Modulus, E. The wire length is 1001.80 mm, with respect to its optimised height at the angle of 3.43° from the tip which is depicted in Figure 3.8.
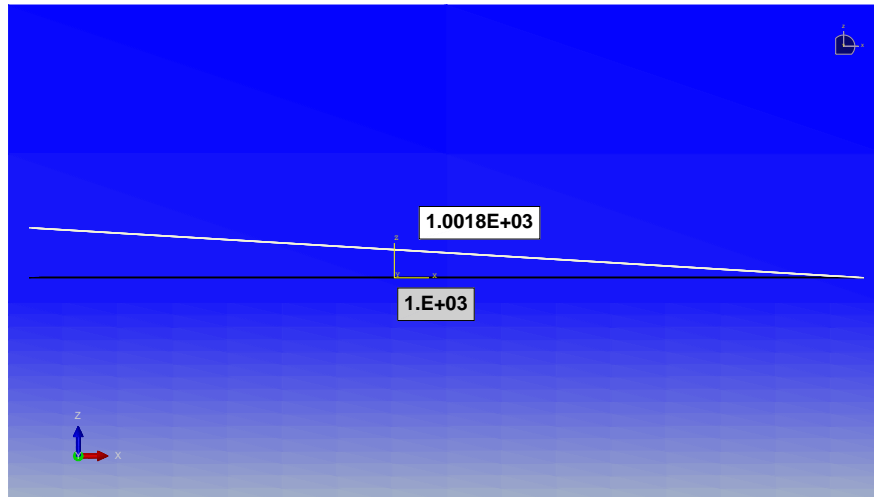
Figure 3.7: Sketching part of the wire
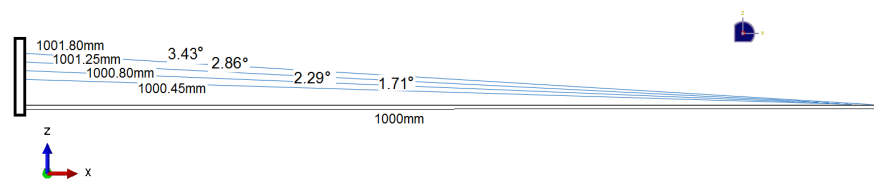
Figure 3.8: The orientation of the angle between the SMA wire and the
GFRP plate in the side view angle

3.5   ANN Model Development

ANN has been considered as a tool to predict the performance of the proposed wind turbine blade model. The terminology Artificial Neural Network (ANN) has been used in recognition of the way the human brain computes information. The human brain thinks in an entirely different way from the conventional computer: the brain is a highly complex, non-linear and parallel information processing system. The brain computing process to perform a certain computation is many times faster than the fastest digital computer in existence today, due to its capability to organise its structural constituents, known as neurons. The brain accomplishes perceptual recognition tasks routinely, e.g. recognising a familiar face embedded in an unfamiliar scene. A neural network is a machine that is designed to model the way in which the brain performs a particular task. The network is implemented using electronic components or is simulated in software on a digital computer. A neural network is a massively parallel distributed processor made up of simple processing units, which has a natural propensity for storing experimental knowledge and making it available for use. It resembles the brain in two respects:

(i) Knowledge is acquired by the network from its environment through a learning process;

(ii) Interneuron connection strengths, known as synaptic weights, are used to store the acquired knowledge.

The procedure used to perform the learning process is called a learning algorithm. The function of this is to modify the synaptic weights of the network in an orderly fashion to attain a desired design objective.

Like the human nervous system, it can be broken down into three stages, which can be represented in the block diagram as shown in Figure 3.9. ANNs are

parallel processing models which can be generated in predicting outcomes based on input-output data (parameter and variables relationships), demonstrating a degree of robustness and self-learning capability. The accuracy and reliability of the predicted outcomes can be increased based on the number of input values. In this way, the accumulation of data sets into an ANN system can enhance its outcome and predictability as the likelihood of any value will be based on previous experimental data (Sapuan & Iqbal 2010). It is composed of a large number of highly interconnected processing elements (neurones) working in unison to solve specific problems. Like people, ANNs learn by example. An ANN is configured for a specific application, such as pattern recognition or data classification, through a learning process. Learning in biological systems, which is shown in Figure 3.9, involves adjustments to the synaptic connections that exist between the neurons.
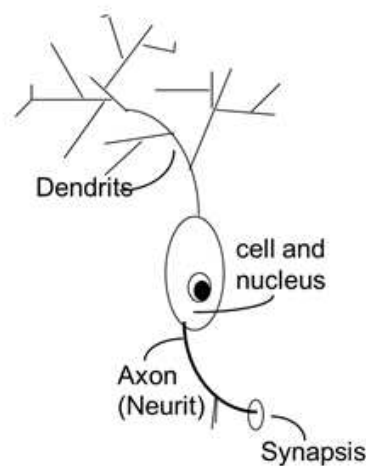
Figure 3.9: Biological diagram of a neuron

The characteristics and mechanism of the actual ANN details are as follows:

(i) Dendrit: acts an input which is receiving other activations;

(ii) Axon: acts as an output which generates the activation;

(iii) Synapse: acts as a transfer of the activation;

(iv) Cell nucleus: acts as a processor which evaluates the activation work.

As neural networks can work in a non-linear way, they can be used to extract patterns and detect trends that are too complex to be noticed by either humans or other computer techniques. With their great ability to give meaning to complex data or imprecise data, neural networks need training. A trained neural network can be described as the learning process of humans in this case it can be thought of as an expert in the category of information it has been given to analyse (e.g. in school, the human will have a teacher for history and another one for physics, so is an expert in this particular information). This expert (input training data) should be able to provide projections given new situations of interest and answer the questions. The other advantages are as follows:

(i) Adaptive learning: An ability to learn how to do tasks based on the data given for training or initial experience;

(ii) Self-organisation: An ANN can create its own organisation or representation of the information it receives during the learning time;

(iii) Real-time operation: ANN computations may be carried out in parallel, and special hardware devices are being designed and manufactured which take advantage of this capability;

(iv) Fault tolerance via redundant information coding: Partial destruction of a network leads to a corresponding degradation of performance. However, some network capabilities may be retained even with major network damage.

Neural network simulations appear to be a recent development. However, this field was established before the advent of computers, and has survived at least one major setback. Many important advances have been boosted by the use of inexpensive computer emulations. Following an initial period of enthusiasm, the field survived a period of frustration and disrepute. During this period when funding and professional support was minimal, important advances were made by relatively few researchers. These pioneers were able to develop convincing

technology which surpassed the limitations identified by Minsky & Papert (1969). In their book (1969), they summed up a general feeling of frustration (against neural networks) among researchers, and this was thus accepted by most without further analysis. Currently, the neural network field enjoys a resurgence of interest and a corresponding increase in funding.

The benefits of using ANNs are as follows:

(i) Extremely powerful computational devices;

(ii) Massive parallelism makes them very efficient;

(iii) Particularly fault tolerant: this is equivalent to the graceful degradation found in biological systems;

(iv) Noise tolerant: so they can cope with situations where normal symbolic systems would have difficulty.

This makes the ANN system robust as it is an adaptive system which can change based on the information it has already acquired or will obtain. This study describes the use of ANN to predict the characteristic number of SMA wires with the relationship of the parameters measured.

Parameters of the measured data, such as the applied load, time response, electrical current and vertical deflection, were produced by experiments with a number of SMA wires. The model used was based on a feed-forward system based on sintering temperature and material composition.

A specific form of ANN, multilayer perceptrons (MLPs) - also referred to as multilayer feed forward neural networks - consist of an input layer, one or more hidden (inner) layers, and an output layer. Inside the network, weights are adjusted when data passes between the artificial neurons along the connections. For given training data consisting of input-output vectors, the values of the synaptic weights

in an MLP are iteratively updated by a learning algorithm to approximate the target behaviour. This process is called learning or training. Training is usually performed by back-propagating (BP) the error signal, layer by layer, and adapting synaptic weights with respect to the magnitude of the error signal (Beigy & Meybodi 2009). This process is briefly described mathematically as follows in the illustration in Figure 3.10.
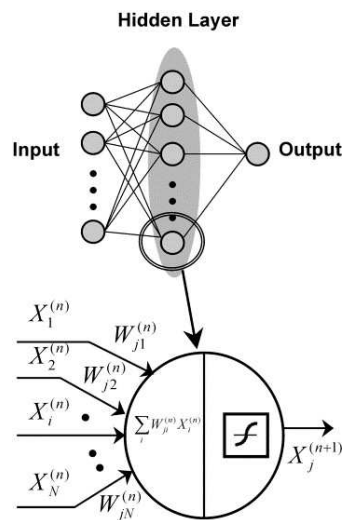
Figure 3.10: Artificial neuron diagram

An artificial neuron receives information (a signal) from other neurons, processes it, and then relays the filtered signal to other neurons. Figure 3.10 illustrates a multi-layer feed-forward ANN configuration in its upper part. It can be observed that ANNs are conventionally constructed with three layers, i.e. input, output and hidden layers. Hidden layers can contain one or several layers for practical application. Each layer has different numbers of neural elements. Basically, the network function is largely determined by the connections between these elements. As schematically shown in the lower part of Figure 3.10 the relationship between the input vector $X_i^{(n)}$ and the output vector $X_j^{(n+1)}$ of this element can be described as follows:

The parameters can be expressed in the form of the following equations:

$$X_j^{n+1} = F[\sum_i W_{ji}^{(n)} X_i^n] \tag{3.1}$$

where F(x) is the tan-sigmoid function F(x)$=\frac{1}{1+e^x}$

or other non-linear transfer function, e.g. log-sigmoid function, and $X_j^{(n+1)}$ is the output of unit j in the n th layer, $W_{ji}^{(n)}$ is a weight from unit i in n th layer to unit j in ($n+1$) th layer. An input vector is presented in the units of the input layer. Units in the next layer compute a weighted sum of the input, and output the result of a non-linear function of the sum. The learning procedure is based on a gradient search, with a least sum squared optimum criterion of errors between the predicted and desired values:

$$E = \sum_{p=1}^p (d_p - o_p)^2 \tag{3.2}$$

The total sum squared error E is averaged over all patterns in the training set, in which d_p is the target output (predicted) for the p th pattern and o_p is the actual output (measured). In the minimisation process, the weights of all the connecting nodes are adjusted until the desired error level is achieved or the maximum number of cycles is reached. The learning algorithm used here for the weights is:

$$W_{ji}^{(n)}(t+1) = W_{ji}^n(t) + \Delta W_{ji}^{(n)}(t) \tag{3.3}$$

with its correction:

$$\Delta W_{ji}^{(n)}(t+1) = -\eta \frac{\delta E}{\delta W_{ji}^n} + \mu \Delta W_{ji}^n(t) \tag{3.4}$$

where $W_{ji}^{(n)}(t)$ is the training signal of the correct answer at the t th learning step, $\Delta W_{ji}^{(n)}(t)$ is the correction of the weight at the t th learning step, η is the learning rate, and μ is the momentum factor. η is a small parameter to adjust the correction each time, and μ reduces oscillation and aids rapid convergence. Appropriate values of these parameters aid network learning. A linear transfer function is employed between the hidden and the output layer, to avoid limiting the output to a small range. It is believed that the two-layer sigmoid network can represent any functional relationship between input and output if the sigmoid layer has enough neurons.

3.6   Performance Criteria

This study is to evaluate the predictive ability using machine learning (ML) which is MBP and NARX. The performance comparison between MBP and NARX is undertaken. To facilitate the performance comparison, all networks simulated have been designed and trained accordingly from the output layer, hidden layer and output layer. The output neuron uses hyperbolic tangent activation functions. The standard back-propagation algorithm is used to train the networks with a learning rate equal to 0.01. Once a given network has been trained, it is required to provide estimates of the future sample values of a given time series for a certain prediction. The predictions are executed in a recursive curve until the desired prediction horizon is reached, i.e., during N time steps the predicted values are fed back in order to take part in the composition of the regressors. The networks are evaluated in terms of the root mean square error (RMSE).

There are various methods available for evaluating model performance, including numerical indicators and graphical representations. In this study, some numerical measures are as follows: the epoch that gave the lowest RMSE for the test set was selected as the optimum epoch at stopping point. The comparison between the three gradient descent versions is also made by considering the CPU time elapsed

at the end of the training.

3.6.1 Multi-Back Propagation (MBP)

Figure 3.11 illustrates the learning process of a multi-layer neural network employing a back propagation algorithm. To illustrate this process a three layer neural network with, for example, three inputs, three hidden layers and one output is implemented. Two types of sigmoid activation functions are selected for several numbers of the hidden and output layers which are: logarithmic sigmoid function (logsig) and hyperbolic tangent sigmoid function (tansig) respectively. The adjustable weights used to propagate errors back are equal to those used during computing the output value. Only the direction of data flow is changed (signals are propagated from output to inputs one after the other). This technique is used for all the network layers. Free software has been used to generate the MBP, which uses programming code C (Noel & Bernardete 2001, Noel & Bernardete 2003, Kahandawa 2012, Kahandawa et al. 2013).
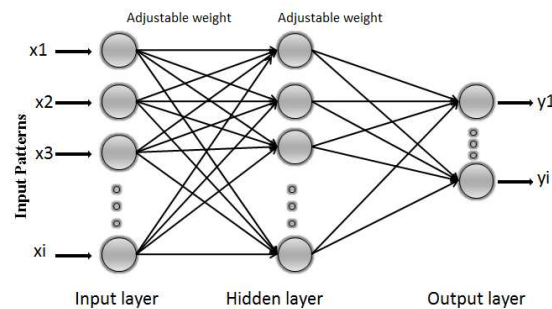
Figure 3.11: Graphical representation of the MBP network

3.6.2 Non-Linear Auto-Regressive with Exogenous (NARX) Input

Non-linear auto-regressive with exogenous (external) input (NARX), which is depicted in Figure 3.12, has been used in order to produce future prediction values

of the time series, y(t), from past values of that time series and past values of a second time series, x(t). In this experiment, NARX consists of numbers of hidden layers, numbers of delay lines (D) and one output neuron with a two layer feed forward network. The standard Lavenberg-Marquardt (LM) back propagation algorithm is used to train the network with a learning rate close to 0.001. Method regularisation has been used which consists of 1000 epoch, and the regularisation parameter used is 1.00e-05. MATLAB® code has been used to run the ANN toolbox (`nntool`), which has been generated using the mode LM back-propagation (Mark et al. 2013).
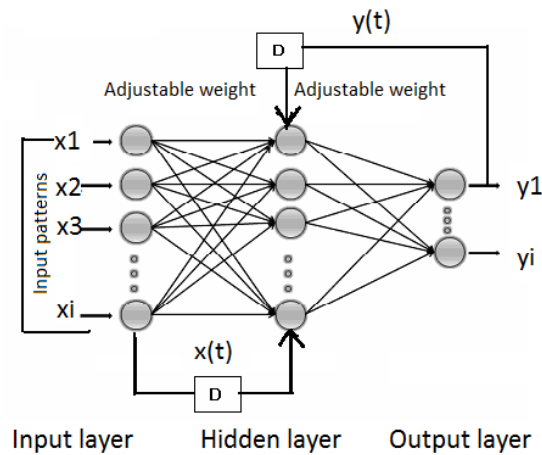
Figure 3.12: Graphical representation of NARX network

Throughout this section, the ANN can be generated using the mode Levernberg-Marquardt back-propagation (`trainlm`). Data division has been selected at random (`dividerand`) based on the training out of 80 % and 10 % for testing and the remaining 10 % for validation. The performance was based on the Mean Squared Error (`MSE`) and the derivative in default mode (`defaultderiv`). `MSE` is the average squared difference between outputs and targets. As a rule of thumb, lower values are better. However, zero means no error. Regression values measure the correlation between outputs and targets. An `R` value of 1 means a close relationship, and 0 a random relationship.

3.7   Summary of FEA Model and ANN Development

In this chapter, the development of the FEA model was presented. To identify the proposed design that will be used in the study, the characteristics and general mechanisms of SMAs (such as calibration and application) in the case study were also elaborated. The finite element modeling of composite wind turbine blade using plate was created using the conventional shell element of ABAQUS® and has been presented. ANN has been considered as a tool to predict the performance of the proposed wind turbine blade model. The results have given an essential prediction for the feasiblity of the smart wind turbine blade design. The main contribution of this chapter is that it has proposed guidelines for the methodology. Most previous work on SMAs has focused on a posteriori knowledge which can give a sense of application of SMAs in large deflection.

Chapter 4

Experimental Setup

4.1 Introduction

This chapter presents the experimental arrangement including the specimen fabrication and the smart wind turbine blade fabrication. Next, explains the SMA characterisation. Finally, describes the whole experiment for the deflection test, followed by a summary at the end of the chapter.

4.2 Specimen Fabrication

Unidirectional GFRP with ply configurations of 0°, 45°, -45° and 90° were measured using a protractor. The GFRP specimens were cut into the specified length and angle orientation as shown in Figure 4.1a, 4.1b and 4.1c which are illustrated respectively.

The steel base plate was completely cleaned before carrying out the specimen preparation. It was cleaned using acetone solvent to remove any dirt and contamination. Then steel plate was wiped with a dry cloth until fully dry. Once it was
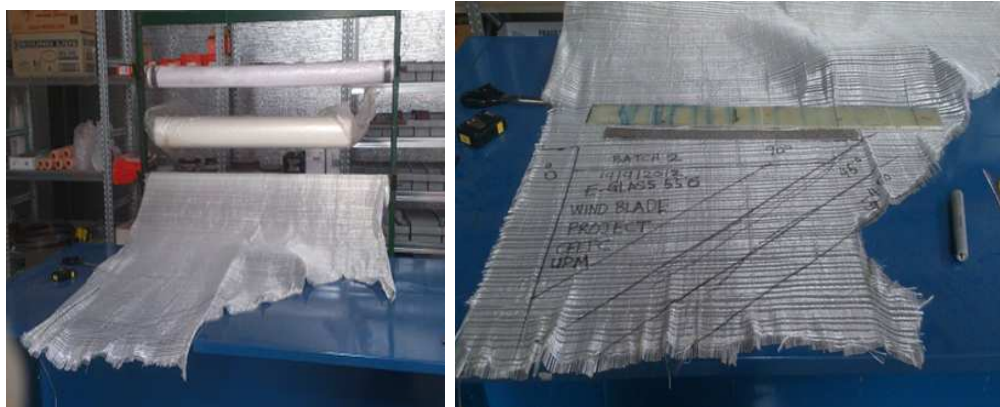
(a) Roll of fibre

(b) Angle orientation measurement

(c) Material specimen preparation

Figure 4.1: Photograph of specimen preparation

cleaned, the steel plate was waxed with carnauba wax eight times. The wax agent was used as a release agent, which provided a smooth surface coating like a release film, enabled to remove the two layers between the fabricated specimen and the steel plate. This technique has been widely used in the fabrication of GFRP.

Specimens of fibreglass were cut from the roll with respect to their orientation into A3 paper size. Then, the cut GFRP was weighed to estimate the quantity of epoxy and hardener that would be needed for fabrication. In this fabrication, a hand lay-up method was used to control the specimen size.

Bear in mind the following factors: the direction of the rollers must be in the direction of the ply orientation, a uniform distribution must be applied when rolling, and also any contamination must be avoided during preparation operations.

Ensure that personal protective equipment (PPE) is worn for health and safety reasons because the preparation and handling of the specimen involves hazardous chemicals and caustic solvents.

4.2.1 Preparation of the Epoxy Resin

GFRP with different orientations was weighed using a digital weighing scale. Let's say the total mass of the fibreglass in gram is m_{total}. The mass of the epoxy is m_{epoxy} and the mass of the hardener is $m_{hardener}$. These are determined by the weight fraction which is shown in Equation 4.1.

As stated in the instruction manual, use Kinetix Laminating/R240 High Performance 25 parts hardener to 100 parts resin weight (See Appendix F) (Composites 2011). The fraction mixtures of the epoxy and hardener are shown as follows:

$$m_{total} = \frac{4}{5} \times m_{epoxy} + \frac{1}{5} \times m_{hardener} \tag{4.1}$$

The hardener solvent was stirred with the spatula until thoroughly mixed. The composition of the capacity of the resin and hardener mixture mainly depends on the total number of plies. For example, if there are four plies then the mixture of resin and hardener will be in a quarter ratio respectively.

4.3 Investigation of SMA Wires Transition Using DSC

In order to ensure that the SMA wire is reliable and practical for use, the SMA solid-solid transition is studied using differential scanning calorimetry (DSC), which reveals the reversible and hysteretic nature of this transition. This can be

used to provide information on the composition of the Nitinol alloy. It also serves as a tool to detect the existence of, and changes in, the intermediate R-phase. This kind of preliminary approach gives a deeper and better understanding of SMA behaviour especially in the physical observations.

Based on the same specifications of the quantity of atoms in SMA, Tsoi et al. (2004) proved experimentally that for a 50.0–55.2 % Ni proportion in the NiTi shape memory alloy, the ultimate recovery force depends mainly on the initial pre-strain of the SMA. A small amount of pre-strain of the NiTi can induce a significant recovery force/stress.

A recoverable strain up to a maximum of about 8 % is achieved in this alloy. Another interesting feature is the estimation of a 200 % increase in Young's Modulus at the high temperature phase as compared to the low temperature phase. If the SMA encounters any external loads during the phase transformation, it can generate extremely large forces. This phenomenon provides a unique mechanism for actuation.

In this study, the main concern was on the A_s and A_f values for the martensite-austenite phase transformation during the actuation (heating) process. It should be noted that the two phases, austenite and martensite can coexist (overlap) at some intermediate temperatures. It is important to have a knowledge of these values of these transformation temperatures for the particular shape memory alloy in the application. For actuation purposes, the austenite finish temperature (A_f) is the most important.

Since the means of actuating the wire would be by electric current resistive heating, predetermined values of the transformation temperatures would predict the maximum required actuating/heating temperature of the SMA and the optimal electric current required to achieve the austenite finish transformation temperature (A_f).

In order to design a smart wind turbine blade, the transformation temperature of SMA as shown in Figure 4.2b has been experimentally investigated. The stable transformation temperatures determined by the DSC, which were provided in the Centre of Excellence Engineered in Fibre Composites (CEEFC) Laboratory at the University of Southern Queensland, Australia, are shown in Figure 4.2a. The specimen was encapsulated in an aluminium pan with the model DSC Q100 TA Instrument. The scan of heating and cooling rates were set at 10°C/min. The phase transformation temperatures were characterised by a tangent line intersection method (using A_s, A_f, M_s and M_f in Figure 4.3) in accordance with the Standard Test Method for the Transformation Temperature of Nickel-Titanium alloys by Thermal Analysis (F2004 2010).

(a) Photograph of DSC apparatus   (b) Roll of NiTi specimen

Figure 4.2: Photograph of DSC test equipment and the SMA specimen used

Figure 4.3 shows graphically the DSC curve for SMA wire. The power (W/g) required to maintain a constant heating or cooling rate for the SMA specimen is represented on the ordinate axis and the temperature of the chamber is shown on the abscissa axis.

The transformation curve of the NiTi alloy was tested from cooling to heating -60°C to 140°C respectively. Table 4.1 illustrates the four characteristic temperatures of the SMA.

When the specimen is heated in the twinned martensitic state, the transformation
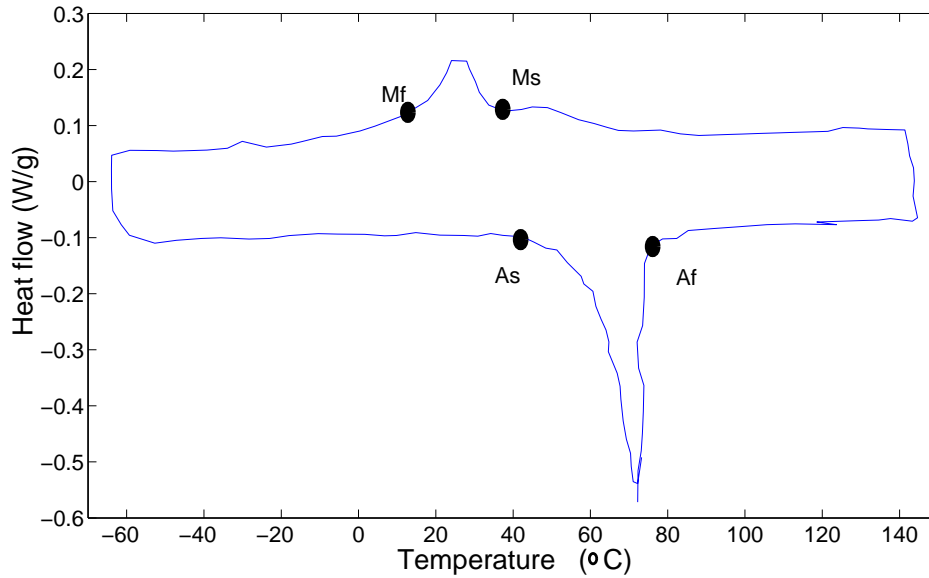
Figure 4.3: DSC curve for 0.50 mm diameter NiTi

Table 4.1: Transformation temperature of SMA

Specimen	SMA wire
diameter (mm)	0.51
A_s (°C (K))	47.07 (280)
A_f (°C (K))	90.04 (363.04)
M_s (°C (K))	75.19 (348.19)
M_f (°C (K))	16.42 (289.42)

to austenite initiates at A_s. The endothermic reaction during the reverse trans-
formation requires that the additional heat needs to be supplied to the specimen
to maintain the prescribed constant heating rate. This change in the power
supplied as the temperature increases is recorded as a transformation denoted as
a peak during the heating process. A similar peak is also recorded during the
cooling process, during which the exothermic transformation from austenite to
martensite process occurs. The transformation temperatures from the acquired
data are generally measured by drawing tangents to the start and end regions of
the transformation peak and the baseline of the heating and cooling curves. The

specific heat capacity can be computed by normalising the power by the heating rate and the weight of the specimen. The associated latent heat for the phase transformation can be calculated by integrating the specific heat over the range of the transformation temperatures. The DSC software packages include the ability to directly compute the latent heat due to the transformation.

4.4 Calibration of SMA Wires Attached to a Plate-Like Structure

A 300 mm length of the SMA wires is tested for calibration, which is shown in Figure 4.4. When the SMA wires are heated, they will contract by up to 10 % of their original length, but the total volume remains constant. A Technique Transducer, a load cell with a measuring limit up to 40 N, is used to determine the load during the test.
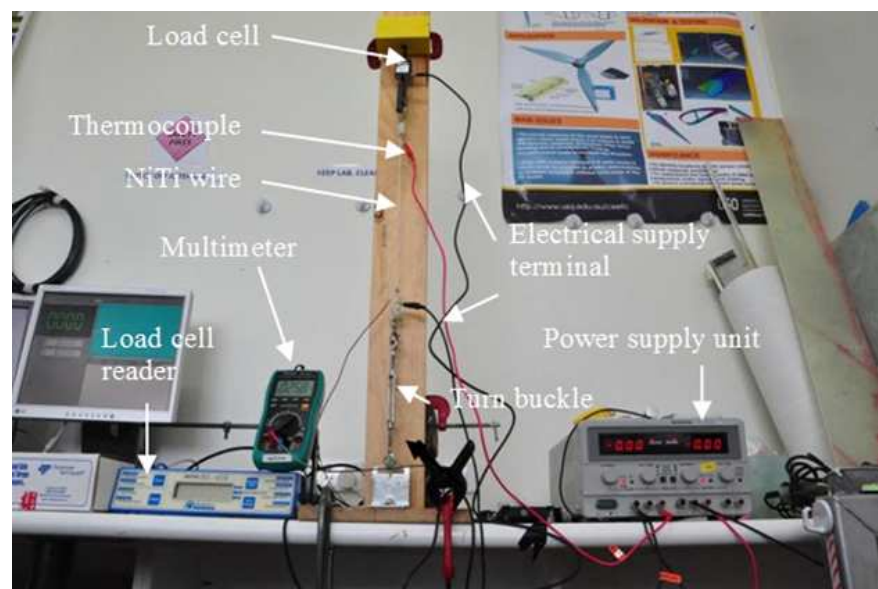
Figure 4.4: Photograph of the calibration setup for SMA

The wire is mounted vertically and stretched with a turn buckle at 4 % elongation. The top end of the wire is connected to the load cell while the bottom end has

been connected with a turn buckle.

A support block, which acts as a vertical pole, was used as a platform. The calibration was made with the aim of obtaining the readings for the tension force exerted with the amount of the electric current applied to the wire. The connection of the cable must be sturdy and the coupling connection is inelastic.

From these observations, the applied load can be estimated with respect to the electrical current. As the SMAs were electrically heated, there was a temperature rise.

4.5   Deflection Test for a GFRP Plate

In order to demonstrate the deflection test for a GFRP plate, a test rig was custom designed and constructed at the Workshop of the Faculty of Engineering and Surveying, at the University of Southern Queensland. The schematic diagram of the drawing layout, which is shown in Appendix C, was designed using the Pro/ENGINEER® Wildfire 5.0. The test rig was made of square hollow steel with a dimension of 50(W) x 50(H) x 0.5(D)mm which is shown in Figure 4.5. The test rig is capable of a maximum hold load up to 700 N. The test rig is placed on a flat and roughly level surface in order to ensure body stability. To ensure that the plate is held tightly, the clamping zone has been fitted with two nuts and a gripper.

4.6   Experimental Setup Arrangement

In this section, an adequate power supply of GW GPC-3030DQ was used to generate a constant current flow through the six wires for a large scale model which is about 1/10 scale to 2.5 m blade size. In order to supply a relatively high
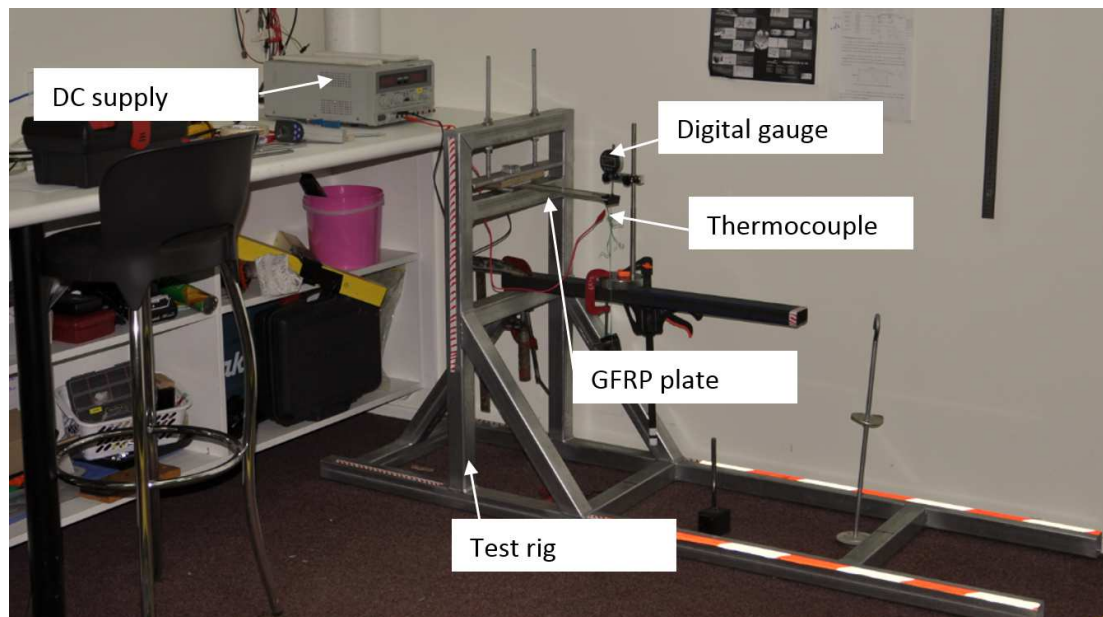
Figure 4.5: Experimental setup arrangement with the test rig

voltage (up to 21 V), the driven switches on the slave and master panels were turned into series mode.

In the present work, SMA wires are deformed by straining them using a designated frame and then they are integrated with GFRP cantilevers that serve as bias springs. In the cold state, the GFRP plate cantilevers assume their flat shape, except for a slight residual bending that results from the static equilibrium with the wires in the martensitic phase. The detail of the experimental setup is shown in Figure 4.6.

Upon heating, the wires contract and bend the cantilevers out of the plane. In order to translate the axial forces generated upon heating into a bending moment and thus to allow out-of-plane displacement, the wires are placed eccentrically onto the GFRP plate. This was accomplished by anchoring one end of the wires to the fixed clamp of the GFRP cantilever (fixed anchor) and the other end of the wires to the flexible side of the cantilever (moving anchor).

The SMA wires on the GFRP plate assembly were mounted at the end plate and in parallel. The cable wire was connected to the tower installation height
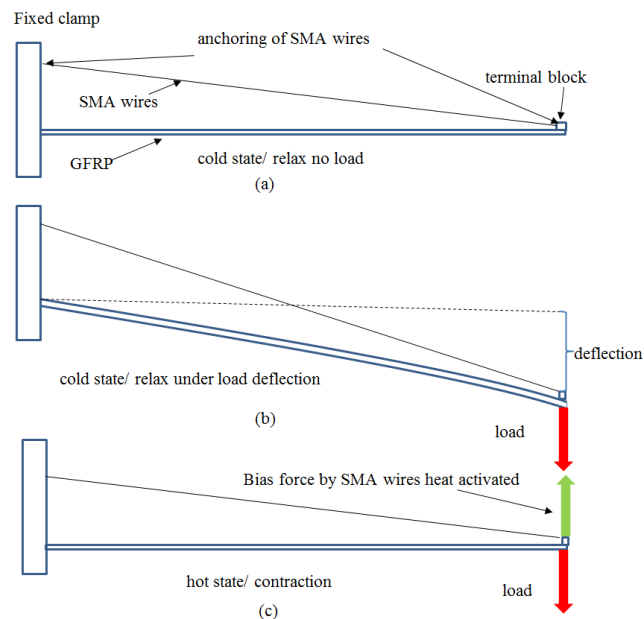
Figure 4.6: Schematic operating principle

adjustable anchors, which is displayed in Figure 4.7.
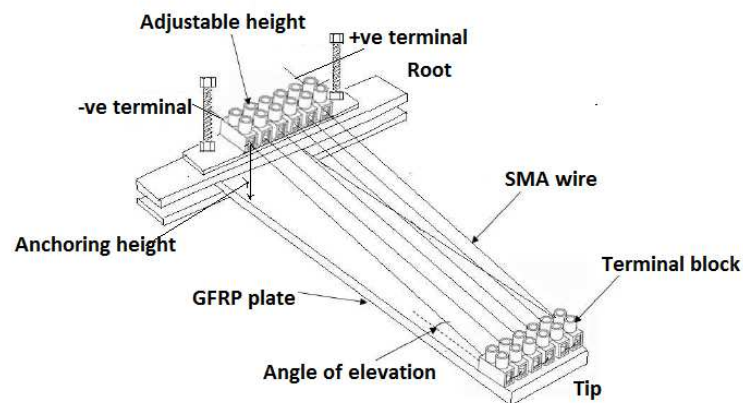
Figure 4.7: Schematic diagram of SMA wires arrangement

The arrangement for ordering the wire, such as 2, 4 and 6, was quite easy, whereby, the wire electrical terminals were installed at the end of where the wire was clamped. For an odd order of wire arrangement, for examples 1, 3 and 5 , the terminal wirings were made at both sides of the plate which were at the tip and the root side.

For safety considerations, all the wires have been insulated with the fibreglass

sleeve cloth material. Similar to the deflection test in 300 mm, the SMA wires have been mounted parallel to the GFRP plate. The same arrangement of the SMA wires has been implemented, but the blade is longer as well as the angle being bigger (Figure 4.8). The size of the angle is determined by an angle of elevation to the plate. As the anchoring height increases, the angle of elevation increases as well.
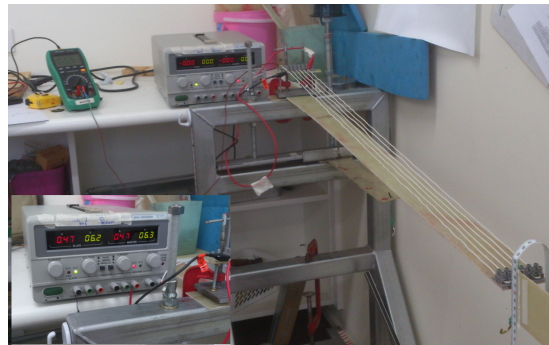
Figure 4.8: Photograph of experimental setup and values reading of the power supply in series mode driven when is current is activated (insert picture)
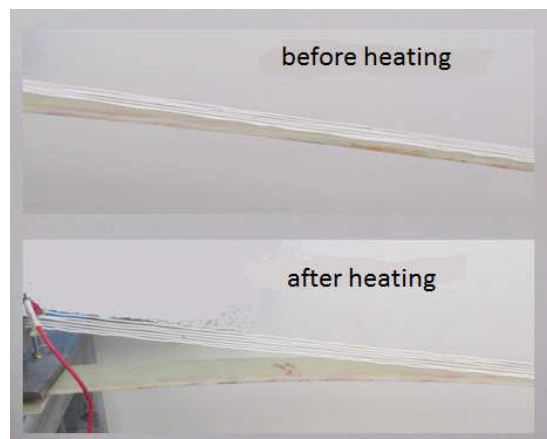
Figure 4.9: Photograph of the tip deflection (a) before heating (b) after heating (section view)

A series of tests have been undertaken to determine the response of the deflection under heating condition as shown in Figure 4.9. A constant current has been generated to contract the SMA wires.

The purpose of the experiment, which is shown in Figure 4.10, was to straighten
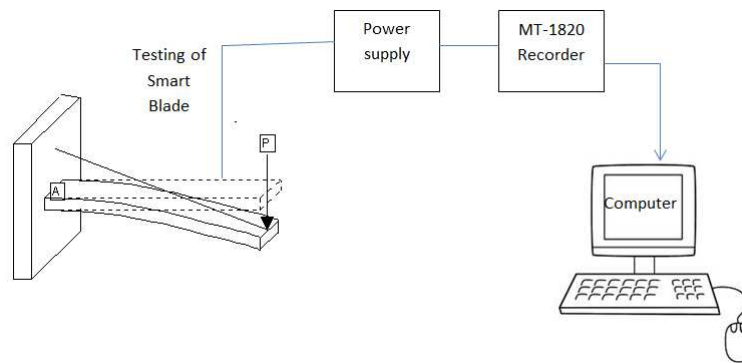
Figure 4.10: Schematic diagram of the experimental setup

the smart blade which was modelled by the plate. The straightening mechanism was actuated by the SMA wires. An MT-1820 recorder was used for the process of obtaining the temperature and time response and was recorded by the computer. The measurement of the tip deflection was precisely measured by a digital dial gauge. The SMA wires were powered by a current supplied in the range 0–25 V or 0–5 Amp: this was manually controlled by the dial knob which was provided on the constant power supply unit. The experiment was carried out at room temperature in the P2 Building, in the Structural Health Monitoring Laboratory, CEEFC, USQ Australia.

4.7   Summary of the Experimental Setup

In this chapter, the findings and associated discussion were presented in detail. A feasible study of the application of smart material has also been highlighted. The observations and data collected from the experimental work were used to estimate the capability of the SMA wires to recover the large deflection of the composite plate. These include the amount of the electrical current with the applied load. The SMA wires arrangement also has been conducted. It has been observed that the stress recovery of the smart blades also has been successfully performed.

A neural network model has been developed to perform the deflection with respect

to a number of wires required as the output parameter. The parameter includes load, current, time taken and deflection as input parameters. The network has been trained with experimental data obtained from experimental work.

In order to remove all the technological difficulties related to the complicated composite fabrication, a simple proof-of-concept specimen was built by mounting pre-strained SMA wires on top of the laminated composite plate strip.

Chapter 5

Results and Discussion

5.1   Introduction

This chapter presents the results and discussion according to the analyses that were proposed in Chapters 3 and 4. The content in this chapter is subdivided into five main sections, namely the characterisation of the GFRP and the thermo-mechanical behaviour. Next, describes the calibration test, the deflection test and the deflection of the graded beam. Then, discusses the tuning FEA for large deflection and the tuning-up the ANN. After that, analyses the preliminary study of the mechanism, deflection and load relationship. Finally, discusses the SMA wires arrangement, stress recovery and performance analysis, followed by a concluding remark at the end of the chapter.

5.2   Characterisation of the GFRP

The tensile test of the composite materials glass fibre-reinforced plastic (GFRP) was performed using the well-established techniques and is governed by the standard test method. The test speed used is 50 mm/min for measuring strength

and elongation and 1 mm/min for measuring modulus. The tensile test is performed in accordance with ASTM D3039 (D3039/3039M 2008). Figure 5.1 shows the tensile test setup with a contact extensometer used to measure elongation.

Figure 5.1: Tensile test setup with measurement of longitudinal and transverse strains by a contact extensometer

The purpose of the test is to validate the mechanical properties of the E-glass unidirectional (UD), namely to determine the value of the mechanical properties such as Elastic Modulus and Poisson's ratio. The results of the tensile test are plotted in figures which are shown in Appendix B. Table 5.1 shows the four parts of the coupon specimen which are described in the ply configurations.

Table 5.1: Four parts of graded beam assembly

Part	Material	No. of plies	Ply configuration
1	GFRP	4	[0°/90°/-45°/+45°]
2	GFRP	8	[0°/90°/-45°/+45°/-45°/+45°/90°/0°]
3	GFRP	12	[0°/90°/-45°/+45°/-45°/+45°/90°/0°/90°/0°/+45°/-45°]
4	EPS	N/A	N/A

5.3 Thermo-Mechanical Behaviour of an SMA Wire

To measure the effect of temperature on the critical stress that induces the martensitic transformation, tensile tests were performed on as-received SMA wires heated from -50 °C to 200 °C (see Figure 5.2). The samples were loaded to 4 % strain and then unloaded at a strain rate of 0.002 s^{-1}. At temperatures below the martensite to the austenite transformation, the material does not exhibit pseudoelastic behaviour. This is due to deformation caused by the martensite reorientation. The SMA wires show increasing stress with increasing test temperature. At temperatures greater than 125 °C, the austenite phase remains stable upon loading and stress-induced martensite transformation is not observed.
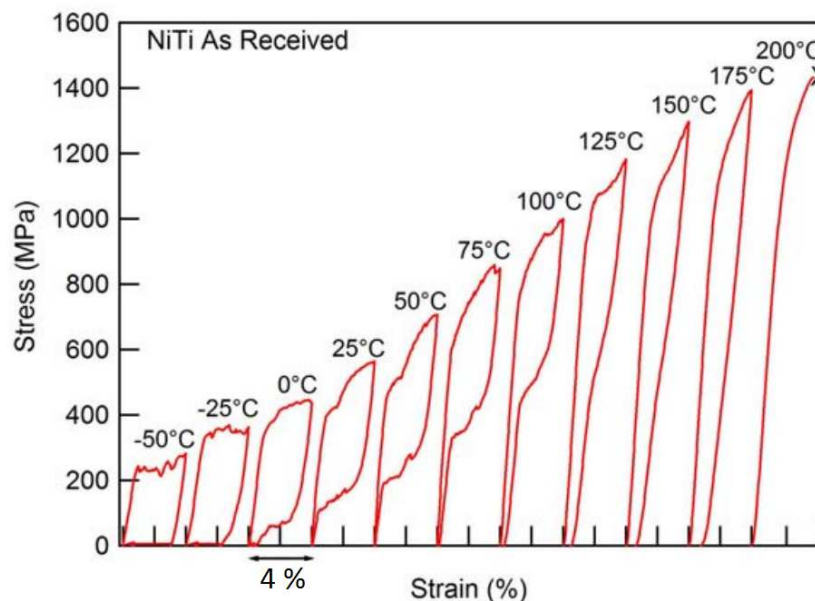
Figure 5.2: Stress-strain response as a function of temperature for the SMA wire. All tests were performed on as-received.

5.4   Calibration of an SMA Wire

The calibration curve in Figure 5.3 shows a proportional, a linear relationship between the load and the dead weight. The load cell is loaded in tension using the vertical platform frame. A load which is hanging on the SMA wire will be recorded as the load cell attached to the SMA wire. The electrical output signal of the load cell is compared to the known force of the load that was applied. This procedure will be repeated for the lowest four consecutive readings as depicted in Figure 5.3. At one minute intervals, the current was applied from 0.1 Amp incrementally until 1 Amp and the load cell reading measurement was recorded.
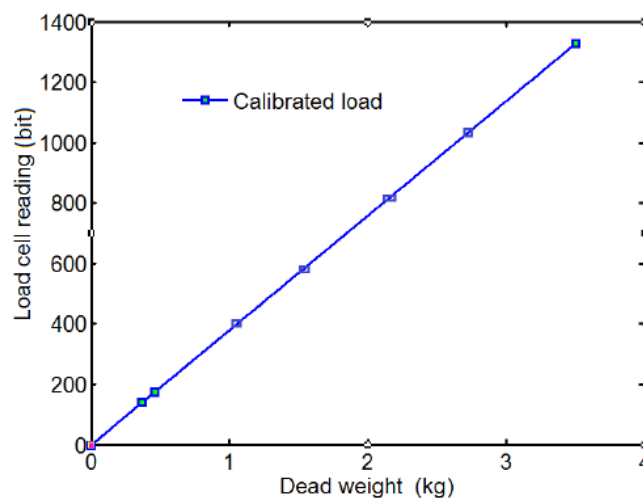
Figure 5.3: Calibration test curve

Figure 5.4a shows a relationship between current and temperature in the calibration test. The heating of the SMA wires is constantly monitored so as not to exceed the austenite temperature limit. To monitor the effect of the heat loss to the surroundings, a comparison study using an insulating sleeve has been carried out. Figure 5.4b shows the comparison of the test, with the heating sleeve and without the heating sleeve. The heat sleeve, which was covered by fibreglass cloth, has retained more heat as there was less heat loss to the surroundings. Consequently, the temperature rises faster. The heat dissipation is enhanced, and energy is conserved. Considering that there is not much difference in the
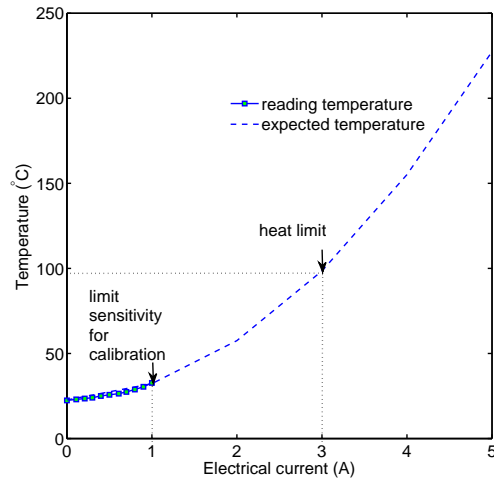
(a) Calibration test curve
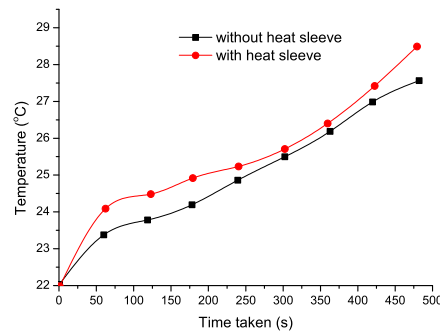
(b) Heat sleeve and non-heat sleeve curve

Figure 5.4: Calibration test and heat sleeve/non-heat sleeve test

heat loss (<5 %), the non-heat sleeve was used for this experiment. From the observational study, this figure also denotes the relationship between the current which generated the heat and the time , and shows that the temperature rise is directionally proportional to the time taken.

The load test setup shown in Figure 5.5a is intended to determine the relaxation/contraction capability of a 0.5 mm SMA wire. The SMA wire is clamped at one end and connected to a weight via a non-elastic cable at the other end, through a linear pulley. The weight is hung freely so as to provide a load to the wire.
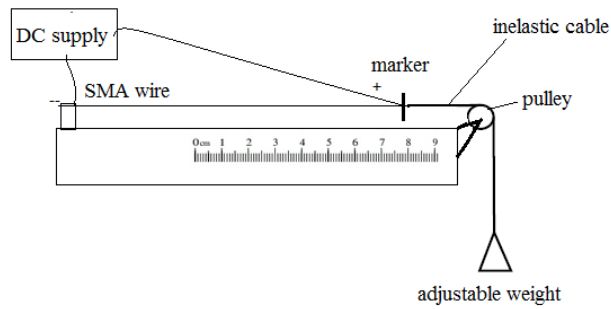
(a) Schematic diagram of the load test
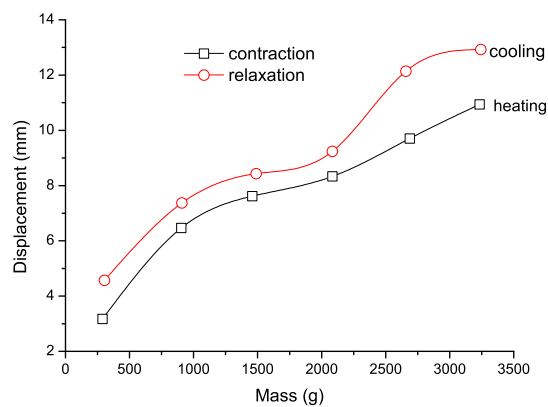
(b) Load test

Figure 5.5: Load test of 0.5 mm SMA between relaxation and contraction

Figure 5.5b shows the results of the experimental observations of the static loads. It has been found that there are two curves respectively representing relaxation and contraction. It has been observed that during the relaxation, the SMA is in a state of calm and that larger displacement occurs when the force is applied. However, during contraction when the wire was electrically heated, there was little displacement due to the wire being in tension. The difference between the contraction and relaxation can be described as the amount of force needed for recovery to its original condition.

5.5   Deflection Test

In this analysis, two specimens of the plate have been tested for comparison. The first specimen, (A), whose dimensions were 300(W)× 60(H) × 4(D)mm and the second specimen, (B), whose dimensions were 1000(W) × 60(H) × 4(D)mm. Figure 5.6 shows that the tip deflection for a long plate as expected is higher than for the short plate as the bending moment in a long plate is higher than in a short plate one.
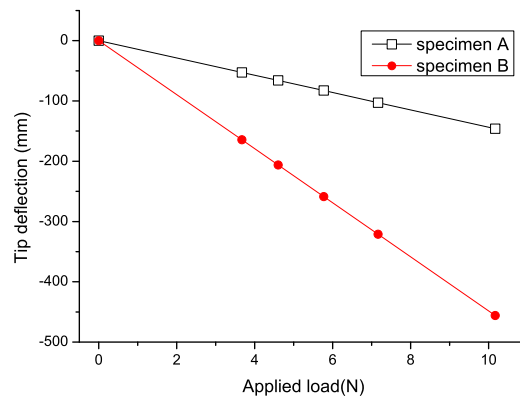
Figure 5.6: Load-deflection curves for Flexinol 90

The deflection depends on the ratio of length to the thickness plate. However, using the same thickness as tested in the experiment with the longer plate, it was expected that the tendency to deflect is greater. By comparison, as the geometrical length of the plate increased, the deflection increased. The aspect ratio (length/thickness) significantly plays an important role in the stiffness of the plate.

5.6   Deflection of the Graded Beam

The full assembly of the graded beam was drawn precisely in two parts, which were made of GFRP and expanded polystyrene (EPS), as depicted in Figure 5.7, 5.8 and 5.9.
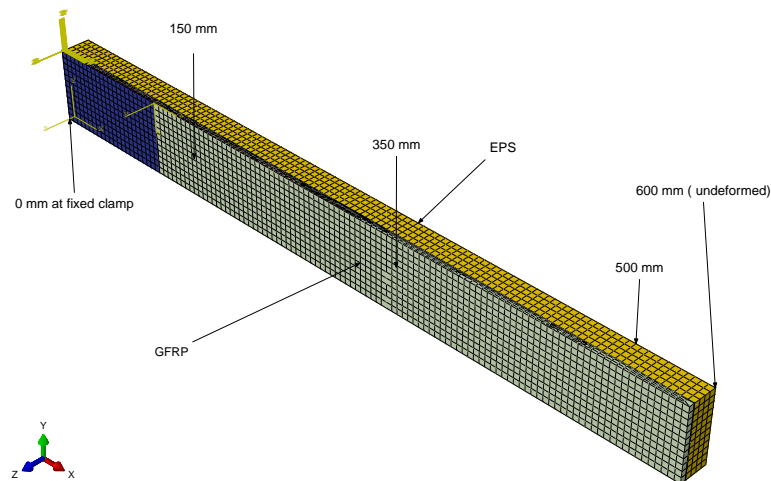
Figure 5.7: Graphical model representation with part of the assembly layout
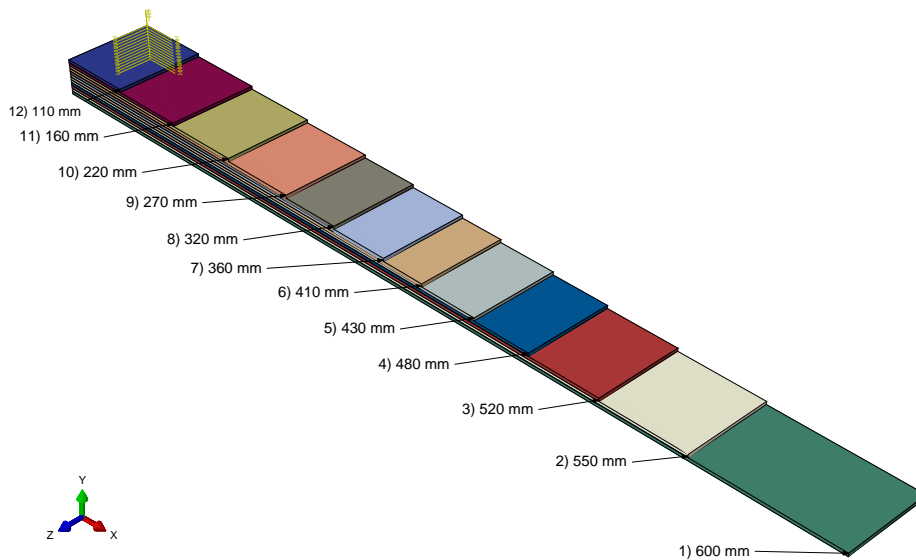
Figure 5.8: Graded beam specimen representing plies drop off imitation

Figure 5.9 depicts the graphical model representation with part of the assembly layout. There are 12 sections which represent like a ply drop off in the turbine blade.
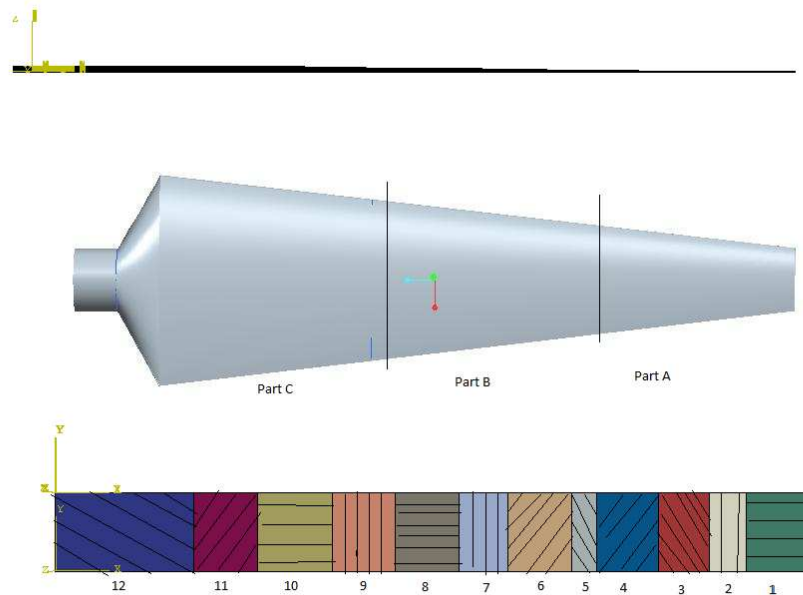
Figure 5.9: Graphical model representation with number of plies configuration (top view)

Figure 5.10 illustrates the deflection pattern when the foam has been mounted to the beam. The deflection happened because the core of EPS has reduced the load bearing between the graded beam as there is less deflection when the load is applied.
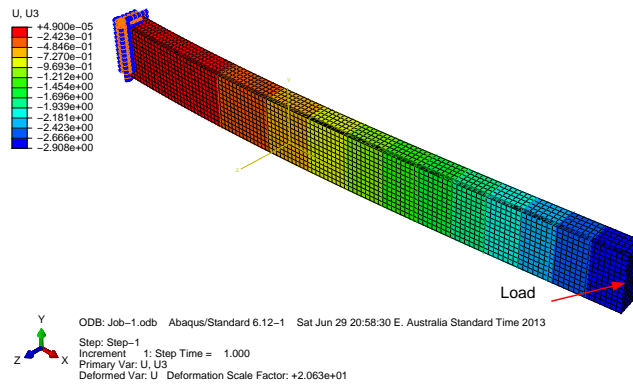
Figure 5.10: Deflection pattern profile for the whole graded beam
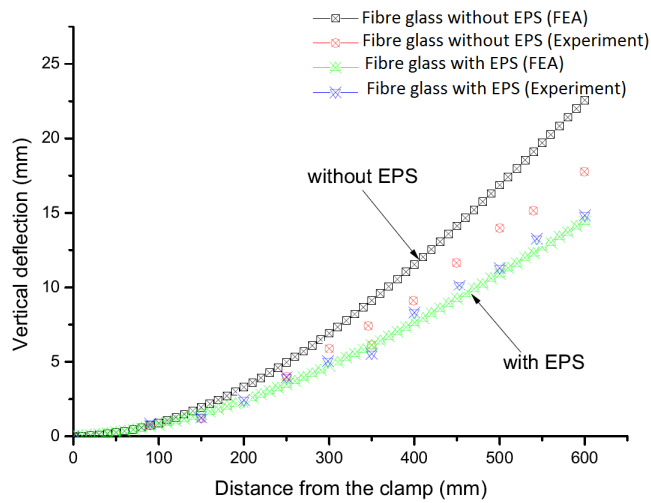
Figure 5.11: Comparison of vertical deflection of GFRP
(with EPS/without EPS) between FEA and experiment

Figure 5.11 shows the deflection is reduced remarkably with the EPS included in the sample. For comparison, this simulation was carried out using ABAQUS®, both models were tested without SMA.

5.7 Tuning FEA for Large Deflection of the Model

A preliminary study was carried out without the SMAs incorporated, to simulate
large deflections of the plate-like structure whose dimension was $300(W) \times 60(H) \times 4(D)$mm. This study was undertaken in order to visualise both models which were
SC8R and S4R for deflection contours without SMA subjected to a concentrated
load. Specifically, a sample loaded with 3.6 N was used to validate the model
before the SMA wires were incorporated into the GFRP. The tip deflection curves
were very similar along with the load applied to the specimen. This model is only
accurate for the first portion of the load-deflection curve as it is not designed
to predict the load-deflection at failure. Both figures, Figures 5.12 and 5.13,
confirm that the theoretical model is accurate. In both model specimens, the
curve predicted by FEA was able to match this value in experimental condition
very accurately. This value has been shown in Table 5.2. S4R recorded values
close to the experimental values. So, it has been used for future element type
modelling.
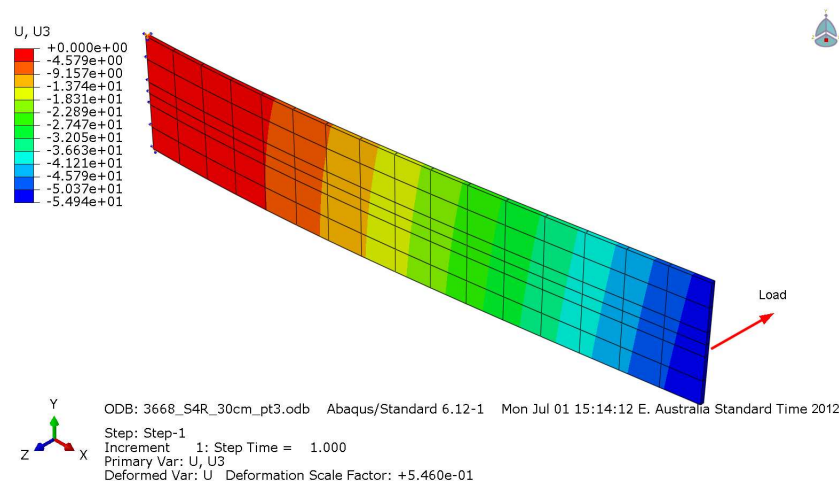
Figure 5.12: Deflection contour S4R of the GFRP plate

Either conventional shell elements or continuum shell elements might be used for
the GFRP plates. However, using continuum shell elements would consume a
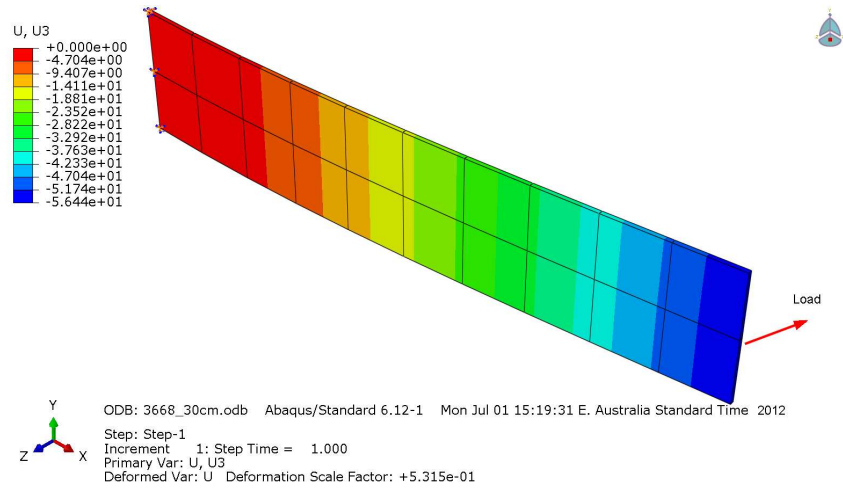
Figure 5.13: Deflection contour of SC8R of the GFRP plate

Table 5.2: Comparison of FEA and experimental work without SMA for validation

Method	FEA		Experiment
Element type	S4R conventional shell reduced integration	SC8R continuum shell reduced integration	
Tip deflection (mm)	54.78	56.44	55.40

great deal of computation time. It would also cause many convergence problems due to the complicated geometric arrangement using 8 nodes and very thin webs in the test specimen. Using conventional shell elements would be a more desirable option. Table 5.2 compares the simulation results for using both solid and shell elements. The results are almost the same, giving a high confidence level in using conventional shell elements.

5.8 Tuning-Up ANN

The data obtained from the experiment based on the plate-like structure of dimension 300(W) × 60(H) × 40(D)mm was used to train and construct the network structure as shown in Appendix G.

The network structure of the proposed ANN was divided into three randomly selected batches. The batches are as follows: the training batch, the testing batch and the validation batch. The regression analysis capacity of the network could be checked after the training phase. The mean square error (MSE), determination coefficient R, and root mean square errors (RMSE) were measured by the suggested neural network.

The number of SMA wires applied has been considered as an output vector. The applied current, the deflection and the load are considered as the input vectors. All the calculations of the neural network were made in MATLAB (Levenberg-Marquardt) and MBP open source code.

5.9   Prediction of ANN

In order to ensure the samples tested at low rates with minimum error, ANN, which is considered as a black box, was applied to predict the error. This is used for verifying confidence that the experiments have a high level of reliability, and subsequently for exploitation for model structure selection where the parameters are estimated by minimising the predicted error.

In this section, the analysis using ANN was carried out in three models, which are as follows:

(i)   Development of ANN 1;

(ii)   Development of ANN 2;

(iii)   Development of ANN 3.

All M-files for three models are generated and shown in Appendix L. Then, the sample of running ANN model simulation are illustrated in Appendix M.

5.10   Development of ANN 1

5.10.1   Predicting the Number of SMA Wires (NW) using Load (L), Current (I) and Deflection (d) as the Input Vector

A series of experiments were conducted to determine the number of SMA wires with the specified loads 3.668 N, 4.601 N, 5.768 N, 7.163 N and 10.167 N. A total of 4 variables in columns × 162 rows, which is a total of 648 data sets, have been recorded for which the schematic diagram is illustrated in Figure 5.14.
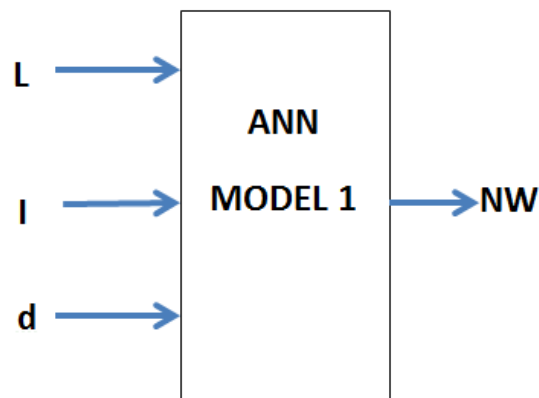
Figure 5.14: Schematic diagram representation for model ANN 1

Quantities of 1, 2, 3, 4, 5 and 6 wires have been tested for deflection in which the current has been applied. Out of these data sets 80 % have been used for training, with the other remaining 10 % for testing and 10 % for validation.

For a comparison study, a model simulated in MATLAB® and MBP has been carried out as in the examples illustrated in Figures 5.15 and 5.16 respectively. In both models, as a first trial, the same number of neurons has been applied, which was 10 layers. After several random tests were run, it was found that NARX1 recorded the lowest MSE value.
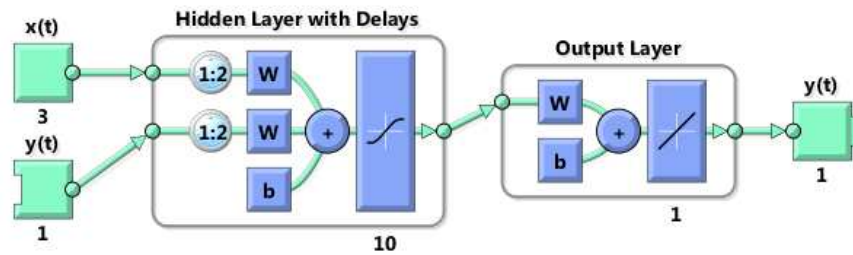
Figure 5.15: Example of NARX network with 10 hidden layers and 2 delay time by MATLAB
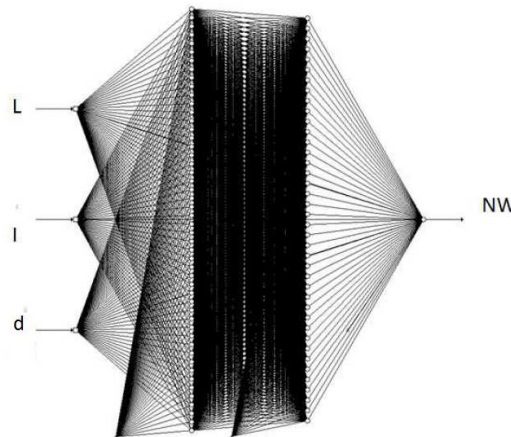
Figure 5.16: Example of MBP diagram network with 50-40 hidden layers

Figure 5.17 indicates the performance curve of one of the best overall networks for predicting the number of SMA wires. The training values have been recorded showing that at 25.97478 the MSE is 8.12988E-5. While during validation, the 25.97478 Epoch shows an MSE of 3.08830E-4, and for testing the 25.97478 Epoch, the MSE is 3.49000E-3.
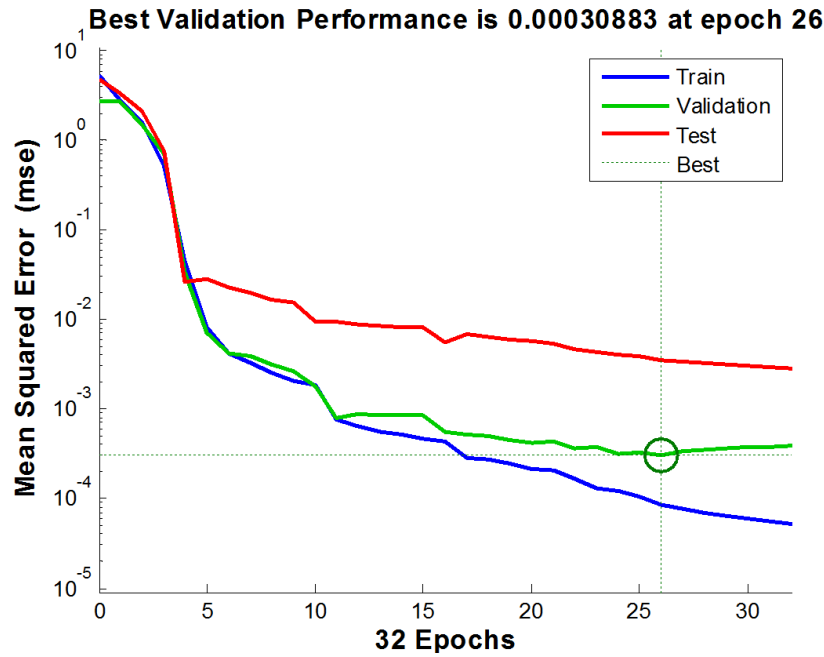
Figure 5.17: Best performance curve for ANN 1

Table 5.3 shows that the NARX1 model has the lowest MSE off all the models of ANNs and the fastest mode convergence training network.

Table 5.3: Prediction of the deflection with respect to the number of SMA wires using various models

Model	Input vector vector	Output vector	Structure/No hidden layer neuron	Epoch (No. of Iteration)	Mean Square Square
MBP1	L,I,d	NW	50-40	1,273,277	0.009999
MBP2	L,I,d	NW	50-40-30-20	437,788	0.009997
NARX1	L,I,d	NW	10 delay time 2	26	0.000308
NARX2	L,I,d	NW	10 delay time 3	10	0.001542
NARX3	L,I,d	NW	10 delay time 4	7	0.002337

As can be seen from Table 5.4, the smallest values of MSE and the high values of R give a reason to consider that the obtained NARX model is adequate as they are almost at unity. It has been observed that the process of the networks' performance improved during training. This performance is measured in terms of MSE and it is shown in log scale. It is evident that the MSE is decreasing rapidly along epochs while the network is trained. In this case, the results are reasonable, because of the following: the final mean-square error is very small; the test set error and the validations set error have similar characteristics.

Table 5.4: The results of the NARX model training for ANN 1

	Target value	MSE	R
Training	130	8.12988E-5	9.99145e-1
Validation	16	3.08830E-4	9.99289e-1
Testing	16	3.49000E-3	9.99597e-1
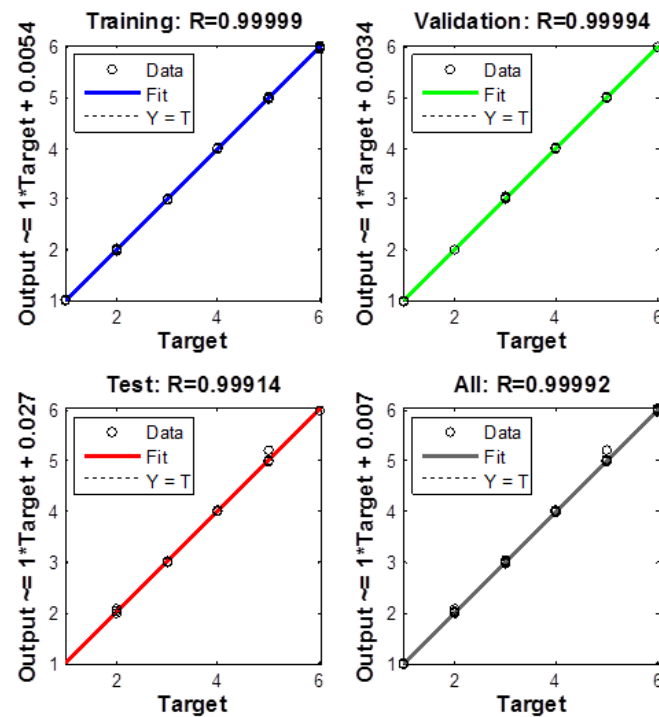
Figure 5.18: The networks performance for ANN 1

In Figure 5.18, the training, test and validation data indicate good curve fitness. The results show that R has overall values greater than 0.9. It can be seen in

Figure 5.18 that the error values between the training and the target are within the limits. Generally, for the evaluation of the robustness of the modelling technique, R of the test dataset should be computed and a value greater than 0.9 can be regarded as a good overall fit.

In a statistical study, a histogram is a graphical representation of the distribution of data. It is an estimate of the probability distribution of a continuous variable and was first introduced by Pearson (1895). In this context of the analysis of errors, a histogram is a representation of tabulated error frequencies, shown as adjacent rectangles, erected over discrete intervals denoted as bins, with an area equal to the errors frequency of the observations in the interval. The height of a rectangle, denoted as an instance is also equal to the errors frequency density of the interval, i.e., the error frequency divided by the width of the interval. The total area of the histogram is equal to the number of data. A histogram may also be normalised displaying relative error frequencies.

Figure 5.19 shows the error histogram of the NARX prediction model for ANN 1. It has been observed that a minimum error was recorded, seen in the middle, which was -0.02117 for 45 instances. This value reveals the errors frequency of the response. It has been seen that if there is a large amount of training, the zero error would tend to be greater.
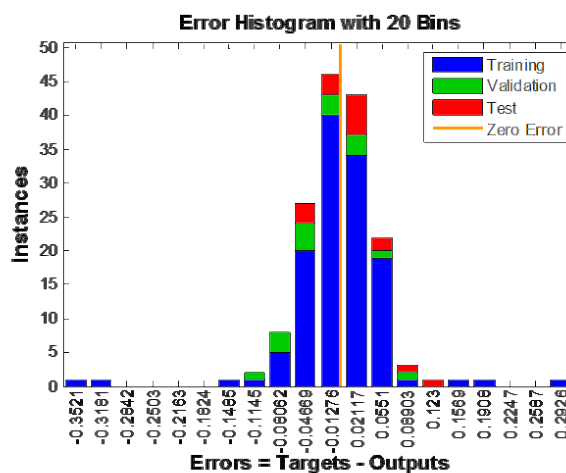
Figure 5.19: Error histogram of the NARX prediction model for ANN 1

Figures 5.20 and 5.21 show the time response, the deflection output, and the network output respectively. However, the MBP simulated some overshoots along 3 SMA wires and 4 SMA wires. The overshoots are due to some errors generated during the training and testing.
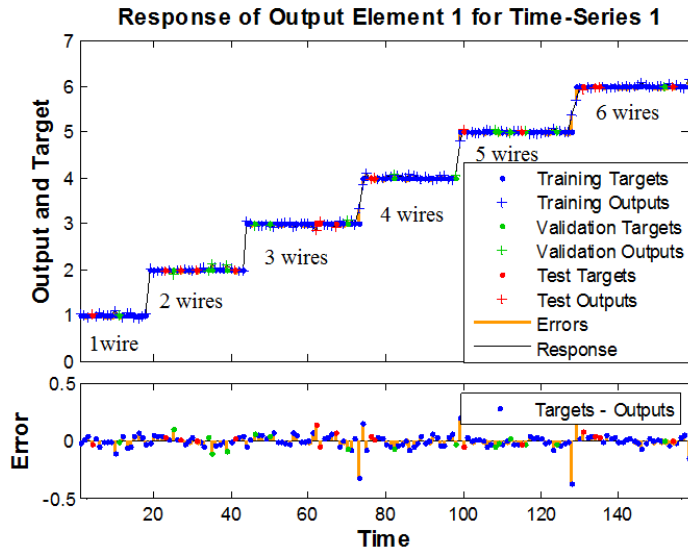
Figure 5.20: Response of NARX model for output deflection for ANN 1 by MATLAB®
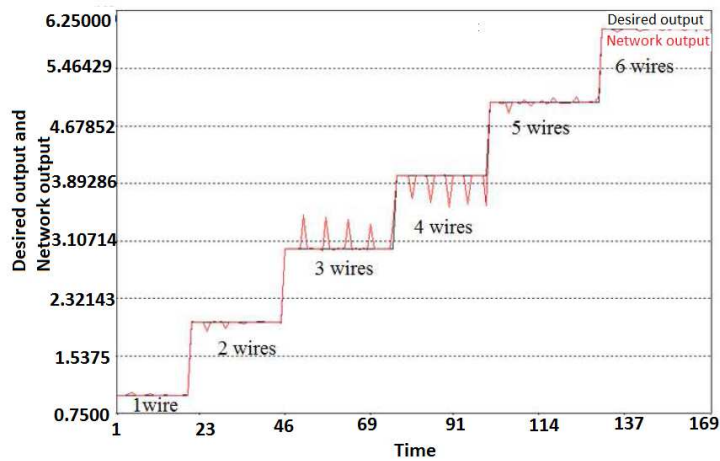
Figure 5.21: The deflection output and network output for ANN 1 by MBP

5.11 Development of ANN 2

5.11.1 Predicting Current (I) using Load (L), the Number of SMA Wires (NW) and Deflection (d) as the Input Vector

In this analysis, the previously output, which was the number of SMA wires, has been replaced by the applied current. The schematic model diagram is illustrated in Figure 5.22. The input vectors, which have been called `*input_NN2.txt`, were simulated into output vectors `*output_NN2.txt`.
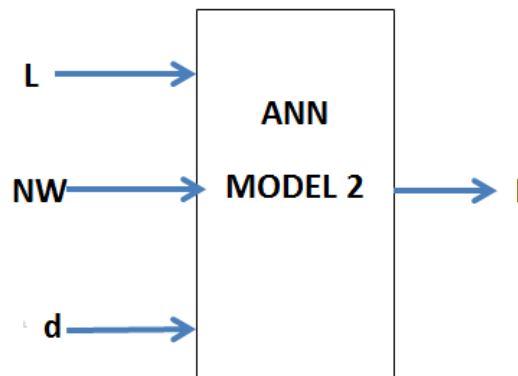
Figure 5.22: Schematic diagram for model ANN 2

Figure 5.23 shows the training, test and validation error decay which has reached a value as low as 10^{-2}. The tabulated data was recorded in Table 5.5. The results improved a little, which is close to 0.01 MSE. It has been observed that the changes in the number of the hidden layers and neurons had no significant effect in this case.
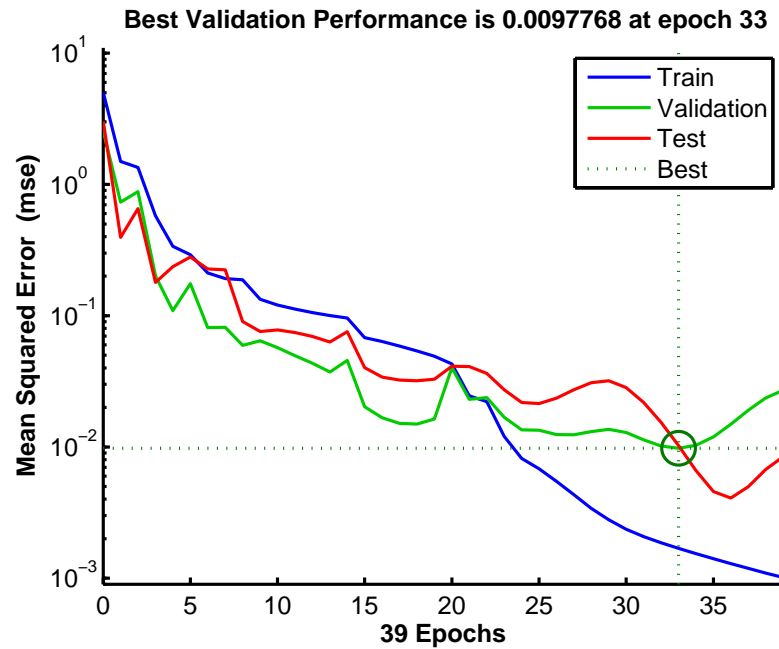
Figure 5.23: Best performance curve for ANN 2

Table 5.5: The results of the NARX model training for ANN 2

	Target value	MSE	R
Training	130	5.8431E-2	9.9999E-1
Validation	16	1.5415E-2	9.9994E-1
Testing	16	1.5415E-2	9.99914E-1

Figure 5.24 depicts the error distribution, which shows that it is slightly not fairly distributed. The zero error was 0.000246 at 58 instances. However, there is justification for this network to be used for prediction as the correlation analysis recorded 0.999984 for validation.
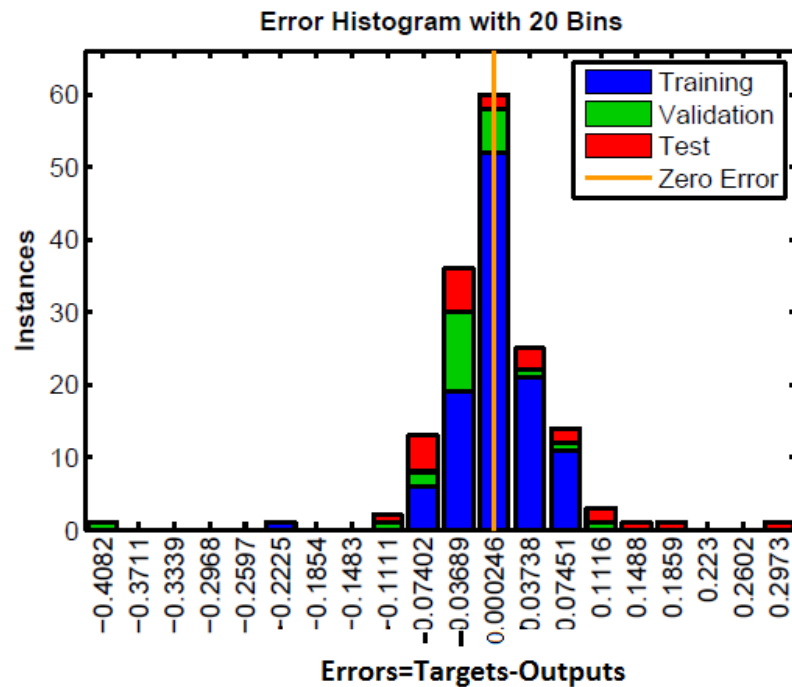
Figure 5.24: Error histogram of the NARX prediction model for ANN 2

The network performance has been modelled and the results are shown in Figure 5.25. Although it shows that the MSE values were not as good as for ANN 1, the desired output almost reached the target of the performance. Some important qualities of NARX networks with a gradient-descending learning gradient algorithm have been reported: e.g. learning was more effective in NARX networks than in other neural networks (the gradient descent was better in NARX) and these networks converged much faster and generalised better than other networks.

In these response of NARX prediction for ANN 2 model, for a random type of input, the results revealed that the generalisation of the prediction values has been sufficiently satisfactory, which is illustrated in Figure 5.26.
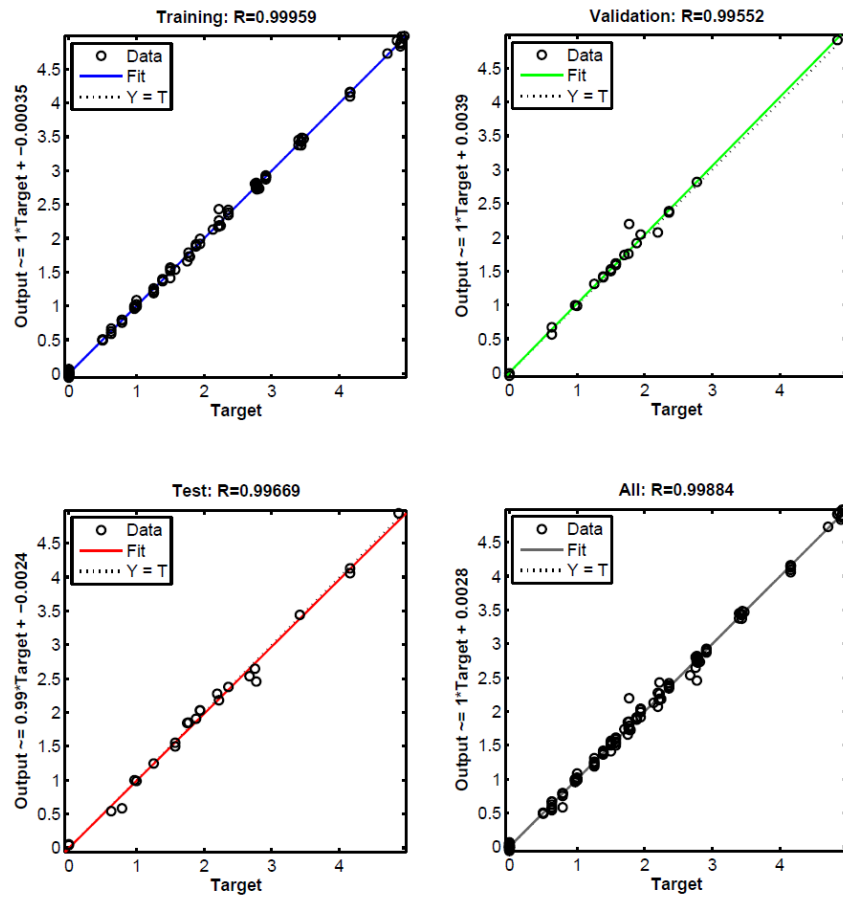
Figure 5.25: The networks performance for ANN 2
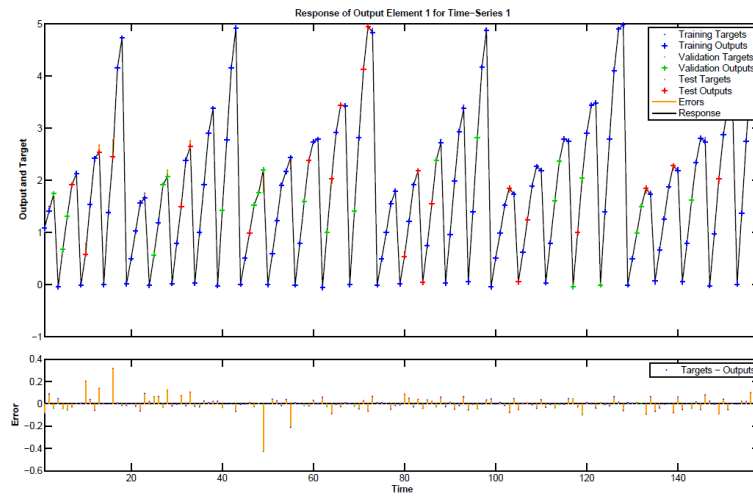
Figure 5.26: NARX prediction model for performance for ANN 2

5.12 Development of ANN 3

5.12.1 Predicting Deflection using Load (L), the Number of SMA Wires (NW) and Current (I) as the Input Vector

In this analysis, the previous output (ANN1), which was the number of SMA wires, has been replaced by the deflection. The schematic diagram is shown in Figure 5.27. The input vectors, which are called `*input_NN3.txt`, were simulated into output vectors `*output_NN3.txt`.
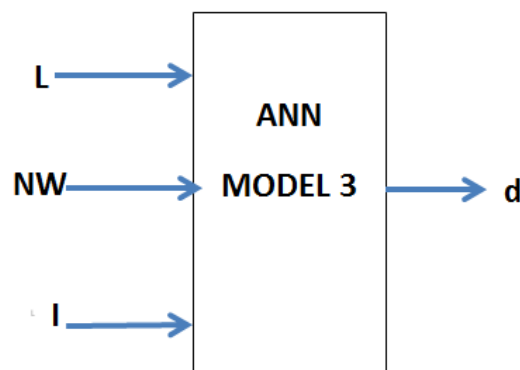
Figure 5.27: Schematic diagram for model ANN 3

Figure 5.28 shows the best performance curve for model ANN 3. The error has decayed at epoch 17.
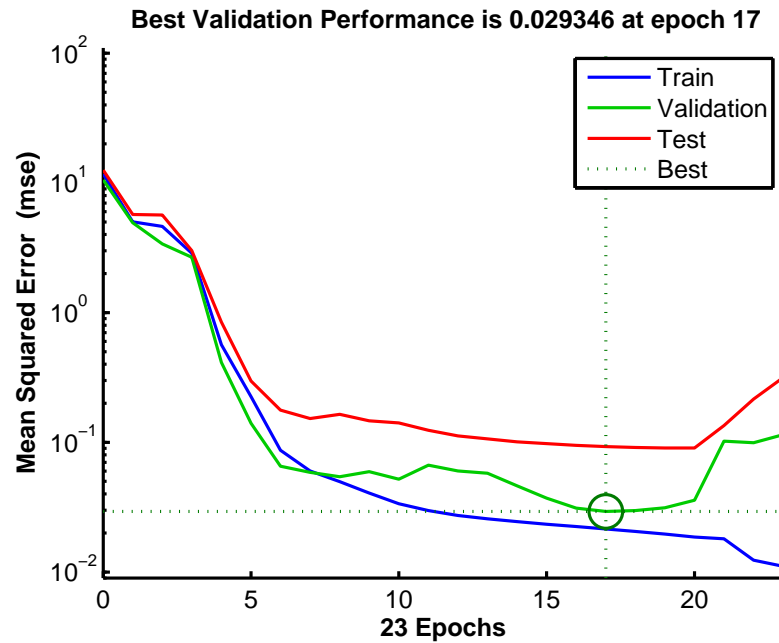
Figure 5.28: Best performance curve for ANN 3

From Table 5.6 the values of training, testing and validation were lower compared with the other ANNs tested. It can be concluded that it was difficult to predict the network. Only 0.02 MSE has been recorded for this network.

Table 5.6: The results of the NARX model training for ANN 3

	Target value	MSE	R
Training	130	2.14688E-2	9.85613E-1
Validation	16	2.93455E-2	9.91057E-1
Testing	16	9.27072E-2	9.19889E-1

Figure 5.29 also reveals that the distribution of data is not uniform, unlike in the other networks.
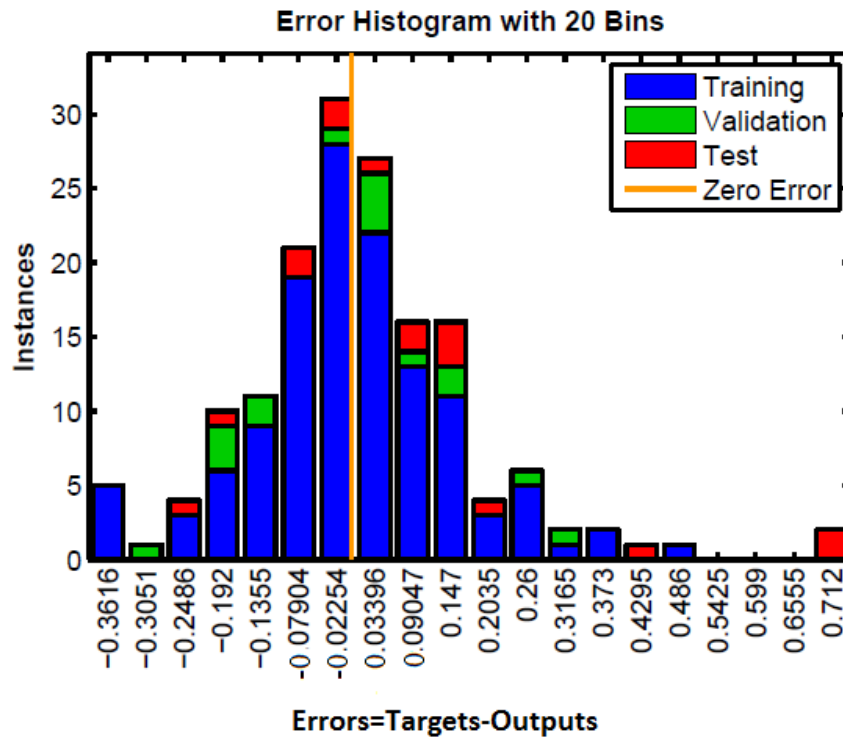
Figure 5.29: Error histogram of the NARX prediction model for ANN 3

Figure 5.30 shows that the majority of the data did not lie along a straight in best curve fitness. It deviates from a unity value. Most of the data points either from training, testing or validation were found to be scattered from the equation R=1. This clearly shows that the prediction performed by this model was not as convincing as expected.
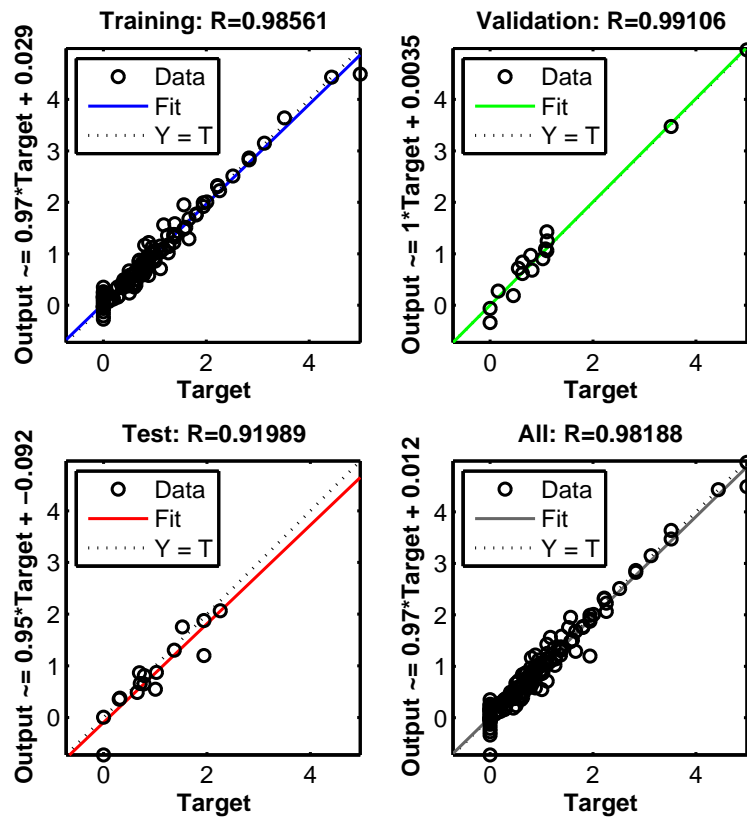
Figure 5.30: The regression analysis for ANN 3

Figure 5.31 shows that many errors discovered in this network. It has proven that the network had difficulty predicting the performance of deflection as the output vector.
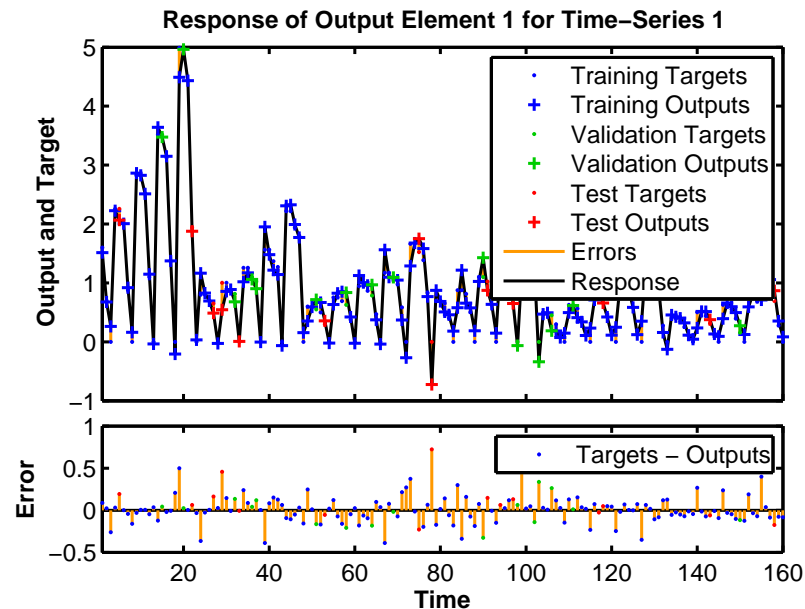
Figure 5.31: Response of the NARX prediction model for performance for ANN 3

5.13 Implementing Robustness Testing

Robustness testing is a part of the validation process, which consists of testing the behaviour of a system implementation under exceptional execution conditions in order to check whether it really meets some robustness requirements. It was shown that the ANN can be used as a tool to predict the deflection of the plate and can also optimise the the performance as mentioned in Chapter 3. This chapter explains the theoretical framework for model based robustness testing together with the implementation within the validation environment, for example, on a large scale. Robustness test cases are generated from an operational specification. This generation technique is derived from the ones used in conformance testing in order to be used in the actual condition.

5.14 Specification of Specimen

The actual beam plate, with a configuration of 8 plies, was fabricated in the facilities room at CEEFC, USQ Toowoomba, Australia. In this fabrication a large scale GFRP panel was used to fabricate the smaller plates. The plate has dimensions of $1000(W) \times 60(H) \times 4(D)$mm. The plies configuration of the plate is shown in Table 5.7.

Table 5.7: Plies configuration of the plate

Configuration	Ply Orientation (°)
1	0
2	90
3	-45
4	45
5	45
6	-45
7	90
8	0

The fabrication of this specimen has the same mechanical properties used in Chapter 3. The ply configuration and the orientation is shown in Figure 5.32 below.
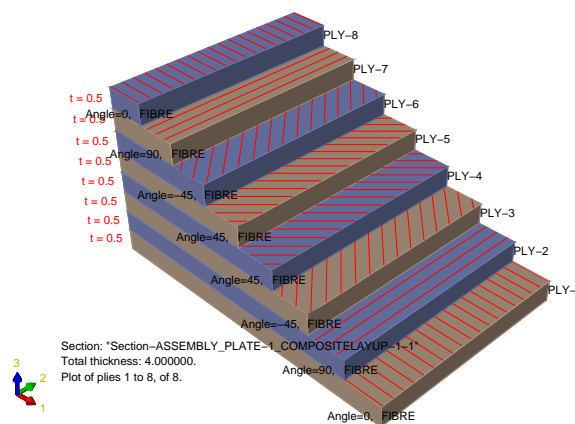
Figure 5.32: Schematic ply configuration of the actual blade

5.15   Preliminary Study: Use of the SMA Mechanism

In this study, two case studies were conducted in order to realise the mechanism of the use of an SMA composite plate model.

The design of two case studies is discussed as follows:

  (i) Embedded SMA;

 (ii) Suspended SMA.

5.15.1   Embedded SMA Wires

A blade with embedded SMA wire is a type of internal reinforcement of the GFRP blade in which the load that has been faced by the GFRP plate/skin, which is the load-bearing portion, is transferred to be embedded with the SMA wires.

In this experiment, two specimens have been fabricated to simulate the deflection using three wires and six wires.
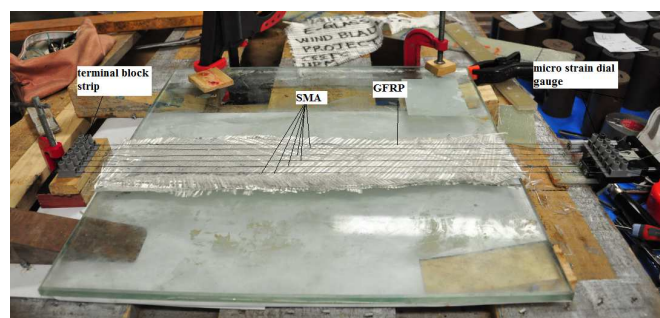
Figure 5.33: Embedded SMA fabrication

Figure 5.33 shows that six SMA wires have been embedded beneath the final layer and is easily fabricated. Among other reasons, the wire is to be arranged away

from the neutral axis so that the wire is in a small amount of tension due to the compression of the epoxy matrix.

For the purpose of pre-strain, a micrometer strain gauge was used to measure the strain.

To ensure that the process of relaxation and contraction runs smoothly and uniformly, all SMA wires should be aligned in parallel. For this reason, the fabrication must be be performed carefully to yield the best possible sample.

During the fabrication, the ends of the wires were tied while the other side was pegged at a micrometer strain gauge. This will adjust the micrometer strain gauge reading value stretching to 4 %.

A horizontal level surface check has been undertaken to ensure that the levels are the same so that no angle is made. This procedure was checked using the spirit level.

Joule heating of the SMA wire was accomplished by connecting the two ends of the SMA wire to a power supply of 12 V direct current (DC). The data, such as the temperature and the time response, were recorded via a personal computer using the available MT-1820 Pro's Kit softwares (MT-1820 2011). The deflection of the plate was measured by the digital gauge micrometer with an accuracy of +/- 0.01 mm.

In the design of the embedded SMA , there were four aspects considered, which are listed as follows:

(i) Orientation location:

In a wind blade section subjected to a flapwise bending moment, the highest stress and strain distribution will occur a the the skin. However, due to changing cross sections along the blade axis cause a significantly complex stress/strain field on the skin.

(ii) Alignment position:

The wires must be aligned equidistance from each other;

(iii) Pre-strain condition:

The wire must be clamped at both sides at 4 % pre-strain in order to ensure that the contraction and relaxation are uniforms;

(iv) Bonding interaction:

The SMA wires are perfectly embedded and assumed to be tightly bonded. This can also contribute to the effectiveness of the contraction as a defect factor concern.
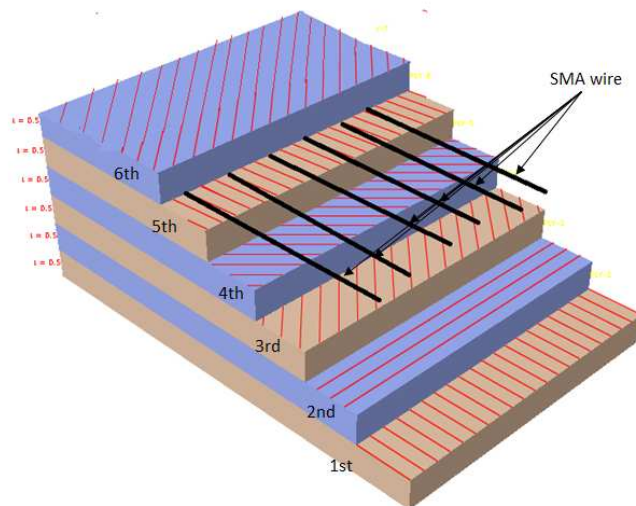
Figure 5.34: Schematic diagram of embeded SMA wires

Figure 5.35 shows a photograph of the experimental setup, in which embedded SMAs and suspended SMAs were tested under static conditions. The physical dimensions (length and width) of both plates were kept the same in order to perform the deflection test for comparative study.
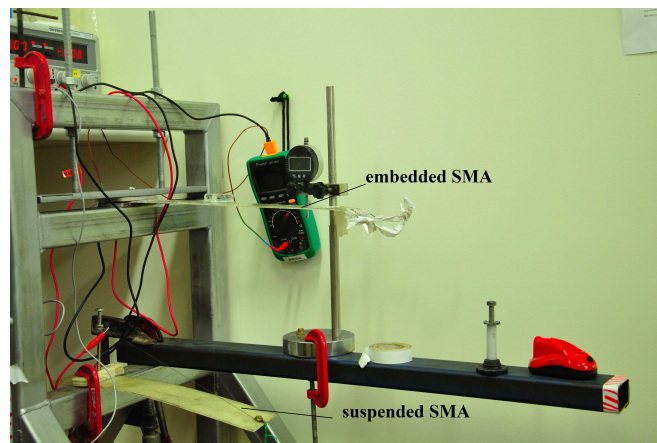
Figure 5.35: Photograph preliminary study setup for embedded SMA and suspended SMA

Figure 5.36 denotes the temperature curves versus period graph for a number of loading cycles, showing at different maximum temperatures. Contrary to what has been observed in the embedded laminate plate experiment, the actuation is rather repeatable and the hysteresis between the heating and cooling branches is nearly absent. These are related partly to the type of SMA alloy wires used in these experiments, and partly to the different specimen manufacturing process and experimental setup. Indeed, trained wires tend to have a more stable behaviour than untrained ones, with a smaller hysteresis related to the presence of the austenite phase. Moreover, the heating of the SMA wires occurring during hand lay-up manufacturing is expected to partially remove the effect of the loading history on the shape memory alloy SMA wires, which constitutes the main cause of the different responses observed in the beam. Finally, in the different experimental setup (Joule heating) it was more difficult to achieve controlled SMA cooling. Thus the thermocouple response time may have influenced data acquisition, especially in the cooling process.
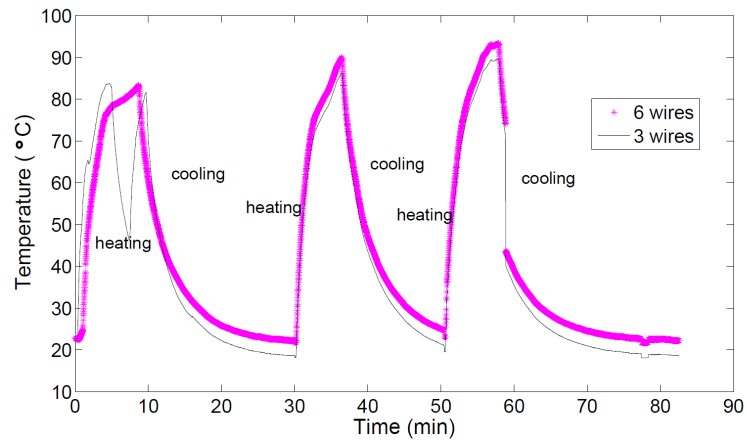
(a) Suspended SMA wires
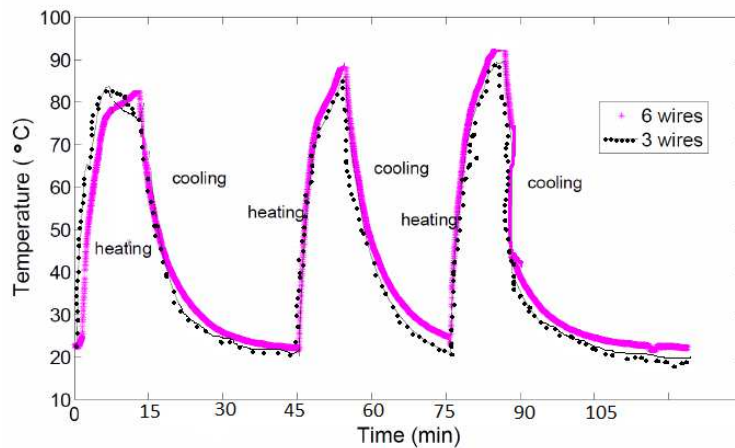
(b) Embedded SMA wires

Figure 5.36: Heating and cooling curves of the SMA mechanism design

As seen in Figures 5.36a and 5.36b for suspended SMA wires, the time response to completely heat was faster compared to the embedded SMA wires. It took around 10 minutes to heat in the suspended SMA wires whilst in the embedded SMA wires it took about 15 minutes to completely heat at a constant current of 1.5 Amp.

The temperature control and acquisition were indeed a critical point in the experimental design. In this experiment, no thermocouples were embedded in the plate in order to prevent the creation of interlaminar defects. For this reason, only the temperature in the external part of the shape memory alloy wires could

be recorded, where the significant movements occurring during actuation made it difficult to achieve perfect contact interaction between the thermocouple and the wires. Besides providing useful information for the evaluation of the laminate plate response and the validation of the numerical model, good temperature measurements are a crucial feedback for the control system. One idea to improve temperature acquisition for control purposes is to use micrometric thermocouples or optical sensors, which could be directly embedded in the composite without causing significant delamination or interlaminar defects. Safety precautions have been taken into account particularly at both ends where the wires were crimped and coated with the insulating tape. This step is taken in order to ensure that no short circuit will occur.
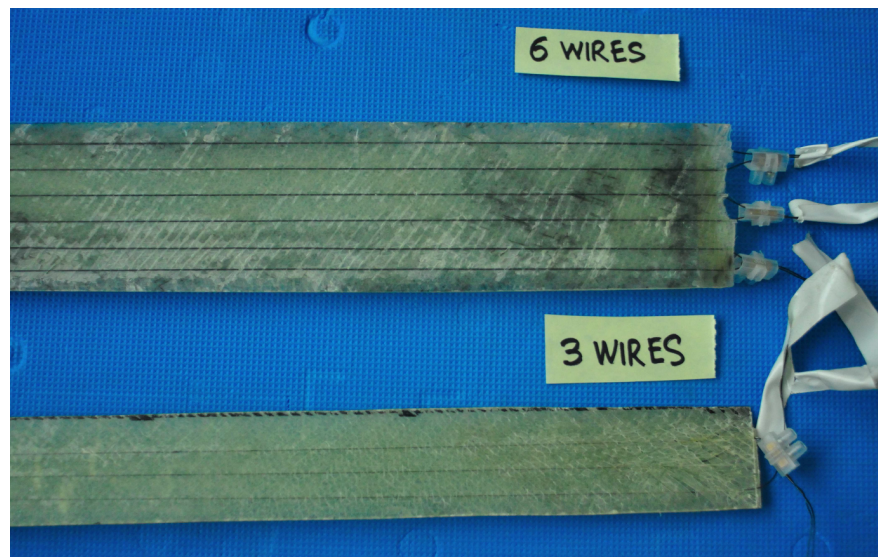
Figure 5.37: Photograph of the specimen embedded SMA wires fabrication

Figure 5.37 depicts the six SMA wires and the three SMA wires that have been fabricated for the deflection test. It has been observed that there was significantly less actuation power in the three embedded SMA wires compared to the six embedded SMA wires. This could have happened due to the heat dissipated through the GFRP. Another possible reason was that the SMA wires were overlapping and the wire movement was in a narrow environment because of the restrictions between the dual interfaces, which were the SMA wire and the GFRP.

In Figure 5.36a, it had been observed that it took a longer time to generate heat as well as requiring a lot of heat to contract the wires. A rattling sound, like cracks, might be heard when the contractions took place. This kind of phenomenon can cause the layers to separate, forming the structure of separate layers, with significant loss of mechanical stiffness (Wang 2007).

Figure 5.38 illustrates the delamination that happened after a few cyclic loadings. Therefore, the embedded SMA was considered not viable as it created defects.
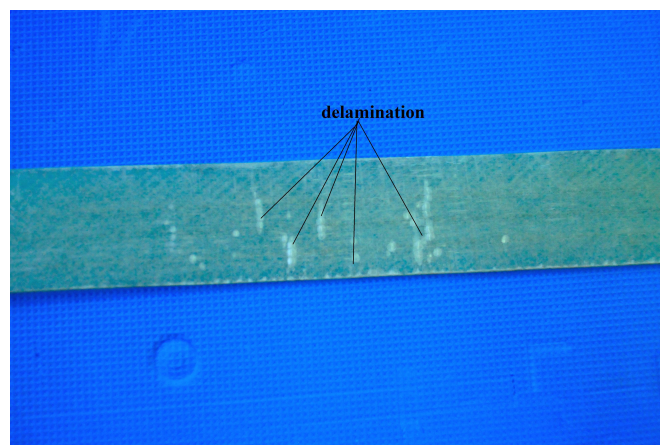
Figure 5.38: Photograph showing that delamination occurred along the embedded SMA wires

5.15.2 Suspended SMA Wires

The blade with the suspended SMA wire was categorised as a type of external reinforcememt of a GFRP blade in which the GFRP plate/skin (the load-bearing portion) hung below the suspended SMA wires as shown in Figure 5.39. The suspended SMA wires must be anchored at each end of the GFRP plate. One end was clamped to the tower.

The reaction of using suspended SMA emerged after the previous response was unsuccessful. The embedded model was not only ineffective and non-robust in performance, but also created damage (as mentioned in Section 5.15.1) in Figure 5.38. The action of the suspended wires to restore the original condition is shown in Figure 5.39. When the load was imposed, the deflected plate returned to its original condition as in a straight form. Even when a single wire was used, it was quick to respond (Daniel et al. 2010). The heat generated was also lower than the embedded one which is compared in Figure 5.40.
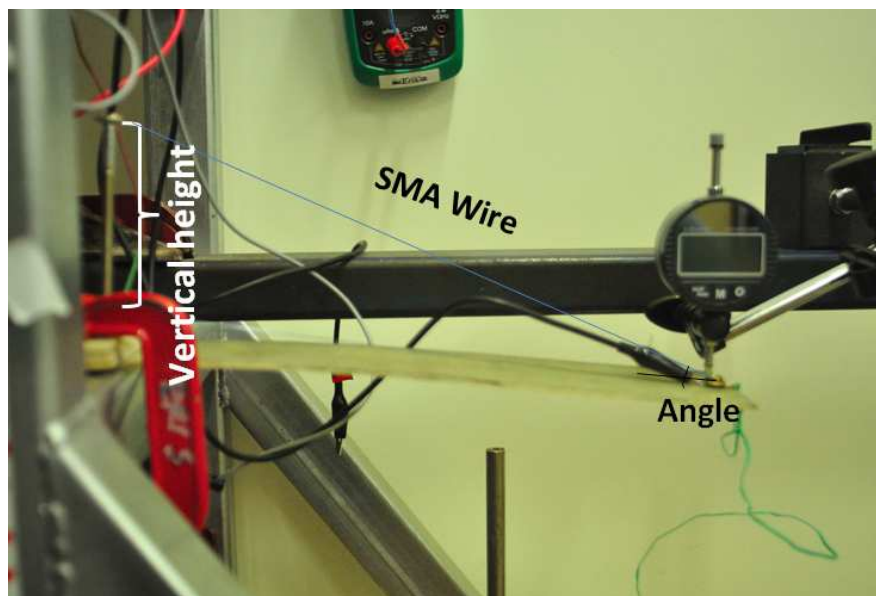
Figure 5.39: Photograph of preliminary suspended SMA wires

As shown in Figure 5.40, the vertical deflection decreases as the number of SMA wires increases from to 2, to 4 to 6 respectively, and at increases in anchoring height in which h3, h4, h5 and h6 represent 30 mm, 40 mm, 50 mm and 60 mm respectively. cf denotes the curve fitting line.
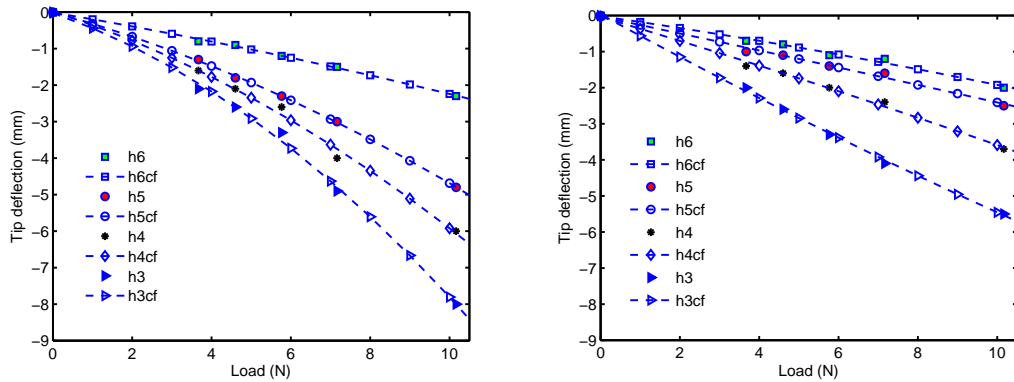
(a) 2 SMA wires

(b) 4 SMA wires
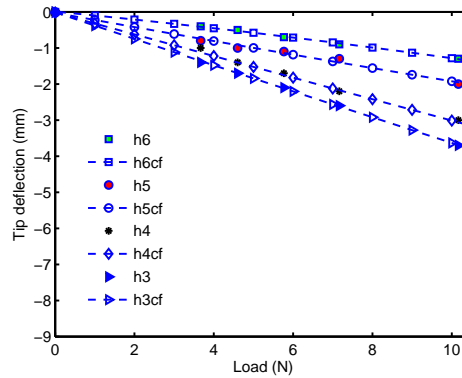
(c) 6 SMA wires

Figure 5.40: Comparison of suspended SMA wires under deflection testing with different numbers of SMA wires at specific heights

Figure 5.41 shows that the suspended wire under deflection was tested at vertical heights of 60 mm, 50 mm, 40 mm and 30 mm with respect to the inclination angles of 11.3º, 9.46º, 7.59º and 5.7º respectively. The time response to actuate was fast compared to the embedded mode. There was no interlaminar noise heard in the suspended mode as there was no debonding interaction. As can be seen from Figure 5.41, even with shorter heights and lower inclination angles, the time taken to actuate was faster compared to the rest of wires which was less than 10 minutes approximately.
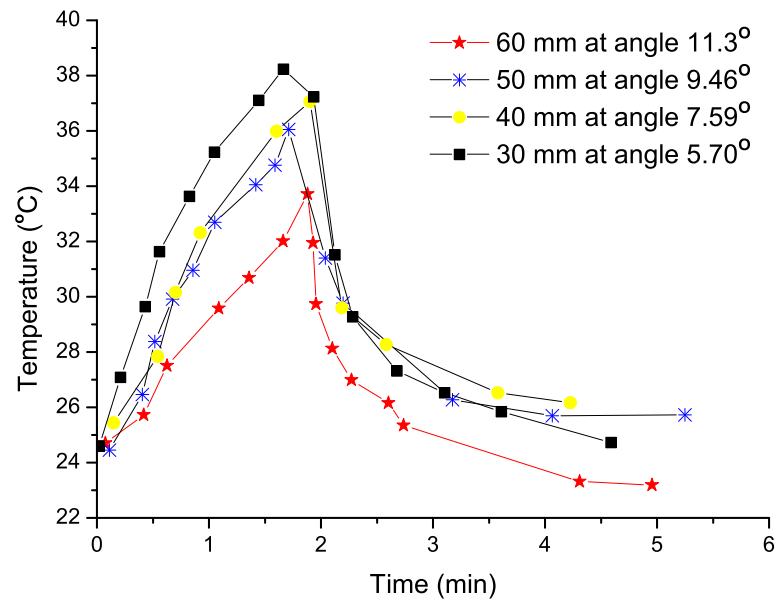
Figure 5.41: Response time of suspended wire

A decrease in the length demonstrated a more dramatic effect on the time response as the resistance reduced. The heating and cooling time also decreases rapidly with the shortening of the wire. Figure 5.42 reveals good agreement between the calculated time response against the resistance per meter and technical information supplied by Dynalloy (Flexinol 2010).
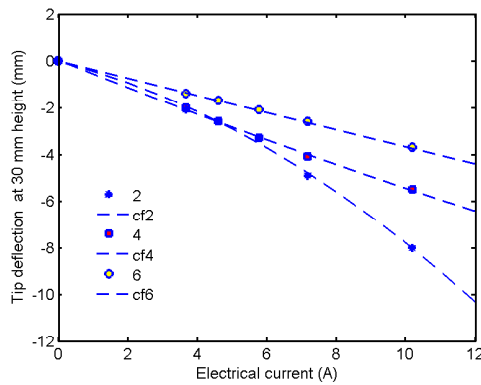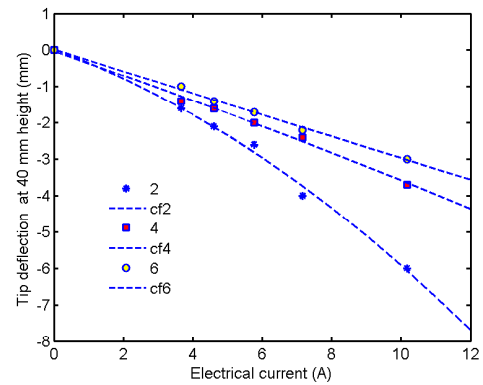
(a) 30 mm   (b) 40 mm
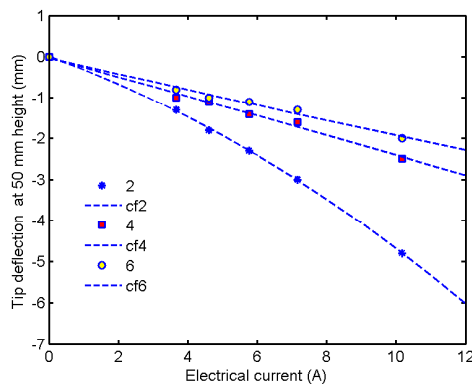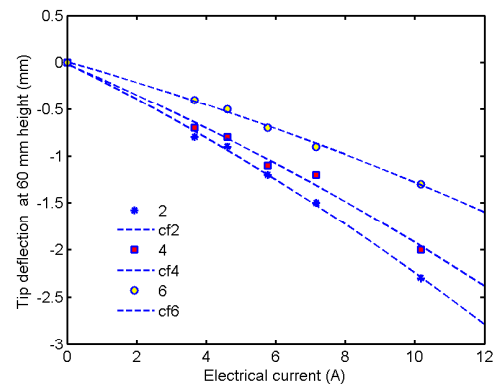
(c) 50 mm   (d) 60 mm

Figure 5.42: Tips deflection with different number of SMA wires under variable load at specific height

Figure 5.43 shows that the current and voltage characteristic curves at specific height for single of the SMA wire. According to Ohm's law, being an empirical law, relates the voltage V across an element to the current I through it:
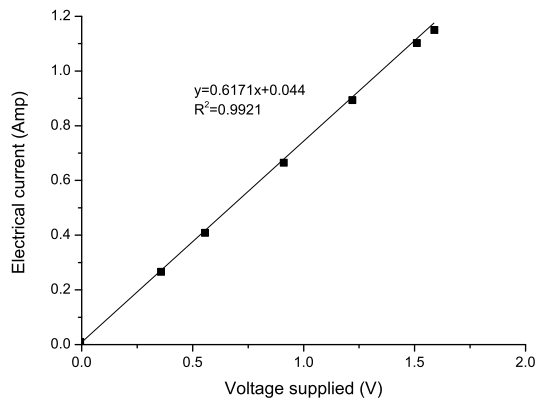
(a) 60 mm
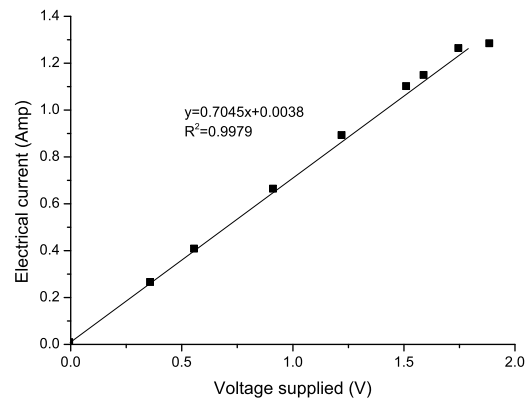
(b) 50 mm
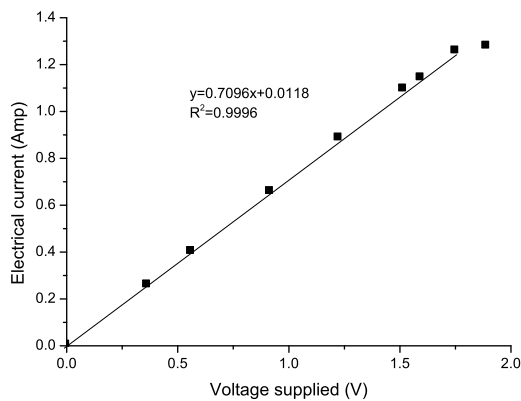
(c) 40 mm
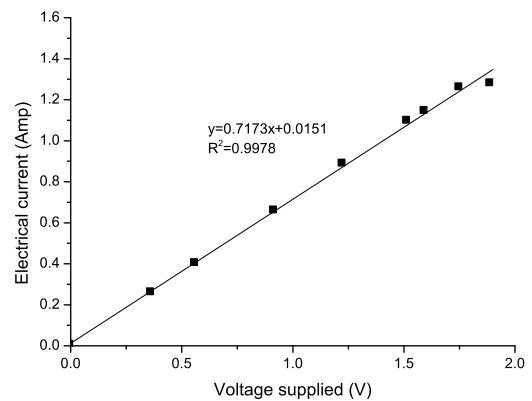
(d) 30 mm

Figure 5.43: Current and voltage curves at specific height

$$V \propto I \tag{5.1}$$

It also illustrates that a steady increase in voltage, in a circuit with constant resistance, produces a constant linear rise in current. It could produce a very good approximation for wires as resistors (assuming that the other conditions, including the temperature, are fixed).

As the value of the gradient became higher, the resistance value became less (Song et al. 2011, Yorke 1986). Ohm's law is satisfied when the graph is a straight line through the origin. The comparison of each curve based on the gradient is summarised in Table 5.8.

Table 5.8: Gradient response for suspended wire

Vertical height (mm)	Gradient value
60	0.6171
50	0.7045
40	0.7096
30	0.7173

5.16   Deflection and Load Relationship

An advantage of the deflection simulation method developed here, in which separate elements for the wires and composite matrix are used, means that material properties or composite geometry can be changed easily. Other approaches in which particular composite elements are developed which combine both SMA and matrix properties, are more application specific. The flexibility of the current approach allows the technique to be used to explore design issues for a composite. This capability was illustrated here by selecting the appropriate matrix softening characteristics to allow self-straightening to occur. A deflection test for a 6 SMA wire, for example, has been meshed as shown in Figure 5.44b. A concentrated load was applied at the tip. The nodes at the root of the blade had a fixed displacement clamped with respect to 6 DOF at each node. This simulation showed the ability of a numerical tool in modelling the shape memory effect - the thermo-mechanical behaviour of shape memory alloys.
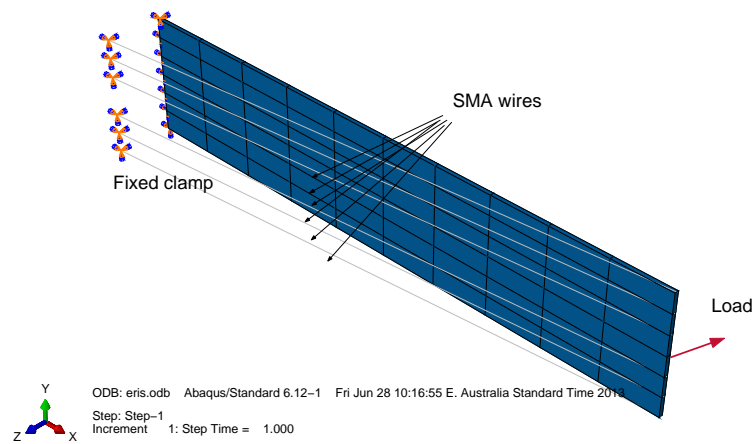
(a) Detailed assembly of the complete structure
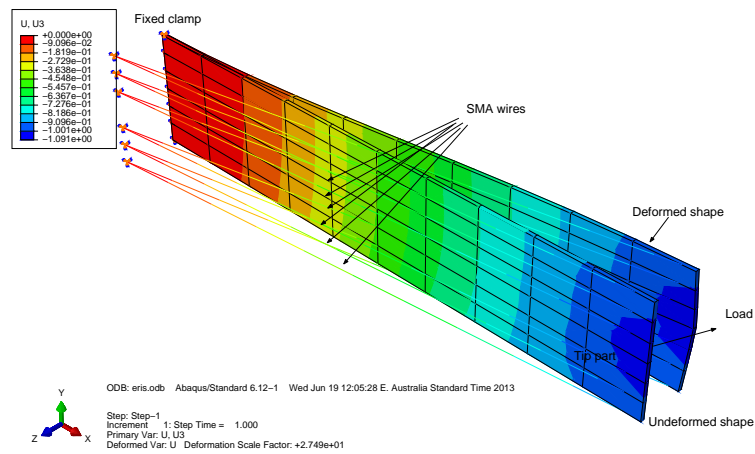
(b) Graphical contour distribution for number of wires and the

plate - undeformed and deformed

Figure 5.44: Simulation of smart wind blade model

Figure 5.45 shows the deflection and load relationship with different numbers of SMA wires. To determine the load-tip deflection relationship, a simulation using FEA was carried out using the specimen as shown in Section 3.2. As illustrated in Figure 5.45, as the number of SMA wires increases, the tip deflection is gradually reduced when the load is applied. This means that the force needed to lift the plate as well as the remaining deflection is caused by increasing the SMA wire temperature using the electrical current.
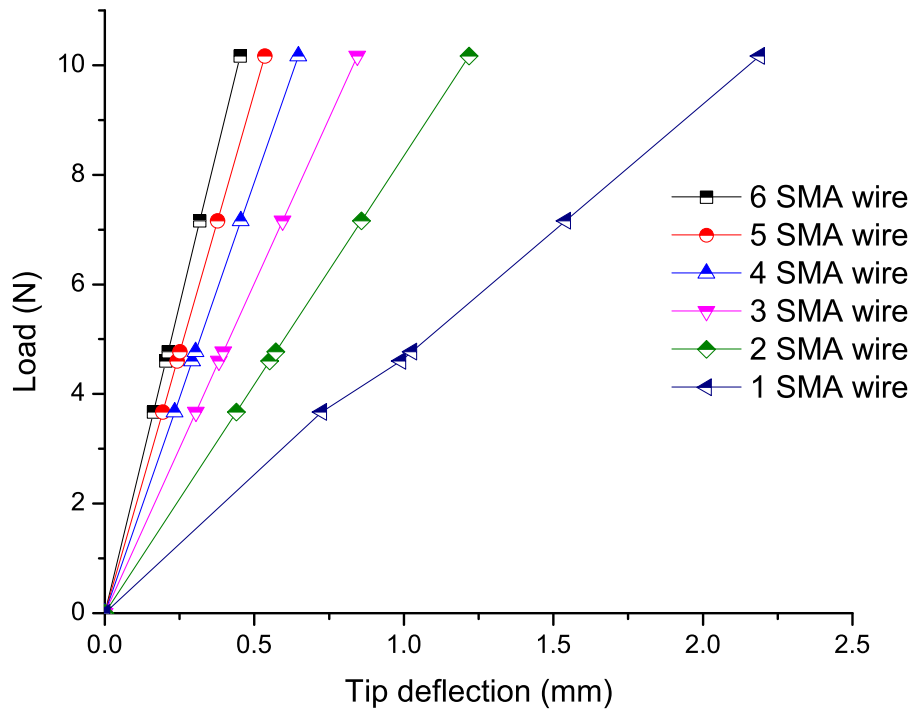
Figure 5.45: Calibration of the smart wind blade model under deflection

In this section, 3D structures under load conditions were analysed using plate elements, being provided with both in-plane and deflection load carrying capacity for the elements. The procedure to be adopted for the blade is illustrated using a strip blade element. A typical finite element idealisation is considered in the analysis of a wind turbine blade. The blade root is fixed to the rotor hub and is treated as a cantilevered box beam. The same geometry of the test specimen and the ply configuration as given in Table 5.7 has been modelled in ABAQUS®. The

test specimen is made to imitate the real geometry as closely as possible. For the comparison study, the model was developed with a three- dimensional, deformable shell planar feature for the shell model and a three-dimensional, deformable solid extrusion feature for the solid models (Simulia 2012).

5.17 SMA Wires Arrangement

The SMA wires, which were pre-strained by 4 %, were mounted at the anchoring height. The orientation of the SMA mounted to the GFRP plate has to be aligned with the anchoring height. The SMA wires at the tip plate were mounted using a modified terminal block which was available as an electrical power connector. This is to ensure that the wire moves freely along the terminal block. The SMA wire at the the root end, where it was clamped, will be tightly crimped by a screw terminal slot. Soldering is not to be used in this section as the solder itself could potentially melt, leading to slip-off.

Although the terminal block tightly locked the SMA wire at the root plate, eventually the SMA wire would experience tension and relaxation continuously. Hence, the SMA wire would become a bit slack.

5.18 Results of Parametric Studies

5.18.1 Effect of Anchoring Heights in 300 mm plate

To see the change that the anchoring heights (using a single SMA wire) have on the 300 mm long plate, tests were undertaken at different loads. Figure 5.46 depicts the curves of the deflection test at different loads. Strong evidence has been observed that when there is an increment in the anchoring heights, the tip

deflections were reduced. As expected from simple engineering theory, the force exerted by the SMA wires is a tension force. If the anchoring height increases, the tension force reacts upwards, creating more magnitude of force since the angle of the elevation is made towards 90 °.
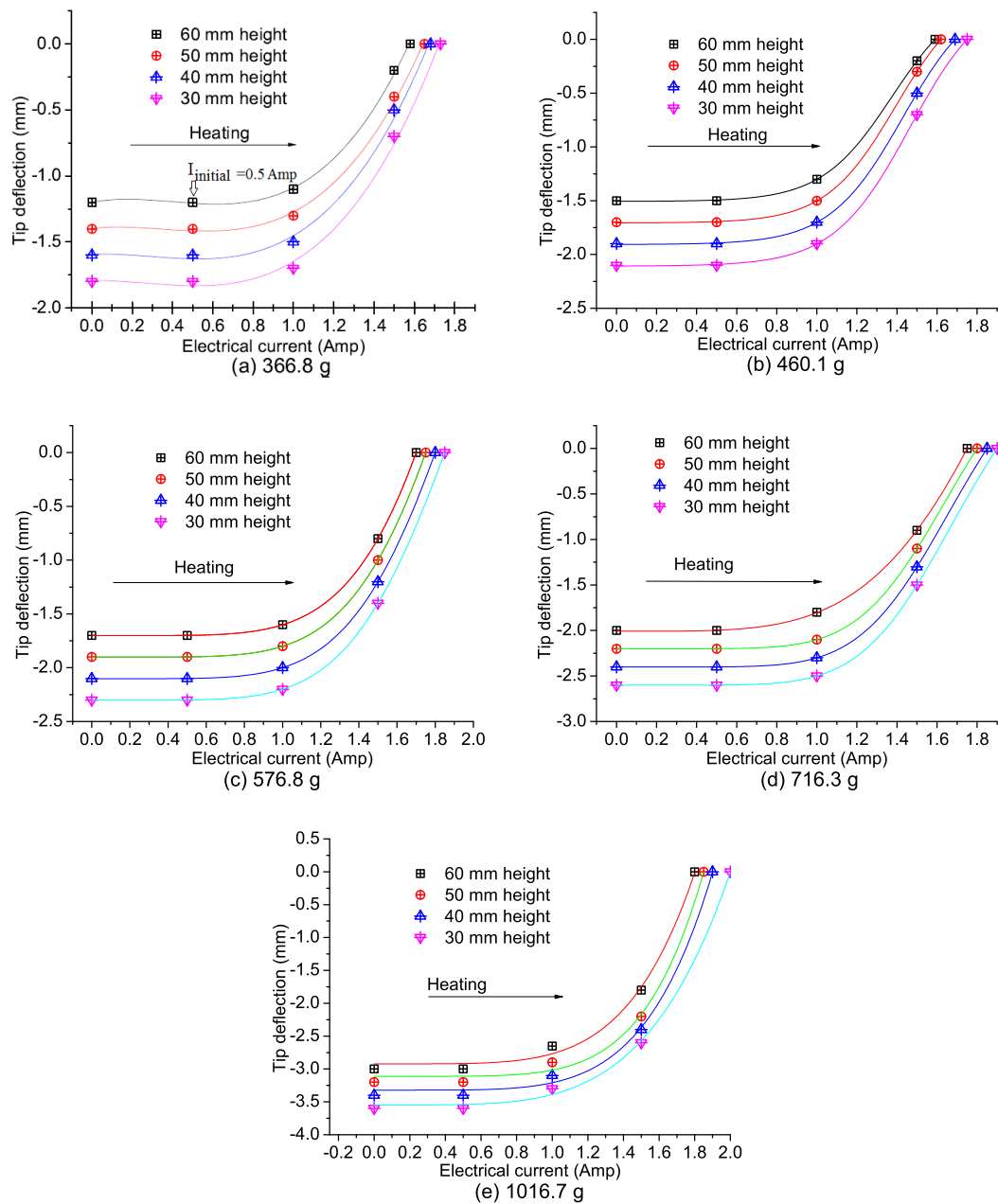
Figure 5.46: Tip deflection against current at different anchoring heights

Figure 5.46 indicates the same general response of the tip deflection with respect to the electrical current. As the load was increased, the response of the plate

shows the same general response to the load of 3.668 g, which is shown in Figure 5.46a. There was the same trend for the rest of the responses in Figure 5.46b, c, d and e.

The value of the current at which the tip deflection starts to lift is called $I_{initial}$ for example Figure 5.46 was 0.5 Amp. Below the $I_{initial}$ value, there was no such changes of the actuating movement which is shown as a flat curve. The tip deflection begin to lift after exceeding the $I_{initial}$ value. This happened as there was an actuation force generated in the SMA wire. If there is zero current, there is no force exerted on the SMA wire. As the current is increased, the slope of the curve increases until it is fully recovered to the original configuration. Here, the lift force, F_{lift}, is proportional to the electrical current applied, I. F_{lift} is greater than zero as there is current flowing. Assuming the resistance is constant, the power increases as the current increases.

Figure 5.47 reveals the tip deflection curve profiles at various loads at 300 mm of anchoring height. As the heat was generated by the electrical current flow, there were temperature rises in the SMA wires. The temperature rise is an exponential curve whilst the tip deflection rise is a quadratic curve. However, there was a discrepancy in values after applying an incremental load, which was due to heat recovery taking place, and the system might be experiencing hysteresis (Huang et al. 2004).

There are also similar trends for the anchoring heights of 40 mm, 50 mm and 60 mm which are shown in Appendix J.
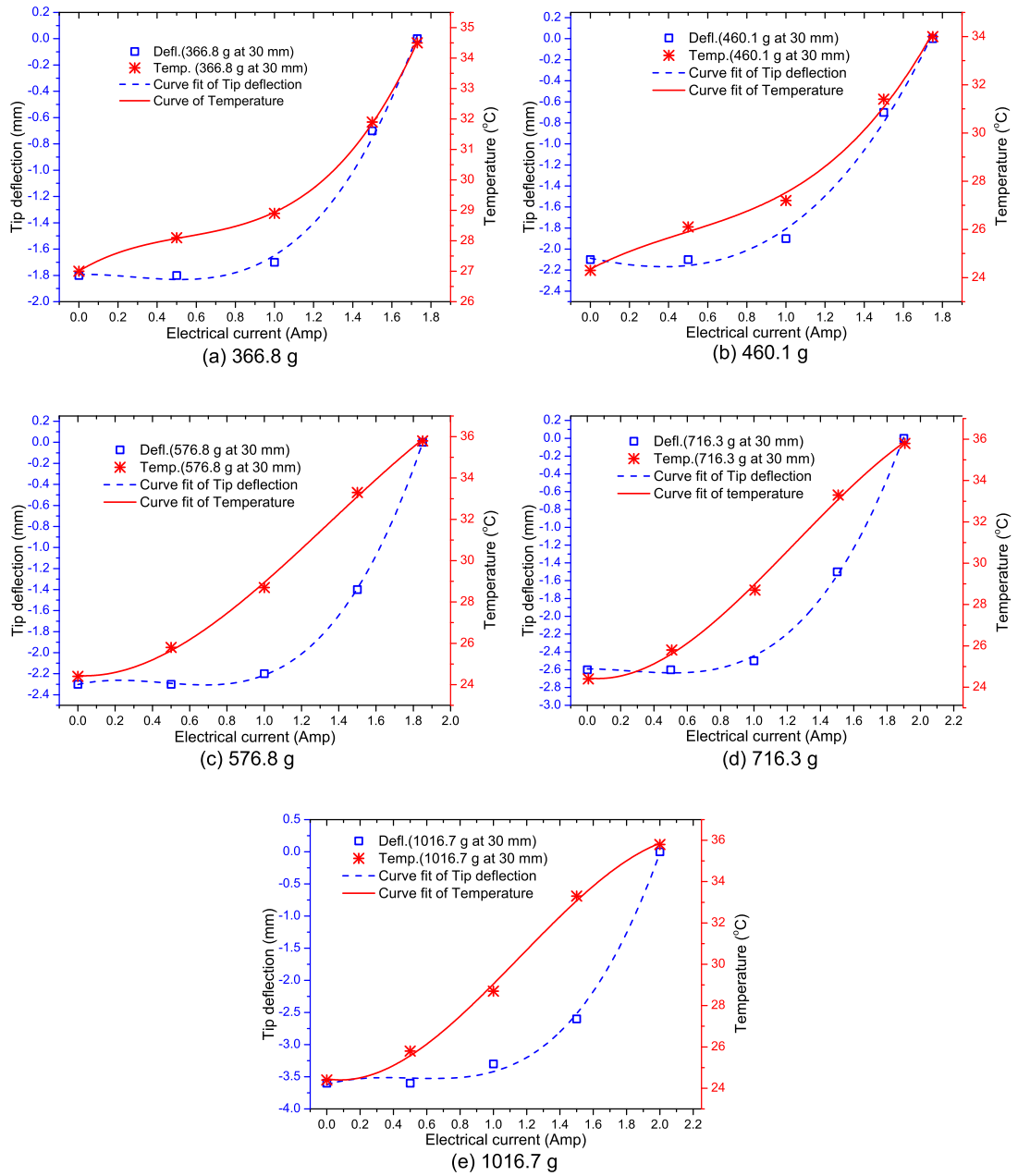
Figure 5.47: Tip deflection against current at various load at 30 mm height, respectively

5.18.2   Effect of the Number of SMA Wires in the 300 mm plate

A series of experimental tests were conducted with the different numbers for SMA wires in the 300 mm plate. Adding more SMA wires can give significantly better performance in causing the deflection to recover. This obviously occurs given the difference between 1 and 2 or more SMA wires.

By adding more SMA wires, there is more tension in the assembly members. The SMA wires behave more strongly as consequently less deflection happened with 2, 3, 4, 5 and 6 SMA wires.

As can be seen in Figure 5.48, as the number of SMA wires increases the deflection decreases. The current varied at 0.5 Amp intervals until the tip deflection became 0.0 mm. The findings for varying the current with different numbers of SMA wires are considerably consistent with those when different loads are applied. The experiment regarding changing the number of SMA wires with respect to the applied load shows significant performance as there is an incremental number of SMA wires taking the plate back to its original position.

The results were promising, a few overshoots were recorded. Assuming that the heat generated is constant along the wire and that the heat dissipation is negligible, it is observed from the graph in Figure 5.48 with a single wire that there is a large deflection compared to the rest. This is because there is a strong relationship with the existing forces acting during the loading at zero current. The actuation performance of the SMA wires is expected to respond starting at 1.5 Amp. This reaction happened due to the SMA wires were being electrically heated, causing the wire contraction process to occur. Consequently, the deflected plate was being straightened by the actuation force of the SMA wires.
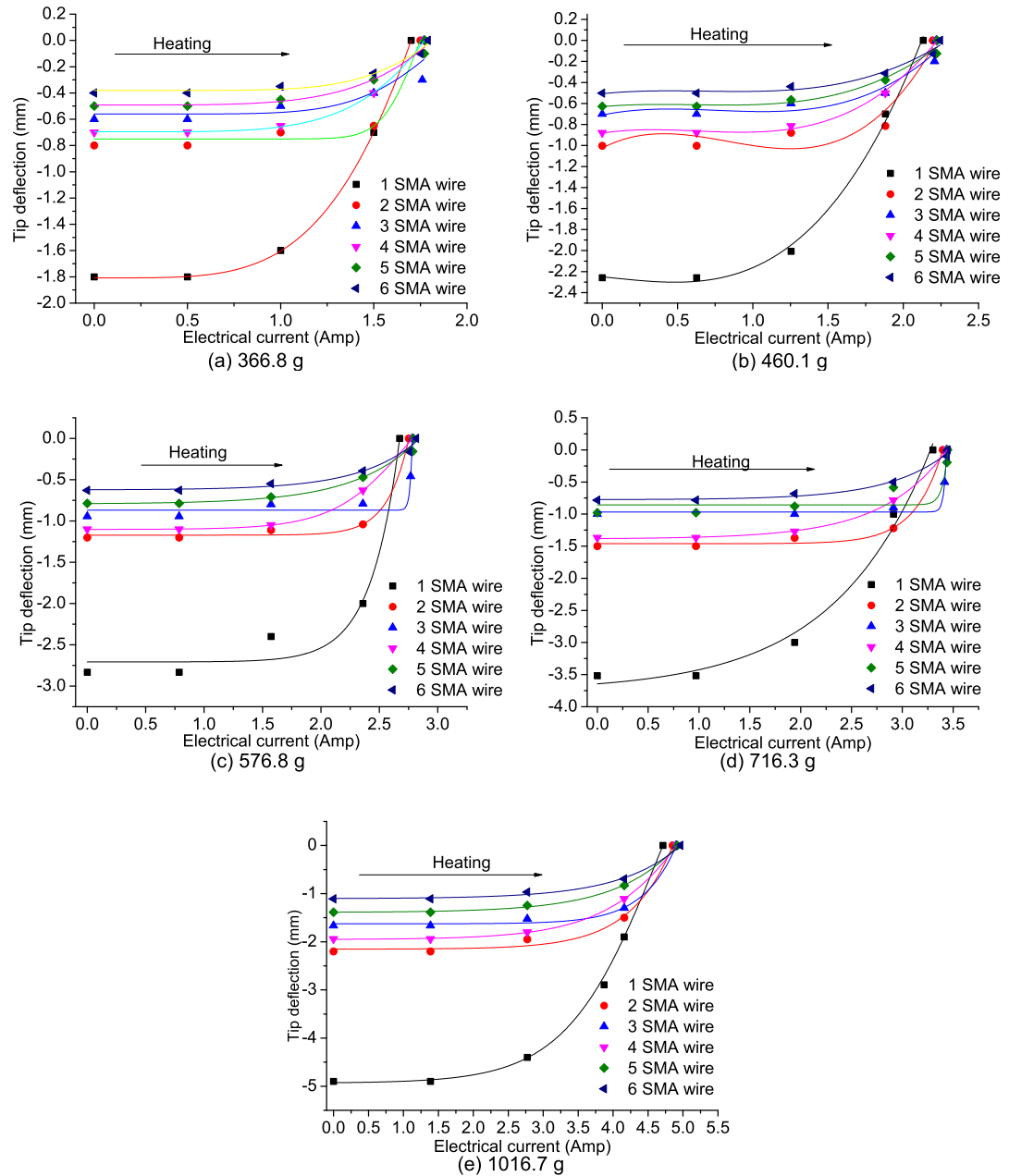
Figure 5.48: Tip deflection against current at different number of SMA Wires

5.18.3   Effect of Heat Sleeving

Figure 5.49 shows the effect of using heat sleeves on the SMA wires. Four different anchoring heights are used to observe the difference in the temperature increment due to the position of the anchoring point.

Fibreglass cloth was used to cover the SMA wires as the heat sleeve. It is observed that there are two distinct sets of curves, which are SMA with the heat sleeve and SMA without heat sleeve. It shows that heat sleeving gives a significant performance increase to the SMA wires. The reason for this is that the sleeve reduces the heat loss from the SMA wires through convection.

With the heat sleeve, the SMA wires were insulated. The rate of heat generation was higher than for the non-heat sleeve case, which is shown in the slope of the gradient with respect to time taken. The heat was conserved in the wrapping, unlike the non heat sleeve case, where heat escaped to the surroundings.

The same general trend of curves was discovered using heat sleeving in the cases where there were 4 and 6 SMA wires. These curves are shown in Appendix K.

(a) 30 mm height

(b) 40 mm height

(c) 50 mm height

(d) 60 mm height
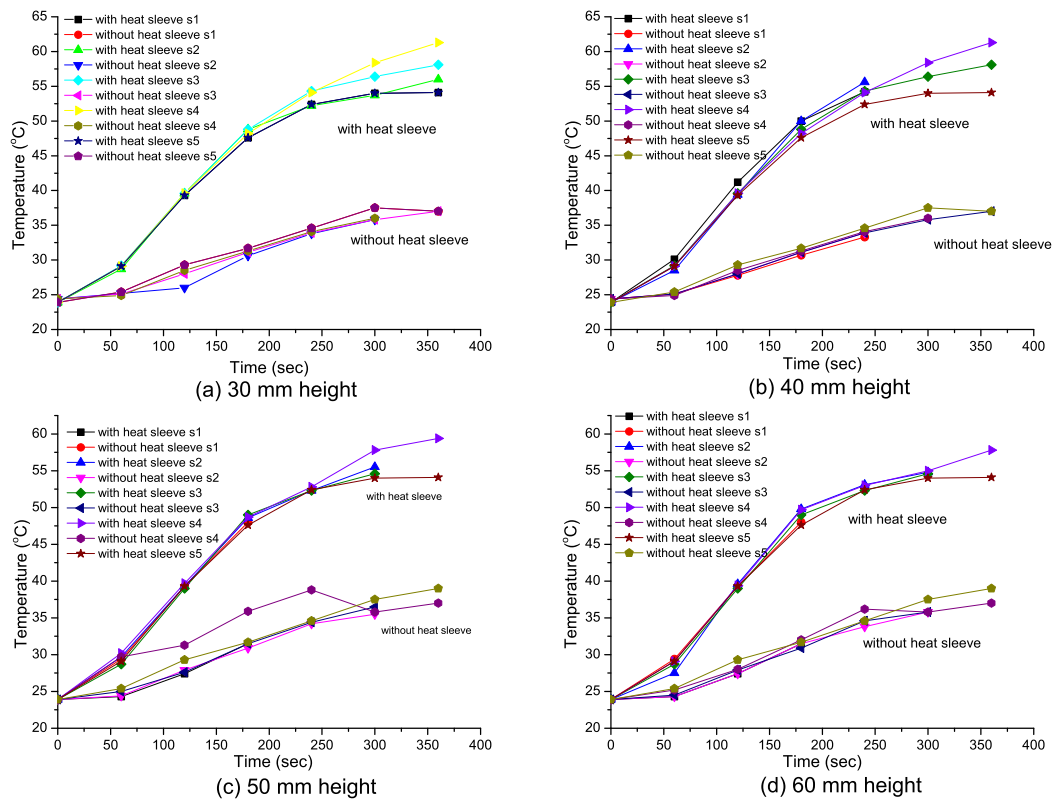
Figure 5.49: Effect of heat sleeving and without heat sleeving at s1=366.8 g, s2=460.1 g, s3=576.8 g, s4=716.3 g and s5=1016.7 g for 2 SMA wire

5.18.4 Smart Wind Blade Deflection for Stress Recovery

The deflection of the smart wind blade using SMA wires has been monitored and the stress recovery driven by the SMA wires was studied. To activate the SMA wires, they were heated above their transition temperature . These SMA wires are one-way actuators that when heated contract about 3-4 % in length exerting significant stress. Their contraction-heating can be accomplished using an electrical current. The contraction movement has been applied to straighten a deflected plate which has experienced a loading condition. When the SMA wires are getting cool (or when it is allowed to cool), they can be stretched back to their original length for subsequent contractions.

5.18.5 Stress Recovery of SMA Wires in 1000 mm plate
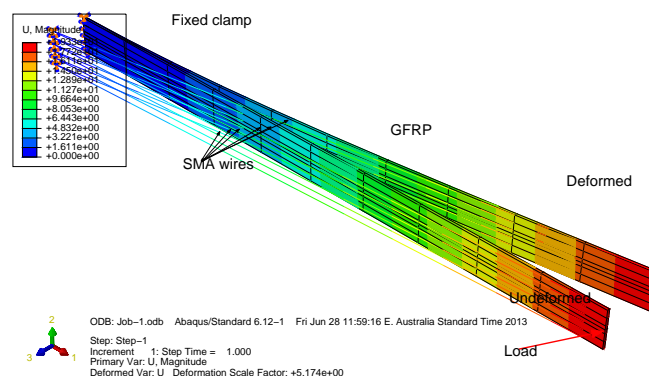
Figure 5.50: Deflection and alleviation response of the smart blade

Figure 5.50 shows the result of the 1000 mm model with respect to a variable load compared to the simulation in FEA. The criteria of good handling in taking back the deflection depends on the load applied and the current supplied. However, it is recommended that to supply more current should be applied as the load increases and if the plate is longer. For tests from the minimum tested load from 3.67 N until the maximum load 10.17 N there was almost full return to the original position (0.0 mm). In the results, all the data collected are averaged values obtained from the experimental results.

The voltage and current supply have also been recorded in Table 5.9. As can be observed, the deflection distribution patterns observed in the FEA are almost the same as the experimental results.

Table 5.9: Deflection d, reading values for 6 SMA wires at 1000 mm,

60 mm anchoring height

Load (N)	d before heated (mm)		d after partially heated (mm)		Final d final (mm)		Electrical power supply		
	FEA	Exp	FEA	Exp	FEA	Exp	Voltage V (Volt)	Current I (Amp)	Power Q (watts)
0.00	0.00	0.00	0.00	0.00	0.00	0.00	0.00	0.00	0.00
3.67	-10.17	-11.17	-5.62	-6.98	-4.55	-4.19	12.5	0.47	5.875
4.60	-12.76	-14.16	-7.12	-9.01	-5.64	-5.15	14.4	0.55	7.92
4.77	-15.99	-17.39	-8.84	-10.02	-7.15	-7.37	16.6	0.63	10.46
7.16	-19.86	-21.26	-10.97	-12.01	-8.89	-9.25	18.8	0.70	13.16
10.17	-28.19	-29.59	-15.59	-16.98	-12.60	-12.61	21.6	0.83	17.93
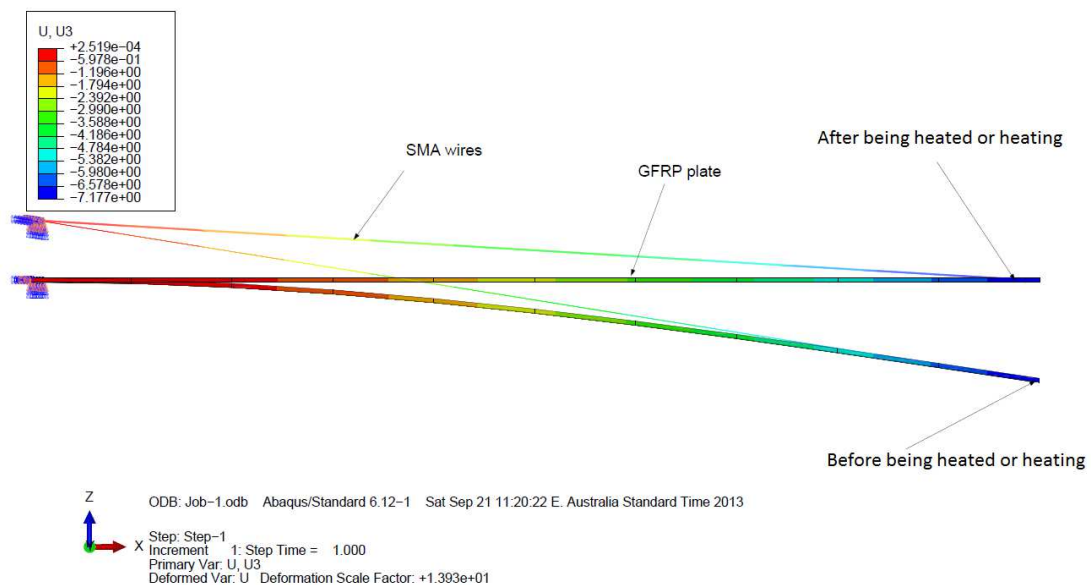
Figure 5.51: Simulation of the smart blade under deformation and stress recovery

Figure 5.51 illustrates the simulation of the GFRP plate before and after SMA wires were heated. If SMA was used, the deflection test was performed by assuming a concentrated load such as wind loads during operation. Stress recovery, which was through the contraction of the SMA wires, at least, would be able to alleviate the load. This mechanism has been accomplished by heating the SMA wire using a constant power supply unit. However, it suffers from insufficient power to fully

contract the wire at a considerable burden. Consequently, a small deflection occurred although stress recovery took place. The effectiveness of the mechanism can be improved if the power supply system is further developed.

Figure 5.52 illustrates the stress of the blade gradually increases along the blade towards the fixed clamp. At the free end section there were no boundary conditions and therefore the displacement is larger at the tip rather in the hub. However, it was constrained at the hub as there is a restriction point.
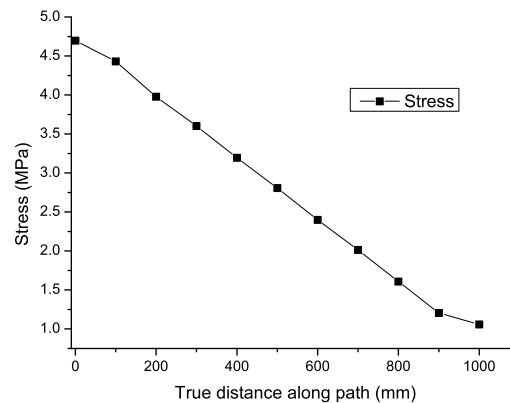
Figure 5.52: Stress of the blade under deflection for 1000 mm

In contrast in Figure 5.53, a higher contribution of the strain at the root (0.14 microns) rather than at the tip (0.02 microns) was observed. Negative values were obtained as there were in compression.

For testing the actual blade on a large scale, there should be a set of constraints to be met. Here, the common constraints for smart wind turbine blades are listed which are likely to affect the design of actuators using SMA wires. The constraints are as follows:

(i) Power voltage. The amount of power available is an obvious constraint for this mechanism in general. Here, the power available has to be large enough to allow for complete heating of the SMA wires in a reasonable time;
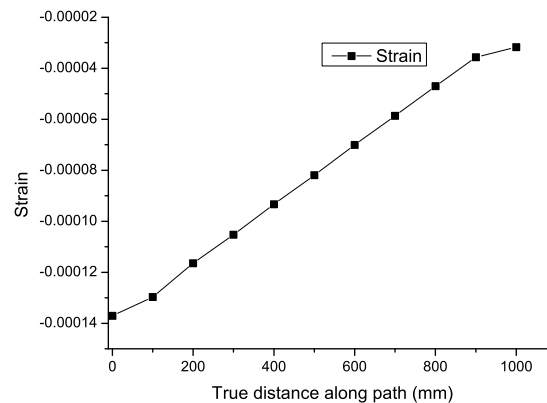
Figure 5.53: Strain under deflection - the blade under deflection for 1000 mm

(ii) Response time. Any application has a time requirement associated with it. The response time is a function of the input power (current);

(iii) Temperature range. The range of the transition temperatures is critical for SMA wires, as this material is driven by temperature. The working temperatures should be set to lie outside of the ambient temperature range. Furthermore, the maximum temperature attained by the SMA wires should not be harmful for the rest of the SMA wires;

(iv) The device should be able to perform a significant numbers of cycles, while remaining a fairly consistent and with the predictable performance and degradation.

5.18.6 Effect of the Number of SMA Wires for Stress Recovery

Figure 5.54 illustrates the current and voltage applied at various loads with respect to the number of SMA wires. It was recorded that as there is an increase in SMA wires due to the resistance being higher, so more current is needed to generate heat through the wire; this assumes that the heat generated along the SMA wires is uniform and that heat loss to the surroundings is minimal since the SMA wires

are insulated with a heat sleeve.
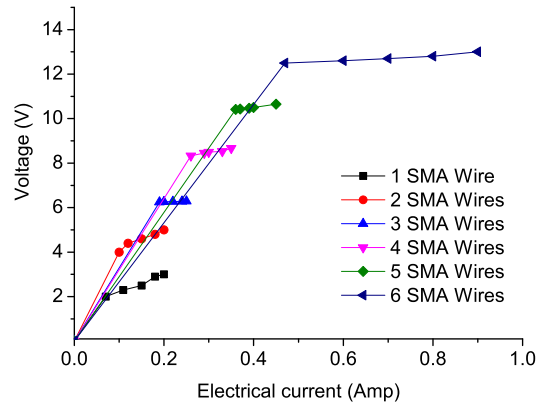
Figure 5.54: Voltage and current curve for 1000 mm specimen

Figure 5.55 reveals the performance of the number of SMA wires in taking the deflection back to its original configuration with respect to the load. It can be seen from the deflection curve, which worked by the SMA wires taking action in which the deflection at each load is reduced to zero deflection. Once it achieves the stress recovery, the curves of the seven lines overlap each other forming a single line.
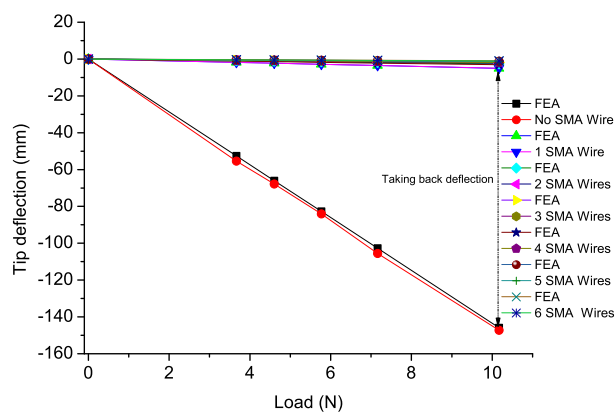
Figure 5.55: Deflection curve for 1000 mm specimen

Test results indicate that the recovery forces of the SMA wires considerably decrease the deflection of the wind blade. When the wind blade is subjected to

a large load this will result in a large deflection. The deflection can be reduced effectively and stress alleviation can be achieved.

Figure 5.56 indicates the current and voltage for heating in the 1000 mm plate. As expected, there is a proportional relation between the current and the voltage.
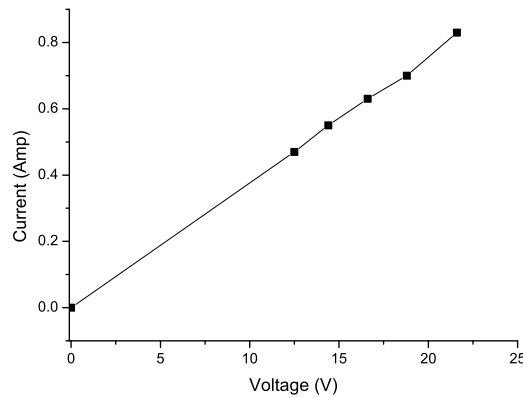
Figure 5.56: Voltage and current curve for 1000 mm specimen

5.19   Comparison of Power Performance

The power coefficient (C_p) indicates how efficiently the conversion of wind power to rotational mechanical power is performed by the wind turbine. The Betz limit is the maximum theoretical value reached by the power coefficient which is 0.5923 for three bladed HAWT. This limit is derived from the principles of the conservation of the mass and the momentum of the air stream flowing through an idealised actuator disk that extracts energy from the wind stream.

A rotor equation model, developed by Slootweg et al. (2003), has been used to approximate the power coefficient of the three bladed wind turbine. The governing equation for power extraction is given below

$$P_{wt} = \frac{\rho}{2} C_p(\lambda, \beta) v_w^3 \tag{5.2}$$

with P_{wt} the power extracted from the wind, ρ the air density (kg/m^3) , C_p the performance coefficient or power coefficient, λ the tip speed ratio, v_t/v_w the ratio between blade tip speed (m/s) and wind speed at hub height upstream of the rotor (m/s), the pitch angle β (°), and the area covered by the wind turbine rotor (m^2). In the case of a stall controlled wind turbine, β is left out and C_p is a function of λ only.

Based on the equation of the power coefficient derived by Slootweg et al. (2003)

$$C_p(\lambda, \beta) = c_1 \left(\frac{c_2}{\lambda} - c_3\beta - c_4\beta^{c_5} - c_6 \right) e^{-\frac{c_7}{\lambda}} \tag{5.3}$$

and

$$\lambda = \left(\frac{1}{\lambda + c_8\beta} - \frac{c_9}{\beta^3 + 1} \right)^{-1} \tag{5.4}$$

This equation of C_p was experimentally developed from the curve plotted based on the wind turbine manufacturer's data arranged by Slootweg which is calculated in Equation 5.5. By using this equation, C_p was determined to predict the effect of deflection on the smart wind turbine blade model.

The nine coefficients from c_1 to c_9 were taken from the curve fitting and the values are presented in Table 5.10. Based on this equation, regression analysis using MATLAB$^\circledR$ has been used to plot the curve. The equation was modified, β_{SMA} is the pitch angle when SMA is used. The equation becomes:

$$C_p(\lambda, \beta_{SMA}) = 0.73 \left(\frac{151}{\lambda} - 0.58\beta_{SMA} - 0.002\beta_{SMA}^{2.14} - 13.2 \right) e^{-\frac{18.4}{\lambda}} \tag{5.5}$$

where

$$\lambda = \left(\frac{1}{\lambda - 0.02\beta_{SMA}} + \frac{0.003}{\beta_{SMA}^3 + 1} \right)^{-1} \tag{5.6}$$

Table 5.10: Optimised values of the curve equations

presented in Equation 5.5 (Slootweg et al. 2003)

c_1	c_2	c_3	c_4	c_5	c_6	c_7	c_8	c_9
0.73	151	0.58	0.002	2.14	13.2	18.4	-0.02	-0.003

$$\beta_{SMA} = \beta_{deflect} - \beta_{upwards} \tag{5.7}$$

$$\beta_{upwards} \propto I.nw \tag{5.8}$$

Figure 5.57 shows three power coefficient curves with respect to tip ratio. The graph shows the performance coefficient for a theoretical three-blade turbine with and without SMA wires. Figure 5.57 reveals very promising results for the performance of the HAWT. The theoretical C_p has been discovered for the three-blade wind turbine with the SMA wire, which is higher than for the three-blade without SMA wire. For the wind blade without SMA wires, the deflection becomes larger as the pitch angle increases. The peak curve of the wind blade without SMA wires occurs further away from the Betz limit. Compared to the the wind blade with the SMA wires, the peak curve location is closer to the Betz limits.

Based on Equation 5.7, β_{SMA} is the total deflection of $\beta_{deflect}$ and $\beta_{upwards}$. As can be seen Equation 5.8 shows that the relationship of β is proportional to the electrical current applied (I) and the number of SMA wires (nw).

Although the study of the response time taken is not considered in detail, nevertheless the generated electric current is related to time for the purpose of heating the wire. So it can be concluded that the time taken to rectify the situation of deflection was slow. However, this does not hinder the effectiveness of the smart blade. During the rotation of the blade, corrective actions were taken
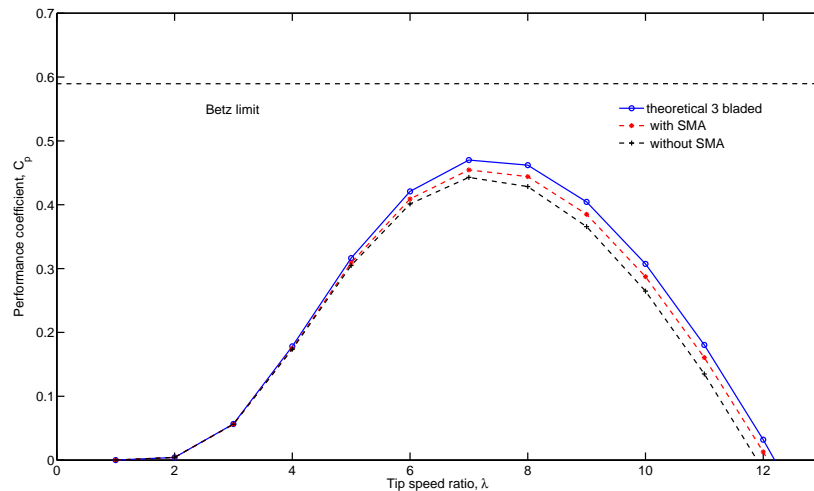
Figure 5.57: C_p- λ performance curve for a modern three-blade turbine

to enforce the deflection, but it takes a bit of effort with the help of the SMA wires. This investigation of the effectiveness on the time response has been proven by Abdullah (2011). It has been found that the time taken for actuating the morphing control was slow but was adequate enough for controlling the airfoil shape and maintaining the shape during flight which has been tested in a wind tunnel.

5.20   Summary of the Results

In this chapter, the findings and associated discussion were presented in detail. A feasible study of the application of smart material has also been highlighted. The observations and data collected from the experimental work were used to estimate the capability of the SMA wires to recover the large deflection of the composite plate. These include the amount of the electrical current with the applied load. The SMA wires arrangement also has been conducted. It has been observed that the stress recovery of the smart blades also has been successfully performed.

A neural network model has been developed to perform the deflection with respect

to a number of wires required as the output parameter. The parameter includes load, current, time taken and deflection as input parameters. The network has been trained with experimental data obtained from experimental work.

In order to remove all the technological difficulties related to the complicated composite fabrication, a simple proof-of-concept specimen was built by mounting pre-strained SMA wires on top of the laminated composite plate strip.

Chapter 6

Conclusions and Further Work

The work described in the previous chapters shows the feasibility and effectiveness, via a proof-of-concept design, of a smart wind turbine blade on a laboratory scale. This chapter concludes the work of this thesis with comments on the results and recommendations for future investigation. From the realisation of the present thesis work, the main conclusions with regards to smart wind turbine blades (a pilot study) and about knowledge acquired related to the design process, are summarised as follows.

6.1 Conclusions

This dissertation delivers a number of issues related to development of the pilot study of the smart blade composites. Their different constituents, namely fibreglass and shape memory alloy elements, were first examined separately and the conclusion obtained extends beyond smart composites' blade applications.

In this study, the ability of the SMA wires to enable the plate-like structure to return to its original shape under load condition has been examined. This study shows that the proposed smart wind turbine blade, incorporating SMA as an

active actuator, is feasible.

The results from the developed model show good agreement with the experimental result given the same system parameters. The model allows the performance parameters of the proposed smart turbine design to be analysed.

It has been proven that the stress recovery can be successfully achieved by straightening the deflection experienced by the wind turbine blade. In this work, a pilot study of the smart wind turbine blade was carried out in which a structural analysis based on the FEA was simulated and the results have been validated by the experimental results.

It has been shown that the prediction of performance can be analysed using ANN, which has been simulated by MATLAB. Throughout this analysis, the relationship between the number of SMA wires, the load, the current and the deflection have been successfully investigated. It was shown from ANN that all the models have predicted satisfactorily the performance behaviour of the SMA wires provided that the correlation factors (such as training, test and validation) which have been represented in the overall of data are interpreted properly.

The development of a smart blade using SMA wires has been efficiently proven not only to improve the performance coefficient close to 0.5923 (Betz limit) but also the stress recovery. In this study, the large deflection has been reduced by the SMA reaction in straightening the blade into the original shape, which is an undeformed shape. SMA wires are materials that have the ability to undergo relatively large deformations and then recover the deformation when they are heat activated.

It is also felt that only time limitations and unprecedented experimental complications prevented further improvements in the control system as well as the development of the mechanism control. There is scope for practical innovation for the real scale application.

From the technological point of view, the choice of the composite constituents, the shape memory materials, and the manufacturing processes should be optimised according to the actual application, addressing the problems which were encountered in the present experimental work, such as the adherence of the shape memory elements to the fibre-reinforced composite.

6.2   Limitations of the Study

The results obtained from this case study of SMA wires which were in (i) an embedded mode and (ii) a suspended mode are discussed and demonstrated to determine the feasibility of the SMA wires actuator concept. Significant operational inadequacies were, however, observed. Elimination of these inadequacies forms the basis for an improved actuator design, which is the subject of the current work.

The improvements required are detailed as follows:

(i) In the embedded mode, the temperature rise during contraction was not capable of actuating the SMA wires in large deflections of the wire since there is a restriction and uneven force acting on the wires. Increasing the number of wires is the best way to compensate, but it will cost more and be less efficient since there are lot of SMA wires involved;

(ii) Using the suspended SMA wires has been found that to be more practical compared to embedded ones. The temperature rise has been successful in actuating the SMA wires although for lower numbers of wires. However, the method of gripping the SMA wires was found to be ineffective and resulted in slippage of the wires which were connected between the GFRP and the SMA wires. Consequentially, uneven deflection angles in the pull up orientations were observed. This behaviour was notable as the loads on the system increased;

(iii) Stress concentration at the points of attachment of the wires damaged the fibreglass hinge tube especially in the embedded mode. This resulted in material degradation and failure was more likely to occur;

(iv) Due to the presence of multiple wires in both modes, which were the embedded and the suspended mode, difficulties were encountered in applying an equal amount of pre-strain to all the wires. It has been suggested that the uniformity of the pre-strain of the wire can be controlled by individual strain gauges;

(v) The locking mechanism was found to be unreliable in taking back the deflection to the recovery position.

These limitations to be considered responsible for hindering the reliable tracking capability of the actuation system/self-straightening blade. The objective of this thesis is to eliminate these drawbacks to ensure a consistent tracking capability.

6.3 Further Work

In terms of future work, there are many recommendation to be followed. Recommendations for further work are outlined below:

 (i) The static test should not be limited to deflection but also the torsional bending which occur in the real condition;

(ii) Dynamic analysis - for example frequency response, fatigue response should be performed in order to thoroughly investigate the performance of the wind turbine blade;

(iii) The implementation used in the actual condition as such in actual scale wind turbine blade with the whole system should be synchronously coupled with the data acquisition system with a software controlling programme;

(iv) It might be possible to discover the relationship between tension behaviour and behaviour under other load conditions, e.g. compression, torsion, and even multi-axial loading, by using the thermo-mechanical properties of SMAs. This relationship will be very useful in order to develop realistic finite element models for structures including smart blades;

(v) To see the effectiveness of using SMA particularly for a large scale, a rigorous study should be carried out mainly in the deployment of SMAs in the market for small wind blades. Aerodynamic experiments on scale models of small wind blades in wind tunnels and on a full scale wind turbines at the test sites.

References

Abdullah, E. 2011, Control system design for a morphing unmanned air vehicle wing using shape memory alloy actuators, PhD thesis, School Of Aerospace, Mechanical & Manufacturing Engineering College of Science, Engineering and Health RMIT University.

ACEC 2012*a*, Benefit of the renewable energy target to australias energy markets and economy, Technical report, Australia Clean Energy Council.

ACEC 2012*b*, Theres power in wind: fact sheet, Technical report, Australia Clean Energy Council.

Armstrong, W. & Lilholt, H. 2000, 'The time dependant, super-viscoelastic behavior of NiTi shape memory alloy fiber reinforced polymer matrix composites', *Materials Science and Engineering: B* **68**, 149–155.

Ashwill, T. 1992, Measured data for the sandia 34 m vertical axis wind turbine, Technical report, Sandia National Laboratory.

Auto, G. 2013, Heat-activated smart-material debuts in 2014 Corvette, *in* 'Materials Australia', Materials Australia.

Bak, C., Gaunaa, M., Andersen, P., Buhl, T., Hansen, P., Clemmensen, K. & Moeller, R. 2007, Wind tunnel test on wind turbine airfoil with adaptive trailing edge geometry, *in* '-', Vol. 45.

Baker, J., Standish, K. & Dam, C. V. 2005, 'Two-dimensional wind tunnel

and computational investigation of a microtab modified s809 airfoil', *43th AIAA/ASME, 2005* **-**, *–*.

Barlas, T. & Kuik, G. 2007, 'State of the art and prospectives of smart rotor control for wind turbines', *Journal of Physics: Conference Series* **75**, 1–20.

Beigy, H. & Meybodi, M. 2009, 'A learning automation based algorthm for determination of the number of hidden units for theree -layer networks', *International ournal and System Science* **40**, 101–118.

Besseghini, S., Villa, E. & Tuissi, A. 1999, 'NiTiHf shape memory alloy: effect of aging and thermal cycling', *Materials Science and Engineering* **A27**, 390–394.

BP Energy outlook 2030 2013,

Brondsted, P., Lilholt, H. & Lystrup, A. 2005, *Composite materials for wind power turbine blades*, -.

Buehler, W., Gilfrich, J. & Wiley, R. 1963, 'Effect of low temperature phase changes on the mechanical properties of alloys near composition NiTi', *Journal of Applied Physics* **34**, 475–478.

Burton, T., Jenkins, N., Sharpe, D. & Bossanyi, E. 2011, *Wind energy handbook*, John Wiley & Sons, Ltd.

Burton, T., Sharpe, D., Jenkins, N. & Bossanyi, E. 2001, *Wind energy handbook*, John Wiley & Sons.

Cairns, D., Mandell, J., Scott, M. & Maccagnano, J. 1997, Design considerations for ply drops in composite wind turbine blades, *in* 'ASME Wind Energy Symposium, ASME/AIAA'.

Caprile, C., Sala, G. & Buzzi, A. 1995, 'Environmental and mechanical fatigue of wind turbine blades made of composites materials', *Journal of Reinforced Plastics and Composites* **15**, 673–691.

Chang, L. & Read, T. 1951, 'Plastic deformation and diffusionless phase changes in metals - the gold-cadmium beta phase', *Transaction of the American Institute of Mining, Metallurgical and Petroleum Engineers* **191**, 47–52.

Chopra, I. 2002, 'Review of state of art of smart structures and integrated system', *American Insitute of Aeronaitics and Astronautics Journal* **40**, 2145–2187.

Churchill, C., Shaw, J. & Ladicola, M. 2009, 'Tips and tricks or characterizing shape memory alloy wire: Part 2 - fundamental isothermal responses', *Experimental Techniques* **33**, 51–62.

Composites, A. 2011, *Kinetix laminating/r240 high performance.*

D3039/3039M, A. 2008, 'Standard test method for tensile properties of polymer matrix composite materials D 3039/D 3039M 08'.

Dahl, K., Fuglsang, P. & Antoniou, I. 1999, 'Experimental verifications of the new Riso-A1 airfoil family for wind turbines', *Proceeding of EWEC* **-**, 85–88.

Dam, V., Mayda, E., Chao, D., Jackson, K., Zuteck, M. & Berry, D. 2005, 'Innovative structural and aerodynamic design approaches for large wind turbine blades', *ASME/AIAA Wind Energy Symposium* **0973**, –.

Daniel, A., Calin, M., Ion, V., Marius, T. & Cornel, M. 2010, 'Contributions to design of systems actuated shape memory active elements', *World Academy of Science, Engineering and Technology* **7**, 222–227.

Delft, D., Winkel, G. & Joosse, P. 1997, Fatigue behaviour of fibre glass wind turbine blade material under variable amplitude loading, *in* 'Proc. AIAA/ASME Wind Energy Symposium, no. AIAA-97-0951'.

Duerig, T. 1999, *Shape Memory Actuators for Automotive Applications in: Engineering Aspects of Shape Memory Alloys*, Stoneham, Massachusetts: Butterworth-Heinemann.

Eggleston, D. & Stoddard, F. 1987, *Wind turbine engineering design*, RV Nostrand.

Eker, B., Ovan, A. & Vardar, A. 2006, 'Using of composite material in wind turbine blades', *Journal of Applied Sciences* **6**, 2917–2921.

Enekl, B., Klopper, V. & Preibler, D. 2002, Full scale rotor with piezoelectric actuated blade flaps, *in* '-', Vol. 28.

Epaarachchi, J. 2006, 'A study on estimation of damage accumulation of glass fibre reinforce plastic (gfrp) composites under a block loading situation', *Composite Structures* **75**, 88–92.

Epaarachchi, J. & Clausen, P. 2006, 'The development of a fatigue loading spectrum for small wind turbine blades', *Journal of Wind Engineering and Industrial Aerodynamics* **94**, 207–223.

EWEA 2006, 'No Fuel: Wind power without fuel, EWEA Campaign'.

EWEA 2009, 'Wind energy - the facts, a guide to the technology, economics and future of wind power'.

F2004, S. A. 2010, 'Standard test method for transformation temperature of nickel-titanium alloys by thermal analysis'.

Flexinol 2010, Technical characteristics of flexinol actuator wires, Technical report, Dynaalloy.

Galileo, G. 1638, *Discourses and mathematical demonstrations relating to two new sciences*, Galileo.

Glauert, H. 1983, *The element of airfoil and airscrew theory*, Cambridge University Press.

Golding, E. 1976, *The generation of electricity by wind power*, A Halsted Press Book; Second edition London.

Gourieres, L. 1982, *Wind power plants: theory and design*, Pergamon Press, New York.

Greninger, A. & Mooradian, V. 1938, 'Strain Transformation in Metastable Beta Copperzinc and Beta Copper-tin Alloys', *Transaction of the American Institute of Mining, Metallurgical and Petroleum Engineers (Trans AMIE)* **128**, 337–368.

Griffth, D. & Ashwill, D. 2011, The Sandia 100 m all-glass baseline wind turbine blade, Technical report, Sandia National Laboratories, Report.

Grujicic, M., Arakere, G., Subramaniam, E., Sellapan, V., Vallejo, A. & Oze, M. 2010, 'Structural responce analysis, fatigue-life prediction, and material selection for 1MW HAWT wind blade turbine', *Journal of material engineering and performance* **-**, 790–801.

Hanc, A., Dragan, K., Mcgugan, M. & Uhl, T. 2011, *Structural integrity monitoring of the critical zones in the wind turbine compoiosite vlades with the use of integrated sensors-SESS project:*, -.

Hansen, A. & Butterfield, C. 1993, 'Aerodynamics of HAWT wind turbines', *Annual Review of Fluid Mechanics* **25**, 115–149.

Harrison, R., Hau, E. & Snel, H., eds 2000, *Large wind turbines : design and economics*, Chichester, J. Wiley & Sons.

Hartl, D. & Lagoudas, D. 2007, 'Aerospace applications of shape memory alloys proc. imeche vol. 221 part g: J. aerospace engineering', *Proceeding of IMechE Aerospace Engineering* **221 PART g**, –.

Hau, E. 2006, *Wind turbines: fundamentals, technologies, application, economics*, Springer, Germany.

Hess, J. & Year, J. 1990, 'Review of the source panel technique for flow computation', *Annual Review of Fluid Mechanics* **22**, 255–274.

Hodges, D. & Yu, W. 2007, 'A rigorous, engineer-friendly approach for modelling realistic, composite rotor blades', *Wind Energy* **10**, 179–193.

Hsio, F., Bai, C. & Chong, W. 2013, 'The performance test of three diffrent horizontal axis wind turbine (HAWT) using experimental and numerical methods', *Energied* **6**, 2784–2803.

Huang, W., Liu, Q., He, L. & Yeo, J. 2004, 'Micro NiTi-Si cantilever with three stable positions', *Sensors and Actuators A: Physical* **114**, 118–122.

Huang, W. & Toh, W. 2000, 'Training two-way shape memory alloy by reheat treatment', *Material Science Letter* **19**, 1549–1550.

Hugh, G. 2012, 'Characterisation of composites for wind turbine blades', *Reinforced Plastics* **56 Issue 5**, 34–36.

Jensen, F., Falzon, B., Ankersen, J. & Stang, H. 2006, 'Structural testing and numerical simulation of a 34 m composite wind turbine blade', *Composite Structures* **76**, 52–61.

Jureczko, M., Pawlak, M. & Mezyk, A. 2005, 'Optimization of wind turbine blades', *Material processing and technology* **167**, 473–471.

Kahandawa, G. 2012, Monitoring damage in advanced composite structures using embedded fibre optic sensors, PhD thesis, Faculty of Engineering and Surveying.

Kahandawa, G., Epaarachchi, J., Hao, W. & Lau, K. 2013, 'Prediction of obsolete FBG sensor using ANN for efficient and robust operation of SHM systems', *Key Engineering Materials* **558**, 546–553.

Kovarik, T., Pipher, C. & Hurst, J., eds 1979, *Wind energy*, Domus.

Kudva, J., Sanders, B., JLPinkerton-Floranc & Garcia, E. 2002, 'DARPA/AFRL/NASA Smart Wing program: final overview', *Proceedings of SPIE* **4698**, 37–43.

Kunt, R. & Larsen, G. 2000, 'Reliability based design of wind turbine rotor blades against failure in ultimate loading', *Engineering Structures* **22**, 565–574.

Kurdjumov, G. & Khandros, L. 1949, 'First reports of the thermoelastic behaviour of martensitic phase of Au-Cd alloy', *Proceedings of the Russian Academy of Sciences (Doklady Akedemii Nauk USSSR)* **66**, 211–213.

Lagoudas, D. 2008, *Shape memory alloys: modeling and engineering applications*, Springer.

Lagoudas, D., Entchev, P. & Kumar, P. 2003, 'Thermomechanical characterisation of sma actuators under cyclic loading', *ASME Interntaional Mechanical Engineering Congress and R&D Expo* **-**, –.

Lain, S., Quintero, B. & Lopez, Y. 2010, 'Aeromechanical evaluation of large HAWTs blades', *Journal of Scientific and Industrial Research* **69(2)**, 142–145.

Lange, C. 1996, Probabilistic fatigue methodology and wind turbine reliability, Technical report, Sandia National Laboratory report: SAND96-1246, 1996.

Larsen, T., Hansen, A. & Buhl, T. 2004, 'Aeroelastic effects of large blade deflections for wind turbines', *Proceedings of The Science of Making Torque from Wind* **-**, 237–249.

Lee, A., Ciarlo, D., Krulevitch, P., Lehew, S., Trevino, J. & Northrup, M. 1996, ' A practical microgripper by fine alignment, eutectic bonding and SMA actuation', *Sensors and Actuators A* **54**, 755–759.

Leo, D. 2007, *Engineering analysis of smart material systems*, John Wiley & Sons, Inc.

Mabe, J., Cabell, R. & Butler, G. 2005, 'Design and control of morphing chevron for take-off and cruise noise reduction', *AIAA Aeroacoustics Conference* **26**, 1–15.

Malcolm, D. 2003, 'Market, cost, and technical analysis of vertical and horizontal axis wind turbines', *Global Energy Concepts, Lawrence Berkeley National Laboratory* .

Manwell, J., Mcgowan, J. & Rogers, eds 2009, *Wind energy explained : theory, design and application*, Wiley Chichester, UK.

Mark, B., Martin, T. & Howard, B. 2013, *Neural Network Toolbox R2013a - Users Guide*, The MathWorks, Inc.

Marques, F., Rodrigues, L., Rebolho, D., Caporali, A., Belo, E. & Ortolan, R. 2005, 'Application of time-delay neural and recurrent neural networks for the identification of a hingeless helicopter blade flapping and torsion motions', *Journal of the Brazilian Society of Mechanical Sciences and Engineering* **27**, 97–103.

Melton, K. 1999, *General applications of SMA's and smart materials," in: Shape Memory Materials*, Cambridge, United Kingdom: Cambridge University Press.

Minsky, M. & Papert, S. 1969, *Perceptrons*, Cambridge, MA: MIT Press.

Morgan, C., Gardner, P., Mays, I. & Anderson, M. 1989, The demonstration of a stall regulated 100 kW vertical axis wind turbine, *in* '-', Vol. -, pp. –.

MT-1820, P. K. P. D. M. 2011, Pro's kit professional digital multimeter manual handout, Technical report, Pro's Kit Industries Co. Ltd.

Mukhawana, M. 2006, Effects of thermo-mechanical cycling and aging on quasi-plastic material response exhibited by NiTi shape memory alloys, PhD thesis, MTech (Mechanical Engineering) Cape Peninsula University of Technology.

Muljadi, E., Pierce, K. & Migliore 1989, 'Control strategy for variable-speed, stall-regulated wind turbines', *National Renewable energy laboratory* **-**, –.

Musgrove, P. 2010, *Wind power*, Cambridge University Press.

Nakafuji, D., Dam, C. V., Michel, J. & Morrison, P. 2002, ' Load control for wind turbines - a non-traditional microtab approach', *In 40th AIAA/ASME* **-**, –.

Nelson, V., ed. 2009, *Wind energy : renewable energy and the environment*, CRC, London.

Nii, Q., Zhang, R., Natsuki, T. & Iwamoto, M. 2007, 'Stiffness and vibration of SMA/ER composites with shape memory alloy short fibres', *Composite Structures, 79, 501-507.* **79**, 501–507.

Nitin, T., Mittal, N. & Siraj, A. 2010, 'Design and finite element analysis of horizontal axis wind turbine blade', *International Journal of Applied Engineering Research* **1**, 500–507.

Noel, L. & Bernardete, R. 2001, 'Hybrid learning multi neural architecture', *IEEE International Joint Conference on Neural Networks* **4**, 2788–2793.

Noel, L. & Bernardete, R. 2003, 'An efficient gradient-based learning algorithm applied to neural networks with selective actuation neurons', *Neural Parallel and Scientific Computations* **11**, 253–272.

Nolet, S. 2011, Composite wind blade engineering and manufacturing. TPI Composites, Inc.

Otsuka, K. & Kakeshita, T. 2002, 'Science and technology of shape-memory alloys: new developments', *Materials Research Society* **27(2)**, 91–100.

Otsuka, K. & Ren, X. 2005, 'Physical metallurgy of tini-based shape memory alloys', *Progress in Materials Science* **50**, 511–678.

Parthenios, J., Psarras, G. & Galiotis, C. 2001, 'Adaptive composites incorporating shape memory alloy wires. Part 2: development of internal recovery stresses as a function of activation temperature', *Composites: Part A* **32**, 1735–1747.

Patoor, E., Lagoudas, Brinson, L., Centchev & Gao, X. 2006, 'Shape memory alloys, part I: general properties and modeling of single crystals', *Mechanics of Materials* **38**, 391–429.

Pearson, K. 1895, 'Contributions to the mathematical theory of evolution. ii. skew variation in homogeneous material', *Philosophical Transactions of the Royal Society A: Mathematical, Physical and Engineering Sciences* **186**, 343–414.

Perkins, J. & Hodgson, D. 1999, *The two-way shape memory effect in engineering aspects of shape memory alloys*, Stoneham, Massachusetts, Butterworth-Heinemann.

Peter, J. & Richard, J. 2012, 'Wind Turbine Blade Design: Review', *Energies* **5**, 3425–3449.

Petersen, L. & Davis, O. 2011, 'Manufacturing wind turbine generator blade having a spar'.

Portella, P. 2006, 'Adolf Martens and his contributions to materials engineering', *Federal Institute for Materials Research and Testing* **-**, 1–30.

Pozrikidis, C., ed. 2009, *Fluid dynamics - Theory, computation, and numerical simulation*, Springer Verlag.

Rask, O., Harrison, S., Munday, D., Harris, C., Mihaescu, M. & Gutmark, E. 2007, 'Jet aircraft propulsion noise reduction research at University of Cincinnati', *American Institute of Aeronautics and Astronautics* .

Rasmussen, F. & Hansen, M. 2003, 'Present status of aeroelasticity of wind turbines', *Wind Energy* .

Reed, H. & Abbaschian, R., eds 1992, *Physical metallurgy principles*, PWS-Kent Publishing Company.

Riziotis, V. & Voutsinas, S. 2000, 'Fatigue loads on wind turbines of different control strategies operating in complex terrain ', *Journal of Wind Engineering and Industrial Aerodynamics* **85**, 211–240.

Roth, D., Enenkl, B. & Dietrich, O. 2006, Active rotor control by flaps for vibratyion reduction-full scale demonstator and first flight test results, *in* '-', Vol. 32.

Rumsey, M. & Paquette, J. 2008, Structural health monitoring of wind turbine blades, *in* 'Procceeding of SPIE Smart Sensor Phenomena, Technology, Networks, and Systems', Vol. 6933, p. 15.

Sandra, E., Hans, B. & Mats, L. 2008, 'Evaluation of different turbine concepts for wind power', *Renewable and Sustainable Energy Reviews* **12**, 1419–1434.

Sapuan, S. & Iqbal, M., eds 2010, *Composite materials technology : Neural Network Applications*, CRC Press Taylor and Francis Group.

Shaw, J., Churchill, C. & Ladicola, M. 2008, 'Tips and tricks for characterizing shape memory alloy wire: Part 1 - differential scanning calorimetry and basic phenomena', *Experimental Techniques* **32**, 55–62.

Shimamoto, A., Ohkawara, H. & Nogata, F. 2004, 'Enhancement of mechanical strength by shape memory effect in TiNi fiber-reinforced composites', *Engineering Fracture Mechanics* **71**, 737–746.

Simulia 2012, *ABAQUS release note 6.12*, Dassault Systems.

Slootweg, J., Polinder, H. & Kling, W. 2003, 'Representing wind turbine electrical generating systems in fundamental frequency simulations', *IEEE transactions on energy conversion* **18**, 516–524.

Somers, D. & Tangler, J. 1996, 'Wind tunnel test of the S814 thick root airfoil', *Journal of Solar Energy Engineering* **118**, 217–221.

Song, H., Kubica, E. & Gorbet, R. 2011, 'Resistance modelling of SMA wire actuators', *International Workshop Smart Materials, Structures & NDT In Aerospace Conference* pp. 1–10.

Sorensen, B., Jorgensen, E., Christian, P. & Jensen, F. 2004, Improved design of large wind turbine blade of fibre composites based on studies of scale effects, PhD thesis, Ris National Laboratory Roskilde Denmark.

Spera, D., ed. 2009, *Wind turbine technology : fundamental concepts of wind turbine engineering*, America Society of Mechanical Engineering.

Stoneham, Massachusetts, B.-H. 1999, *Shape memory applictions in space systems*, Stoneham, Massachusetts,Butterworth-Heineman.

Straub, K. 1996, 'A feasibilty study of using smart materials for rotor control', *Smart Materials and Structures* **5**, 1–5.

Strelec, J., Lagoudas, D., Khan, M. & Yen, J. 2003, 'Design and implementation of a shape memory alloy actuated reconfigurable airfoil', *Journal of Intelligent Material Systems and Structures* **14**, 257–273.

Suleman, A. 2001, *Smart structures: application and related technologies*, Springer-Verlag Wien, New York.

Sun, L., Huang, W., Ding, Z., Zhao, Y., Wang, C. C., Purnawali, H. & Tang, C. 2012, 'Stimulus-responsive shape memory materials: A review', *Journal of Materials and Design* **33**, 577 – 640.

Sutherland, H. 1996, 'Frequency domain analysis of the fatige loads on typical wind turbine blades', *Journal of Solar Energy Engineering, Transactions of ASME* **118**, 204.

Svensson, T. 1997, 'Prediction uncertainties at variable amplitude fatigue', *International Journal of Fatigue* **19**, 295–302.

Tangler, J. & Somers, D. 1995, 'NREL Airfoil Families for HAWTs', *American Wind Energy Association* .

Tawfik, M., Sylvain, N., Jeng, J. & Mei, C. 2000, Vibration of laminated composite plates embedded with shape memory alloy at elevated temperatures, *in* 'Industrial and Commercial Applications of Smart Structures Technologies', Vol. 3991, p. 366.

Thompson, S. & Loughlan, J. 2001, 'Enhancing the post-buckling response of a composite panel structure utilising shape memory alloy actuators -a smart structural concept', *Composite Structures* **51**, 21–36.

Timmer, W., Rooy, R. & Jom, R. 1993, 'Wind tunnel results for 25blade airfoil', *Proceeding of of European Wind Energy Conference* **-**, 416–419.

Trethewey, B., Gillespie, J. J. & Wilkins 1990, Interlaminar performance of tapered composite laminates, *in* 'Proceedings of the American Society for Composites, Fifth Technical Conference'.

Tsai, X. & Chen, L. 2002, 'Dynamic stability of a shape memory alloy wire reinforced composite beam', *Composite Structures* **56**, 235–241.

Tsoi, K., Zheng, J. & Anderson, R. 2004, 'Thermomechanical characteristics of shape memory alloy composites', *Materials Science and Engineering* **-**, 299–310.

Umezaki, E. 2000, 'Improvement in separation of SMA/epoxy from matrix in SMA embedded smart structures', *Materials Science and Engineering* **332**, 362–369.

Volk, B. & Lagoudas, D. 2005, Characterisation of high temperature shape memory alloys. Undergraduate Summer Research Grant (USRG) Poster Presentations, Texas A & M University, College Station, TX. 10 August 2005.

Wang, Q. 2007, 'Application of piezoelectric materials on repair of delaminated structures', *The Open Civil Engineering Journal,* **1**, 25–29.

Wasserman, P., ed. 1993, *Advanced methods in neural computing*, John Wiley & Sons.

Wayman, C. & Harrison, J. 1989, 'The origins of the shape memory effect', *Journal of the Minerals, Metals and Materials Society* **41, (9)**, 26–28.

Wayman, C. & Otsuka, K. 1999, *Shape Memory Materials*, Cambridge, Cambridge University Press.

Yi, S. & Gao, S. 2003, 'Experimental study on the anisotropic behaviour of textured NiTi pseudoelastic shape memory alloys', *Materials Science and Engineering* **362**, 107–111.

Yorke, R., ed. 1986, *Electric circuit theory :Applied electricity and electronics*, Pergamon Press.

Zhang, R., Ni, Q., Natsuki, T. & Iwamoto, M. 2007, 'Mechanical properties of composites filled with SMA particles and short fibres', *Composite Structures* **79**, 90–96.

Zheng, Y., Cui, L. & Schrooten, J. 2005, 'Basic design guidelines for SMA/epoxy smart composites', *Materials Science and Engineering* **390**, 139–143.

Appendix A

Mechanical Properties of Specimens of SMA

FLEXINOL®

DYNALLOY, Inc.
Makers of Dynamic Alloys

Technical Characteristics of

FLEXINOL®

Actuator Wires

Flexinol® Actuator Wires are small diameter wires which contract like muscles when electrically driven. Smaller than motors or solenoids, cheaper and generally easier to use, these wires perform physical movement across an extremely wide variety of applications.

Table of Contents

14762 Bentley Circle, Tustin, California 92780 USA 714-436-1206 714-436-0511 fax http://www.dynalloy.com

F1140Rev H

FLEXINOL®

DYNALLOY, Inc.
Makers of Dynamic Alloys

NICKEL - TITANIUM ALLOY PHYSICAL PROPERTIES

1. Density 0.235 lb/in^3 (6.45 g/cm^3)

2. Specific Heat 0.20 BTU/lb * °F (0.2 cal/g * °C))

3. Melting Point 2370 °F (1300 °C)

4. Latent Heat of Transformation 10.4 BTU/lb (5.78 cal/g)

5. Thermal Conductivity 10.4 BTU/hr * ft * °F (0.18 W/cm * °C)

6. Thermal Expansion Coefficient
    Martensite 3.67×10^{-6}/°F (6.6×10^{-6}/°C)
    Austenite 6.11×10^{-6}/°F (11.0×10^{-6}/°C)

7. Electrical Resistivity (approx.)
    Martensite: 32 micro-ohms * in (80 micro-ohms * cm)
    Austenite: 39 micro-ohms * in (100 micro-ohms * cm)
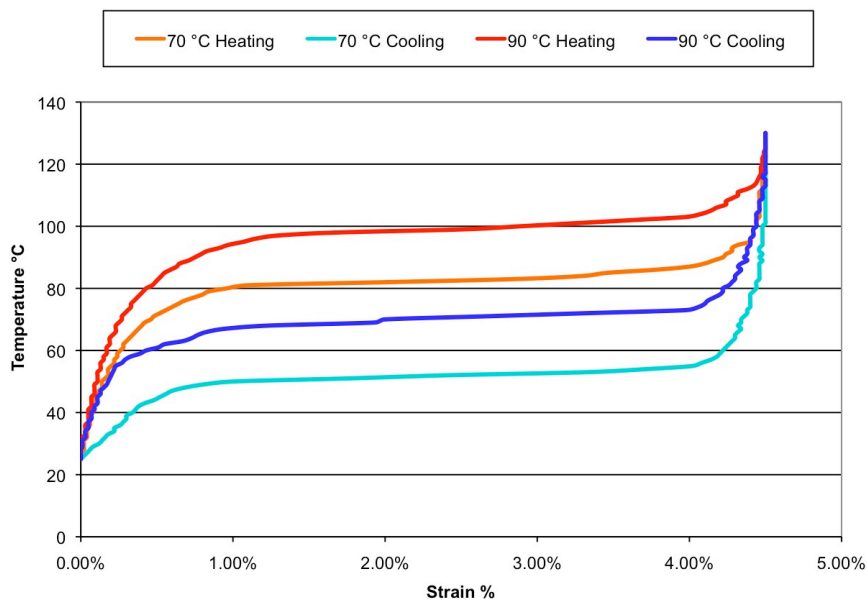
Typical Temperature vs. Strain Characteristics for Dynalloy's standard 158°F (70°C) "LT" and 194°F (90°C) "HT" Austenite start temperature alloys, at 172 MPa

F1140Rev H

FLEXINOL®

Introduction

Flexinol® is a trade name for shape memory alloy actuator wires. Made of nickel-titanium these small diameter wires contract like muscles when electrically driven. This ability to flex or shorten is characteristic of certain alloys that dynamically change their internal structure at certain temperatures. The idea of reaching higher temperatures electrically came with the light bulb, but instead of producing light these alloys contract by several percent of their length when heated and can then be easily stretched out again as they cool back to room temperature. Like a light bulb both heating and cooling can occur quite quickly. The contraction of Flexinol® actuator wires when heated is opposite to ordinary thermal expansion, is larger by a hundredfold, and exerts tremendous force for its small size. The underlying technology that causes the effect is discussed in Section 5. The main point is that movement occurs through an internal "solid state" restructuring in the material that is silent, smooth, and powerful.

This effect can be used in many ways. The list of viable applications is too long for any single listing. A safe assumption is that any task requiring physical movement in a small space with low to moderate cycling speeds is something that most likely will be better done with actuator wires. Many of the tasks currently being done with small motors or solenoids can be done better and cheaper with Flexinol® actuator wires. Since the actuator wires are much smaller for the work they do a number of new products and improved designs on existing products are readily accomplished.

For new users of Flexinol® actuator wires Dynalloy, Inc. strongly recommends that an overview of what can be done first be established. This can be done by obtaining one of the Dynalloy, Inc. kits, which are made for such familiarization. Secondly, new users should consider obtaining from Dynalloy, Inc. or other consultants a "Proof of Concept" working model. This is not only useful as an internal marketing and sales tool, it also helps the new user to see how those with more experience approach the specific task in hand. Knowing this provides immeasurable insight into how to proceed and helps reduce the redundancy of reinventing existing techniques. One can always improve on existing methods and sufficient legal and other safeguards can be readily employed to ensure protection of proprietary ideas.

14762 Bentley Circle, Tustin, California 92780 USA 714-436-1206 714-436-0511 fax http://www.dynalloy.com

FLEXINOL®

Section 1. Movement

The movement or stroke of Flexinol® actuator wire is measured as a percentage of the length of the wire being used and is determined, in part, by the level of stress one uses to reset the wire, or to stretch it in its low temperature phase. This opposing force, used to stretch the wire, is called the bias force. In most applications, the bias force is exerted on the wire constantly, and on each cycle as the wire cools, this force elongates it. If no force is exerted as the wire cools, very little deformation or stretch occurs in the cool, room temperature state and correspondingly very little contraction occurs upon heating. Up to a point the higher the load the higher the stroke. The strength of the wire, its pulling force and the bias force needed to stretch the wire back out are a function of the wire size or cross sectional area and can be measured in pounds per square inch or "psi". If a load of 5,000 psi (34.5 MPa) is maintained during cooling, then about 3% memory strain will be obtained. At 10,000 psi (69 MPa), about 4% results, and with 15,000 psi (103 MPa) and above, nearly 5% is obtained. However, there is a limit to how much stress can be applied.

Far more important to stroke is how the wire is physically attached and made to operate. Dynamics in applied stress and leverage also vary how much the actuator wires move. While normal bias springs that increase their force as the Flexinol® actuators contract have only 3-4% stroke, reverse bias forces which decrease as the actuator wires contract can readily allow the wire to flex up to 7%. Mechanics of the device in which it is used can convert this small stroke into movements over 100% of the wires' length and at the same time provide a reverse bias force. The stress or force exerted by Flexinol® actuator wires is sufficient to be leveraged into significant movement and still be quite strong. Some basic structures, their percent of movement, and the approximate available force they offer in different wire sizes are as follows:

14762 Bentley Circle, Tustin, California 92780 USA 714-436-1206 714-436-0511 fax http://www.dynalloy.com

Normal Bias Spring

Flexinol®
Actuator
Wire

Spring

3% Stroke

Dead Weight Bias

Flexinol®
Actuator
Wire

Weight

4% Stroke

Leaf Spring Bias

Leaf Spring

7% Stroke

Flexinol®
Actuator
Wire

F1140Rev H

FLEXINOL®
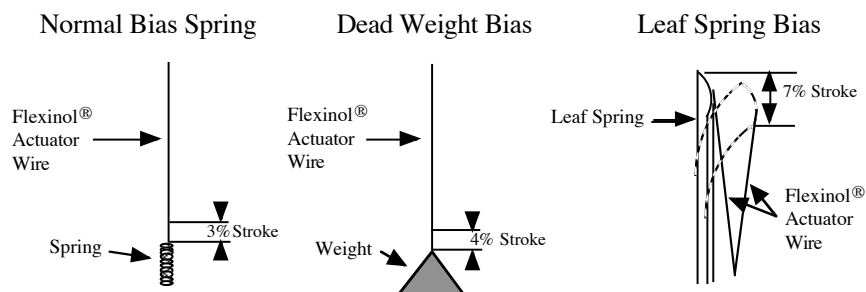
DYNALLOY, Inc.
Makers of Dynamic Alloys

Right Angle Pull
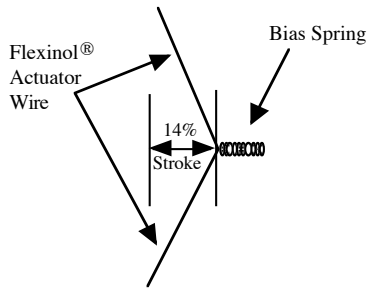
Simple Lever
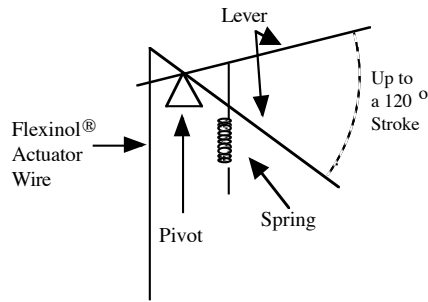
Adjusting Curvature
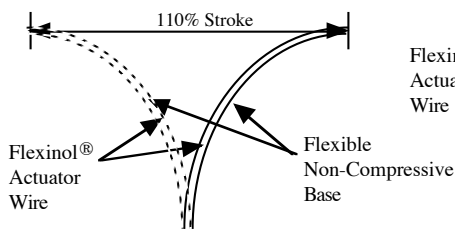
Clam Shell
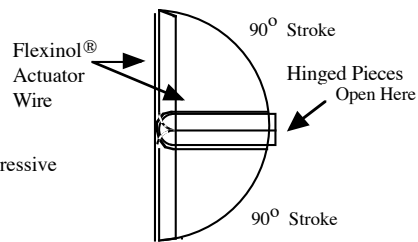
Stroke and Available Force Table

	Approx. Stroke	0.003" Wire (0.076 mm)	0.006" Wire (0.15 mm)	0.010" Wire (0.25 mm)
Normal Bias Spring	3%	0.18 lb (80 g)	0.73 lb (330 g)	2.05 lb (930 g)
Dead Weight Bias	4%	0.18 lb (80 g)	0.73 lb (330 g)	2.05 lb (930 g)
Leaf Spring Bias	7%	0.18 lb (80 g)	0.73 lb (330 g)	2.05 lb (930 g)
Right Angle Pull	14%	0.04 lb (20 g)	0.18 lb (83 g)	0.51 lb (232 g)
Simple Lever (6:1 ex)	30%	0.024lb (11 g)	0.10 lb (47 g)	0.29 lb (133 g)
Adjusting Curvature	110%	0.006 lb (3 g)	0.026 lb (12 g)	0.075 lb (34 g)
Clam Shell	100%	0.007 lb (3.2 g)	0.028 lb (13 g)	0.082 lb (37 g)

14762 Bentley Circle, Tustin, California 92780 USA 714-436-1206 714-436-0511 fax http://www.dynalloy.com

F1140Rev H

5

FLEXINOL®

Section 2. Electrical Guidelines

If Flexinol® actuator wire is used in the appropriate conditions then obtaining repeatable motion from the wire for tens of millions of cycles is reasonable. If higher stresses or strains are imposed, then the memory strain is likely to slowly decrease and good motion may be obtain for only hundreds or a few thousands of cycles. The permanent deformation that occurs in the wire during cycling is heavily a function of the stress imposed and the temperature under which the actuator wire is operating. Flexinol® wire has been specially processed to minimize this straining, but if the stress is too great or the temperature too high some permanent strain will occur. Since temperature is directly related to current density passing through the wire care should be taken to heat, but not overheat, the actuator wire. The following charts give rough guidelines as to how much current and force to expect with various wire sizes.

Diameter Size inches (mm)	Resistance ohms/inch (ohms/meter)	Pull Force* pounds (grams)	Approximate** Current for 1 Second Contraction (mA)	Cooling Time 158°F, 70°C "LT" Wire *** (seconds)	Cooling Time 194°F, 90°C "HT" Wire *** (seconds)
0.001 (0.025)	36.2 (1425)	0.02 (8.9)	45	0.18	0.15
0.0015 (0.038)	22.6 (890)	0.04 (20)	55	0.24	0.20
0.002 (0.050)	12.7 (500)	0.08 (36)	85	0.4	0.3
0.003 (0.076)	5.9 (232)	0.18 (80)	150	0.8	0.7
0.004 (0.10)	3.2 (126)	0.31 (143)	200	1.1	0.9
0.005 (0.13)	1.9 (75)	0.49 (223)	320	1.6	1.4
0.006 (0.15)	1.4 (55)	0.71 (321)	410	2.0	1.7
0.008 (0.20)	0.74 (29)	1.26 (570)	660	3.2	2.7
0.010 (0.25)	0.47 (18.5)	1.96 (891)	1050	5.4	4.5
0.012 (0.31)	0.31 (12.2)	2.83 (1280)	1500	8.1	6.8
0.015 (0.38)	0.21 (8.3)	4.42 (2250)	2250	10.5	8.8
0.020 (0.51)	0.11 (4.3)	7.85 (3560)	4000	16.8	14.0

* The pulling force is based on 25,000 psi (172 MPa), which for many applications is the maximum safe stress for the wire. However, many applications use higher and lower stress levels. This depends on the specific conditions of a given design.

** The contraction time is directly related to current input. The figures used here are only approximate since room temperatures, air currents, and heat sinking of specific devices vary. On small diameter wires (<= 0.006" diameter) currents that heat the wire in 1 second can typically be left on without over-heating it.

*** Approximate cooling time, at room temperature in static air, using a vertical wire. The last 0.5% of deformation is not used in these approximations.

Section 3.   Cycle Time

The contraction of the Flexinol® actuator wire is due solely to heating and the relaxation solely to cooling. Both contraction and relaxation are virtually instantaneous with the temperature of the wire. As a result mechanical cycle speed is dependent on and directly related to temperature changes. Applying high currents for short periods of time can quickly heat the wire. It can be heated so fast in fact that the limiting factor is not the rate at which heating can occur but rather the stress created by such rapid movement. If the wire is made to contract too fast with a load, the inertia of the load can cause over stress to the wire. To perform high speed contractions inertia must be held low and the current applied in short high bursts. Naturally, current which will heat the wire from room temperature to over 212 °F (100 °C) in 1 millisecond, will also heat it much hotter if left on for any length of time.

While each device has quite different heat sinking and heating requirements, a simple rule of thumb test can be used to prevent overheating. Measuring the actual internal temperature of the wire across such short time periods is somewhat problematic, however, one can tell if the actuator wire is overheated simply by observing if the wire immediately begins to cool and relax when the current is shut off or not. If it does not begin to relax and elongate under a small load promptly, when the power is cut, then the wire has been needlessly overheated and could easily be damaged. Simple visual observation is all that is needed to design measured heating circuitry.

Flexinol® actuator wire has a high resistance compared to copper and other conductive materials but is still conductive enough to carry current easily. In fact one can immerse the wire in regular tap water and enough current will readily flow through it to heat it. All of the conventional rules for electrical heating apply to the wire, except that its resistance goes down as it is heated through its transformation temperature and contracts. This is contrary to the general rule of increased resistance with increased temperature. Part of this drop in resistance is due to the shortened wire, and part is due to the fact that the wire gets thicker as it shortens, roughly maintaining its same three-dimensional volume. It makes no difference to the wire whether alternating current, direct current, or pulse width modulated current is used.

Again relaxation time is the same as cooling time. Cooling is greatly affected by heat sinking and design features. The simplest way to improve the speed of cooling is to use smaller diameter wire. The smaller the diameter the more surface to mass the wire has and the faster it can cool. Additional wire, even multiple strands in parallel, can be used in order to exert whatever force is needed. The next factor in improving the relaxation or cooling time is to use higher temperature wire. This wire contracts and relaxes at higher temperatures. Accordingly the temperature differential between ambient or room temperature and the wire temperature is greater and correspondingly the wire will drop below the transition temperature faster in response to the faster rate of heat loss.

Other methods of improved cooling are to use: forced air, heat sinks, increased stress (this raises the transition temperature and effectively makes the alloy into a higher transition temperature wire), and liquid coolants. Combinations of these methods are also effective. Relaxation time can range from several minutes (i.e. delay switches) to fractions of milliseconds (i.e. miniature high speed pumps) by effective and proper heat sinking. The following page gives some idea of the effect these various methods have.

F1140Rev H

Relative Effects of Cooling Methods

	Improvement in Speed
Increasing Stress	1.2:1
Using Higher Temperature Wire	2:1
Using Solid Heat Sink materials	2:1
Forced Air	4:1
Heat Conductive Grease	10:1
Oil Immersion	25:1
Water with Glycol	100:1

*These improvements are not accumulative on the same basis when used together.

Better cooling methods are likely to require more current or heat to move and/or hold the wire in an "on" position. In some cases one may wish to quickly turn the wire on (that is electrically heat it until it contracts) then hold it on for some time. This will likely require a two-step driving current with a larger current to heat the wire and a reduced current to keep it hot without overheating it. There are a number of simple circuits, which will do this.

FLEXINOL®

Section 4. Miscellaneous

Cutting - Flexinol® actuator wire is a very hard and anti-corrosive material. It is so hard that cutting it with cutters designed to cut copper and soft electrical conductors will damage the cutters. If you plan to do much work with Flexinol® actuator wires a good high quality pair of cutters like those used to cut stainless steel wires will be a good investment.

Attaching - Attaching Flexinol® actuator wires to make both a physical and an electrical connection can be done in several ways. It can be attached with screws, wedged onto a PC board, glued into a channel with conductive epoxies, and even tied with a knot. The simplest and best way is usually by crimping or splicing. With crimping machines both electrical wires and hooks or other physical attachments can be joined at once. Flexinol® wires tends to maintain the same volume, so when they contract along their length, they simultaneously grow in diameter. This means the wires expand inside the crimps and hold more firmly as the stress increases through pulling. While this works to the advantage in crimps it can be a disadvantage if glues or solder is used, as the material tends to work itself loose in those cases. Flexinol® wire is a very strong material and is not damaged by the crimping process. Dynalloy, Inc. can provide wire that is already crimped at specified intervals. One can then solder or spot-weld to the crimps if such manufacturing methods are preferred.

Accompanying Materials - Flexinol® actuator wires work by internal resistance or other heating methods. Their temperature is often over 212 °F (100 °C) and they often apply pressure with a high force over a small area of the device they are attached to, so it is a good idea to use temperature resistant materials in connection with them. Such materials if used in direct contact with the wire will also need to be non conductive so as to not provide an electrical path around the Flexinol® actuator wire. Silicone rubber, Kapton (used to make flexible circuit boards), ceramics, and glass are good examples.

Strain Reliefs - Over stress can damage Flexinol® wires by permanently stretching (or elongating) them or by reducing the stroke over which they contract. To prevent this one should design products with strain reliefs in them. Care should also be taken to prevent manual interference with their contraction or movement as this can over stress the wire. In other words if the device gets stuck and cannot move or is forced backwards while operating a problem can be created breaking or adversely affecting the actuator wires' performance. Protective measures against this should be used.

Reverse Biases - Although Flexinol® actuator wire moves about 4.5% when lifting a weight or when contracting against a constant force, one can improve this stroke by designing mechanisms which have a reverse bias force. The bias force is the force that elongates the wire in its rubber-like martensitic phase. A reverse bias force is one that gets weaker as the stroke gets longer. This can be done with leaf springs or with designs that give the Flexinol® actuator wires a better mechanical advantage over the bias spring or force as the stroke progresses.

Performance Margins - Although very stable compared to other similar alloys Flexinol® actuator wires will permanently stretch out or strain with large cycles strokes and high stresses. At stresses below 15,000 psi (103 MPa), permanent strain will remain less than 0.5% strain even after hundreds of thousands of cycles. At 20,000 psi (138 MPa), perhaps 1% permanent strain will occur after 100,000 cycles, and with higher stresses proportionally more will occur.

F1140Rev H

FLEXINOL®

Section 4.   Miscellaneous cont'd.

Good engineering design dictates that one should take into account the amount of memory strain, possible small decreases in the amount of that strain during operation, and some permanent deformation of the wire during cycling if the design is to meet expectations. Pushing all performance aspects of the wire to the limit from the outset of its cycling is likely to lead to disappointment at an early stage in the product life.

Longevity Testing - Flexinol® actuator wire can be over stressed and damaged even though it seems to be working. Much like actual muscles can be strained when called upon to do work above their actual capacity. The device may work in such a way that it is difficult to calculate the actual stresses involved. A good suggestion is to perform life cycle tests before assuming that a device which has worked a few times will continue to work millions more times. Fatigue which is damaging to Flexinol® actuator wire will usually show up in the form of wire elongation or reduced stroke within the first few hundred strokes. As one works with the material a "feel" for what is "working" will develop. The best rule of thumb is to use enough Flexinol® actuator wire to be sure one is well within the parameters in which it can work.

Precise Positioning - Given close temperature control under a constant stress one can get quite precise position control. Control in microns or less is to be expected. The problem is precise temperature control. The temperature is determined by an equilibrium between the rate of heating and the rate of cooling. Heating by electricity makes control of that easy, but the cooling is dynamically affected by changes in room temperature, airflow and so on. In practical terms this means that precise control is usually not feasible unless one can control the heat loss or has dynamic feedback through a closed loop system and can use this to control the heating rate.

Contact Dynalloy, Inc. Freely - There is no practical way for the authors to include everything that has been learned or will be learned in this short document. We have thousands of customers who call and contribute to our general understanding of typical application solutions. In most cases, we have already encountered problems which seem new to the first time user, so whenever possible we are happy to pass on these suggestions and be of help. We want your project to succeed, so please do not hesitate to call for assistance.

F1140Rev H

Section 5. Underlying Technology

Flexinol® is a trade name for very high performance, shape memory alloy, actuator wires. Made of nickel-titanium these small diameter wires have been specially processed to have large, stable amounts of memory strain for many cycles. In other words, they contract like muscles when electrically driven. This ability to flex or shorten is characteristic of certain alloys that dynamically change their internal structure at certain temperatures. Flexinol® wires contract by several percent of their length when heated and then easily elongate again by a relatively small load when the current is turned off and they are allowed to cool.

The function of the Flexinol® wire is based on the shape memory phenomenon which occurs in certain alloys in the nickel-titanium family. When both nickel and titanium atoms are present in the alloy in almost exactly a 50%/50% ratio, the material forms a crystal structure which is capable of undergoing a change from one crystal form to another (a martensitic transformation) at a temperature determined by the exact composition of the alloy. In the crystal form that exists above the transformation temperature (the austenite) the material is high strength and not easily deformed. It behaves mechanically much like stainless steel. Below the transformation temperature, though, when the other crystal form (the martensite) exists, the alloy can be deformed several percent by a very uncommon deformation mechanism that can be reversed when the material is heated and transforms. The low temperature crystal form of the alloy will undergo the reversible deformation fairly easily, so the "memory" strain can be put into the material at rather low stress levels.

The resultant effect of the shape memory transformation of the Flexinol® wire is that the wire can be stretched about 4-5% of its length below its transformation temperature by a force of only 10,000 psi (69 MPa) or less. When heated through the transformation temperature, the wire will shorten by the same 4-5% that it was stretched, and can exert stresses of at least 25,000 psi (172 MPa) when it does so. The transformation temperature of the NiTi alloys can be adjusted from over 212 °F (100°C) down to cryogenic temperatures, but the temperature for the Flexinol® actuator wire has been chosen to be 140 – 230 °F (60 - 110 °C). This allows easy heating with modest electrical currents applied directly through the wire, and quick cooling to below the transformation temperature as soon as the current is stopped. Heating with electrical current is not required, but it is perhaps the most convenient and frequently used form of heat.

Flexinol® actuator wires' prime function is to contract in length and create force or motion when it is heated. There are limits, of course, to how much force or contraction can be obtained. The shape memory transformation has a natural limit in the NiTi system of about 8%. That is the amount of strain that can occur in the low temperature phase by the reversible martensitic twinning which yields the memory effect. Deformation beyond this level causes dislocation movement throughout the structure and then that deformation is not only non-reversible but degrades the memory recovery as well. For materials expected to repeat the memory strain for many cycles, it is best to utilize a cyclic memory strain of no more than 4-5%, and that is what is recommended with Flexinol® actuator wire.

The force that the Flexinol® actuator wire can exert when heated is limited by the strength of the high temperature austenitic phase. The phase transformation, or crystal change, that causes the memory effect has more driving force than the strength of the parent material, so one must use care not to exceed that yield strength. The yield strength of Flexinol®'s high temperature phase is over 50,000 psi (345 MPa), and on a single pull the wire can exert this force. To have repeat cycling, however, one should use no more than 2/3 of this level, and forces of 20,000 psi (138 MPa) or below give the best repeat cycling with minimal permanent deformation of the wire.

F1140Rev H

FLEXINOL®

DYNALLOY, Inc.
Makers of Dynamic Alloys

ACTUATOR WIRE
A SOLID STATE ACTUATOR THAT MOVES BY
"MOLECULAR RESTRUCTURING"!

FOR BETTER MECHANICAL PERFORMANCE...

- In really tight places - Flexinol® actuator wires are smaller by far than alternatives. At least 1,000 times smaller than solenoids for the same work done.

- To simplify designs - Flexinol® actuator wires can often be used "as is", eliminating gear boxes, housings, bearings, and so on. Their flexible forgiving performance is easier to work with.

- In corrosive environments - Flexinol® actuator wires' high corrosion resistance really pays off.

- To reduce noise levels - Flexinol® actuator wires' movement by molecular restructuring is both electrically and acoustically quiet.

- To lower costs - Flexinol® actuator wires are inexpensive to buy and cost less to use in many applications. A nice combination for that bottom line.

SAMPLE APPLICATIONS

ELECTRONICS
Micro Circuit Breakers
PC Mount Relays
Chassis Temp. Controls
Electronic Locks
PC Mount Pilot Valves
Mechanical Latches
Subminiature Door Openers
Micro Manipulators
Retrofit Switch to Relay
Micro Clutches
Spring Loaded Releases
Board Temperature Sensors
"Clean" Actuators
Remote Switch Controllers
Read/Write Head Lifters

MEDICAL
Intravenous Med. Controllers
Steerable Catheters
Prosthetic Limbs
Surgical Instruments
Braille Displays

Vacuum Test Manipulators
Micro Pumps
Blood Pressure Test Valve
Exoskeletal Assistance

AUTOMOTIVE
Door Locks
Environmental Controls
Gear Changing Triggers
Clutch Engagement Triggers
Mirror Controls
Heater Cutoff/Sensors
Pneumatic Valve
Remote Latches
Remote Releases
Alarm Devices

APPLIANCES
Moving Louvers
Spring Releases

Door Openers
Electronic Locks

Mechanical Volt. Regulator
Mechanical Curr. Regulator
Motor Protectors
Box Temperature Control
Overheating Controllers
Hair Dryer Cutoff/Sensors
Safety Cutoffs

MISCELLANEOUS
Ultralight Remote Control
Mechanical Scanners
Camera Manipulators
Magnetic Free Positioners
Manipulator Safety
PC Cutoffs
Fiber Gate
Camera Shutters
Cuckoo Clocks
Alarm Devices Light
Light Fiber Switches
Smart Materials
Mechanical IC's
Robotic Limbs

Flexinol® Actuator Wires are small diameter wires which contract like muscles when electrically driven. Smaller than motors or solenoids, cheaper and generally easier to use, these wires perform physical movement for an extremely wide variety of applications.

14762 Bentley Circle, Tustin, California 92780 USA 714-436-1206 714-436-0511 fax http://www.dynalloy.com

F1140Rev H

Appendix B

Mechanical Specification of GFRP Specimens

Table B.1: Tensile test for part 1 : 4 plies

Sample	mass (g)	length (mm)	thickness(mm)			width(mm)		
1	17.4	250	2.38	1.93	2.05	25	25	25
2	19.4	250	2.79	1.97	2.03	25	25	25
3	18.9	250	2.38	1.93	2.37	25	25	25
4	19.7	250	2.55	1.95	1.94	25	25	25
5	20.8	250	2.48	2.73	2.41	25	25	25

Table B.2: Tensile test for part 2 : 8 plies

Sample	mass (g)	length (mm)	thickness(mm)			width(mm)		
1	42.3	290	4.29	3.94	4.39	25	25	25
2	43.6	290	4.67	3.98	4.16	25	25	25
3	42.9	290	4.44	3.76	4.82	25	25	25
4	39.1	290	4.01	3.72	4.18	25	25	25
5	38.8	290	4.59	3.82	3.98	25	25	25

Table B.3: Tensile test for part 3 : 12 plies

Sample	mass (g)	length(mm)	thickness(mm)			width(mm)		
1	66.7	290	6.29	6.47	5.38	25	25	25
2	67.2	290	6.10	6.33	6.28	25	25	25
3	69.8	290	6.27	6.16	5.48	25	25	25
4	69.2	290	6.18	5.94	6.35	25	25	25
5	69.7	290	4.59	3.79	3.84	25	25	25

STRUCTURAL TESTING SERVICES
Centre of Excellence in Engineered Fibre Composites
USQ | West Street | Toowoomba | Qld | 4350
Reception tel : 07 4631 2548   fax : 07 4631 2110
web : www.fcdd.com.au

structural testing services

Test ID #:
Report Date: 31/05/2012

TENSILE TESTING REPORT
ISO 527-4/2/2: 1997 Plastics – Determination of Tensile Properties

Test Date:	**Test Method:**	**Operator:**
31/05/2012	Laminate Tension - Biaxial Ext (ISO 527).msm	ERIS SUPENI

Sample Information:

(A) Sample Info Line 1:	4P
(B) Sample Info Line 2:	S1
(C) Sample Info Line 3:	UNIDIRECTIONAL
(D) Sample Info Line 4:	0/90/-45/45
(E) Specimen Orientation:	0 Degrees
(F) Testing Speed (mm/min):	2

Test Equipment Details:

Test Machine:	MTS 810 Material Test System
Location:	Z104 Test Laboratory, Faculty of Engineering and Surveying, USQ
Accuracy Grading:	Grade A
Machine Calibration Date:	15/02/2007
Expiration Date:	15/02/2008
Strain Measurement Device:	MTS Extensometer Model No. 632.85F-14
Extensometer Calibration Date:	15/02/2007
Load Cell Calibration Date:	15/02/2007
Expiration Date:	15/02/2008

Specimen Results:

Specimen #	Thickness 1 mm	Thickness 2 mm	Thickness 3 mm	Width 1 mm	Width 2 mm	Width 3 mm	Avg Thick mm	Avg Width mm	Area mm^2
1	2.38	1.93	2.03	25.00	25.00	25.00	2.11	25.00	52.83
2	2.79	1.97	2.03	25.00	25.00	25.00	2.26	25.00	56.58
3	2.09	2.23	2.37	25.00	25.00	25.00	2.23	25.00	55.75
4	2.55	1.95	1.94	25.00	25.00	25.00	2.15	25.00	53.67
5	2.48	2.73	2.41	25.00	25.00	25.00	2.54	25.00	63.50
Mean	**2.46**	**2.16**	**2.16**	**25.00**	**25.00**	**25.00**	**2.26**	**25.00**	**56.47**
Std Dev	**0.26**	**0.34**	**0.22**	**0.00**	**0.00**	**0.00**	**0.17**	**0.00**	**4.21**

Specimen Results:

Specimen #	Peak Load N	Peak Stress MPa	Modulus of Elasticity MPa	Poisson's Ratio mm/mm					
1	8318	157.43	11267	0.379					
2	8261	146.00	11273	0.341					
3	7843	140.69	9774	0.198					
4	9769	182.03	11989	0.298					
5	7313	115.16	10229	0.322					
Mean	**8301**	**148.26**	**10906**	**0.308**					
Std Dev	**914**	**24.41**	**892**	**0.068**					

Specimen Comments:

Specimen #	Failure Status
1	Acceptable
2	Acceptable
3	Acceptable
4	Acceptable
5	Acceptable

Load vs Extension Plot

Checked By: **Wayne Cromwell**

Authorised Signature: _____ **Date:** _____

STRUCTURAL TESTING SERVICES
Centre of Excellence in Engineered Fibre Composites
USQ | West Street | Toowoomba | Qld | 4350
Reception tel : 07 4631 2548   fax : 07 4631 2110
web : www.fcdd.com.au

structural testing services

Test ID #:
Report Date: 31/05/2012

TENSILE TESTING REPORT
ISO 527-4/2/2: 1997 Plastics – Determination of Tensile Properties

Test Date:	**Test Method:**	**Operator:**
31/05/2012	Laminate Tension - Biaxial Ext (ISO 527).msm	ERIS SUPENI

Sample Information:

(A) Sample Info Line 1:	8P
(B) Sample Info Line 2:	S2
(C) Sample Info Line 3:	UNIDIRECTIONAL
(D) Sample Info Line 4:	0/90/-45/45/-45/45/-45/45
(E) Specimen Orientation:	0 Degrees
(F) Testing Speed (mm/min):	2

Test Equipment Details:

Test Machine:	MTS 810 Material Test System
Location:	Z104 Test Laboratory, Faculty of Engineering and Surveying, USQ
Accuracy Grading:	Grade A
Machine Calibration Date:	15/02/2007
Expiration Date:	15/02/2008
Strain Measurement Device:	MTS Extensometer Model No. 632.85F-14
Extensometer Calibration Date:	15/02/2007
Load Cell Calibration Date:	15/02/2007
Expiration Date:	15/02/2008

Specimen Results:

Specimen #	Thickness 1 mm	Thickness 2 mm	Thickness 3 mm	Width 1 mm	Width 2 mm	Width 3 mm	Avg Thick mm	Avg Width mm	Area mm^2
1	4.29	3.94	4.39	25.00	25.00	25.00	4.21	25.00	105.17
2	4.67	3.98	4.16	25.00	25.00	25.00	4.27	25.00	106.75
3	4.00	3.76	4.82	25.00	25.00	25.00	4.19	25.00	104.83
4	4.00	3.82	3.98	25.00	25.00	25.00	3.93	25.00	98.33
5	4.59	3.82	3.98	25.00	25.00	25.00	4.13	25.00	103.25
6	4.59	3.79	3.84	25.00	25.00	25.00	4.07	25.00	101.83
Mean	**4.36**	**3.85**	**4.20**	**25.00**	**25.00**	**25.00**	**4.13**	**25.00**	**103.36**
Std Dev	**0.31**	**0.09**	**0.36**	**0.00**	**0.00**	**0.00**	**0.12**	**0.00**	**2.98**

Specimen Results:

Specimen #	Peak Load N	Peak Stress MPa	Modulus of Elasticity MPa	Poisson's Ratio mm/mm				
1	18151	172.59	10861	0.386				
2	19998	187.33	10933	0.398				
3	16538	157.76	10957	0.416				
4	18411	187.23	11772	0.406				
5	13681	132.51	10255	0.390				
6	18834	184.95	11193	0.426				
Mean	**17602**	**170.40**	**10995**	**0.404**				
Std Dev	**2223**	**21.83**	**493**	**0.015**				

Specimen Comments:

Specimen #	Failure Status
1	Acceptable
2	Acceptable
3	Acceptable
4	Acceptable
5	Acceptable
6	Acceptable
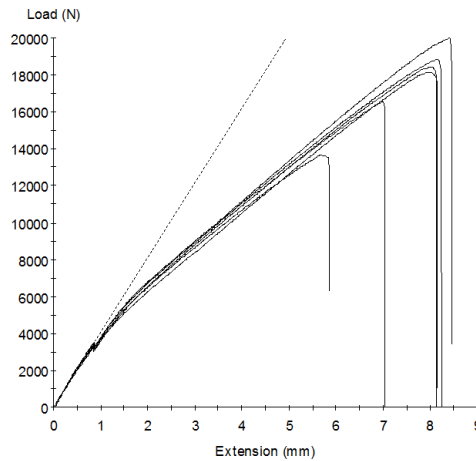
Load vs Extension Plot

Checked By: **Wayne Cromwell**

Authorised Signature: _____   **Date:** _____

STRUCTURAL TESTING SERVICES
Centre of Excellence in Engineered Fibre Composites
USQ | West Street | Toowoomba | Qld | 4350
Reception tel : 07 4631 2548   fax : 07 4631 2110
web : www.fcdd.com.au

Test ID #:
Report Date: 31/05/2012

TENSILE TESTING REPORT
ISO 527-4/2/2: 1997 Plastics – Determination of Tensile Properties

Test Date:
31/05/2012

Test Method:
Laminate Tension - Biaxial Ext (ISO 527).msm

Operator:
ERIS SUPENI

Sample Information:

(A) Sample Info Line 1:	12P
(B) Sample Info Line 2:	S3
(C) Sample Info Line 3:	UNIDIRECTIONAL
(D) Sample Info Line 4:	0/90/-45/45/-45/45/-45/45/90/0/90/0/-45/45
(E) Specimen Orientation:	0 Degrees
(F) Testing Speed (mm/min):	2

Test Equipment Details:

Test Machine:	MTS 810 Material Test System
Location:	Z104 Test Laboratory, Faculty of Engineering and Surveying, USQ
Accuracy Grading:	Grade A
Machine Calibration Date:	15/02/2007
Expiration Date:	15/02/2008
Strain Measurement Device:	MTS Extensometer Model No. 632.85F-14
Extensometer Calibration Date:	15/02/2007
Load Cell Calibration Date:	15/02/2007
Expiration Date:	15/02/2008

Specimen Results:

Specimen #	Thickness 1 mm	Thickness 2 mm	Thickness 3 mm	Width 1 mm	Width 2 mm	Width 3 mm	Avg Thick mm	Avg Width mm	Area mm^2
1	6.29	6.47	5.38	25.00	25.00	25.00	6.05	25.00	151.17
2	6.10	6.33	6.28	25.00	25.00	25.00	6.24	25.00	155.92
3	6.27	6.16	5.48	25.00	25.00	25.00	5.97	25.00	149.25
4	6.18	5.94	6.35	25.00	25.00	25.00	6.16	25.00	153.92
5	5.80	6.42	5.33	25.00	25.00	25.00	5.85	25.00	146.25
6	5.72	6.50	5.31	25.00	25.00	25.00	5.84	25.00	146.08
Mean	**6.06**	**6.30**	**5.69**	**25.00**	**25.00**	**25.00**	**6.02**	**25.00**	**150.43**
Std Dev	**0.24**	**0.22**	**0.49**	**0.00**	**0.00**	**0.00**	**0.16**	**0.00**	**4.01**

Specimen Results:

Specimen #	Peak Load N	Peak Stress MPa	Modulus of Elasticity MPa	Poisson's Ratio mm/mm				
1	26267	173.76	12827	0.390				
2	30570	196.07	12705	0.375				
3	29347	196.63	13353	0.352				
4	29184	189.61	13642	0.397				
5	33206	227.05	14046	0.397				
6	17033	116.60	10955	0.345				
Mean	**27601**	**183.29**	**12921**	**0.376**				
Std Dev	**5643**	**36.97**	**1086**	**0.023**				

Specimen Comments:

Specimen #	Failure Status
1	Acceptable
2	Acceptable
3	Acceptable
4	Acceptable
5	Acceptable
6	Acceptable

Load vs Extension Plot
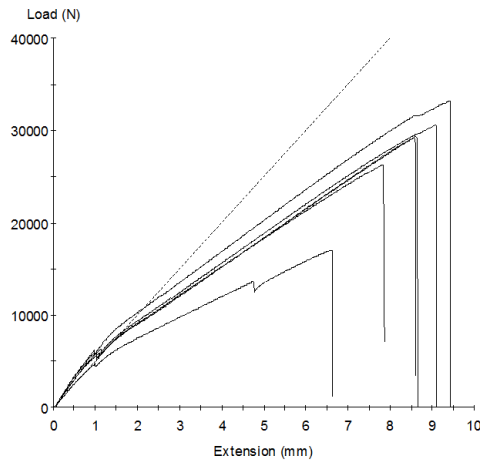
Checked By: **Wayne Cromwell**

Authorised Signature: _____   **Date:** _____

STRUCTURAL TESTING SERVICES
Centre of Excellence in Engineered Fibre Composites
USQ | West Street | Toowoomba | Qld | 4350
Reception tel : 07 4631 2548 fax : 07 4631 2110
web : www.fcdd.com.au

structural testing services

Test ID #: STS-06-109-T
Report Date: 28/05/2012

TENSILE TESTING REPORT

ASTM Designation: ASTM D1623-03
Standard Test Method for Tensile and Tensile Adhesion Properties of Rigid Cellular Plastics
Modified Type A Specimen

Test Date·
26/05/2012

Test Method:
STS - Foam Tension (ASTM D1623).msm

Operator:
Wayne Crowell

Sample Information:

(A) Client Name:	Huntsman Composites
(B) Mailing Address:	Unit 4/61 Brandl Street
(C) Mailing Address:	Eight Mile Plains
(D) Mailing Address:	Qld 4113
(E) Attention:	Julie Woolley
(F) Phone:	07 33408644
(G) Fax:	07 33408601
(H) Client Job ID:	Foam Sample (White)
(I) STS Job Number:	STS-06-109-T
(J) Sample Description:	Foam Sample
(L) Nominal Specimen Gage Length:	40mm
(M) Test Room Conditions:	21°C, 65% RH
(N) Sample Conditioning:	23°C, 50% RH Constant for 88 Hours
(O) Test Speed (mm/min):	6

Test Equipment Details:

Test Machine:	MTS Alliance RT/10
Location:	P9 110 Test Laboratory, Fibre Composites Research Centre, USQ
Accuracy Grading:	Grade A
Machine Calibration Date:	23/05/2006
Expiration Date:	23/05/2007
Strain Measurement Device:	MTS Extensometer - Model LX300
Strain Calibration Date:	23/05/2006
Expiration Date:	23/05/2007
Load Cell Calibration Date:	23/05/2006
Expiration Date:	23/05/2007

Specimen Results:

Specimen #	Thick-ness 1 mm	Thick-ness 2 mm	Thick-ness 3 mm	Width 1 mm	Width 2 mm	Width 3 mm	Avg Thick mm	Avg Width mm	Area mm^2
1	18.98	19.06	19.02	24.28	24.24	24.47	19.02	24.33	462.76
2	18.95	18.95	18.94	24.07	24.17	24.13	18.95	24.12	457.06
3	18.96	19.00	18.91	25.03	24.91	24.81	18.96	24.92	472.34
4	19.59	19.56	19.52	25.10	25.17	25.09	19.56	25.12	491.26
5	19.52	19.57	19.56	24.51	24.60	24.59	19.55	24.57	480.28
Mean	19.20	19.23	19.19	24.60	24.62	24.62	19.21	24.61	472.74
Std Dev	0.33	0.31	0.32	0.45	0.43	0.36	0.32	0.41	13.65

Specimen Results:

Specimen #	Peak Load N	Peak Stress MPa	% Strain At Peak %	% Strain At Break %	Elastic Modulus MPa				
1	342	0.74	10.96	10.96	21.8				
2	365	0.80	12.49	12.49	26.3				
3	371	0.79	9.42	9.42	26.5				
4	383	0.78	11.64	11.64	25.7				
5	397	0.83	11.89	11.89	22.2				
Mean	372	0.79	11.28	11.28	24.5				
Std Dev	21	0.03	1.18	1.18	2.3				

Specimen Comments:

Specimen #	Failure Status
1	Acceptable
2	Acceptable
3	Acceptable
4	Acceptable
5	Acceptable
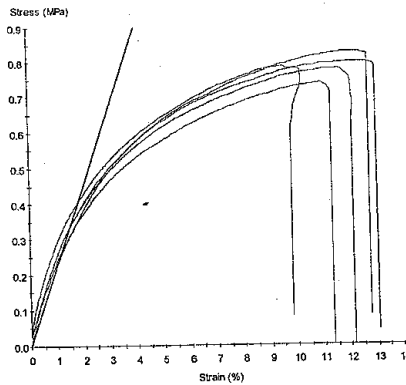
Stress vs Strain Plot

Appendix C

Test Rig Design

-Right View-

-Top View-

-Front View-
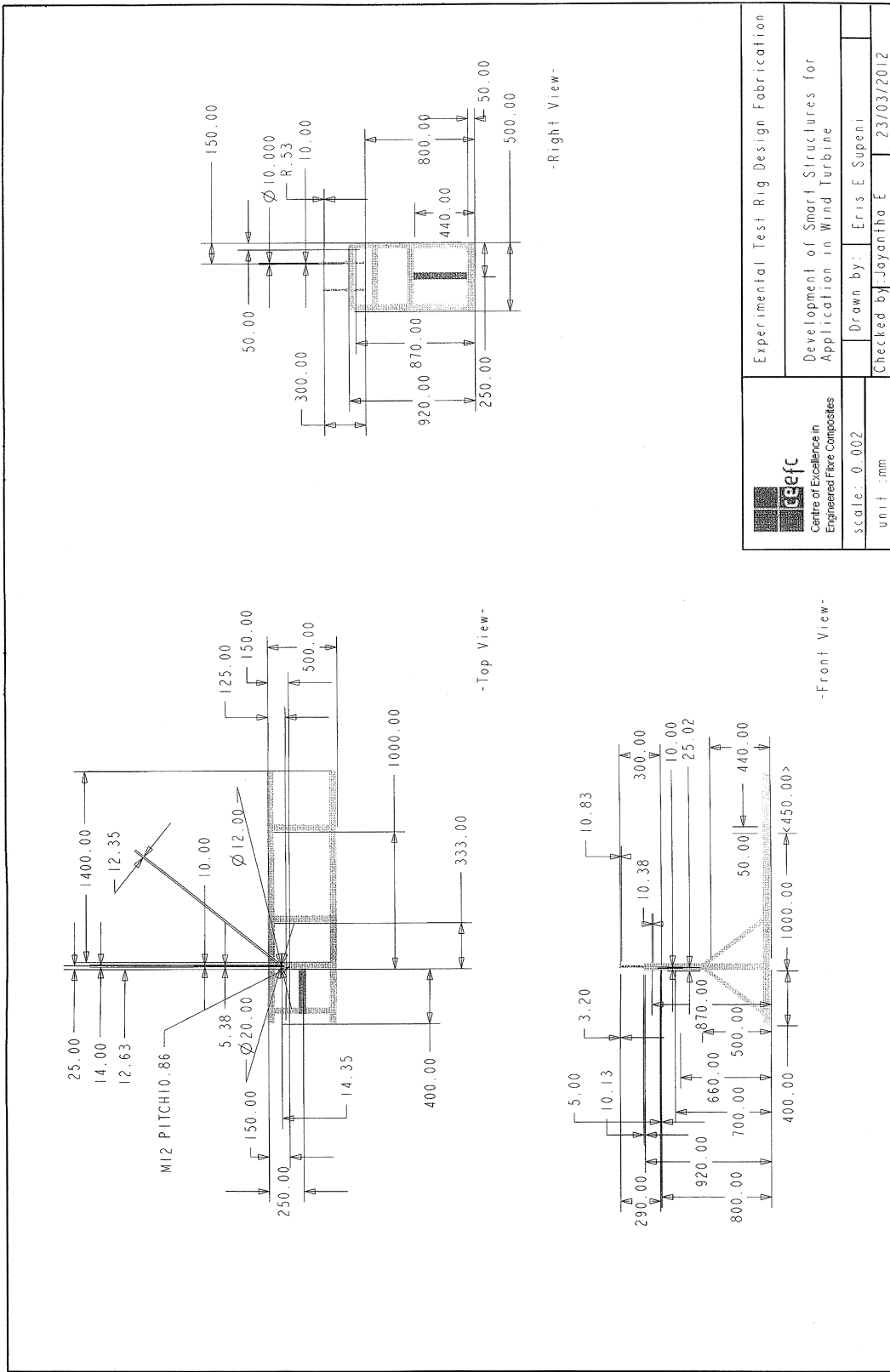
Experimental Test Rig Design Fabrication

Development of Smart Structures for
Application in Wind Turbine

Drawn by: Eris E Supeni

Checked by: Jayantha E   23/03/2012

cefc
Centre of Excellence in
Engineered Fibre Composites

scale: 0.002

unit :mm
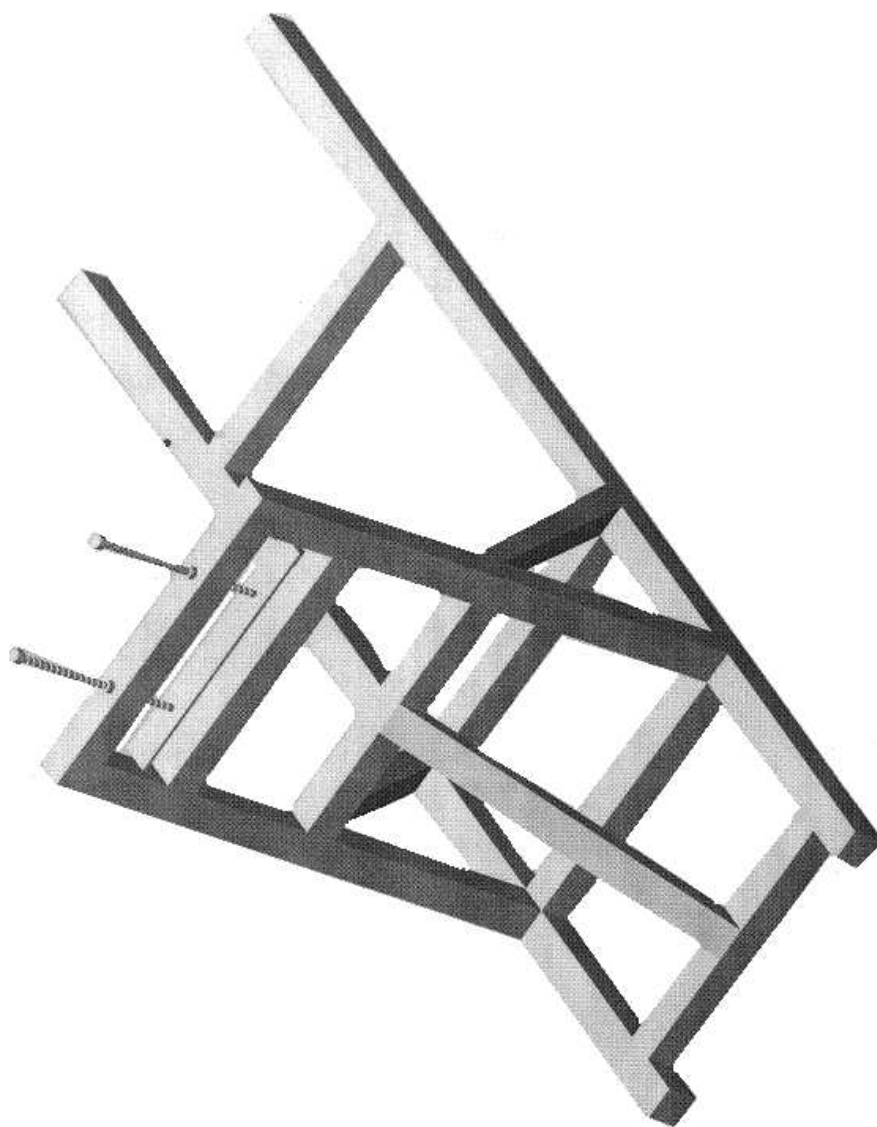
Appendix D

DC Power 1 Supply Unit

TRIPLE OUTPUT LINEAR D.C. POWER SUPPLY

The GPC-Series are triple output, 195 to 375W, linear DC power supplies. Channel 1 and 2 are fully adjustable (model dependant) and channel 3 is fixed at 5V/3A with ripple and noise at less than 2mVrms. Overload and reverse polarity protection keep GPC-Series and its loads safe from unexpected conditions. The GPC-3030DQ contains a temperature controlled cooling fan for thermal protection. The GPC features continuous or dynamic internal load selection and series or parallel tracking for application flexibility. The GPC-Series is an ideal solution for inexpensive bench-top applications requiring low noise and multiple outputs.

GPC-1850D/3030D/3060D/6030D

Patent No: 81011
(Note: GPC-3060D/6030D are not CE appoved.)

GPC-3030DQ

CE

FEATURES

* Four Digital Panel Meters (GPC-3030DQ)
* Triple Output
* Auto Tracking
* Auto Series and Parallel Operation
* Constant Voltage and Constant Current Operation
* Low Ripple and Noise
* Internal Select for Continuous or Dynamic Load
* Overload and Reverse Polarity Protection
* 3 1/2 Digits 0.39" LED Display(GPC-3030DQ)
* 3 1/2 Digits 0.5" LED Display(GPC-1850D/ 3030D/3060D/6030D)
* 5V, 3A Fixed Output

POWER SUPPLIES

SPECIFICATIONS

OPERATION MODE

Independent	Two independent outputs and 5V fixed output
	Output from 0 to rating volts and 0 to rating amperes
Series	Output from 0 to ± rating volts at rating amperes each
	Output from 0 to double rating volts at rating amperes
Parallel	Output from 0 to double rating amperes at rating volts

CONSTANT VOLTAGE OPERATION

Regulation	Line regulation≦0.01% + 3mV
	Load regulation≦0.01% + 3mV (rating current≦3A)
	≦ 0.01% + 5mV(rating current ≦10A)
	≦ 0.02% + 5mV (rating current ≧10A)
Ripple & Noise	≦1mVrms 5Hz ~ 1MHz
Recovery Time	≦100μS (50% Load change, Minimum load 0.5A)

CONSTANT CURRENT OPERATION

Regulation	Line regulation≦0.2% + 3mA
	Load regulation ≦0.2% + 3mA (for GPC-1850D/GPC-3030D/GPC-3030DQ)
	Load regulation ≦0.2% + 5mA (for GPC-3060D/GPC-6030D)
Ripple Current	≦3mArms

5V FIXED OUTPUT

Regulation	Line regulation ≦5mV
	Load regulation ≦10mV
Ripple & Noise	≦2mVrms
Voltage Accuracy	5V±0.25V
Output Current	3A

TRACKING OPERATION

Tracking Error	≦ 0.5% + 10mV of the master
Series Regulation	≦ 300mV

METER

Digital	3½ digits 0.5" LED display
	3½ digits 0.39" LED display (for GPC-3030DQ)
	Accuracy±(0.5% of rdg + 2 digits)

INSULATION

Chassis and Terminal	20MΩ or above (DC 500V)
	100MΩ or above (DC 1000V)(for GPC-3060D/6030D)
Chassis and AC Cord	30MΩ or above (DC 500V)
	100MΩ or above (DC 1000V)(for GPC-3060D/6030D)

POWER SOURCE
AC 100V/120V/220V/240V±10%, 50/60Hz

DIMENSIONS
255(W) x 145(H) x 346(D) mm

ORDERING INFORMATION

Model		Independent	Series	Parallel	Weight (kg)
GPC-1850D	195W D.C. Power Supply	(0 ~ 18V/0 ~ 5A) x 2 , (5V/3A MAX) x 1	36V 5A	18V 10A	11.5
GPC-3030D	195W D.C. Power Supply	(0 ~ 30V/0 ~ 3A) x 2 , (5V/3A MAX) x 1	60V 3A	30V 6A	11.5
GPC-6030D	375W D.C. Power Supply	(0 ~ 60V/0 ~ 3A) x 2 , (5V/3A MAX) x 1	120V 3A	60V 6A	18.5
GPC-3060D	375W D.C. Power Supply	(0 ~ 30V/0 ~ 6A) x 2 , (5V/3A MAX) x 1	60V 6A	30V 12A	18.5
GPC-3030DQ	195W D.C. Power Supply	(0 ~ 30V/0 ~ 3A) x 2 , (5V/3A MAX) x 1	60V 3A	30V 6A	11.5

ACCESSORIES :
User manual x 1 , Power cord x 1
Test lead GTL-105 x 1 (≦ 3A) or GTL-104 x 2 (≦10A)
European test lead GTL-203 x 1 (≦ 3A)or GTL-204 x 2 (≦10A)

OPTIONAL ACCESSORIES
GRA-401 Rack Adapter Panel

Appendix E

DC Power 2 Supply Unit

SPS-Series

High Current with Remote Sensing & Control
Switching Mode DC Regulated Power Supply

SPS-9600

Description

This high current switching mode DC regulated output power supply is designed with a highly efficient active power factor correction. The constant current limiting protection allows the output current to remain stable but the output voltage decreases to a level that permits safe operation of the power supply.

The remote sensing terminals are used to compensate for output line losses so that a precise regulation can be achieved for critical voltage application away from the power supply.

The output voltage level and ON-OFF can be externally controlled via the remote terminal.

It is ideal for applications that need good quality high DC current network with precise point of voltage regulation.

SPS-9600 / SPS-9602 has a small footprint for its 900W continuous maximum power.

It is suitable for a wide range of applications such as street blaster super high power car audio demonstration console, radio equipment and etc.

Features

- ◻ Total max. continuous output current 60A (SPS-9600) / 30A (SPS-9602)
- ◻ Main Output / Remote Sensing / Remote Control / terminals at the back
- ◻ Front terminals 5A (SPS-9600) / 3A (SPS-9602) limiting.
- ◻ (Precise Load Point Voltage)
- ◻ Remote Sensing for remote point of regulation.
- ◻ Remote control terminals for output voltage adjustment and *on/off*
- ◻ 29HR Count Down Timer (Optional) for Output ON/OFF
- ◻ Floating Ground Design
- ◻ Overload / Over-temperature / Short Circuit Protections
- ◻ Constant Current mode with LED indicator prevents overloading
- ◻ Variable speed thermally controlled fan
- ◻ High RFI stability
- ◻ Active power factor correction (P.F. >0.97)
- ◻ Housing are available in Pantone warm grey 1C or Pantone 433C dark grey
- ◻ Overload protection with constant current
- ◻ Low Ripple & Noise
- ◻ *Remote output on/off is an added function for production after Oct. 2004*

Specifications

Models	SPS-9600	SPS-9602
Variable Output Voltage	1-15VDC	1-30VDC
Total Rated Output Current		
(Main Output + Front Output)	60A	30A
Rated Output Current (Main Output)	60A	30A
Rated Output Current (Front Output)	5A	3A
Load Voltage Regulation (Main Output) 0-100% load	0.1% +5mV	
Line Voltage Regulation (Main Output) 190-254VAC variation	0.05% +3mV	
Ripple & Noise (peak-peak)	50mVp-p	
Input Voltage	200-240VAC 50Hz~ (or on request)	
Efficiency	>85%	
Meter Type	LED Meter	
Volt. Meter Range	3 digit display	
Curr. Meter Range	3 digit display	
Meter's Accuracy	±1% +1 count	
Protection Devices	Overload (Constant Current Limiting), Over Temperature, Short Circuit, OVP Protection	
Cooling System	Variable speed thermally controlled fan (from 1/3 to full speed)	
Special Feature	Remote Sensing, Remote Output Voltage Control and *ON/OFF* *Remote output ON/OFF only for production after Oct. 2004*	
Approvals	CE EMC: EN 55022 LVD: EN 60950	
Dimensions (WxHxD)	220x110x360 mm 8.7x4.3x14 inch	
Weight	Approx. 5.8 kgs 12.8 lbs	
Remarks	Power factor correction >0.95 at optimal load	

◻ All values are based on the Standard ambient Temperature 25℃ and Pressure 0.1Mpa.
◻ SPECIFICATIONS ARE SUBJECT TO CHANGE WITHOUT PRIOR NOTICE

Appendix F

Kinetix Laminating/R240 High Performance

KINETIX R240 is a low viscosity resin specifically formulated for use with H126, H160, H161, H162 hardeners to offer a variety in pot-life and working times as a room temperature laminating system.

Designed for laminating, R240 resin and hardeners produce stronger, stiffer and tougher laminates than conventional general purpose epoxy systems. Excellent mechanical properties are produced in carbon fibre, aramid and fibreglass laminates.

MIX RATIO
25 parts hardener to 100 parts resin by weight

Note: Care should be taken when dispensing and mixing. Do not attempt to control the cure time by altering the hardener ratio. Contact ATL Composites for specific information.

UNCURED PROPERTIES

	R240	H126 SuperFast	H160 Medium	H161 Slow	H162 Super Slow
Physical State	Clear liquid	Clear pale brown liquid	Clear pale yellow liquid	Clear pale yellow liquid	Clear pale yellow liquid
Viscosity mPas @ 25°C	1600	160	30	25	20
Specific Gravity g/ml @ 25°C	1.15	0.99	0.95	0.94	0.93

CURE CHARACTERISTICS

	H126	H160	H161	H162
Pot Life - 100g @ 25°C (in air)	20 minutes	35 minutes	50 minutes	75 minutes
Thin-laminate OpenTime @ 25°C	2 hours	4 hours 20 mins	4 hours 40 mins	5 hours 30 mins
Demould time @ 25°C	5 hours	12 hours	12 hours	14 hours
Mix viscosity mPas @ 25°C	880	600	470	400
Shore D Hardness -1 day	79	80	74	76
- 2 weeks	82	82	76	77
HDT after 1 day @ 25°C	49°C	42°C	40°C	39°C
2 weeks @ 25°C	56°C	49°C	49°C	47°C
16 hrs @ 40°C	65°C	57°C	55°C	58°C
16 hrs @ 50°C	75°C	67°C	65°C	66°C
8 hrs @ 60°C	79°C	73°C	73°C	71°C
8 hrs @ 80°C	89°C	79°C	78°C	82°C
Ultimate HDT	95°C	82°C	82°C	87°C

MONITORING OF CURE

A laminator wishing to monitor progress of cure has a number of on the spot options open to him. Small test aliquots of mixed resin can be placed in waxed lids during lamination. These should be subjected to the same cure conditions as the actual laminate, and later compared with standard samples which are known to be fully cured. The samples should be flat on the bottom and approximately 2 to 3 mm thick.

Allowance should be made for the possible effect of foam core insulating the curing resin, and reducing the cure of the inner layer.

To monitor the development of Heat Distortion Temperature (HDT) immerse the sample in a container of warming water, noting the temperature at which the sample becomes rubbery. Providing sample thickness is kept constant, this simple technique gives surprisingly reproducible results

The cure time will vary based on the resin and hardener selected, the ambient temperature and laminate thickness.

CALCULATING RESIN/HARDENER FOR A FIBREGLASS LAMINATE

As a rough rule for the amount of resin/hardener required to achieve proper wetting out and consolidation of a laminate, use a 1:1 ratio of fibreglass weight per m^2 to resin/hardener weight, plus wastage

e.g. $1m^2$ of 600grm biaxial E-fibreglass will require 600grms of mixed resin and hardener + a 10% wastage factor

PACK SIZES

Order Code		Order Code		PACK
Resin		**Hardener**		
RC 240	4kg	HC 126	1kg	5kg
		HC 160	1kg	
		HC 161	1kg	
		HC 162	1kg	
RD 240	18kg	HD 126	4.5kg	22.5kg
		HD 160	4.5kg	
		HD 161	4.5kg	
		HD 162	4.5kg	
RF 240	192kg	HF 126	48kg	240kg
		HF 160	48kg	
		HF 161	48kg	
		HF 162	48kg	

STORAGE

KINETIX R240 resin and H126, H160, H161, H162 hardeners will keep for 2 years if kept in original containers at room temperature (15°C to 32°C), and out of direct sunlight. Containers should be tightly sealed to prevent moisture absorption.

HEALTH & SAFETY

KINETIX R240 resin and H126, H160, H161, H162 hardeners have moderate sensitising potential, and should be kept out of the eyes and off the skin.

• Use with good ventilation and adequate safety equipment including impervious gloves and safety glasses.

• If skin contact occurs, remove contaminated clothing immediately, and wash the affected area thoroughly with ATL's 845 hand cleaner and water, avoiding the use of solvents except in the case of massive contamination.

• If eye contact occurs, immediately flush with running water for at least 15 (fifteen) minutes and seek medical advice.

• If swallowed:
Resins - DO NOT induce vomiting, and contact a doctor or the Poisons Information Centre.
Hardeners - DO NOT induce vomiting, give plenty of milk or water and contact a doctor or the Poisons Information Centre.

Appendix G

Data for ANN

Load (N)	Current (A)	Deflection (mm)	No. of Wire
3.668	0.000	1.80	1
3.668	0.500	1.80	1
3.668	1.000	1.60	1
3.668	1.500	0.70	1
3.668	1.700	0.00	1
4.601	0.000	2.26	1
4.601	0.627	2.26	1
4.601	1.254	2.01	1
4.601	1.881	0.88	1
4.601	2.132	0.00	1
5.768	0.000	2.83	1
5.768	0.786	2.83	1
5.768	1.573	2.52	1
5.768	2.359	1.10	1
5.768	2.673	0.00	1
10.167	0.000	4.99	1
10.167	1.386	4.99	1
10.167	2.772	4.44	1
10.167	4.158	1.94	1
10.167	4.712	0.00	1
3.668	0.000	0.80	2
3.668	0.500	0.80	2
3.668	1.000	0.70	2
3.668	1.500	0.65	2
3.668	1.750	0.00	2
4.601	0.000	1.00	2
4.601	0.627	1.00	2
4.601	1.254	0.88	2
4.601	1.881	0.82	2
4.601	2.195	0.00	2
5.768	0.000	1.26	2
5.768	0.786	1.26	2
5.768	1.573	1.10	2
5.768	2.359	1.02	2
5.768	2.752	0.00	2
7.163	0.000	1.56	2
7.163	0.971	1.56	2
7.163	1.941	1.37	2
7.163	2.912	1.27	2
7.163	3.397	0.00	2
10.167	0.000	2.22	2
10.167	1.386	2.22	2
10.167	2.772	1.94	2
10.167	4.158	1.80	2
10.167	4.851	0.00	2
3.668	0.000	0.60	3
3.668	0.500	0.60	3
3.668	1.000	0.55	3
3.668	1.500	0.50	3

3.668	1.760	0.30	3
3.668	1.769	0.00	3
4.601	0.000	0.75	3
4.601	0.627	0.75	3
4.601	1.254	0.69	3
4.601	1.881	0.63	3
4.601	2.208	0.38	3
4.601	2.219	0.00	3
5.768	0.000	0.94	3
5.768	0.786	0.94	3
5.768	1.573	0.87	3
5.768	2.359	0.79	3
5.768	2.768	0.47	3
5.768	2.782	0.00	3
7.163	0.000	1.17	3
7.163	0.971	1.17	3
7.163	1.941	1.08	3
7.163	2.912	0.98	3
7.163	3.416	0.59	3
7.163	3.434	0.00	3
10.167	0.000	1.66	3
10.167	1.386	1.66	3
10.167	2.772	1.52	3
10.167	4.158	1.39	3
10.167	4.878	0.83	3
10.167	4.903	0.00	3
3.668	0.000	0.70	4
3.668	0.500	0.70	4
3.668	1.000	0.65	4
3.668	1.500	0.40	4
3.668	1.770	0.00	4
4.601	0.000	0.88	4
4.601	0.627	0.88	4
4.601	1.254	0.82	4
4.601	1.881	0.50	4
4.601	2.220	0.00	4
5.768	0.000	1.10	4
5.768	0.786	1.10	4
5.768	1.573	1.02	4
5.768	2.359	0.63	4
5.768	2.783	0.00	4
7.163	0.000	1.37	4
7.163	0.971	1.37	4
7.163	1.941	1.27	4
7.163	2.912	0.78	4
7.163	3.436	0.00	4
10.167	0.000	1.94	4
10.167	1.386	1.94	4
10.167	2.772	1.80	4
10.167	4.158	1.11	4

10.167	4.906	0.00	4
3.668	0.000	0.50	5
3.668	0.500	0.50	5
3.668	1.000	0.45	5
3.668	1.500	0.30	5
3.668	1.771	0.10	5
3.668	1.775	0.00	5
4.601	0.000	0.63	5
4.601	0.627	0.63	5
4.601	1.254	0.56	5
4.601	1.881	0.38	5
4.601	2.221	0.13	5
4.601	2.226	0.00	5
5.768	0.000	0.79	5
5.768	0.786	0.79	5
5.768	1.573	0.71	5
5.768	2.359	0.47	5
5.768	2.785	0.16	5
5.768	2.791	0.00	5
7.163	0.000	0.98	5
7.163	0.971	0.98	5
7.163	1.941	0.88	5
7.163	2.912	0.59	5
7.163	3.438	0.20	5
7.163	3.445	0.00	5
10.167	0.000	1.39	5
10.167	1.386	1.39	5
10.167	2.772	1.25	5
10.167	4.158	0.83	5
10.167	4.909	0.28	5
10.167	4.920	0.00	5
3.668	0.000	0.40	6
3.668	0.500	0.40	6
3.668	1.000	0.35	6
3.668	1.500	0.25	6
3.668	1.750	0.10	6
3.668	1.790	0.00	6
4.601	0.000	0.50	6
4.601	0.627	0.50	6
4.601	1.254	0.44	6
4.601	1.881	0.31	6
4.601	2.195	0.13	6
4.601	2.245	0.00	6
5.768	0.000	0.63	6
5.768	0.786	0.63	6
5.768	1.573	0.55	6
5.768	2.359	0.39	6
5.768	2.752	0.16	6
5.768	2.815	0.00	6
7.163	0.000	0.78	6

7.163	0.971	0.78	6
7.163	1.941	0.68	6
7.163	2.912	0.49	6
7.163	3.397	0.20	6
7.163	3.474	0.00	6
10.167	0.000	1.11	6
10.167	1.386	1.11	6
10.167	2.772	0.97	6
10.167	4.158	0.69	6
10.167	4.851	0.28	6
10.167	4.962	0.00	6

Appendix H

Dynalloy Inc. Invoice & Test Rig Approval

FLEXINOL®

DYNALLOY, Inc.

Makers of Dynamic Alloys
14762 Bentley Circle, Tustin, CA 92780

36894
INVOICE No:
3/22/2012
INVOICE Date:
Tel: (714) 436-1206
fax: (714) 436-0511

20680	Sold To:		Ship To:	20680

Sold To:
Martin Geach
University of Southern Queensland,
Central Store, West Street
Toowoomba, Queensland, Australia   4350
Phone: 61-7-4631-1334
Fax:

Ship To:
Martin Geach
University of Southern Queensland,
Central Store, West Street
Toowoomba, Queensland, Australia   4350
Phone: 61-7-4631-1334
Fax:

P.O. No: 40234732081	Salesperson EA/ea	Terms Credit Card	Shipping via FedEx Int'l Priority	FCA Tustin	Date shipped 3/22/2012
100	meter(s) of 0.020" Ø Flexinol® Actuator Wire 90°C			$5.000	$500.00

Made in USA

Sales Tax Number

Sales Tax		$0.00
Shipping etc.		$83.46
Other		

A service charge of 1.5% per month will be charged on all past due amounts.   **Total Invoice USD**   **$583.46**

Dear Armando,
We need your approval
to built this test
rig. this is essential
to perform Eric's
testing.

Regards
Jay;

& Surveying – Quality Management System

Work Request Form

ator in consultation with the relevant Work Centre Manager.

	Job Number

Contact Phone No/Ext: **1335**

Funding Source						
(Please circle appropriate code)						
Teaching:	S	M	E	C	A	En U/G
Research:	(FOES)				USQ	EXT
Postgraduate:	(FOES)				USQ	EXT
Support:	Admin				Tech	Maint
Other:	NCEA				USQ	EXT

SUPERVISOR APPROVAL (to be completed for student initiated requests)	Cost Centre Details :					

Name : **JAYANTHA ERPAARACHCHI**

Signature:

Operations Manager Approval (if applicable)

Signature:

Cost Centre Approval:
(to be completed by authorised signatory only)

Name:

Signature:

Work Required

Job Name: **TEST RIG FABRICATION (SMART STRUCTURE FOR WIND TURBINE**

Details:(attach all drawings and other pertinent information) **YES**

Date Submitted :	Agreed Completion Date :

For Workshop Use Only

Work Centre Manager Approval:

Work Allocated To:

Date Completed: Completion Date Met: Y N

Total Hours: Total Cost: $

Work Satisfactorily Completed:

Signature: Date:

Appendix I

Performance Coefficient M-File

% appendix - Appendix J Coefficient of Power

```matlab
%FUNCTION HANDLE
% Equation of performance from Slootweg (Rotor Model)
%The mechanical power that the rotor extracts from the wind is calculated
using equation (2.1),

% J. G. Slootweg (M'01) received the M.Sc. degree in
% electrical engineering from Delft University of Technology,
% Delft, The Netherlands, in 1998. He is currently
% pursuing the Ph.D. degree on large-scale integration
% of dispersed generation into existing electric
% grids at the Electrical Power Systems Laboratory of
% Delft University of Technology.
%------------------------------------------------------------------------
--------------------
%Eris has used Slootweg eqn for his comparison study.


clear all; clc;
c_1=0.73; c_2=151; c_3=-0.58; c_4=0.002; c_5=2.14; c_6=13.2; c_7=18.4;
c_8=-0.02; c_9=-0.003;
lambda_i=@(lambda,beta) 1./(1./(lambda+c_8*beta)-c_9/(beta^3+1));
cp=@(lambda,beta) c_1*(c_2./lambda_i(lambda,beta)-c_3*beta-c_4*beta^c_5-
c_6).*exp(-c_7./lambda_i(lambda,beta));

%coefficient no. =c_1..........c_9
%performance coefficient = Cp
%pitch angle = beta is the deflection can be initiated one is deflected
%tip speed ratio = lambda



%  0< beta < 1

beta=1; %decide---------------------------------------------------------
--------------------------------------
lambda=0:1:15;
Cp=cp(lambda,beta);
figure,
plot(lambda,Cp,'b-o')
%legend('\beta=0.5')

xlabel('Tip speed ratio, \lambda ','FontSize',14)
ylabel('Performance coefficient, C_p','FontSize',14)
% title('Cp -\lambda performance curve for a modern three-blade
turbine','FontSize',14)
%legend('\beta=0.5','\beta=0.5 using SMA')


hold on

beta=0.2; %decide------------------------------------------------------
--------------------------------------
lambda=0:1:15;
Cp=cp(lambda,beta);
% figure,
plot(lambda,Cp,'r--*')
% legend('\lambda=0.5')
```

```
hold on
%
% beta=2; %decide-----------------------------------------------------------
---------------------------------------
% lambda=0:1:15;
% Cp=cp(lambda,beta);
% % figure,
% plot(lambda,Cp,'k--+')
% % legend('\lambda=0.7','\lambda=0.5')
% % legend('Betz limit','\beta=0.5','\beta=0.5 using SMA','\beta=0.5 when
it deflected')


% xlabel('Tip speed ratio, \lambda ','FontSize',14)
% ylabel('Performance coefficient, C_p','FontSize',14)
% title('Cp -\lambda performance curve for a modern three-blade
turbine','FontSize',14)

hold on

xlim([0 15])
ylim([0 1])
%legend('\beta=0.5','Betz limit','\beta=0.5 using SMA','\beta=0.5 when it
deflected')
legend('\beta=0.5^{\circ} no loss','\beta=0.5^{\circ} using
SMA','\beta=0.5^{\circ} when it deflected')


% beta=0.9;
% lambda=0:1:20;
% Cp=cp(lambda,beta);
% % figure,
% plot(lambda,Cp,'k--+')
% legend('\lambda=0.7','\lambda=0.5','\lambda=0.9')
%
% % xlabel('Tip speed ratio, \lambda ','FontSize',14)
% % ylabel('Performance coefficient, C_p','FontSize',14)
% % title('Cp -\lambda performance curve for a modern three-blade
turbine','FontSize',14)
% %
% hold on
```

Appendix J

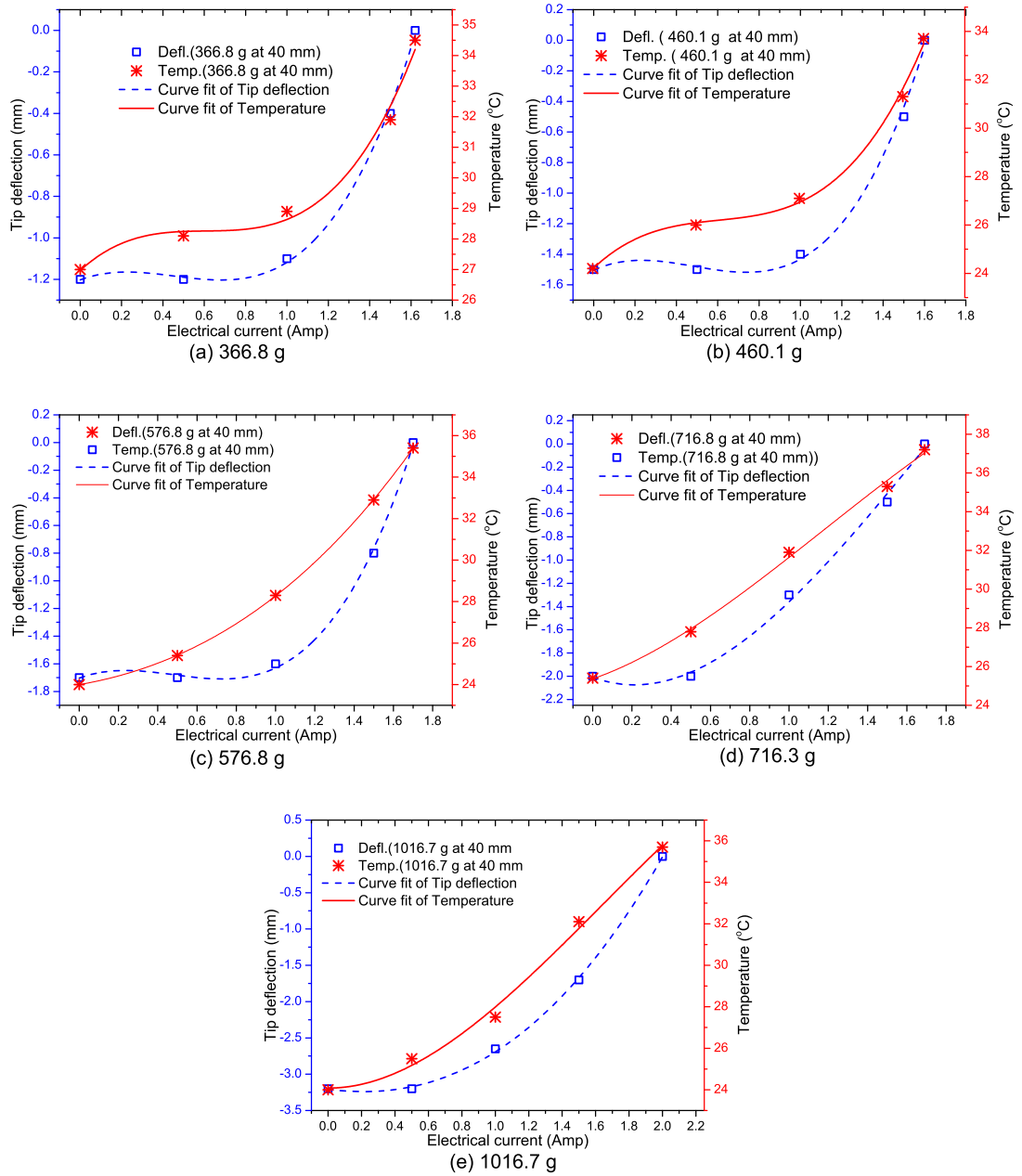# Tip deflection against current at various load at 40, 50 and 60 mm

Figure J.1: Tip deflection against current at various load at 40 mm height, respectively
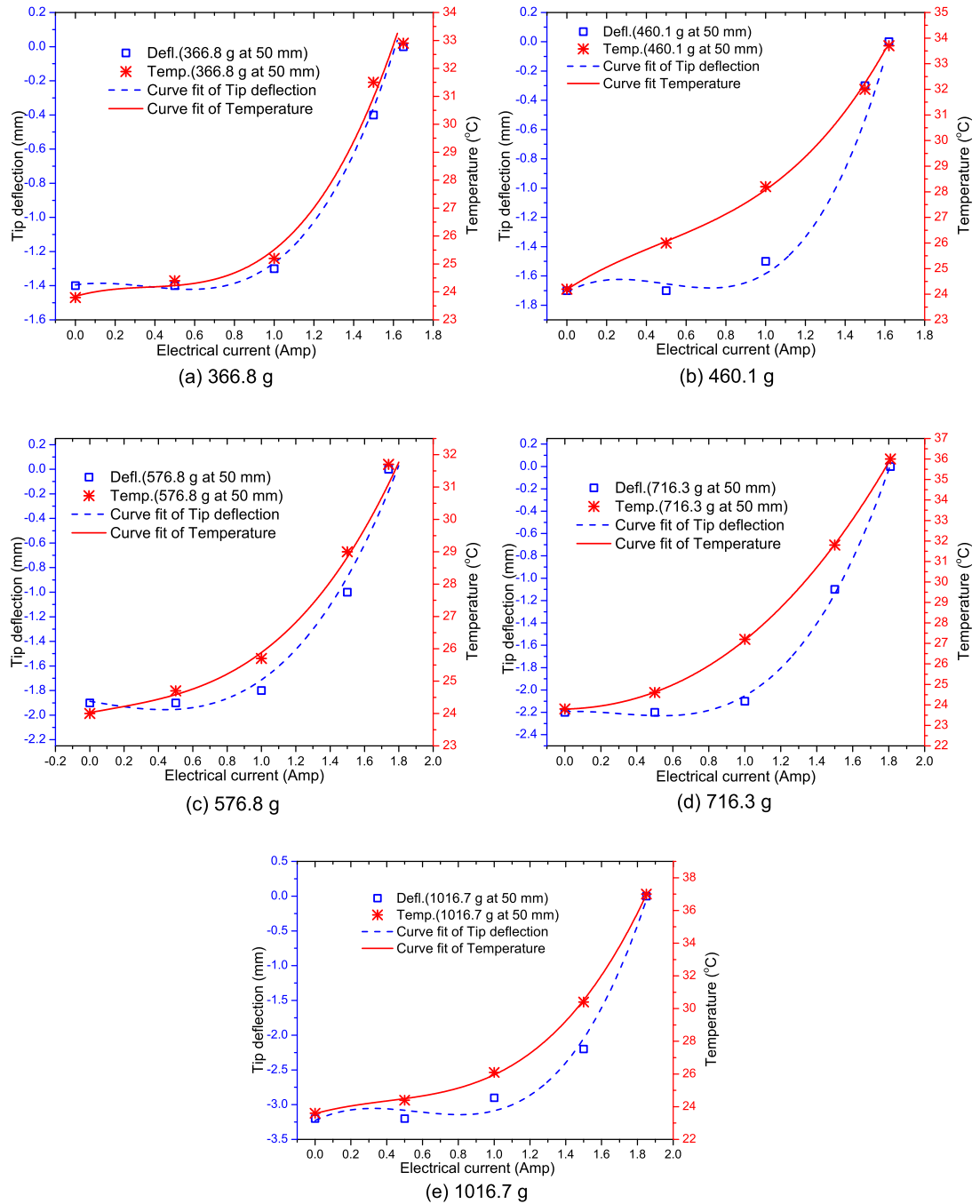
Figure J.2: Tip deflection against current at various load at 50 mm height, respectively
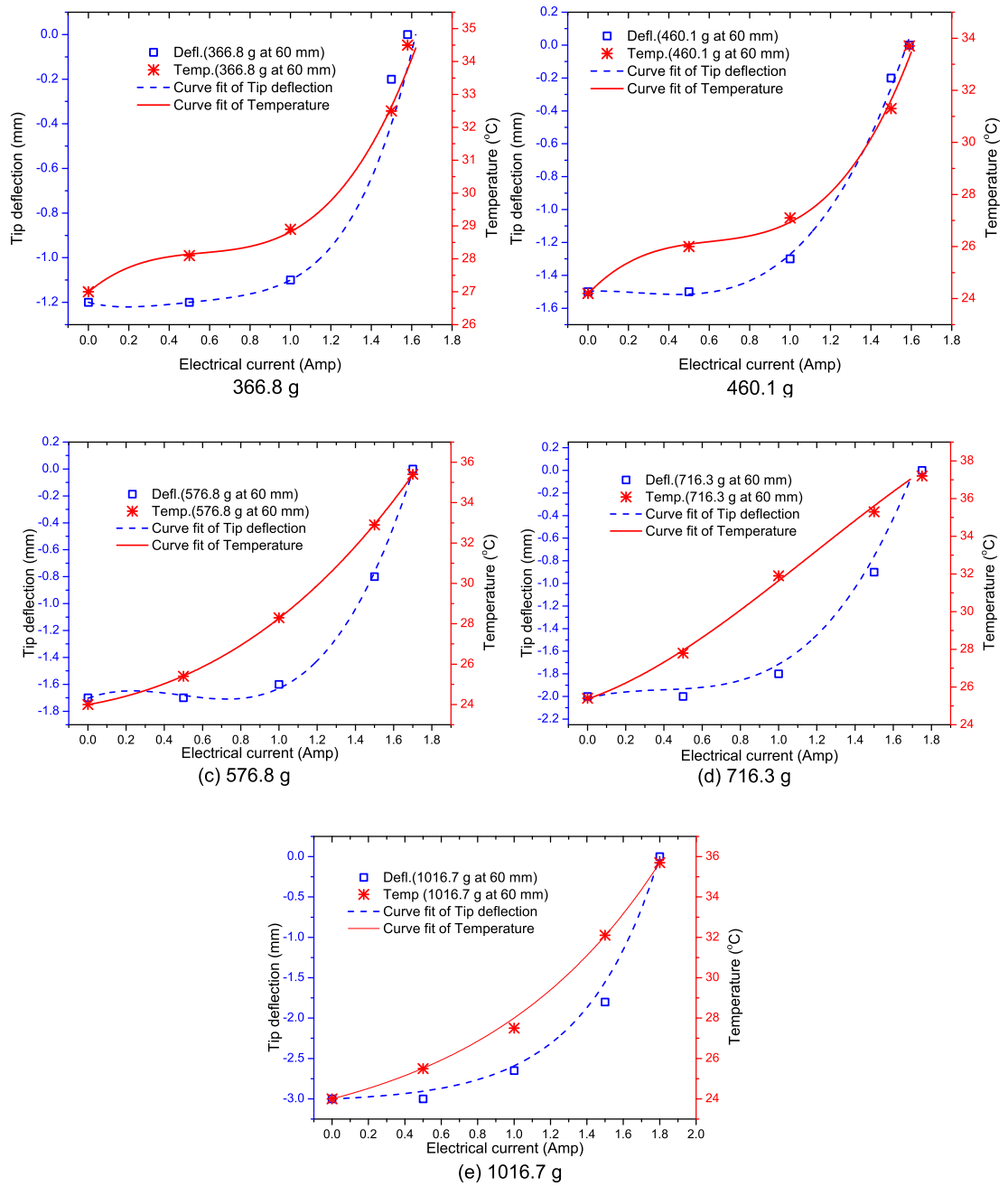
Figure J.3: Tip deflection against current at various load at 60 mm height, respectively.

Appendix K

Effect of Heat Sleeving

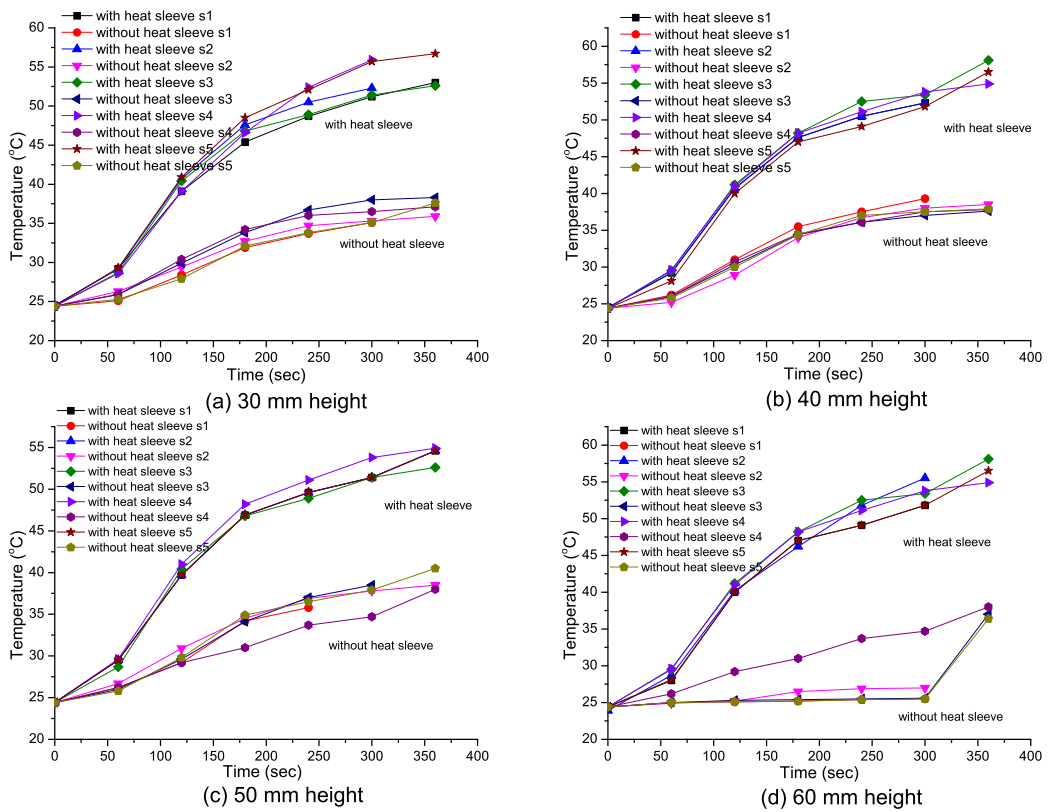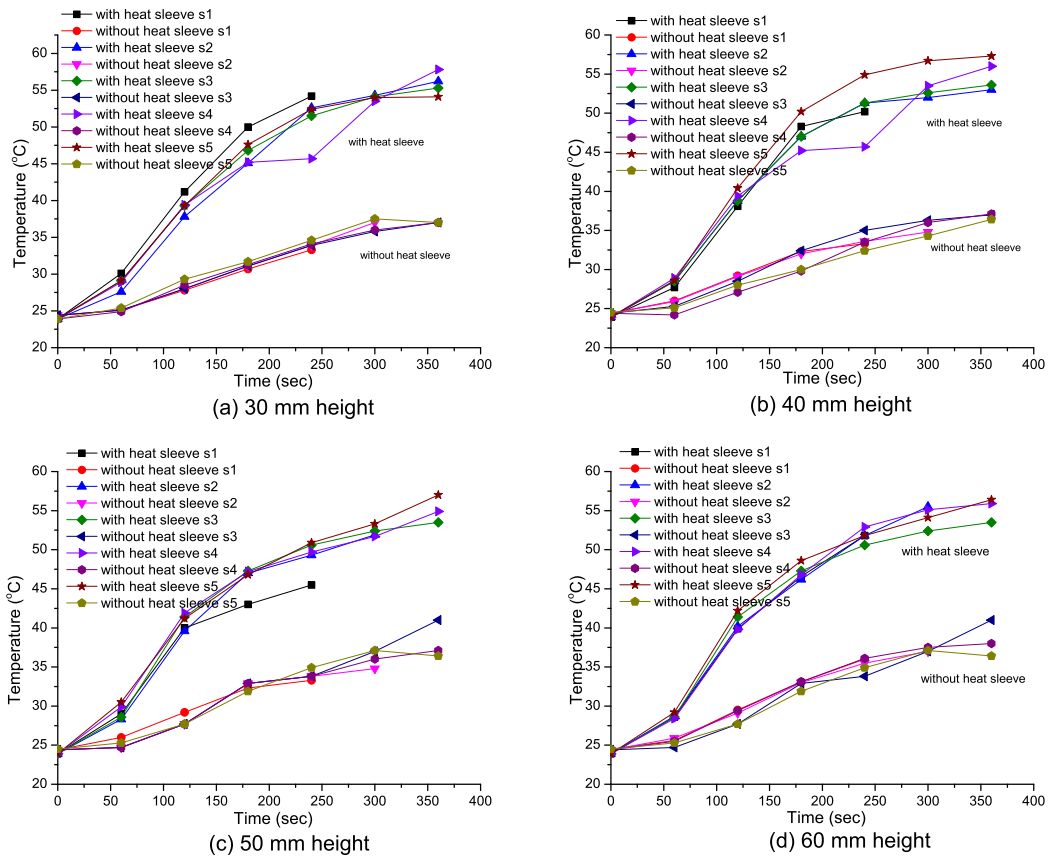Figure K.1: Effect of heat sleeving and without heat sleeving at s1=366.8 g, s2=460.1 g, s3=576.8 g, s4=716.3 g and s5=1016.7 g for 6 SMA wire

Figure K.2: Effect of heat sleeving and without heat sleeving at s1=366.8 g, s2=460.1 g, s3=576.8 g, s4=716.3 g and s5=1016.7 g for 4 SMA wire

Appendix L

Script M-file for ANN 1, ANN 2 and ANN 3

```matlab
% Development of ANN 1 model for performance prediction
% for smart wind turbine blades in which
% applied load (L) electrical current(I),
% deflection (d) as the input vector and
% number of SMA wires (NW) as the
% ouput
% provided by Eris Elianddy Supeni

% Solve an Input-Output Fitting problem with a Neural Network
% Script generated by NFTOOL
% Created Thu Jan 02 09:09:54 SGT 2014
%
% This script assumes these variables are defined:
%
%   input_NN1_matlab - input data.
%   output_NN1_matlab - target data.

inputs = input_NN1_matlab';
targets = output_NN1_matlab';

% Create a Fitting Network
hiddenLayerSize = 10;
net = fitnet(hiddenLayerSize);

% Choose Input and Output Pre/Post-Processing Functions
% For a list of all processing functions type: help nnprocess
net.inputs{1}.processFcns = {'removeconstantrows','mapminmax'};
net.outputs{2}.processFcns = {'removeconstantrows','mapminmax'};


% Setup Division of Data for Training, Validation, Testing
% For a list of all data division functions type: help nndivide
net.divideFcn = 'dividerand';  % Divide data randomly
net.divideMode = 'sample';  % Divide up every sample
net.divideParam.trainRatio = 70/100;
net.divideParam.valRatio = 15/100;
net.divideParam.testRatio = 15/100;

% For help on training function 'trainlm' type: help trainlm
% For a list of all training functions type: help nntrain
net.trainFcn = 'trainlm';  % Levenberg-Marquardt

% Choose a Performance Function
% For a list of all performance functions type: help nnperformance
net.performFcn = 'mse';  % Mean squared error

% Choose Plot Functions
% For a list of all plot functions type: help nnplot
net.plotFcns = {'plotperform','plottrainstate','ploterrhist', ...
  'plotregression', 'plotfit'};
```

```matlab
% Train the Network
[net,tr] = train(net,inputs,targets);

% Test the Network
outputs = net(inputs);
errors = gsubtract(targets,outputs);
performance = perform(net,targets,outputs)

% Recalculate Training, Validation and Test Performance
trainTargets = targets .* tr.trainMask{1};
valTargets = targets  .* tr.valMask{1};
testTargets = targets  .* tr.testMask{1};
trainPerformance = perform(net,trainTargets,outputs)
valPerformance = perform(net,valTargets,outputs)
testPerformance = perform(net,testTargets,outputs)

% View the Network
view(net)

% Plots
% Uncomment these lines to enable various plots.
%figure, plotperform(tr)
%figure, plottrainstate(tr)
%figure, plotfit(net,inputs,targets)
%figure, plotregression(targets,outputs)
%figure, ploterrhist(errors)

% Development of ANN 2 model for performance prediction
% for smart wind turbine blades in which
% applied load (L) , deflection (d), number of SMA wires (NW)
% as the input vector and electrical current(I) as the ouput
% provided by Eris Elianddy Supeni

% Solve an Input-Output Fitting problem with a Neural Network
% Script generated by NFTOOL
% Created Thu Jan 02 09:09:54 SGT 2014
%
% This script assumes these variables are defined:
%
%   input_NN2_matlab - input data.
%   output_NN2_matlab - target data.

inputs = input_NN2_matlab';
targets = output_NN2_matlab';

% Create a Fitting Network
hiddenLayerSize = 10;
net = fitnet(hiddenLayerSize);

% Choose Input and Output Pre/Post-Processing Functions
```

```
% For a list of all processing functions type: help nnprocess
net.inputs{1}.processFcns = {'removeconstantrows','mapminmax'};
net.outputs{2}.processFcns = {'removeconstantrows','mapminmax'};


% Setup Division of Data for Training, Validation, Testing
% For a list of all data division functions type: help nndivide
net.divideFcn = 'dividerand';  % Divide data randomly
net.divideMode = 'sample';  % Divide up every sample
net.divideParam.trainRatio = 70/100;
net.divideParam.valRatio = 15/100;
net.divideParam.testRatio = 15/100;

% For help on training function 'trainlm' type: help trainlm
% For a list of all training functions type: help nntrain
net.trainFcn = 'trainlm';  % Levenberg-Marquardt

% Choose a Performance Function
% For a list of all performance functions type: help nnperformance
net.performFcn = 'mse';  % Mean squared error

% Choose Plot Functions
% For a list of all plot functions type: help nnplot
net.plotFcns = {'plotperform','plottrainstate','ploterrhist', ...
  'plotregression', 'plotfit'};


% Train the Network
[net,tr] = train(net,inputs,targets);

% Test the Network
outputs = net(inputs);
errors = gsubtract(targets,outputs);
performance = perform(net,targets,outputs)

% Recalculate Training, Validation and Test Performance
trainTargets = targets .* tr.trainMask{1};
valTargets = targets  .* tr.valMask{1};
testTargets = targets  .* tr.testMask{1};
trainPerformance = perform(net,trainTargets,outputs)
valPerformance = perform(net,valTargets,outputs)
testPerformance = perform(net,testTargets,outputs)

% View the Network
view(net)

% Plots
% Uncomment these lines to enable various plots.
figure, plotperform(tr)
figure, plottrainstate(tr)
%figure, plotfit(net,inputs,targets)
```

```matlab
%figure, plotregression(targets,outputs)
%figure, ploterrhist(errors)



% Development of ANN 3 model for performance prediction
% for smart wind turbine blades in which
% applied load (L) , electrical current(I), number of SMA wires (NW)
% as the input vector and deflection (d) as the ouput
% provided by Eris Elianddy Supeni

% Solve an Input-Output Fitting problem with a Neural Network
% Script generated by NFTOOL
% Created Thu Jan 02 09:09:54 SGT 2014
%
% This script assumes these variables are defined:
%
%   input_NN3_matlab - input data.
%   output_NN3_matlab - target data.

inputs = input_NN3_matlab';
targets = output_NN3_matlab';

% Create a Fitting Network
hiddenLayerSize = 10;
net = fitnet(hiddenLayerSize);

% Choose Input and Output Pre/Post-Processing Functions
% For a list of all processing functions type: help nnprocess
net.inputs{1}.processFcns = {'removeconstantrows','mapminmax'};
net.outputs{2}.processFcns = {'removeconstantrows','mapminmax'};



% Setup Division of Data for Training, Validation, Testing
% For a list of all data division functions type: help nndivide
net.divideFcn = 'dividerand';  % Divide data randomly
net.divideMode = 'sample';  % Divide up every sample
net.divideParam.trainRatio = 70/100;
net.divideParam.valRatio = 15/100;
net.divideParam.testRatio = 15/100;

% For help on training function 'trainlm' type: help trainlm
% For a list of all training functions type: help nntrain
net.trainFcn = 'trainlm';  % Levenberg-Marquardt

% Choose a Performance Function
% For a list of all performance functions type: help nnperformance
net.performFcn = 'mse';  % Mean squared error

% Choose Plot Functions
% For a list of all plot functions type: help nnplot
net.plotFcns = {'plotperform','plottrainstate','ploterrhist', ...
```

```
  'plotregression', 'plotfit'};


% Train the Network
[net,tr] = train(net,inputs,targets);

% Test the Network
outputs = net(inputs);
errors = gsubtract(targets,outputs);
performance = perform(net,targets,outputs)

% Recalculate Training, Validation and Test Performance
trainTargets = targets .* tr.trainMask{1};
valTargets = targets  .* tr.valMask{1};
testTargets = targets  .* tr.testMask{1};
trainPerformance = perform(net,trainTargets,outputs)
valPerformance = perform(net,valTargets,outputs)
testPerformance = perform(net,testTargets,outputs)

% View the Network
view(net)

% Plots
% Uncomment these lines to enable various plots.
figure, plotperform(tr)
figure, plottrainstate(tr)
%figure, plotfit(net,inputs,targets)
%figure, plotregression(targets,outputs)
%figure, ploterrhist(errors)
```

Appendix M

Running ANN Model Simulation

Sample of Neural Network Training (nntraintool) after Running Simulation